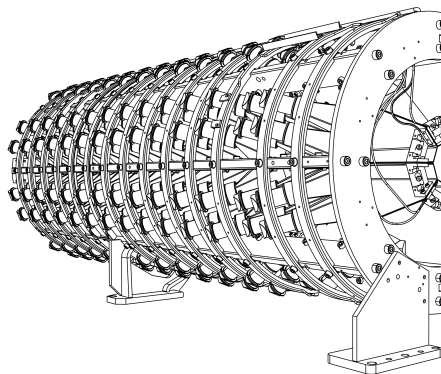


SEARCH FOR GLUON SATURATION IN PROTON-LEAD COLLISIONS AT
 $\sqrt{s_{NN}} = 5.02$ TeV WITH THE VERY FORWARD CASTOR
CALORIMETER AT THE CMS EXPERIMENT

*Navorsing van gluon saturatie in proton-lood botsingen bij
 $\sqrt{s_{NN}} = 5.02$ TeV met de zeer voorwaartse CASTOR
calorimeter bij het CMS experiment*



Dissertatie voorgelegd tot het behalen van de graad van
doctor in de wetenschappen
aan de Universiteit Antwerpen, te verdedigen door

Merijn Hendricus Franciscus van de Klundert

Promotor: Prof. Dr. Pierre Van Mechelen

Antwerpen, maart 2018

Doctoral Committee**Chairman**

Prof. dr. Jan Sijbers, Antwerp University, Belgium

Promotor

Prof. dr. Pierre van Mechelen, Antwerp University, Belgium

Members

Dr. Hans Van Haevermaet, Antwerp University, Belgium

Prof. dr. Jacques Tempere, Antwerp University, Belgium

Dr. Jonathan Hollar, Lisbon Institute of Physics, Portugal

Assoc. Prof. dr. Salim Çerçi, Adiyaman University, Turkey

Contact information

Merijn Hendricus Franciscus van de Klundert

Antwerp University - Department of physics

EDF - Elementaire Deeltjes Fysica

Groenenborgerlaan 171

2020 Antwerp

Belgium

Merijn.VandeKlundert@uantwerpen.be

Merijn Hendricus Franciscus van de Klundert: *Search for gluon saturation in proton-lead collisions at $\sqrt{s_{NN}} = 5.02$ TeV with the very forward CASTOR calorimeter at the CMS experiment,*

© maart 2018

Dedication

Dedicated to my family: Yvonne, Bram, Maarten, and Myrte van de Klundert

INTRODUCTION

Mankind has asked itself fundamental questions about Nature since their very existence, and the modern scientific era has expanded the horizons of our understanding of Nature. We study and understand the universe on larger scales than ever before. Simultaneously, our knowledge about the fundamental particles and forces that govern our universe has grown spectacularly over the past century, which is the domain and goal of particle physics.

The scientific endeavour of particle physics has resulted in, amongst other, the *Standard Model Lagrangian*, which is a mathematical description of three fundamental forces that occur in Nature¹ and the origin of the mass of particles. All known interactions of the fundamental particles are encoded in the Lagrangian.

There exist various methods to study the interactions of the fundamental particles. One approach is to accelerate particles and collide these with high energies. For centuries particle physicists have exploited this method, leading to the discovery of many particles and the extraction of the previously mentioned Standard Model Lagrangian.

The largest collider that has ever been built is the CERN Large Hadron Collider near Geneva. This machine collides (mostly) protons and lead ions with each other at unrivalled energies. The collisions are recorded with cathedral-sized detectors, which are installed underground. The experimental efforts of the LHC research program culminated in the (relatively) recent discovery of the Higgs boson.

Hadrons consist of smaller, fundamental constituent particles that are called quarks. The strong force, which is called QCD, *confines* the quarks into hadrons. This force is mediated by the exchange of messenger-particles, which are called gluons. These gluons have a peculiar behaviour though: they also interact with each other. For this and other reasons, it is not trivial to predict the structure of hadrons from first principles from the Standard Model Lagrangian. Therefore, approximations and assumptions need to be made when calculating either the structure or the interactions of hadrons.

It is hypothesised that in a certain kinematic regime of hadrons the gluon density becomes large, and that this leads to *recombination reactions* between the gluons. Such non-linear QCD reactions would manifest themselves in various observables in hadronic collisions. This topic has been at the focal point of the particle physics community for decades².

In this thesis, we aim to impose a stringent test to the hypothesis of gluon saturation. To this purpose we study proton-lead collisions at the LHC, since the non-linear reactions are expected to be enhanced in a heavy ion w.r.t. a proton. Since we cannot observe the gluons directly, we study their *remnants* instead, which are jets. To enhance the sensitivity of our

¹ The fourth fundamental force, which is gravity, is currently not successfully included

² We refer to a recent article in The Guardian closely related to the hypothesis of this thesis: <https://www.theguardian.com/science/life-and-physics/2017/dec/28/after-40-years-of-studying-the-strong-nuclear-force-a-revelation>.

analysis, we present a jet measurement in an unprecedented part of the phase-space, where effects of saturation are expected to manifest themselves very pronounced.

To perform the actual measurement, we utilise the CASTOR calorimeter, which is a subsystem of the CMS experiment. This detector is unique at the LHC, since no other calorimeter is installed in this region of phase-space at any other experiment. Since this is the first analysis of CASTOR jets to target journal publication, the results of this thesis do not only address the hypothesis on gluon saturation, but also aim at firmly establishing the experimental viability of a measurement of jets with CASTOR.

In the first part of this thesis, we start with providing a general introduction to modern particle physics. This is followed by a discussion on the structure of hadrons and evolution equations, which allows us to introduce the concept of gluon saturation. Next, we provide an explanation on how the theory translates to experimental observables. We finish the part with discussing the experimental state-of-the-art concerning gluon saturation.

The second part is entirely devoted to specifying the hypothesis of this thesis and the strategy towards addressing it.

In the third part, we introduce the experimental setup, and present a succinct introduction to the LHC and the CMS experiment. This is followed by a more in-depth discussion on the principle of calorimetry and CASTOR, since this is the key detector of the analysis.

In the fourth part we discuss the data analysis. This ultimately leads to the conclusions chapter, in which we finally reflect on the thesis hypothesis. A summary in English and Dutch is provided.

PUBLICATIONS, PRESENTATIONS, AND PERSONAL CONTRIBUTIONS

PUBLICATIONS AND PRESENTATIONS ON ORIGINAL WORK FROM THE AUTHOR

Results on CASTOR jets in proton-lead collisions

A paper on the final results of this analysis with title:

Measurement of the inclusive very forward jet cross sections in $p+Pb$ collisions at $\sqrt{s_{NN}} = 5.02$ TeV is in collaboration wide review for submission to JHEP (Journal of High Energy Physics). The following figures are included in the paper: Fig. 62, 63, 85, 81, 82, 83, and 84.

Preliminary results on the CASTOR jet cross sections appeared in [1]:

Very forward inclusive jet cross sections in $p+Pb$ collisions at $\sqrt{s_{NN}} = 5.02$ TeV. Tech. rep. CMS-PAS-FSQ-17-001. Geneva: CERN, 2017. URL: <https://cds.cern.ch/record/2258273>.

The preliminary results were presented by the author at the DIS'17 conference and published in the Proceedings of Science [2]:

Merijn H. F. van de Klundert. "Very forward inclusive jet cross sections in $p+Pb$ collisions at $\sqrt{s_{NN}} = 5.02$ TeV at CMS." in: *PoS DIS2017* (2018), p. 045.

A seminar was presented by the author on January 11, 2018 on "Probing gluon saturation using very forward jets in $p+Pb$ at CMS" at the Institut Physique Nucleaire, Orsay (Paris).

Results on the performance of CASTOR during LHC Run II

Results on the performance of the CASTOR calorimeter appeared as preliminary result in [3]: "Results on CASTOR Performance during LHC Run 2." In: CMS-DP-2016-006 (2016). URL: <http://cds.cern.ch/record/2133152>.

The results that were mentioned above were presented as plenary talk by the author at the CALOR'16 conference [4]:

Merijn H F Van De Klundert. "Performance of the CASTOR calorimeter at CMS during Run II of LHC." in: CMS-CR-2016-156 (2016). URL: <http://cds.cern.ch/record/2203099>.

A draft paper with title:

The CASTOR very forward calorimeter of CMS

is prepared for submission to JINST (Journal of Instrumentation)[5].

Ten results (which are original work of the author) are included in the following figures:

Fig. 40, 41, 42, and 43.

A plenary talk was given by the author on "The performance of CASTOR during LHC Run II" at the CMS General Weekly Meeting, February 25th 2016, CERN.

GENERAL REVIEW PRESENTATIONS

A plenary talk on soft QCD at ATLAS and CMS was given at the Moriond'17 conference [6]: Merijn H F Van De Klundert. *SOFT QCD AT ATLAS AND CMS*. tech. rep. CMS-CR-2017-121. Geneva: CERN, 2017. URL: <https://cds.cern.ch/record/2263388>.

A presentation on "Forward and Small-x QCD Physics with CASTOR" was presented at the Inter-university Attraction Pole meeting at the Vrije Universiteit Brussel, December 12, 2016:

<http://indico.ihe.ac.be/indico/contributionDisplay.py?contribId=15&sessionId=0&confId=1067>.

ORIGINAL WORK FROM THE AUTHOR IN THIS THESIS

Every figure that does not have an explicit citation or declaration in its caption represents a result obtained by the author.

ACKNOWLEDGEMENTS

Pursuing a PhD in a foreign country is a great opportunity that comes with a variety of challenges, and I'm deeply grateful and indebted to everyone who helped me in one way or another to reach this point. It would be impossible to list everyone who contributed to this thesis. Nonetheless, I'd like to thank a (non-exclusive) number of people in particular for all their help, commitment, and advice.

Firstly, I'd like to thank my supervisor Pierre van Mechelen for the great opportunity to pursue a PhD in the Antwerp EDF group. It was a pleasure to work with an absolute scientific authority in our field. I benefitted from all the advice, directions, and commitment that occasionally extended well beyond office hours. Besides of his insight in all aspects of QCD and priorities in experimental analyses, Pierre has an exceptional talent to play the Devils Advocate when needed. This was not only helpful in preparing my analysis and conference talks, but also helped in shaping a more critical academic attitude. I'm also very grateful for all the academic and logistical support for attending conferences and travelling to CERN; all these great opportunities are certainly not evident for a doctoral student.

Further, I'd like to thank Wim Beaumont for the nice and intensive introduction to the hardware, commissioning, and operation procedures of a calorimeter. I very enjoyed the (intensive) working days at point five, and the work contributed enormously to my development as an experimental particle physicist.

This work would never have been completed without the kind help of Hans van Haevermaet. His calm and thorough attitude towards research is inspiring. I greatly benefitted in particular from his vast knowledge on CASTOR, and in a later phase also from his advice as FSQ convenor.

Besides of these key figures, I'd like to express my gratitude to the other members of the Antwerp EDF group, in particular my former CMS office mates Albert, Alex, Benoit, Paolo, and Tom, who made boring days a rare occasion. Also, I'm most grateful for the many interesting discussions I had with Sara Alderweireldt and Pieter Taels. I highly profited from Pieters pedagogical explanations, as well as his didactical and well-written thesis. Also Hannes Jung and Francesco Hautmann deserve a special thanks for their friendly help with my numerous questions. I'm indebted to Sarah van Mierlo for all her logistical support and enjoyed the friendly discussions we had.

Further, I'd like to thank my jury, consisting of Jan Sijbers, Pierre van Mechelen, Hans Van Haevermaet, Jacques Tempere, Jonathan Hollar, and Salim Çerçi, for their commitment, friendly attitude, and their comments which improved the quality of this document. I'd like to thank Jorgen d'Hondt and Kerstin Borrás for their friendly feedback concerning chairing the CMS Young Scientists Committee. Also, I'm indebted for the great support from the Tier-2 team from the IIHE in Brussels and their commitment. Special thanks to Olivier Devroede and Romain Rougny.

Mentioning all the great and inspiring scientists of CMS, TOTEM, and CERN I've met and worked with during my PhD would unfortunately extend the size of this document well beyond its intended length. A few deserve a special thanks though. The CASTOR group is a relatively small group, which nonetheless has been very productive. I cherish good memories to the group and the collaboration with Ralf Ulrich.

Also, I'd like to thank the CMS technical and run coordination teams. Their support was absolutely indispensable when the 2015 proton reference run had to be recorded. In this context I would also like to thank Michael Murray and the ZDC team, and Manfred Jeitler for the nice collaboration.

Furthermore, during this reference run common data-taking with the TOTEM experiment was achieved, and I'd like to thank in particular Valentina Avati for a sleepless night at the TOTEM barracks monitoring the TOTEM detectors. The collaboration with Leszek Grzanka also produced a preliminary common CMS-TOTEM simulation for a CASTOR-T2 jet analysis, and it was inspiring to work and learn from him. I hope a common CASTOR-T2 analysis will once see the light, and we are actually two steps closer in my opinion.

I'm grateful for the support from Axel Naumann from the CERN ROOT team for helping with compatibility problems when installing various software packages together.

The interpretation of the final results of this thesis highly benefitted from the collaboration of the Antwerp group with Krzysztof Kutak and his team. I'm very grateful for all their efforts and cherish the memories of our nice trips to Krakow. Furthermore, I enjoyed a smooth collaboration with Pablo Rodriguez on behalf of the AAMQS team; I'm very grateful for their predictions, which add to the interpretation of our results.

I'd like to thank my family for their enduring support in reaching this point, and their commitment to my development and wellbeing. I enjoyed the calm writing periods at Hoevelaken. In particular, I'm very grateful to my father. All his advice and support have absolutely helped me in setting priorities and completing my PhD. The inspiration of his gift of Stephen Hawking's book carried a long way. Furthermore, I cherish good memories to our laid-back days and dinners in Antwerp.

Finally, I'd like to thank my friends for their indispensable faith and support. Especially when living abroad there is no place like home. I also met very friendly people in Belgium, who made my time in Antwerp so much more than only doing research. I climbed, hiked, and travelled with many inspiring people, of whom I met many via the ALPUA. In particular, I'd like to thank Anastasia, Celine, Chris, Daan, Elma and Rick, Gabor, Jonas, Jan, Julie, Koen, Martijn, Nils, Philip, Piotr, Stephan, and my friends from USR for all their support and the great times we had!

CONTENTS

I	SATURATION: THEORETICAL AND EXPERIMENTAL STATE-OF-THE-ART	1
1	NATURAL UNITS AND KINEMATICS	3
1.1	Natural units	3
1.2	Four vector kinematics	3
1.3	Cross section definition	5
2	THE STANDARD MODEL OF PARTICLE PHYSICS	7
2.1	Introduction	7
2.2	Relativistic wave equations of boson and matter fields	7
2.3	Gauge invariance and gauge fields	8
2.4	Non-Abelian gauge theories and self-interactions	9
2.5	The Brout-Englert-Higgs mechanism	10
3	INTRODUCTION TO QUANTUM CHROMODYNAMICS	13
3.1	Renormalisation of divergent amplitudes	13
3.2	Renormalisation group equations	14
3.3	The running coupling of QCD	15
4	THE STRUCTURE OF HADRONS	19
4.1	The cross section for elastic e+p scattering	19
4.2	The quark parton model of e+p scattering	21
4.3	Intermezzo: bremsstrahlung general law	25
4.4	QCD Corrections to the quark parton model	26
5	EVOLUTION EQUATIONS FOR PARTON DENSITIES AND EMISSIONS	31
5.1	Collinear factorisation	31
5.2	k_T -Factorisation and gluon saturation	34
5.3	Intermezzo: unitarity violation and gluon saturation	39
5.4	Breakdown of factorisation	42
5.5	Summary	42
6	SOFT HADRONIC INTERACTIONS	45
6.1	Regge-Gribov theory	45
6.2	Nuclear shadowing	48
7	FROM PARTONS TO JETS IN HADRONIC COLLISIONS	51
7.1	QCD Reactions in hadronic interactions	52
8	EXPERIMENTAL STATE-OF-THE-ART	55
8.1	Introduction	55
8.2	Results on e+p collisions	55
8.3	Results on hadron-hadron collision	58
8.4	Summary	59

II	THESIS HYPOTHESIS: AN UNPRECEDENTED EXPERIMENTAL SEARCH FOR SIGNALS OF SATURATION	61
III	THE EXPERIMENTAL SETUP	65
9	THE LARGE HADRON COLLIDER	67
9.1	Introduction	67
9.2	Design of the Large Hadron Collider	68
9.3	Proton-lead collisions at the LHC	69
10	THE COMPACT MUON SOLENOID EXPERIMENT	71
10.1	Introduction	71
10.2	The CMS tracker	74
10.3	Forward instrumentation	76
10.4	The trigger system of CMS	77
10.5	The CMS data acquisition	80
10.6	Software and simulation	82
11	CALORIMETRY	85
11.1	Introduction	85
11.2	Showers in calorimeters	85
11.3	Detection mechanisms	86
11.4	The response and resolution of calorimeters	88
12	THE CASTOR CALORIMETER	89
12.1	Introduction	89
12.2	The performance of CASTOR during LHC Run II	91
12.3	Summary and overview of data-taking campaigns	103
IV	DATA ANALYSIS	108
13	DATA SAMPLES	109
14	EVENT GENERATORS AND SIMULATED EVENT SAMPLES	111
14.1	General-purpose event generators	111
14.2	Hybrid-factorisation models	114
14.3	Sizes of the event samples	117
15	ONLINE AND OFFLINE EVENT SELECTION	119
15.1	Online event selection	119
15.2	Offline event selection	119
15.3	Summary of the event selection	122
16	PERFORMANCE OF CASTOR DURING $\sqrt{s} = 5.02$ TeV LHC RUN I P+Pb DATA TAKING	123
16.1	Alignment	123
16.2	Bad channels	124
16.3	Summary	124
17	CORRELATING VERY FORWARD PARTICLE JETS TO PARTON JETS	125
17.1	Introduction	125
17.2	Event generation and selection, and jet collections	125

17.3	Results	126
17.4	Conclusions	128
18	CALIBRATION AND VALIDATION OF CASTOR JETS	131
18.1	Introduction	131
18.2	Constructing CASTOR jets	131
18.3	Discriminating hadronic CASTOR jets	132
18.4	Calibrating CASTOR jets in data and simulation	133
18.5	Validation of CASTOR jets	138
19	UNFOLDING THE INCLUSIVE CASTOR JET SPECTRUM	139
19.1	Introduction and motivation for unfolding	139
19.2	Event selection on particle level and event-matching results	140
19.3	Constructing and optimising the response object	143
19.4	Unfolding the inclusive CASTOR jet spectrum	146
19.5	The model dependence in the final unfolded spectrum	153
19.6	Validation: the bottom-line test	154
19.7	Summary: procedure and parameters for unfolding	156
20	SYSTEMATIC UNCERTAINTIES	159
20.1	Sources of systematic uncertainty	159
20.2	Uncertainty propagation by an example: the model dependence	160
20.3	Testing the pileup-safeness of the event selection	160
20.4	The final spectra with all uncertainties added cumulatively	162
21	RESULTS	165
21.1	Results on p+Pb collisions	166
21.2	Results on Pb+p collisions	167
21.3	Results on the ratio p+Pb/Pb+p	168
21.4	Results on detector level	168
22	CONCLUSIONS	171
23	SUMMARY	175
24	SAMENVATTING	179
V	APPENDIX	183
A	APPENDICES	185
A.1	Results on p+Pb collisions prepared for journal submission	185
A.2	Global symmetries of the Standard Model	185
A.3	Kinematics in DIS scattering	186
A.4	The optical theorem	187
A.5	Technical analysis information	188
A.6	Generator-level particles for jets	190
A.7	Calculation of the χ^2/N_{dof} between the backsmearred and data spectrum	190
A.8	CASTOR-T2 Flowjets	191
	BIBLIOGRAPHY	195

LIST OF FIGURES

Figure 1	Left: a simple illustration of a general $2 \rightarrow 2$ process. Right: an illustration of the relation between the solid angle θ and η [7].	4
Figure 2	Left: the particles of the standard model. It should be noted that all fermions also occur as anti-particle in Nature [8]. Right: the interactions between the particles of the standard model [9]	7
Figure 3	Divergent amplitudes occurring in QCD to leading order in α_s . Fermions are depicted by solid lines, while the gluons are represented by the wavy lines. The dashed line represents a ghost field, which is needed to retain next-to-leading order amplitudes of non-Abelian theories gauge-invariant. Upper diagrams: the amplitudes contributing to the self energy of the gauge bosons. Lower left diagram: the amplitude contributing to the self energy of the fermions. Lower right diagrams: the amplitudes contributing to the fermion gluon vertex factor	14
Figure 4	Left: vacuum polarisation for an Abelian gauge theory. We observe that fluctuations lead to charge screening. Right: vacuum polarisation for a non-Abelian gauge theory. The $1/r^2$ field is depicted in (a), together with a fluctuation \mathbf{A}^2 . The combination of these two field is a sink of the field \mathbf{E}_3 , illustrated in (b). The field \mathbf{E}_3 , combines with \mathbf{A}^2 . The net effect, illustrated in (c), is that of a dipole. Since the dipole points to the original charge, the latter is enhanced. Fig. from [17]	17
Figure 5	A schematic illustration of an elementary $2 \rightarrow 2$ process	19
Figure 6	Left: the σ/σ_{Mott} distribution of the proton [21]. We observe a dramatic change in the q^2 dependence between elastic and inelastic scattering. Right: a diagram representing a DIS reaction, together with the kinematic variables. Bottom: F_2 for e+p interactions as a function of Q^2 [22]	28
Figure 7	The radiative corrections to $\mathcal{O}(\alpha_s)$ to the QPM. The upper diagrams directly contribute to e+p scattering, while the lower diagrams only contribute directly in hadron-hadron interactions. Upper left diagrams: the QCDC process, which represents the contribution for measuring a quark in a quark. Upper right diagrams: the BGF process, which represents the contribution for measuring a quark in a gluon. Lower left diagram: the contribution for measuring a gluon in a quark. Lower right diagram: the contribution for measuring a gluon in a gluon.	29
Figure 8	A schematic illustration of a Drell-Yan process, including higher order effects	31

Figure 9	A schematic picture of a parton ladder. Solutions to the DGLAP equations are obtained by applying a strong ordering condition on the successive emissions: $k_{T,1}^2 \ll k_{T,2}^2 \cdots \ll k_{T,N}^2 \ll Q^2$	34
Figure 10	The parton distribution functions from HERAPDF1.0, extracted from fits to e+p data from the HERA and ZEUS experiment [29]. We observe the gluon distribution is dominant at low x -values, and grows strongly with Q^2	34
Figure 11	The forward elastic interaction of a photon with a hadron in the dipole formalism. The transversal position of the quark is depicted x and the anti-quark is at y . The hadron, which is highly Lorentz contracted in the dipole frame, is depicted with the grey blob	36
Figure 12	The diagrams representing the virtual (top) and real (bottom) contributions to the dipole	37
Figure 13	The unintegrated pdf [30], obtained by linear and non-linear fits to HERA data. The updf is depicted for $x = 10^{-2} \cdots 10^{-5}$; the linear updf grows progressively with decreasing x , while the peak value of the non-linear updf shifts progressively to higher k_T values for decreasing x -values. The fast rise of the gluon distribution with increasing rapidity, and the non-triviality of modelling the k_T distribution below 1 GeV is manifest for the linear updf (the solution below 1 GeV is fixed by continuity). The increase of the mean value of the non-linear with increasing rapidity can be interpreted as the rise of the saturation scale. Below the saturation scale, the rise of the gluon density with k_T goes as k_T^2 , while above Q_s it is expected to behave as $1/k_T^2$ [32]	40
Figure 14	A schematic overview of the various evolution equations in the $\ln(Q^2), \ln(1/x)$ plane. It should be noted that the transition between BFKL (dilute regime) and BK (dense regime) evolution is expected to set in gradually. The saturation scale, of which the evolution is also described by the BK equation, has also been depicted; it becomes a straight line in this plane. The DLL solution is also indicated	43
Figure 15	Left: two Reggeon trajectories (solid lines) together with measured resonances [43]. The Pomeron trajectory has been drawn with the dashed line. Right: the total p+p and p+p̄ cross section. The experimental data points have been fitted with the Regge equation for the total cross section. The fitted parameters are displayed in the graph [44]	46

Figure 16	The Pomeron in perturbative QCD, in different levels of complexity [44]. The blob diagram, representing the unknown interaction, is given in diagram (a). In (b) the phenomenological Pomeron exchange is depicted. In (c) the Pomeron is envisaged as being due to two-gluon exchange; this exchange may accommodate for the vacuum quantum numbers of the Pomeron. In (d) a "Reggeised" Pomeron is depicted. This corresponds to the perturbatively calculable Regge trajectory of the gluons, including their self-interactions. Diagram (e) represents non-perturbative Pomeron exchange at small- t ; in this situation the partons only interact with the QCD vacuum fluctuations	47
Figure 17	Diffraction event classification [49]. (a) Non-diffractive events. (b) Single-diffractive events, characterised by a rapidity gap. (c) Double-diffractive events, characterised by a rapidity gap. (d) Central diffractive events, which can be classified by multiple rapidity gaps	48
Figure 18	An illustration of a proton-lead collision [50]. The transversal distance between the incoming proton and the centre of the nucleus is denoted by the impact parameter b . The purple nucleons of the nucleus interact with the proton, and are called participants	49
Figure 19	Left: the one-step (upper diagram) and two-step (lower diagram) contributions to lepton-nucleus scattering. The interference of the two-step amplitude is constructive for Reggeon exchange, leading to anti-shadowing at large- x . For Pomeron exchange the interference is destructive, leading to shadowing at low- x values. The effects on F_2^A have been depicted quantitatively in the right-hand graph. The figures are from [52]	50
Figure 20	An illustration of a hadron-hadron collision [53]	51
Figure 21	Hera data on F_2 with rcBK fits. Left: the linear and non-linear fits from the KS collaboration [30]. Right: the fit from the AAMQS collaboration [65]	57
Figure 22	The saturation scale as extracted by the AAMS collaboration, for the GBW (red) and RV model (blue) [68]	57
Figure 23	Forward particle spectra measured at the RHIC experiments together with various model predictions [70]. The fit indicated with h refers to a particular parameterisation as extracted by the AAMQS collaboration. Left: p+p collisions. Right: d+Au collisions	58
Figure 24	Central-inclusive particle spectra in p+p collisions at $\sqrt{s} = 2$ TeV (left, CDF) and $\sqrt{s} = 7$ TeV (right, LHC) [78]. Lower: the ultra-forward neutral pion p_T spectrum for $\sqrt{s} = 5.02$ TeV p+Pb collisions [77]. The rcBK predictions of the AAMQS collaboration have been included for various initial condition	60

Figure 25	The acceptances of the large LHC experiments. These have been adjusted to the centre-of-mass system of a 5 TeV proton-lead collision, with the proton towards CASTOR. The kinematic regime of the HERA measurements is overlaid. The collinearly improved proton saturation scale has been parameterised as $Q_s(x) = ce^{\lambda/x}$. We fixed λ to 0.3 [37]. Given the slope parameter, we adjusted $Q_s^2(p)$ to 0.36 at $x = 0.01$ [68]. The nuclear saturation scale $Q_s^2(p)$ is enhanced with a factor $A^{1/3} = 5.9$ w.r.t. the proton saturation scale. The parameterisation of the Kutak-Sapeta (KS) saturation scales were obtained in a private communication	62
Figure 26	Left: a succinct history of modern particle accelerators and their centre-of-mass energies [81]. Right: an overview of the LHC collider and its experiments [82]	67
Figure 27	A schematic drawing of the design of an LHC magnet [83]	68
Figure 28	The integrated luminosity delivered to CMS during the 2013 proton-lead collision campaign [50]	70
Figure 29	Top: a schematic picture of the CMS detector [87]. Bottom: a transversal view on the central part of the CMS detector, together with the trajectories of various particles [88]	72
Figure 30	A detailed drawing of the CMS inner tracker system. The acronyms are given in the text. Each line denotes a layer of silicon [90]	75
Figure 31	A bunch crossing with multiple collisions. The tracks reconstructed by the tracker are depicted in green. Overall 78 individual vertices could be reconstructed, which are indicated in yellow [91]	75
Figure 32	The forward detectors of the CMS and TOTEM collaborations, installed at the LHC interaction point five [50]	76
Figure 33	A schematic drawing of a channel from the HF detector [90]	78
Figure 34	The architecture of the L1 trigger of CMS [90]	79
Figure 35	The architecture of the data-acquisition system of CMS [90]	80
Figure 36	Left: shower development frozen in a slab of plastic [97]. Right: the stopping power of copper for muons, as function of the muon momentum [15]. It can be observed that different processes are dominant at different energies	87
Figure 37	The location of CASTOR at CMS. The distance between the interaction point (IP) and CASTOR ≈ 14 m [98]	89
Figure 38	Left: schematic drawing of one CASTOR half. The diameter of CASTOR is roughly 0.6 m, its length approx [101]. 1.6 m. Right: schematic drawing of a CASTOR channel [102]	90

Figure 39	Left: a simulation of the impact of an offset of the position of CASTOR on the pseudorapidity acceptance and energy response [5]. Right: the distance of infrared position sensors at the interaction point side of CMS in mm w.r.t beam pipe during a full cycle of the magnet ramp. Near and Far indicate the different halves of CASTOR. The time span on the x -axis is of the order of a few days [5]	92
Figure 40	Pedestal charge spectrum for the noisiest capacitor of a typical CASTOR channel (tower 12, module 12) for various cathode and last dynode voltage settings. A Gauss fit to the data at 0 V is also shown. . . .	93
Figure 41	Overview of pedestal and variance measurements with 1500 V supplied to the PMTs. Two malfunctioning channels were not considered in this analysis. These data were recorded in 2015	94
Figure 42	Left: response of the PMT of tower three module one during the characterisation to changing high voltage settings. Right: the response to physics events for the same channel. It should be noted the normalisation in this graphs is rather arbitrary; the signal strength on the right hand side corresponds to the pulse intensity of the laboratory measurements, while the left hand side signal strength corresponds to 5 TeV p+p collisions	95
Figure 43	Distributions of the weighed difference, $\Delta G = (G_1 - G_2) / \sqrt{\sigma_{G_1}^2 + \sigma_{G_2}^2}$, between two sets of gain correction factors obtained by different methods. Left: muon HV to proton physics HV between LED and characterisation method at $B = 0$ T. Right: between LED and physics events analysis method at $B = 3.8$ T. Bottom: muon HV to heavy-ion physics HV between LED and physics events analysis method at $B = 3.8$ T. . .	97
Figure 44	The signal spectrum of an EM module of CASTOR, after the offline muon selection for $B = 0$ T [5]. The noise distribution is depicted in red, the signal is represented by the blue dots. The green line represents a tuned PMT model, which corresponds well with the measured muon signal. The threshold to distinguish noise from signal is depicted in black. The average number of photoelectrons of the PMT models $\langle N_{p.e.} \rangle$ is 0.58	99
Figure 45	The energy deposit in HF with the model dependent extrapolations to the CASTOR acceptance [107]. The extrapolations were normalised to the HF measurement	101
Figure 46	A visualisation of CASTOR in its installation location [5]. The T2 detector can be seen in front of the detector. The other materials belong to the LHC infrastructure	102
Figure 47	Profiles of MinBias p+p collision data with various event generators. Left: the z -profile of hadronic showers in CASTOR [108]. Right: the ϕ -profile [5]. The data were collected in 2015 at $B = 0$	103
Figure 48	A schematic description of the modelling of soft and hard interactions in RGT-based models [120]	113

Figure 49	Nuclear modification of structure function from nuclear DIS data used by HIJING [126, 127]	114
Figure 50	The nuclear updf as determined by Kutak-Sapeta [30]	115
Figure 51	Distributions of observables used for the offline event selection for ZB+PixelTrack events in data and simulation. Top: the energy distribution in HF-calotowers. Middle: the p_T and p_Z distribution of tracks. Bottom: the number of GPVs in data and simulation	121
Figure 52	Left: a "tomography" of CASTOR, using the correlation between isolated EM electron tracks in the TOTEM tracker and isolated EM energy deposits in the EM sections of CASTOR [141]. Right: the map of the bad channels of CASTOR (in red) during the 2013 data-taking campaign [98]	124
Figure 53	The ΔR distribution of the leading particle jet with all parton jets as function of the particle jet p_T cutoff for various combinations of jet radii. The fraction of events passing the p_T cutoff is also displayed . .	126
Figure 54	The Δp_T distribution of the leading particle jet with the closest parton jet as function of the particle jet p_T cutoff for various combinations of jet radii	128
Figure 55	The ρp_T distribution of the leading particle jet with the closest parton jet as function of the particle jet p_T cutoff for various combinations of jet radii	129
Figure 56	The ρE distribution of the leading particle jet with the closest parton jet as function of the particle jet p_T cutoff for various combinations of jet radii	129
Figure 57	The jet identity distributions that are used in data and simulation to determine whether a jet is hadronic. The distributions are for events that pass the event selection	134
Figure 58	Illustration of the jet matching. The CASTOR jet is indicated with the green area in $\eta - \phi$ space, the centre is represented with the green dot. The particle jet is displayed as a circle with the blue dot in its centre. Top: the containment criterium. In the top left plot the particle jet partially falls outside the η -acceptance of CASTOR. In the top right plot the jet is separated by more than 0.2 in ϕ from the CASTOR jet centre. Bottom left plot: illustration of the isolation criterium. There are particles contributing to the CASTOR jet that do not belong to the particle jet (the green circle). Bottom right: a proper match between a CASTOR jet and a particle jet. The illustrations are from [146]	135
Figure 59	The response of CASTOR jets in simulated p+Pb collisions before and after the application of calibration functions, together with Gaussian fits. We observe that after the calibration the peak of the hadronic jets corresponds well to the electromagnetic-jet peak	137

Figure 60	The multiplicity of CASTOR jets per event in data and simulation, after application of the event selection and calibration functions. Left: p+Pb collisions. Right: Pb+p collisions	138
Figure 61	Event-matching outcome for events selected with the ZB+PixelTrack HLT path. Success (failure) is indicated with 1 (o). Left: the vertex-matching outcome. The vertex demand on particle level consists of requiring a charged particle in the tracker acceptance. It can further be derived that events with more than one good primary vertex without particle-level activity in the tracker do not occur, as expected. Middle: the matching of the HF-AND requirement on particle and detector level. On particle level minimally one particle with $E \geq 4$ GeV in the HF+ and HF- acceptances was demanded. Right: the overall event-matching outcome. The correction factor $(1 - F_{\text{fake}})(1 + F_{\text{miss}})$ is also depicted	142
Figure 62	The response matrices for a set of $\Delta\eta$ and $\Delta\phi$ values. On the x -axis the CASTOR jet energy is depicted, on the y -axis is the particle-level jet energy, for p+Pb collisions. The graphs are normalised to the total number of matched-jet pairs	144
Figure 63	The response matrices for a set of $\Delta\eta$ and $\Delta\phi$ values. On the x -axis the CASTOR jet energy is depicted, on the y -axis is the particle-level jet energy, for Pb+p collisions. The graphs are normalised to the total number of matched-jet pairs	145
Figure 64	The miss jets and the ratio of miss to all particle jets as function of jet energy for a set of $\Delta\eta$ and $\Delta\phi$ values for p+Pb collisions	146
Figure 65	The miss jets and the ratio of miss to all particle jets as function of jet energy for a set of $\Delta\eta$ and $\Delta\phi$ values for Pb+p collisions	147
Figure 66	The fake jets and the ratio of fake to all detector jets as function of jet energy for a set of $\Delta\eta$ and $\Delta\phi$ values for p+Pb collisions	148
Figure 67	The fake jets and the ratio of fake to all detector jets as function of jet energy for a set of $\Delta\eta$ and $\Delta\phi$ values for Pb+p collisions	149
Figure 68	The correction factor is depicted as function of the setup parameters for a set of $\Delta\eta$ and $\Delta\phi$ values for an energy cutoff of 150 GeV. Left: p+Pb collisions. Right: Pb+p collisions	149
Figure 69	The data spectrum with the backsmear spectra for various numbers of Bayesian iterations for p+Pb (left) and Pb+p (right) collisions. The vertical line in the ratio plot indicates from which energy onwards the χ^2/N_{dof} is calculated.	150
Figure 70	The χ^2/N_{dof} between the data and backsmear distribution as function of the number of Bayesian iterations for p+Pb (left) and Pb+p (right) collisions	151

Figure 71	The mean and width of the energy of the matched particle jets per bin of CASTOR jet energy, for p+Pb (left) and Pb+p (right) collisions. The mean is the actual value of the symbol, and the width is depicted by the error bar	152
Figure 72	The χ^2/N_{dof} for unfolded data, calculated between distributions with N and $N + 1$ Bayesian iterations. Results are displayed as a function of the number of Bayesian iterations for p+Pb (left) and Pb+p (right) collisions	153
Figure 73	Left: the unfolded and backsmearred EPOS-LHC CASTOR jet spectrum together with the CASTOR jet spectrum. Right: the unfolded EPOS-LHC CASTOR jet spectrum together with the input EPOS-LHC particle-jet spectrum. The unfolding and backsmearing was performed with a response object that was filled with an independent EPOS-LHC event sample	154
Figure 74	Left: the unfolded HIJING CASTOR jet spectrum together with the HIJING particle-jet spectrum. Right: The unfolded and backsmearred HIJING CASTOR jet spectrum together with the input HIJING CASTOR-jet spectrum. The unfolding was performed with EPOS-LHC	155
Figure 75	The CASTOR jet spectra on particle level, unfolded with a response object created with HIJING, EPOS-LHC, and QGSJETII-04. These are labelled as DATA, Plus-shifted, and Minus-shifted, respectively. In the ratio plot the final value of the uncertainty is depicted. The plots are for p+Pb (left), Pb+p (middle), and p+Pb/Pb+p (right)	161
Figure 76	The CASTOR jets spectra for p+P (left) and Pb+p (right) collisions for different instantaneous luminosity bins	161
Figure 77	The final unfolded spectra with the systematic and statistical uncertainties for p+Pb (left), Pb+p (middle), and p+Pb/Pb+p (right)	162
Figure 78	The energy spectra of CASTOR jets normalised to the cross section. Left: p+Pb. Middle: Pb+p. Right: the ratio p+Pb/Pb+p	163
Figure 79	The correction factor to correct the ratio p+Pb/Pb+p for the boost. The correction factors were obtained by dividing p+Pb/Pb+p in the lab frame by the same result in the centre-of-mass frame. The correction factor is displayed for EPOS-LHC, HIJING, and the KATIE KS non-linear model	166
Figure 80	The stable-particle level differential jet energy cross section for p+Pb. Left: results from data are compared to predictions by KATIE. Right: results from data are compared to predictions by AAMQS	167
Figure 81	The stable-particle level differential jet energy cross section for p+Pb (left) and Pb+p (right). Results from data are compared to predictions by EPOS-LHC, HIJING, and QGSJETII-04	168
Figure 82	The stable-particle level differential jet energy cross section for the ratio of cross sections in p+Pb and Pb+p. Model predictions are included for EPOS-LHC, HIJING, and QGSJETII-04	169

Figure 83	The detector level differential jet energy cross section for p+Pb (left) and Pb+p (right). Results from data are compared to predictions by EPOS-LHC, HIJING, and QGSJETII-04	169
Figure 84	The detector level differential jet energy cross section for the ratio of cross sections in p+Pb and Pb+p. Model predictions are included for EPOS-LHC, HIJING, and QGSJETII-04	170
Figure 85	The stable-particle level differential jet energy cross section for p+Pb. Results from data are compared to predictions by KATIE and AAMQS	185
Figure 86	An schematic illustration of a CASTOR jet and CASTOR-T2 FlowJet .	192

LIST OF TABLES

Table 1	The various contributions to the systematical uncertainty in the energy scale of CASTOR.	101
Table 2	Overview of the running periods of CASTOR during LHC Run I and II. The Run I proton-lead runs were taken with both the proton and ion towards CASTOR. For all Run II data sets, a high-energy jet trigger was active. The Run II proton-lead runs were only recorded in both directions at 8 TeV. The 13 TeV data set was recored at $B = 0$	105
Table 3	Event generators used in this analysis, together with the number of events generated and cross sections. With measured, inwards, and outwards position the position of CASTOR w.r.t. the beam pipe is indicated; the uncertainties are depicted in table 4. We observe that the cross sections for models simulated with KATIE are quite different from the other models. This is due to the fact that these cross sections do not denote the total proton-lead cross section (which is deployed to normalise the AAMQS predictions), but instead the cross section for the particular partonic interaction	118
Table 4	The position of CASTOR during the 2013 p+Pb data taking with the systematic uncertainty. The values are given in mm. The position is quoted w.r.t. the nominal position of CASTOR that is defined as (0.0) .	123
Table 5	Key numbers obtained on the relative resolution ρ , the fraction of selected and correlated events, and the number of constituents for $p_T \geq 3$ GeV. All numbers are for a parton and particle jet radius of 0.5. The tight and loose matching criterium are indicated with (t) and (l), respectively	127
Table 6	The constants for the calibration functions for hadronic CASTOR jets for shower library and Fullsim simulations. The function description is given in eq. 84	136
Table 7	All parameters relevant for filling the response matrix and unfolding the data together with a brief description and their final value	157
Table 8	The contribution of various sources to the systematic uncertainty in the particle-level spectra. The results are quoted for the lowest and highest common energy bin for the p+Pb, Pb+p, and p+Pb/Pb+p spectra. The overall number is also quoted.	163
Table 9	Runs numbers used in this analysis, together with the integrated luminosity and peak pileup	189

ACRONYMS

QCD	Quantum Chromo Dynamics
GeV	Giga electron Volt
TeV	Terra electron Volt
QED	Quantum Electrodynamics
BEH	Brout Englert Higgs
QPM	Quark Parton Model
DIS	Deep Inelastic Scattering
QFT	Quantum Field Theory
pdf	parton density function
DLL	Double Leading Log
LLA	Leading Log Approximation
QCDC	QCD Compton
BGF	Boson Gluon Fusion
DGLAP	Dokshitzer Gribov Lipatov Altarelli Parisi equation
BK	Balitsky Kovchekov equation
updf	unintegrated parton density function
rcBK	running coupling BK equation
RGT	Regge-Gribov Theory
UE	underlying event
MPI	multi-parton interactions
BR	beam remnant
AAMQS	Albacete Armesto Milhano Quiroga-Arias Salgado
KS	Kutak Sapeta
DVCS	deeply virtual Compton scattering

AAMQS-updf AAMQS unintegrated pdf

KS-updf KS unintegrated pdf

LHC Large Hadron Collider

instantaneous luminosity number of collisions per unit of time and cross section

HL-LHC high-luminosity phase of the LHC

L1 trigger level-1 trigger

HLT high-level trigger

prescale factor that suppresses a fraction of a trigger rate

DAQ data-acquisition system

WLCG Worldwide LHC computing grid

LumiSection a period during which the trigger prescales and trigger thresholds cannot be changed

JSON file dedicated file in which the run numbers and their good luminosity sections are stored

data stream specific data partition, containing events obeying a specific L1 trigger or HLT path

global tag a set of files that specify the conditions of the detector at a certain data-taking period

MIP minimally ionising particle

LHC RUN II the operation period between 2015 and 2018 of the Large Hadron Collider

EM electromagnetic

pileup number of events per bunch crossing

fC femto Coulomb

QGP quark-gluon plasma

minbias minimum-bias

GPV good primary vertices

$ak(R)$ anti- k_T jet with radius R

ResponseObject response matrix, and miss and fake spectra

JER jet-energy resolution

MLL minimal log likelihood

BLT bottom-line test

Part I

SATURATION: THEORETICAL AND EXPERIMENTAL STATE-OF-THE-ART

If the doors of perception were cleansed
everything would appear to man as it is,
infinite

William Blake

In this part we review the current theoretical and experimental state-of-the-art concerning gluon saturation. This serves as background to clearly formulate and motivate the hypothesis of this thesis, and will aid the interpretation of our key results. To discuss the concept of gluon saturation, we need to discuss Quantum Chromo Dynamics (QCD), the structure of hadrons, and the concept of factorisation first.

Therefore, the part starts with a brief review of concepts and units commonly used in the field of high energy physics, followed by an introduction to the Standard Model of particle physics. In this chapter we explain, amongst others, the origin of the gluonic self-interactions.

Thereafter, the main features of QCD are presented. We discuss the pivotal consequences of the self-interactions and introduce the running coupling α_s . This is followed by a discussion on the structure of hadrons; the section finishes with the leading order QCD corrections to the Quark Parton Model.

The treatment of the singularities and large logarithms encountered in these corrections is explained subsequently in the chapter on parton evolution equations. Once the concept of factorisation has been explained, we may finally turn our attention to the important role of the *non-linear* reactions; these are expected to cause saturation of the gluon density and a modification of its evolution. This is followed by a chapter on soft QCD, which is needed to understand descriptions of event generators in a later chapter. Thereafter, we explain how the processes on parton level lead to experimentally observable jets.

This part finishes with portraying the experimental data of many experiments together with theoretical predictions; this provides a context to the motivation of the measurement presented in this thesis.

NATURAL UNITS AND KINEMATICS

In this section we introduce the units and certain kinematic variables used throughout this thesis. We finish with defining the cross section.

1.1 NATURAL UNITS

The conventional unit to express energy in high energy physics is the Giga electron Volt (GeV). In high energy physics, momentum is thus expressed in units of GeV/ c (with c the speed of light), and mass has unit GeV/ c^2 .

Certain quantities are expressed in unit of \hbar , for example the Heisenberg uncertainty relation $\sigma_x \cdot \sigma_p \geq \frac{\hbar}{2}$.

For the convenience of not having to cite these units in every statement or calculation, in this thesis natural units are adopted, in which \hbar and c equal 1.

1.2 FOUR VECTOR KINEMATICS

The kinematical momentum (location) of a particle is expressed in terms of its energy E (time t) and spatial momentum \vec{p} (location \vec{x}). The components of the vectors \vec{p} and \vec{x} are in Cartesian coordinates x, y , and z . Roman indices are reserved to distinguish between different particles. These quantities are contained in a Lorentz vector:

$$p_\mu = (E, p_x, p_y, p_z). \quad (1)$$

A Lorentz vector is not boost invariant. A product of two Lorentz vectors however is. The inner product with itself of the Lorentz vector of a particle gives the invariant (rest) mass of the particle squared:

$$p \cdot p = p_\mu p^\mu = E^2 - \vec{p}^2 = m^2 \quad (2)$$

With this, it should be noted that in reactions particles can go off their mass shell. A photon for example has zero mass. However, in reactions the virtuality of a photon is given by the inner product as defined in eq. 2 and can be non-zero.

In order to perform calculations for colliding particles, it is convenient to define the Lorentz invariant Mandelstam variables. A schematic illustration of a $2 \rightarrow 2$ process is given in Fig. 1. For this process, the Mandelstam variables are defined as:

$$s = (p_1 + p_2)^2 \quad t = (p_1 - p_3)^2 \quad u = (p_1 - p_4)^2. \quad (3)$$

At the LHC the beam energies are expressed in Terra electron Volt (TeV). In the analysis discussed in this thesis, the proton-nucleon lab frame has an overall boost w.r.t. the centre-of-mass frame. The proton beam has an E and p_z value of 4 TeV in the laboratory frame,

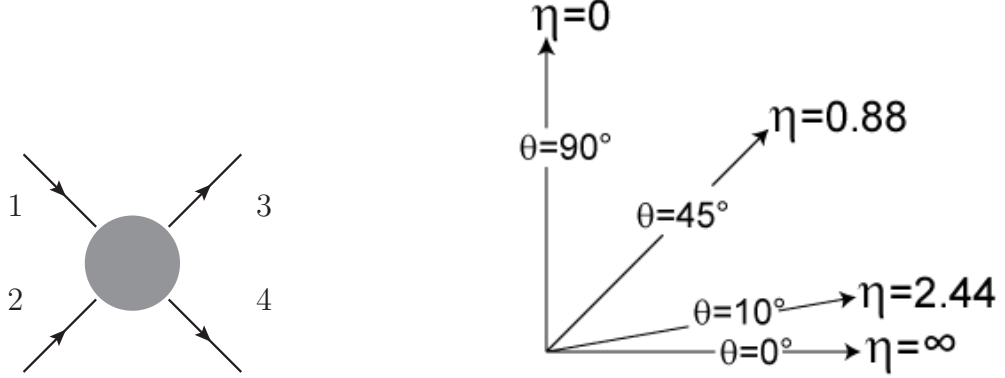


Figure 1: Left: a simple illustration of a general $2 \rightarrow 2$ process. Right: an illustration of the relation between the solid angle θ and η [7].

while the energy per nucleon of the ion is 1.58 TeV. Thus, the invariant centre-of-mass energy $\sqrt{s_{NN}}$ for a proton-nucleon pair is:

$$\sqrt{s_{NN}} = \sqrt{(p_1 + p_2)^2} = 5.02 \text{ TeV}. \quad (4)$$

In certain calculations, it is convenient to express the four vectors in light cone coordinates. These are defined as $p_+ = \frac{1}{\sqrt{2}}(E + p_z)$, $p_- = \frac{1}{\sqrt{2}}(E - p_z)$, and $\vec{p}_T = (p_x, p_y)$. From these definitions, the inner product can be derived to be:

$$A \cdot B = A_+ B_- + A_- B_+ - \vec{A}_T \vec{B}_T \quad A \cdot A = 2A_+ A_- - \vec{A}_T^2 \quad (5)$$

In hadron-hadron collisions, the interacting constituents carry a varying fraction of the hadrons longitudinal momentum. Thus, the constituents centre-of-mass frame may be boosted w.r.t. the hadron-hadron centre-of-mass frame. A quantity that is amongst others convenient to express the effect of these boosts, is the rapidity Y . It is closely related to the pseudorapidity η . The light cone coordinates of a four vector transform under a Lorentz boost with velocity β along the z -axis as follows:

$$p' = (p'_+, p'_-, \vec{p}'_T) = \left(\sqrt{\frac{1+\beta}{2(1-\beta)}}(E + p_z), \sqrt{\frac{1-\beta}{2(1+\beta)}}(E - p_z), \vec{p}_T \right) \quad (6)$$

This leads us to define the the rapidity $Y = \frac{1}{2} \log \left(\frac{1+\beta}{1-\beta} \right)$. Given this definition, we can easily express the effect of the boost as:

$$p'_+ = e^Y \cdot p_+ \quad p'_- = e^{-Y} \cdot p_- \quad (7)$$

By applying a boost to a particle in its rest frame using eq. 7, we can easily obtain the equivalent definition of Y :

$$Y = \frac{1}{2} \log \frac{p'_+}{p'_-} \quad (8)$$

In the approximation where the mass of the particle is neglected w.r.t. its energy ($E \approx |\vec{p}|$), Y equals the pseudorapidity η . The latter relates to the solid angle θ via:

$$\eta = -\log(\tan(\theta/2)). \quad (9)$$

An illustration of the relation between η and θ is given in the right hand illustration of Fig. 1.

1.3 CROSS SECTION DEFINITION

A fundamental observable in particle physics is the cross section σ ¹. The unit of the cross section is the barn.

The cross section is defined in terms of the incoming flux of particles $flux$, the Lorentz invariant phase-space $dLIPS$, and the probability for the process $|M|^2$:

$$d\sigma = \frac{1}{flux} \cdot dLIPS \cdot |M|^2. \quad (10)$$

M is the matrix element (or equivalently the amplitude) of the process, which contains the fundamental physics.

The flux of the two incoming particles² is defined as $flux = 4\sqrt{(p_1 \cdot p_2)^2 - m_1^2 m_2^2}$.

The final state of an interaction consists of n particles k . The Lorentz invariant phase-space simultaneously facilitates the integration over all allowed kinematical final states, preserves energy-momentum conservation, and requires the final outgoing states to be on their mass shell:

$$dLIPS = (2\pi)^4 \delta^4 \left(-p_1 - p_2 + \sum_{i=1}^n k_i \right) \prod_{i=1}^n \frac{d^4 k_i}{(2\pi)^3} \delta(k_i^2 - m_i^2) \theta(E_i). \quad (11)$$

¹ It should be noted that Nature provides us with two fundamental observables, namely the cross section and the decay width. However, one may consider a decay as a two-to-one cross section. In this perspective, the cross section is rather *the* fundamental observable in Nature

² The flux is directly related to the instantaneous luminosity, which is an experimental observable carefully monitored at particle physics experiments

THE STANDARD MODEL OF PARTICLE PHYSICS

2.1 INTRODUCTION

To our current best knowledge and experimental verification, Nature consists of seventeen fundamental particles. These particles and their interactions are depicted in Fig. 2. We observe that twelve matter fields exist; all known matter is build from these particles. Further, four gauge bosons can be distinguished, which mediate three forces between the matter fields. Lastly, the illustrious Higgs boson is depicted. This field is responsible for the fundamental mass¹ of the matter and gauge fields.

This section starts with a concise review of the properties of the matter fields, their interactions via gauge bosons, and a succinct note on the role of the Higgs boson. Special attention is given to the occurrence of *self-interactions* of gauge bosons, since these interactions will be of major importance in the subsequent chapters.

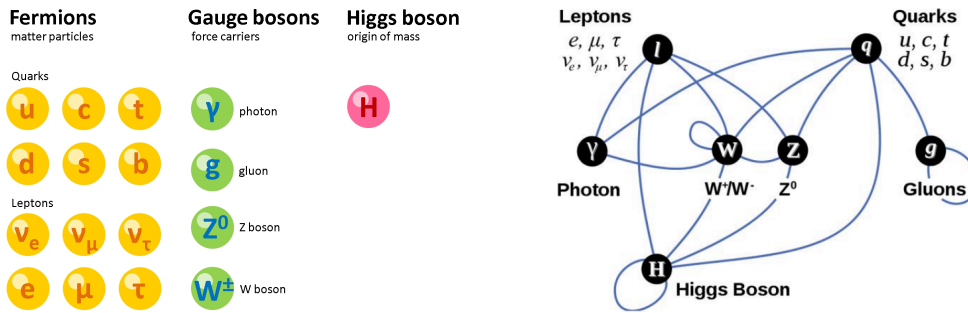


Figure 2: Left: the particles of the standard model. It should be noted that all fermions also occur as anti-particle in Nature [8]. Right: the interactions between the particles of the standard model [9]

2.2 RELATIVISTIC WAVE EQUATIONS OF BOSON AND MATTER FIELDS

The relativistic dispersion relation, derived in the context of the theory of special relativity, states that $E^2 = \vec{p}^2 + m^2$. We introduce a scalar field ϕ (i.e. its field degrees of freedom are invariant under Lorentz transformations), and impose that it obeys the fundamental dispersion relation. For this purpose, we exchange E by the quantum operator $i\frac{\partial}{\partial t}$ and \vec{p} by $-i\nabla$. Thus, we obtain the Klein-Gordon equation, which applies to all free fields in Nature:

¹ With mass we refer in this context to the inertia of matter and its coupling to gravity

$\frac{-\partial^2 \phi}{\partial t^2} = -\nabla^2 \phi + m^2 \phi$. Using the four vector notation $\partial_\mu = (\partial_t, \nabla)$, the equation may be written compactly as:

$$(\partial_\mu^2 + m^2)\phi = 0. \quad (12)$$

When we interpret ϕ as a quantum field operator in Fock space, it follows from the commutation relation of ϕ that its creation (a^\dagger) and annihilation (a) operators obey the equal time commutation relation $[a(\vec{k}), a^\dagger(\vec{k}')] = (2\pi)^3 \cdot 2E(\vec{k}) \cdot \delta(\vec{k} - \vec{k}')$. Scalar fields, but also other particle types (for example vector bosons) obeying this commutation relation, are called bosons.

Eq. 12 is of second order in its derivatives. Dirac formulated instead a first order relativistic wave equation:

$$(i\partial_\mu \gamma^\mu - m)\psi = 0. \quad (13)$$

By imposing that ψ also obeys eq. 12, it is straightforward to deduce the defining relation for the γ matrices:

$$\{\gamma^\mu, \gamma^\nu\} = 2g^{\mu\nu} \cdot \mathbf{I}_{4 \times 4}. \quad (14)$$

It was thus deduced that the γ matrices must minimally be 4×4 matrices, and consequently the field ψ is a four vector referred to as a spinor.

As it turns out, the solutions to eq. 13 lead to fields of which the sign of the quantum numbers can be flipped; these are interpreted as particles and anti-particles. Furthermore, a field with given quantum numbers has two spinor degrees of freedom $s = \pm 1/2$. The creation (d_s^\dagger) and annihilation ($d_{s'}$) operators of eq. 13 can be shown to obey instead the anti-commutation relation $\{d_s(\vec{k}), d_{s'}^\dagger(\vec{k}')\} = (2\pi)^3 \cdot 2E(\vec{k}) \cdot \delta(\vec{k} - \vec{k}') \cdot \delta_{ss'}$. Particles obeying eq. 13 are commonly referred to as fermions.

A key difference between bosons and fermions is that two identical particles obeying commutation relations can occupy the same quantum state, while for particles obeying anti-commutation relations this is forbidden. This property of fermions and bosons is of paramount importance in physics and shapes² Nature as we perceive it.

2.3 GAUGE INVARIANCE AND GAUGE FIELDS

We derived the elementary wave equations of bosons and fermions, and observed a key difference between their quantum field operators. However, so far the theories are sterile, in the sense that no interactions occur.

Let us start by defining the Lagrangian density for the Dirac field:

$$\mathcal{L}_D = \bar{\psi}(i\partial_\mu \gamma^\mu - m)\psi, \quad (15)$$

in which $\bar{\psi} = \psi^\dagger \gamma^0$. We may impose local (or global) gauge invariance to the density. In its simplest local form, this amounts to requiring that the density is invariant under a local phase

² One consequence of the anti-commutation relation is that only a limited number of electrons can occupy a particular orbit in an atom, leading to the chemical properties of elements

(U(1)) transformation $\psi \rightarrow e^{i\phi(x)}\psi$. Inserting the assignment into the Lagrangian density we obtain:

$$\mathcal{L}_D = \bar{\psi}(i\partial_\mu\gamma^\mu - m + i\partial_\mu\phi)\psi. \quad (16)$$

Clearly, the Dirac equation is not invariant due to the term $i\partial_\mu\phi$. We recall however, that the Maxwell equations for the vector potential A^μ are invariant under the gauge transformation $A^\mu \rightarrow A^\mu + \partial_\mu\chi(x)$, with $\chi(x)$ an arbitrary function of x . Thus, if we turn the derivative ∂_μ into a covariant derivative³ $\partial_\mu + ieA_\mu \equiv D_\mu$, we can exploit the gauge freedom of A_μ to restore the local phase invariance.

The introduction of the gauge field A_μ into the Lagrangian density leads to an interaction term of the form $-ieA^\mu\bar{\psi}\gamma_\mu\psi$. In brief, this term is responsible for the interaction of the matter fields via their electromagnetic charge e .

As is well known, a symmetry of the Lagrangian leads to a conserved current (this is Noether's theorem). The conserved current associated with the gauge symmetry can easily be derived to be $ie\bar{\psi}\gamma^\mu\psi$; written in creation and annihilation operators, the first term of the current counts the number of particles and anti-particles. This conserved current takes the role of the current J in the classical inhomogeneous Maxwells equations.

This is, in a nutshell, the governing principle behind local gauge theories. It follows that for this mechanism to work, the gauge field needs to be a vector field.

2.4 NON-ABELIAN GAUGE THEORIES AND SELF-INTERACTIONS

We established previously invariance of the Dirac Lagrangian under local U(1) gauge transformations, provided we introduced the field A^μ . The classical Lagrangian density for the free vector field A_μ is given by:

$$\mathcal{L}_{EM} = \frac{1}{4}F^{\mu\nu}F_{\mu\nu}, \quad (17)$$

in which $F^{\mu\nu}$ is given by $(\partial_\mu A_\nu - \partial_\nu A_\mu)$. It can be easily seen that $F^{\mu\nu}$ is invariant under $A^\mu \rightarrow A^\mu + \partial_\mu\chi(x)$. The quantum of this U(1) gauge symmetry is the photon, which is a massless vector boson.

At this point we have gathered all the ingredients that define the Lagrangian density for Quantum Electrodynamics (QED): the free field description of the gauge field A_μ , the free field equation of matter fields, and the interactions of the gauge field via its coupling to the conserved current of the matter fields.

It is a well established fact that electromagnetism is not the only fundamental force though. One could also impose a more complex gauge symmetry, for example by requiring invariance under rotations of an SU(2) group. For this purpose, we introduce a more complex rotation:

$$\psi \rightarrow e^{igw_j(x)\tau_j}\psi \equiv U\psi. \quad (18)$$

³ This is also known as the minimal substitution

The τ_j are the Pauli matrices; these are the two-dimensional generators of SU(2). In the process we implicitly also created a two-dimensional doublet of matter fields on which the SU(2) matrices act.

In analogy to the minimal substitution of electromagnetism, we introduce a matrix of vector fields $W_\mu(x) \equiv A_\mu^j(x)\tau^j$ to the Dirac equation. Thereby we introduced not one but three gauge fields, which come with three different SU(2) generators. To establish gauge invariance of the Dirac equation, the matrix of vector fields has to obey a more complicated transformation rule though:

$$W'_\mu(x) = UW_\mu(x)U^\dagger + \frac{i}{g}(\partial_\mu U)U^\dagger. \quad (19)$$

This transformation rule has a far reaching consequence. The free field tensor $F^{\mu\nu}$ cannot be written (analogous to QED) as $(\partial_\mu W_\nu - \partial_\nu W_\mu)$ anymore, since this term is not gauge invariant. The commutator $[D_\mu, D_\nu]$ instead transforms as $U[D_\mu, D_\nu]U^\dagger$, and the following gauge invariant Lagrange density is obtained: $\text{Trace}([D_\mu, D_\nu][D^\mu, D^\nu])$. Writing out the new expression for $F^{\mu\nu}$ we obtain:

$$F_{\mu\nu}^j = \partial_\mu A_\nu^j - \partial_\nu A_\mu^j - gf_{jkl}A_\mu^k A_\nu^l. \quad (20)$$

Due to the last term in eq. 20, the Lagrange density for the free field $\frac{1}{4}F_{\mu\nu}^j F^{j\mu\nu}$ leads to triple and quadrupole *self-interactions* of the gauge fields. This is a general property of all non-Abelian gauge theories⁴.

In Nature, an SU(2)_L gauge symmetry is actually realised. It has the peculiarity that it only acts on left-handed chiral states of the matter fields. This force is called the weak force (since the coupling constant is smaller than the electromagnetic coupling constant), and the matter fields are in weak isospin up or down state. The self-interactions of the weak gauge bosons are, amongst others, a topic of active research at the LHC [10] [11] [12]. The three massive vector bosons are called W^\pm and Z .

2.5 THE BROUT-ENGLERT-HIGGS MECHANISM

A very important parameter of the matter and gauge fields discussed above has so far been ignored, namely their mass. The mass term that we audaciously introduced in the matter fields is actually not gauge invariant. This can be inferred from decomposing $\bar{\psi}\psi$ into $\bar{\psi}_L\psi_R + \bar{\psi}_R\psi_L$, and observing that the weak gauge bosons only couple to the left handed spinors; a direct mass term is not gauge invariant. Furthermore, a direct mass assignment $\propto W^\mu W_\mu$ to obtain massive W and Z gauge fields (a so called Procca-Lagrangian) is not gauge invariant either (for this one only needs to apply eq. 19 to the mass term).

The Brout Englert Higgs (BEH) mechanism provides a method to overcome both difficulties *simultaneously*. We start by considering a two-dimensional complex vector Φ in weak isospin

⁴ The main topic of this thesis, to a certain extend, could actually be summarised as a study of self-interactions of a residual SU(3) gauge field

space, which consists of four real scalar boson fields. We add a particular Lagrangian density for Φ to our theory:

$$(D^\mu \Phi)^\dagger (D_\mu \Phi) - \mu^2 \Phi^\dagger \Phi - \lambda (\Phi^\dagger \Phi)^2 + \bar{\psi}_L \psi_R \Phi + \bar{\psi}_R \psi_L \Phi^\dagger. \quad (21)$$

Under the weak gauge transformations, the field Φ transforms as $\Phi \rightarrow U\Phi$, while a covariant derivative transforms as $D \rightarrow UDU^\dagger$. Furthermore, the matter fields in the Yukawa term (the last term in the equation) transform as $\bar{\psi}\psi \rightarrow \bar{\psi}\psi U^\dagger$. Thus, we observe that eq. 21 is gauge invariant under $SU(2)_L$.

In Nature, λ must be positive, but μ^2 may be either positive or negative. In the latter configuration, the symmetry of the theory is spontaneously broken, i.e. the manifest symmetry of eq. 21 is not shared by the ground state of the vacuum. Goldstone's theorem states (for our theory at hand), that this will lead to Goldstone bosons. By adopting the so-called unitary gauge, the degrees of freedom of three of the Goldstone bosons can be absorbed effectively into the W and Z fields, by which the latter acquire mass.

The remaining scalar boson field can be expanded around its vacuum expectation value. Inserting this expression into the Yukawa term leads to the desired mass term for the matter fields. In the unbroken Lagrangian, the gauge symmetry is manifest; despite that this symmetry is hidden after symmetry breaking, the BEH mechanism provides a consistent⁵ way to assign mass to the gauge and matter fields.

Lastly, the BEH mechanism predicts the existence of a scalar boson, of which the existence was confirmed in 2012 by the ATLAS [13] and CMS [14] experiments, 43 years after the first prediction of its existence.

To our current understanding, the matter fields of the standard model are fermions and their interactions are mediated by gauge theories of the form $U(1) \times SU(2)_L \times SU(3)$; the $U(1)$ and $SU(3)$ group are residual gauge groups, i.e. their gauge bosons are massless. The matter fields and W^\pm and Z gauge bosons acquire their mass due to the spontaneous symmetry breaking of the scalar boson field. The origin of the mass of the neutrino is thought not to be mediated by the spontaneous symmetry breaking, and currently not understood⁶.

In appendix A.2 we succinctly review the *global* symmetries of the Standard Model Lagrangian.

⁵ The mechanism also provides a renormalisable theory

⁶ Experiments have confirmed mass *differences* between the three generations of neutrinos, although a *direct* measurement of the neutrino mass has not been performed yet

INTRODUCTION TO QUANTUM CHROMODYNAMICS

The previous chapter finished with citing that the fundamental forces of Nature (gravity excluded) can be described as a local $U(1) \times SU(2)_L \times SU(3)$ gauge symmetry. In this section we will give a succinct review of the characteristic features of the $SU(3)$ residual gauge group called QCD. This force only acts on the quarks.

Historically, QCD was motivated, amongst others, by the observation of the Δ^{++} particle, which consists of three up quarks. In order not to violate the commutation relation for fermions stated in the previous chapter, additional quantum numbers were needed.

The charge associated with QCD is colour; a quark can occupy 3 colour states (for an anti-quark this is anti-colour). The interactions between the colour charges are mediated by eight gluon gauge fields, which carry themselves both colour and anti-colour. A colour neutral gluon (a colour singlet state) does not occur in Nature; this restricts QCD to short-range reactions.

3.1 RENORMALISATION OF DIVERGENT AMPLITUDES

A scattering amplitude between an initial field ϕ_i and final field ϕ_f can be calculated as $\langle \phi_f | e^{-i\hat{H} \cdot t} | \phi_i \rangle$, or with a path integral as $\int \mathcal{D}\phi(t) e^{\int \frac{d^4x}{(2\pi)^4} i\mathcal{L}(\phi, \dot{\phi})}$. The standard model Lagrangian density contains the free field and interaction terms as discussed in chapter 2. A first order expansion in, for example, the parameter α of the QED interaction¹ term allows for perturbatively calculable interactions of the matter fields with the photon. Such a term will contribute directly to, for example, the Compton process.

However, higher order expansions in $\mathcal{O}(\alpha)$ will also contribute to the scattering amplitudes. These processes may contain loops of fields. The momentum flow through these loops is unconstrained and leads to infinite contributions to the amplitudes, superficially invalidating any perturbative calculation of an amplitude. The loop diagrams for QCD to lowest order in the strong coupling α_s are depicted in Fig. 3.

It can be shown that these infinities are equivalent with a pole that occurs when the number of spatial dimensions approaches four. For certain classes of theories these poles can be subtracted by adding appropriate counter-terms to the Lagrangian. This procedure is called renormalisation. If the number of counter-terms is finite (or minimally finite per order of the expansion), the theory is renormalisable². The standard model Lagrangian has been shown to be fully renormalisable.

¹ The coupling α is defined in terms of the electron charge e and the vacuum permittivity ϵ_0 as $\frac{e^2}{4\pi\epsilon_0}$

² It is necessary that the theories have no interaction terms with dimensionality larger than four in order to be renormalisable. Since gravity has such a constant (and hence the gravitational coupling has a negative mass dimension), it can currently not formally be described by a gauge theory

Actually, at a certain renormalisation scale M (a kinematical property of the incoming and outgoing fields with dimension of energy squared, for example s), we simply *define* the counter terms such that the higher order amplitude of the fermion boson interaction has a value equal to the coupling parameter that appears in the interaction term of the Lagrangian. For example, the leading order quark-gluon vertex factor appears in the Lagrangian as α ; we define the counter-term for the lower right diagrams in Fig. 3 such that *at the renormalisation scale M* the amplitude of the process remains α .

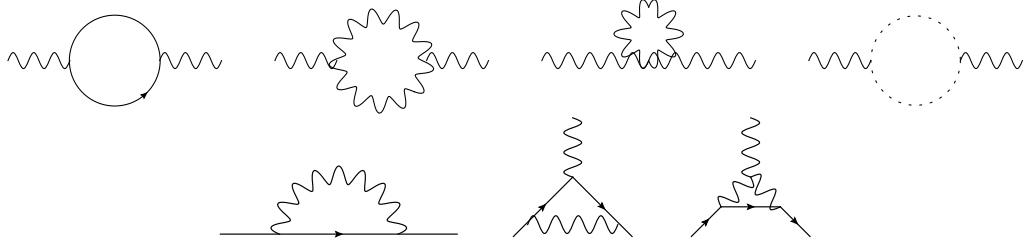


Figure 3: Divergent amplitudes occurring in QCD to leading order in α_s . Fermions are depicted by solid lines, while the gluons are represented by the wavy lines. The dashed line represents a ghost field, which is needed to retain next-to-leading order amplitudes of non-Abelian theories gauge-invariant. Upper diagrams: the amplitudes contributing to the self energy of the gauge bosons. Lower left diagram: the amplitude contributing to the self energy of the fermions. Lower right diagrams: the amplitudes contributing to the fermion gluon vertex factor

3.2 RENORMALISATION GROUP EQUATIONS

In this section is outlined how the renormalisation of α (the coupling parameter in the Lagrangian) leads to a *renormalisation group* equation for *the running coupling* α_s ; the equation is of fundamental importance to the theory of QCD. Besides, the fundamental equations under investigation in this thesis are actually renormalisation group equations, and the discussion of α_s will aid the intuition for the processes discussed in chapter 5.

The value of an amplitude for an n particle interaction G^n determines a physical observable, and thus the amplitude itself cannot depend on the choice of the renormalisation scale. Therefore, a change in the renormalisation scale must be accounted for. This is facilitated by absorbing the effect into the parameters of the theory such as the coupling and the mass³. This invariance is reflected in the Callan-Symanzik equation:

$$\left[M \frac{\partial}{\partial M} + \beta \frac{\partial}{\partial \alpha} \right] G^{(n)}(x_1, \dots, x_n, M, \alpha) = 0, \quad (22)$$

in which $\beta \equiv \frac{M}{\delta M} \delta \alpha$.

³ The field strength is usually also renormalised, but this is not essential for our discussion of the running coupling

From eq. 22 a specific equation can be derived for the running coupling $\alpha_s(p, \alpha)$, which depends on the kinematics of the process and the value of the coupling α at the renormalisation scale M :

$$\frac{d}{d \log(p/M)} \alpha_s(p^2, \alpha) = \beta(\alpha_s(p, \alpha)). \quad (23)$$

The equation describes the *change* in the coupling as function of the kinematics of the process w.r.t. the renormalisation scale. For QCD we can determine the β function by applying eq. 22 to the diagrams and carefully matching orders in α . We obtain:

$$\beta(\alpha) = -\frac{\alpha^3}{(4\pi)^2} \left[\frac{11}{3} C_2(G) - \frac{4}{3} n_f C(r) \right]. \quad (24)$$

In this equation, $C_2(G)$ and $C(r)$ are constants related to the symmetry group and its representation. For $SU(3)$ they are one and two respectively, while n_f is the number of fermions; thus the β function is negative. We can insert this result into eq. 23 to finally obtain the dependence of α_s on the renormalisation scale M :

$$\alpha_s(p^2) = \frac{\alpha}{1 + (b_0(\alpha/2\pi)) \log(p^2/M^2)}. \quad (25)$$

In the equation $b_0 = \frac{11}{3} C_2(G) - \frac{4}{3} n_f C_r$.

In QCD the (arbitrary) scale M is usually replaced with Λ_{QCD} , which is defined via $1 = \alpha^2 \left(b_0 / (2\pi) \right) \ln(M^2 / \Lambda_{QCD}^2)$. The scale Λ_{QCD} has to be determined experimentally; it corresponds to 1 fm, which is roughly the size of the light hadrons. We will succinctly revisit the scale in chapter 4. Since there is no unique manner in which the actual value of the strong coupling can be stated⁴, an approach followed often is to state the value at an interaction scale equal to m_Z^2 ; the current world average at this scale is $\alpha_s(m_Z^2) = 0.1181 \pm 0.0013$ [15].

3.3 THE RUNNING COUPLING OF QCD

At this point it is beneficial to compare and contrast the running coupling of QCD in eq. 24 to the (Abelian) QED coupling, which is given by

$$\alpha_{QED}(p^2) = \frac{\alpha}{1 - (\alpha/3\pi) \ln(p^2/e^5/3 m_e^2)}. \quad (26)$$

We observe that the behaviour w.r.t. the energy of the interaction is *opposite*: while for QED the coupling strength *increases* with energy, for QCD the coupling becomes *small* for high energies. The coupling becomes strong for energy scales of $\sim \Lambda_{QCD}$. In terms of spatial scales, the QED coupling becomes weaker with increasing distances, while the QCD coupling becomes instead stronger⁵.

⁴ No natural scale can be defined for QCD, since quarks only occur as part of a composite hadron

⁵ The observant reader may notice that the QED coupling actually becomes strong at very high energies, and also possesses a Landau pole. Thus, QED is actually not ultraviolet safe. Therefore, QED is believed not to be a *fundamental* symmetry of Nature, while QCD is believed to be fundamental

This fundamental difference in the dependence of the couplings on the momentum and spatial scale of the interaction may be understood more intuitively as a screening effect that is induced by vacuum polarisation. In Fig. 4 we display the dramatic difference in the effect of an Abelian (left) and non-Abelian (right) charge on the vacuum. We observe that for the Abelian charge, the dipoles occurring due to vacuum fluctuations have a screening effect on the bare (unobservable) charge. In contrast, for the non-Abelian charge dipole fluctuations also occur, which lead instead to an anti-screening effect of the bare charge. Via the background field method, it can be formally derived that in QCD the anti-screening effect is actually twelve times stronger than the screening effect⁶.

Thus, the running coupling leads to two important and remarkable consequences:

ASYMPTOTIC FREEDOM For length scales smaller than $1/\Lambda_{QCD}$, the coupling becomes weak. Below this length scale, quarks and gluons are approximated to behave as free particles in certain models.

CONFINEMENT For length scales larger than $1/\Lambda_{QCD}$, the coupling becomes strong. Therefore, a quark or gluon cannot be taken out of the hadron in which it is situated; the energy needed to do so would be larger than the energy required to create instead two hadrons. Thus, quarks and gluons do not appear as free particles in Nature, but only occur confined in the bound states of hadrons⁷.

Another consequence of paramount importance is that perturbation theory is only valid for energy scales somewhat higher than Λ_{QCD} , approximately 1 GeV. Therefore, no perturbative calculations can be made for the quarks confined into a bound state of a hadron; this is only possible for smaller length scales.

Instead, phenomenological approaches have to be followed at these scales. For example, lattice QCD has been used to estimate the actual value of the coupling in the strong regime [16].

⁶ The observant reader may have wondered why the coupling of $SU(2)_L$ does not impose similar problems as in QCD, since the β -function is also negative. This may readily be understood in terms of the vacuum fluctuations; the large mass of the weak gauge bosons highly suppress these fluctuations

⁷ In high energetic heavy ion collisions a quark gluon plasma can be formed; here the energy of the quarks and gluons is high enough for the coupling to become weak. The quarks and gluons form a thermalised medium with properties resembling a perfect liquid

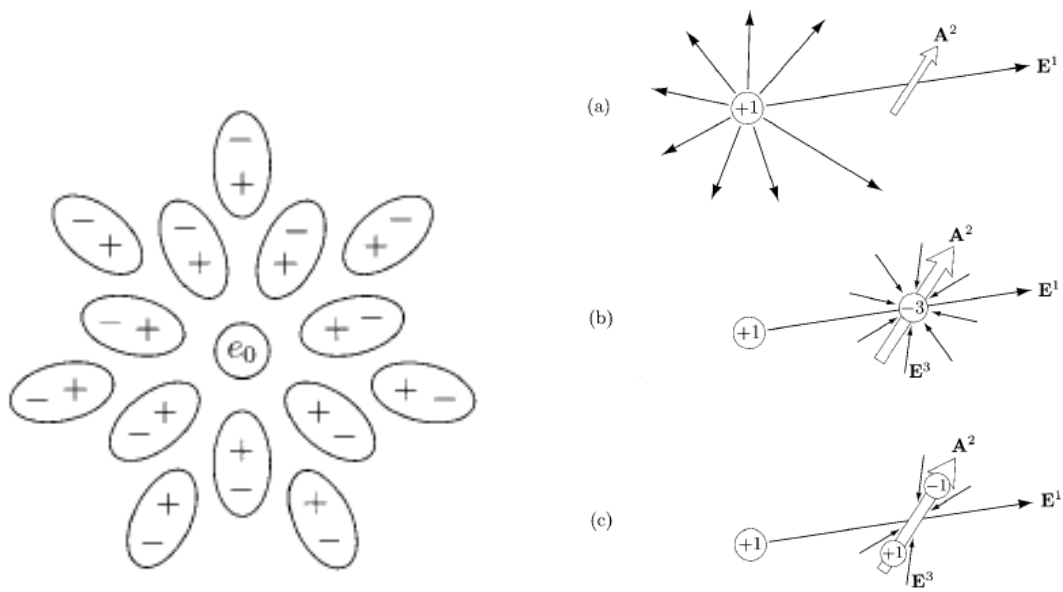


Figure 4: Left: vacuum polarisation for an Abelian gauge theory. We observe that fluctuations lead to charge screening. Right: vacuum polarisation for a non-Abelian gauge theory. The $1/r^2$ field is depicted in (a), together with a fluctuation \mathbf{A}^2 . The combination of these two field is a sink of the field \mathbf{E}_3 , illustrated in (b). The field \mathbf{E}_3 , combines with \mathbf{A}^2 . The net effect, illustrated in (c), is that of a dipole. Since the dipole points to the original charge, the latter is enhanced. Fig. from [17]

THE STRUCTURE OF HADRONS

We introduce the structure of hadrons in the context of e+p scattering, since this allows for a clearer explanation than directly considering hadron-hadron collisions. We start with a brief discussion on elastic e+p scattering, since this provides indispensable insight on non-perturbative quantities such as the size of the proton, and the scale where perturbative QCD becomes relevant. Another cardinal motivation is that the elementary spin $\frac{1}{2} \times \frac{1}{2}$ scattering cross section is a fundamental ingredient for discussing Deep Inelastic Scattering (DIS), and the Quark Parton Model (QPM). After discussing the QPM and DIS, we explain the general soft bremsstrahlung law, which aids the intuition for the difficulties encountered when calculating parton radiation in QCD. The chapter finishes with the radiative QCD corrections to the QPM.

4.1 THE CROSS SECTION FOR ELASTIC E+P SCATTERING

If we consider the proton as an elementary particle, the elementary elastic e+p cross section can be written as:

$$\frac{d\sigma}{d\Omega} = \frac{1}{64\pi^2} \left(\frac{E'_e}{m_p E_e} \right)^2 |M|^2, \quad (27)$$

in which m_p is the rest mass of the proton, while E_e and E'_e are the electron energy before and after the interaction.

By applying the Feynman rules for QED (an introduction can be found in [17]), we find that for single photon exchange $M = J_{k \rightarrow k'}^\mu \frac{-g_{\mu\nu}}{q^2} J_{p \rightarrow p'}^\nu$, in which $J_{p \rightarrow p'}^\nu$ and $J_{k \rightarrow k'}^\mu$ represent the transition current $\bar{\psi}(p')\gamma^\mu\psi(p)$ and $\bar{\psi}(k')\gamma^\mu\psi(k)$, respectively. A schematic illustration is depicted in Fig.5.

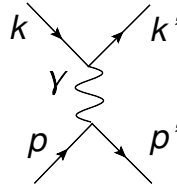


Figure 5: A schematic illustration of an elementary $2 \rightarrow 2$ process

At this point, we slightly deviate from the procedure followed in most literature¹, by considering the Gordon decomposition of the transition current prior to calculating the e+p cross section:

$$J^\mu = \bar{\psi}(p') \left(\frac{(p' + p)^\mu}{2m} + i \frac{\sigma^{\mu\nu} q_\nu}{2m} \right) \psi(p). \quad (28)$$

In this equation $\sigma^{\mu\nu} = \frac{i}{2}(\gamma^\mu \gamma^\nu - \gamma^\nu \gamma^\mu)$ and $q_\mu = (p' - p)_\mu$. Thus, we decomposed the current into a pure Coulomb and spin term. Since in e+p scattering the mass difference between the proton and electron is large, this allows for a convenient distinction between three kinematical regimes *prior* to the calculation of the cross section:

RUTHERFORD SCATTERING: $E_e < m_e$ In this limit we can neglect the spinorial current for both the proton and the electron. This considerably simplifies the calculation, and we find $\frac{d\sigma}{d\Omega}_{Ruth} = \frac{\alpha^2}{16E_e \sin(\frac{\theta}{2})^4}$.

Thus, in this limit the Quantum Field Theory (QFT) amplitude maps smoothly onto first order quantum mechanical perturbation theory, with an incoming charged scalar boson and as perturbation term a Coulomb potential.

MOTT SCATTERING: $m_e < E_e < m_p$ In this limit, we need to take the leptonic spinorial current into account, while for the protonic current it suffices to consider only the Coulomb part. In the limit of no recoil we obtain $\frac{d\sigma}{d\Omega} = \frac{d\sigma}{d\Omega}_{Ruth} \cos(\frac{\theta}{2})^2 \equiv \frac{d\sigma}{d\Omega}_{Mott}$. In the case of recoil (for example for a high energetic $e\pi^\pm$ interaction), the equation extends to $\frac{d\sigma}{d\Omega}_{Ruth} \frac{E'_e}{E_e} \cos(\frac{\theta}{2})^2$.

The new terms are straightforward to interpret: the term $\cos(\frac{\theta}{2})^2$ represents the spin overlap between the incoming and outgoing electron, and without recoil $\frac{E'_e}{E_e}$ reduces to one.

THE RELATIVISTIC LIMIT: $m_p < E_e$ In this limit we cannot neglect any spinorial current or the recoil of the proton. We obtain for relativistic spin $\frac{1}{2} \times \frac{1}{2}$ scattering (neglecting m_e):

$$\frac{d\sigma}{d\Omega} = \frac{\alpha^2}{4E_e^2 \sin(\frac{\theta}{2})^4} \frac{E'_e}{E_e} \left[\cos\left(\frac{\theta}{2}\right)^2 - \frac{q^2}{2m_p^2} \sin\left(\frac{\theta}{2}\right)^2 \right]. \quad (29)$$

We immediately recognise the first term as Mott scattering with recoil; so effectively we only have added an additional term for the spin-spin interaction².

The cross sections outlined so far were for fundamental $s = \frac{1}{2}$ interactions. However, hadrons are known not to be elementary particles. To take this into consideration, it is convenient to split $|M|^2$ into a leptonic and hadronic current $L^{\mu\nu}$ and $W^{\mu\nu}$, respectively. $L^{\mu\nu}$ is defined as $\bar{\psi}(p') \gamma^\mu \psi(p) \bar{\psi}(p) \gamma^\nu \psi(p')$. Although we do not know the (non-perturbative) structure of the hadron, we do know three elementary properties that $W_{\mu\nu}$ should fulfil:

- The tensor must be constructed of linearly independent combinations of p^μ and p'^μ

¹ The procedure we follow was not found in any literature consulted by the author

² This term is responsible for spin flipping between the hadron and electron

- The current must be conserved, leading to $q_\mu W^{\mu\nu} = 0$
- The tensor must be symmetric in μ and ν , since $L^{\mu\nu}$ is symmetric

We construct the tensor in terms of q^2 and the initial hadron momentum p . We conceal our ignorance on the hadronic structure into two structure functions $F_1(q^2)$ and $F_2(q^2)$. Thus, the tensor can be written as [18]:

$$W^{\mu\nu} = 4F_2(q^2) \left[\left(p^\mu - \frac{(p \cdot q)}{q^2} q^\mu \right) \left(p^\nu - \frac{(p \cdot q)}{q^2} q^\nu \right) \right] + 2m_p^2 F_1(q^2) \left(-g^{\mu\nu} + \frac{q^\mu q^\nu}{q^2} \right). \quad (30)$$

Using the identity³ $\frac{q^2}{2} = p \cdot q$ we can identify the first term as the Coulomb current. Thus, we can directly predict the cross section (retrieved after contracting with $L^{\mu\nu}$): we just obtain eq. 29 with the cosine term multiplied with F_2 and the sine term with F_1 .

We can relate the Fourier transform of F_1 directly to the magnetic form factor $G_\mu(q^2)$ of the proton, while the Fourier transform of F_2 is a linear combination of $G_\mu(q^2)$ and the charge form factor $G_E(q^2)$. The e+p cross section expressed in $G_\mu(q^2)$ and $G_E(q^2)$ is the famous Rosenbluth equation[18]:

$$\frac{d\sigma}{d\Omega} = \frac{\alpha^2}{4E_e^2 \sin^4(\frac{\theta}{2})} \frac{E'_e}{E_e} \left[\frac{\cos^2(\frac{\theta}{2}) (G_E^2(q^2) + \tau G_\mu^2(q^2))}{(1 + \tau)} + 2\tau G_\mu^2(q^2) \sin^2\left(\frac{\theta}{2}\right) \right], \quad (31)$$

in which $\tau = \frac{-q^2}{4m^2}$. By determining the width of $G_E(q^2)$, it was determined that the proton radius $\sim 0.8 \text{ fm}$ [19][20], very similar to Λ_{QCD} we found in chapter 3.

However, when the electron deposits $E \geq 2 \text{ GeV}$ to the proton, suddenly the q^2 dependence of the structure functions almost completely drops and the proton breaks up. In Fig. 6 left we display the dramatic difference in q^2 dependence between the elastic and inelastic cross section (in this figure W is the photon-proton centre-of-mass energy, to be explained below). These DIS reactions are the topic of the next section.

4.2 THE QUARK PARTON MODEL OF E+P SCATTERING

So far we discussed only *elastic* e+p scattering, for which the incoming and outgoing particles are equal (up to kinematics). For such processes, the angle of the outgoing electron fully constrains the kinematics. However, when the energy of the reaction is large enough, the proton fragments; this is the aforementioned DIS process. In this section we describe the kinematics of DIS and explain the assumptions of the QPM. It also serves as a preparation for the subsequent discussion on the higher order corrections to the QPM.

4.2.1 Deep Inelastic Scattering

For an inelastic reaction the kinematics is constrained by two observables instead of one, for example the angle and the energy of the outgoing electron. Such a process is more

³ This identity can easily be derived by observing that $q^2 = (p_1 - p_3)^2$ and using the assumption that $p_1^2 = p_3^2 = 0$

conveniently described in a new set of Lorentz invariant observables though. These are defined as follows (with p_1 and p_2 the momentum of the incoming electron and proton, respectively):

- $Q^2 = -q^2 = -(p'_1 - p_1)^2$ is the *virtuality* of the photon⁴
- $x = \frac{Q^2}{2p_2 \cdot q}$; $0 < x < 1$ for inelastic scattering (for elastic scattering $x = 1$). This observable is called Bjorken- x after its inventor
- $y = \frac{p_2 \cdot q}{p_2 \cdot p_1} = 1 - \frac{E'_1}{E_1}$; y is the fractional energy loss of the incoming electron
- $W^2 = (q + p_2)^2$; thus W is the $\gamma + p_2$ centre-of-mass energy, and also equals the invariant mass m_X of the sum of all outgoing particles except the electron

Often, processes are discussed in terms of the scale Q^2 , but this should not be straightforwardly identified with the transversal momentum. The relation between the virtuality Q^2 and the transversal momentum p_T is concisely derived in appendix A.3 for completeness.

We are now prepared to kinematically define DIS: with deep is meant that Q^2 is larger than the proton radius squared, which approximately corresponds to Λ_{QCD}^2 , while with inelastic is meant that $W^2 > m_p^2$; the latter statement means that the proton breaks up.

To formulate a general cross section for inelastic scattering we construct, analogous to eq. 30, a new tensor for the hadron with structure functions that also depend on x :

$$T^{\mu\nu} = \frac{x F_2(Q^2, x)}{m_p Q^2} \left[(p^\mu - \frac{(p \cdot q)}{Q^2} q^\mu) (p^\nu - \frac{(p \cdot q)}{Q^2} q^\nu) \right] + \frac{F_1(Q^2, x)}{m_p} (-g^{\mu\nu} + \frac{q^\mu q^\nu}{Q^2}). \quad (32)$$

Upon contracting the general inelastic hadronic tensor $T^{\mu\nu}$ with the leptonic tensor $L^{\mu\nu}$, and rewriting the lab frame variables in Lorentz invariant variables, we obtain the general inelastic e+p scattering cross section:

$$\frac{d^2\sigma}{dx dQ^2} = \frac{4\pi\alpha^2}{x Q^4} \left[\left(\frac{F_2(x, Q^2)}{x} \right) (1 - y) + \frac{y^2}{2} F_1(x, Q^2) \right]. \quad (33)$$

The resemblance with the previous result should be manifest: the new structure functions conceal our ignorance about the proton structure in inelastic reactions. Further, the cross section has become a differential in two variables, since the reaction cannot be characterised by a single parameter anymore.

4.2.2 The quark parton model

The apparent lack of a Q^2 dependence of the structure functions F_1 and F_2 in the DIS regime (partially) motivated the QPM. Its central assumption is that the proton is a composite particle and consists of fundamental spin $\frac{1}{2}$ partons, which carry electromagnetic charge. When

⁴ In the infinite momentum frame, the proton is approximated to have an infinite momentum. In this frame the virtuality may be interpreted as a *transversal* scale, and thus as if with increasing the virtuality the *transversal resolution* of our measurement improves. This "microscope" analogy is only valid in this particular frame though

the energy of the interaction is high and the resolution of the photon small enough, the photon resolves the constituents. In the interaction a parton is ejected from the proton, which causes the proton to fragment. A DIS reaction is schematically depicted in Fig. 6 right.

Three fundamental assumptions are made in the QPM:

- Before and after the interaction the struck parton is massless
- The intrinsic transversal momentum of the partons is considered small w.r.t. their longitudinal momentum and is neglected
- The partons are considered to behave as free inside the hadron during the interaction⁵

The latter statement is not a trivial assumption, but it can be shown that the ratio of the interaction time τ_i of the process and the fluctuation time τ_f , in which the proton can fluctuate into two partons, is given by [17]:

$$\frac{\tau_i}{\tau_f} \approx \frac{2k_T^2}{Q^2}. \quad (34)$$

In this equation k_T^2 is the transversal momentum of the daughter partons of the proton. Thus we see that, as long as the transversal momentum of the partons is small w.r.t. Q^2 , the partons can be considered as "frozen" during the interaction.

We calculate the cross section for the scattering of an electron with a parton q of the proton: $e + q \rightarrow e' + q'$. We ascertain the quark carries a fraction ξ of the longitudinal momentum of the proton. The first observation that is essential to make is that the previously defined x corresponds to ξ (we use the approximation that the parton is massless):

$$0 = p_q^2 = (\xi p_2 + q)^2 = \xi^2 p_2^2 + q^2 + 2\xi p_2 \cdot q = q^2 + 2\xi p_2 \cdot q. \quad (35)$$

Thus, $\xi = \frac{Q^2}{2p_2 \cdot q} = x$. This only holds for the leading order process though.

The cross section for $\frac{1}{2} \times \frac{1}{2}$ scattering is given in lab frame observables in eq. 29. We rewrite the equation in the Lorentz invariant variables for electron-parton scattering⁶:

$$\frac{d\sigma}{dQ^2} = \frac{4\pi\alpha^2 e_q^2}{q^4} \left[(1-y) + \frac{y^2}{2} \right]. \quad (36)$$

Using the result from eq. 35, we multiply this equation with a resolution of the identity $\int d\xi \delta(\xi - x) = 1$. Next, we turn the equation into a double differential equation:

$$\frac{d\sigma}{dQ^2 dx} = \frac{4\pi\alpha^2 e_q^2}{q^4} \left[(1-y) + \frac{y^2}{2} \right] \delta(\xi - x). \quad (37)$$

Eq. 37 is the double differential cross section for scattering an electron off a parton with momentum $q = \xi p$. By comparing eq. 37 to eq. 33, we would find that the structure functions

⁵ From our previous discussion of QCD and asymptotic freedom this should appear as a rather natural assumption, but at the time the quark parton model was formulated this was not so evident, and only around 1980 partons were commonly believed to be quarks

⁶ The cross section is given in the variables y and Q^2 , which are invariant under changing the proton to a parton

are delta functions. We know from experiments however, that these are distributions instead. Thus, we convolve eq. 36 with a parton density function (pdf) $q^i(\xi)$. The pdf describes the probability to find a parton of species i in a hadron with a longitudinal momentum fraction ξ . We obtain:

$$\frac{d\sigma}{dQ^2 dx} = \frac{4\pi\alpha^2 e_q^2}{q^4} \left[(1-y) + \frac{y^2}{2} \right] \sum_i q^i(x). \quad (38)$$

Comparing eq. 38 to eq. 37, we obtain instead $F_2(x, Q^2) = 2xF_1(x, Q^2) = x \sum_i e_i^2 q^i(x)$. This identity implies Bjorken scaling, i.e. F_1 and F_2 should be independent of Q^2 . This provides an explanation for the previously mentioned dramatic change between elastic and inelastic scattering. Also, we obtain the Callan-Gross relation $F_2(x) = 2xF_1(x)$.

For future purposes, it is useful to factorise the cross section into three parts⁷:

$$\begin{aligned} \frac{d\sigma}{dQ^2 dx} &= F_\gamma \sigma^{\gamma p} \\ &= F_\gamma \sigma^0 \sigma^{QPM}, \end{aligned} \quad (39)$$

in which $F_\gamma = \frac{\alpha}{2\pi Q^2 x} (1 + (1-y)^2)$. The separation of the leptonic part is known as the *equivalent photon approximation*. We conceal (again) our ignorance about the structure of the proton in $\sigma^{\gamma p}$, and $\sigma^0 = \frac{4\pi^2\alpha}{2q \cdot p}$. Thus, $\sigma^{QPM} = \int d\xi \delta(x - \xi) f(\xi)$ contains the lowest order contribution to the photon-proton cross section. For future purposes, it is convenient to rewrite:

$$\sigma^{QPM} = \int d\xi \frac{f(\xi)}{\xi} \delta(1 - x/\xi). \quad (40)$$

Before we proceed to the next section, it is important to note that *the experimental observable is F_2* . In an e+p scattering experiment one can measure the cross section for a set of kinematic observables Q^2 and x , and thus F_2 can be deduced. The structure function $q(x)$ however is not a direct observable, since the relation between $q(x)$ and F_2 depends on the order of α_s in which we perform our calculation.

In summary, we factorised the probability for a deep inelastic e+p scattering in three quantities. First, we separated the equivalent photon flux F_γ . This quantity yields the number of photons emitted by the lepton. This multiplies σ^γ , which comprises our ignorance about the photon-hadron interaction. Using the assumptions of the QPM, we calculated the probability for the photon to interact with a charged spin- $\frac{1}{2}$ constituent of the proton. Thus, we further factorised $\sigma^{\gamma p} = \sigma^0 \sigma^{QPM}$. We contained the unknown (non-perturbative) structure of the proton in parton density functions $q^i(x)$. For the QPM, it is expected that F_2 is independent of the Q^2 of the reaction.

We close the section with inspecting measurements of F_2 in Fig. 6 bottom. A careful inspection reveals that these measurements actually do moderately depend on Q^2 ; this is known as scaling violations. These are a consequence of higher order QCD processes, which we'll introduce in section 4.4.

⁷ The decomposition can easily be proven by a calculation of the elementary $\gamma + q \rightarrow q'$ matrix element

4.3 INTERMEZZO: BREMSSTRAHLUNG GENERAL LAW

Due to the energy of the interaction of the photon with the parton, phase-space opens up for parton radiation. These constitute corrections to the QPM result. In this section we first consider the general bremsstrahlung law, since this allows for a rather accessible summary of most of the difficulties that lie ahead in the subsequent chapters.

The general probability for soft gauge boson emission [23] by a *single* charged spin- $\frac{1}{2}$ particle (for example an electron) can be written as⁸:

$$\frac{dP_{Brems}}{dxdk_T} = \frac{\alpha_s C_f}{\pi} \frac{1}{x} \frac{1}{\pi k_T^2}, \quad (41)$$

in which C_f is a constant (related to the number of fermions), x is the longitudinal momentum fraction of the emitted parton, and k_T its transversal momentum.

When calculating the total probability P_{Brems} , two difficulties arise. Firstly, when we carefully consider the equation we observe that there are two poles, for $x \rightarrow 0$ and $k_T \rightarrow 0$. These are the soft and collinear divergence, respectively. This forces us to introduce two lower cutoffs $x_{min.}$ and μ respectively for the integrals:

$$P_{Brems} = \frac{\alpha_s C_f}{\pi} \ln(1/x_{min.}) \ln(k_T^2/\mu^2). \quad (42)$$

Secondly, from our previous discussions we know that for QCD reactions the coupling α_s may be large. This may invalidate a perturbative expansion in $\alpha_s \ln(k_T^2/\mu^2)$ or $\alpha_s \ln(1/x_{min.})$, since higher order corrections may have a similar probability.

The solution to this problem is to perform a *resummation*; we split the problematic integral into smaller terms, such that $\alpha_s \ln(k_T^{i+1}/k_T^i) < 1$ (the latter equation is in k_T^2 , but can be performed equally well in $\ln(1/x)$). We apply a strong ordering condition on the subsequent evolution steps: $k_{T,i-1}^2 \ll k_{T,i}^2 \ll k_{T,i+1}^2$ (and similar in $1/x$). Consequently, the probability for n -parton emissions is:

$$P_{Brems}^n = \frac{1}{n!n!} \left(\frac{\alpha_s C_f}{\pi} \ln(1/x_{min.}) \ln(k_{T,max.}^2/k_{T,min.}^2) \right)^n. \quad (43)$$

We see at this point the consequence of the strong ordering approximation: effectively we only keep the terms that have a large logarithm, and thus have a large probability. We take the sum of the terms to all orders:

$$\begin{aligned} P_{Brems}^n &= \sum_{n=0}^{\infty} \frac{1}{n!n!} \left(\frac{\alpha_s C_f}{\pi} \ln(1/x_{min.}) \ln(k_{T,max.}^2/k_{T,min.}^2) \right)^n \\ &= I_0 \left(2\sqrt{\frac{\alpha_s C_F}{\pi} \ln(1/x_{min.}) \ln(k_{T,max.}^2/k_{T,min.}^2)} \right), \end{aligned} \quad (44)$$

in which I_0 is the modified Bessel function. To obtain the result in eq. 44, we effectively resummed the large logarithms in $1/x$ and k_T *simultaneously* for the bremsstrahlung of a single parton. This is called the Double Leading Log (DLL) approximation.

⁸ This result is very general, and applies to all standard model gauge theories

Thus, for the particular kinematic situation of an emission with large transversal and low longitudinal momentum transfer, the DLL predicts a very rapid rise of emission probability; the rise is faster than a logarithm, but slower than a power law.

This result has limited practical applicability in hadronic interactions though. A clear limitation is that the result is only for emission by a single particle, while hadrons are composite particles. Furthermore, the DLL region is kinematically (currently) not experimentally accessible. For the regions that are experimentally accessible, either the logarithm in k_T^2 or the logarithm in $1/x$ is large and needs to be resummed (this is the Leading Log Approximation (LLA)). For these interactions eq. 44, which resums both logarithms simultaneously, is instead a too crude approximation. Another important limitation of eq. 44 is that the higher order self-interactions of the gauge bosons are not included.

Therefore, we inspect the QCD corrections to the QPM below.

4.4 QCD CORRECTIONS TO THE QUARK PARTON MODEL

The observant reader may have noticed that so far we have carefully discussed the QPM only in terms of charged spin- $\frac{1}{2}$ partons. Compelling experimental evidence has established that the spin $\frac{1}{2}$ constituents of the proton are indeed quarks, and the gluon was discovered in 1979 [24]. From this section onwards we will thus discuss the proton constituents in terms of quarks and gluons; the word parton is used still to refer to both.

The diagrams with the leading order radiative corrections to the QPM are displayed in Fig.7. The QCD Compton (QCDC) process can be interpreted as the probability to measure a quark (to which the photon couples) in a quark (a quark originating from the hadron). The Boson Gluon Fusion (BGF) process describes the probability to measure a quark in a gluon. The third process denotes the probability to measure a gluon in a quark. The last diagram, in which a gluon splits in two, is for the probability for measuring a gluon in a gluon. The last diagram is strictly reserved for non-Abelian gauge theories⁹. Only the upper diagrams contribute directly in leading order to e+p scattering, since a gluon does not directly couple to leptons. We include the other two processes though for reference in the next chapter.

We briefly outline the calculation of the (photon-proton) QCDC amplitude, for brevity we will only state the result for the other diagrams. Analogous to the QPM, the calculations are done under the assumption of massless partons and we neglect any initial k_T^2 w.r.t. the (large) longitudinal momentum. We define the variable z as the longitudinal momentum fraction that is carried by the emitted partons, and k_T is its transversal momentum. The cross section for the QCDC process is then given by:

$$\frac{d\sigma^{\text{QCDC}}}{dk_T^2} = \sigma_0 e_q^2 \frac{\alpha_s}{2\pi} \frac{1}{k_T^2} P_{qq}(z). \quad (45)$$

The splitting function $P_{qq}(z)$ is given in eq. 48.

⁹ The observant reader may wonder why the four-gluon vertex, which followed from eq. 20, is not included. The reason is that the vertex is beyond leading order in α_s . The process must be included in a next-to-leading order QCD calculation though

To obtain the total cross section we need to integrate over k_T . The maximal k_T that can be reached is given by $\frac{Q^2(1-z)}{4z}$ (and in this sense the virtuality may again be thought of as a transversal resolution). We observe there is an (anticipated) collinear divergence for $k_T = 0$. We will temporarily circumvent this problem with putting the lower cutoff at $k_{T,0}^2$. We obtain:

$$\sigma^{QDC} = \sigma_0 e_q^2 \frac{\alpha_s}{2\pi} P_{qq}(z) (\ln(Q^2/k_{T,0}^2) + \dots). \quad (46)$$

Analogous to the QPM calculation, we need to convolve the cross section with the quark pdf. We introduce an integral over the longitudinal momentum splitting variable z , as well as an integral over the original longitudinal momentum fraction ξ of the quark. We fix longitudinal momentum conservation by introducing $\delta(x - z\xi)$. We obtain:

$$\begin{aligned} \sigma^{QDC} &= \sigma_0 e_q^2 \int dz d\xi \delta(x - z\xi) f(\xi) \frac{\alpha_s}{2\pi} P_{qq}(z) (\ln(Q^2/k_{T,0}^2) + \dots) \\ &= \sigma_0 e_q^2 \int \frac{d\xi}{\xi} f(\xi) \frac{\alpha_s}{2\pi} P_{qq}(x/\xi) (\ln(Q^2/k_{T,0}^2) + \dots). \end{aligned} \quad (47)$$

Actually, the relevant parts of the cross sections of the other three processes are equal, except for the splitting functions, and naturally the right hand diagrams of Fig.7 couple to the gluon pdf instead of the quark pdf. The four splitting functions are[17][25]:

$$P_{qq}(z) = \frac{4}{3} \frac{1+z^2}{1-z} \quad (48) \quad P_{gq}(z) = \frac{1}{2} (z^2 + (1-z)^2) \quad (49)$$

$$P_{qg}(z) = \frac{4}{3} \frac{1+(1-z)^2}{z} \quad (50) \quad P_{gg}(z) = 6 \left(\frac{z}{1-z} + \frac{1-z}{z} + z(1-z) \right) \quad (51)$$

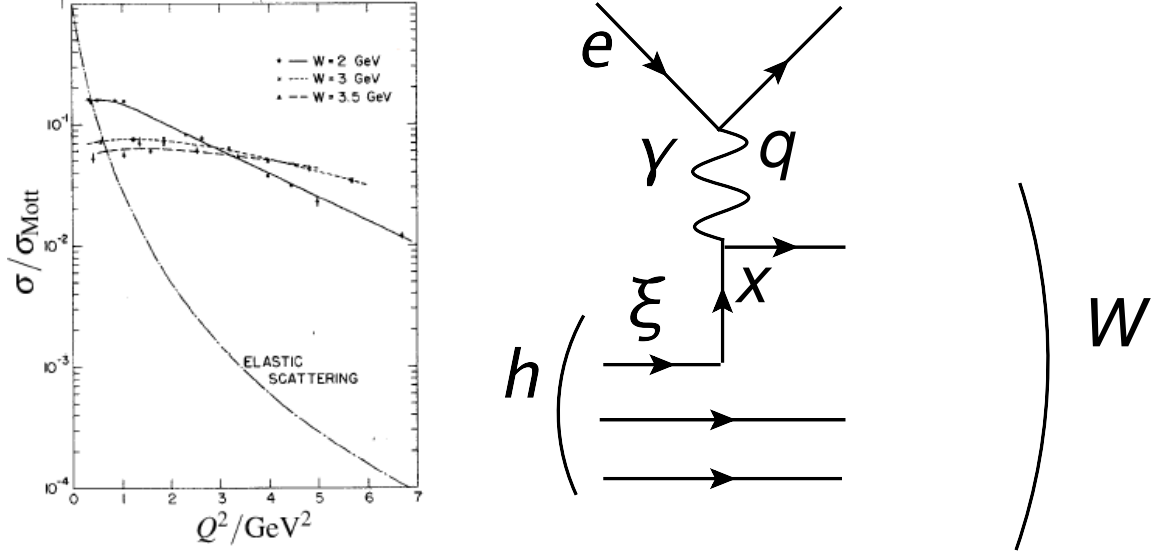
As a last step we put together the terms for F_2 in e+p scattering¹⁰; again we profit from the factorisation we made in section 4.2.2. We obtain:

$$\begin{aligned} F_2/x = \frac{\sigma^{\gamma p}}{\sigma^0} &= \sum_q e_q^2 \int_x^1 \frac{d\xi}{\xi} \left(f(\xi) \left[\delta\left(1 - \frac{x}{\xi}\right) + \frac{\alpha_s}{2\pi} P_{qq}\left(\frac{x}{\xi}\right) \ln\left(\frac{Q^2}{k_{T,0}^2}\right) \right] + \right. \\ &\quad \left. g(\xi) \left[\frac{\alpha_s}{2\pi} P_{qg}\left(\frac{x}{\xi}\right) \ln\left(\frac{Q^2}{k_{T,0}^2}\right) \right] \right). \end{aligned} \quad (52)$$

There are many similarities between the soft bremsstrahlung law (eq. 42) and the QCD radiative corrections. The collinear divergence is present (temporarily hidden in $k_{T,0}^2$), while the soft divergence is present in the splitting function P_{gg} . Furthermore, we notice that F_2 has obtained a Q^2 dependence, which explains the scaling violations discussed in section 4.2.2.

In the next chapter we will outline how different kinematic limits demand a different treatment of the singularities and resummations of these logarithms.

¹⁰ We added the QPM result. In retrospect, we may interpret the $\delta(1 - x/\xi)$ now as the 0^{th} order splitting function



H1 and ZEUS

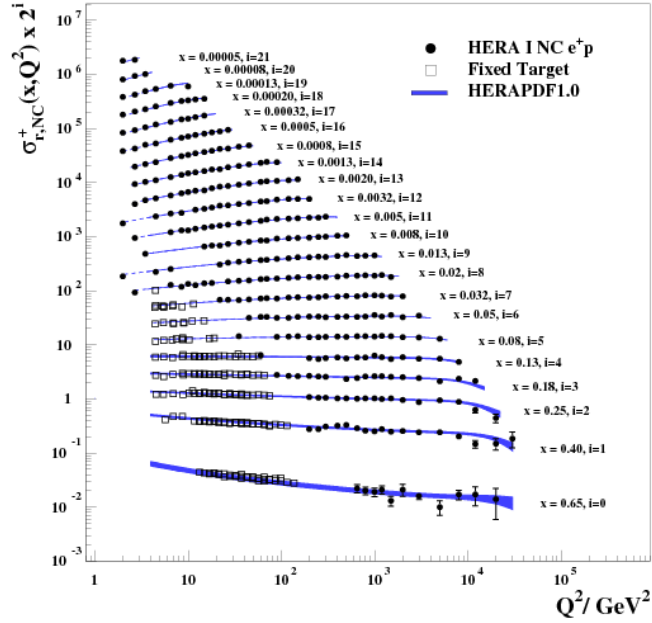


Figure 6: Left: the σ/σ_{Mott} distribution of the proton [21]. We observe a dramatic change in the q^2 dependence between elastic and inelastic scattering. Right: a diagram representing a DIS reaction, together with the kinematic variables. Bottom: F_2 for $e+p$ interactions as a function of Q^2 [22]

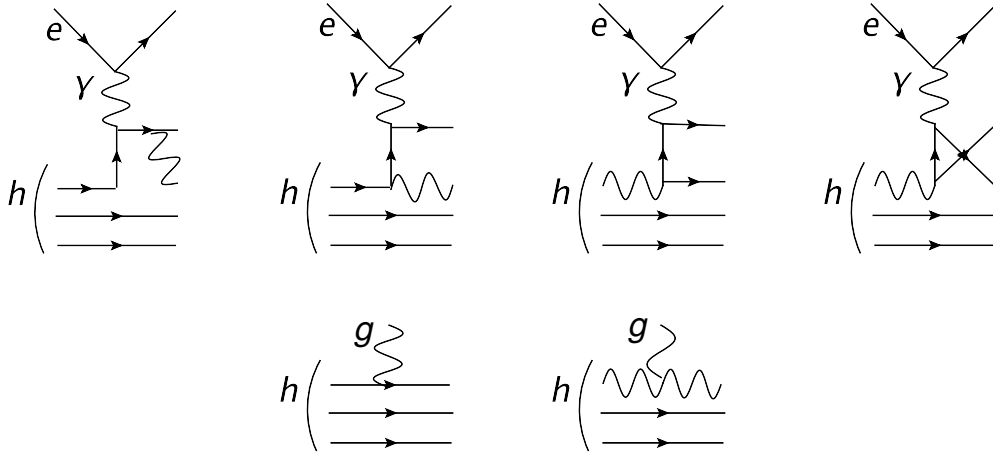


Figure 7: The radiative corrections to $\mathcal{O}(\alpha_s)$ to the QPM. The upper diagrams directly contribute to e+p scattering, while the lower diagrams only contribute directly in hadron-hadron interactions. Upper left diagrams: the QCDC process, which represents the contribution for measuring a quark in a quark. Upper right diagrams: the BGF process, which represents the contribution for measuring a quark in a gluon. Lower left diagram: the contribution for measuring a gluon in a quark. Lower right diagram: the contribution for measuring a gluon in a gluon.

We finished the previous chapter with the derivation of eq. 52 for F_2/x in the context of e+p scattering. In this chapter we will outline strategies to approximate the phase-space integrals in various kinematic regions, including the region we aim to assess experimentally in this thesis. We start with a succinct outline of the general concept of factorisation though, which is common to these different approximations.

The central hypothesis of factorisation is that an interaction involving a hadron can be factorised into a hadron-specific parton distribution (which is not necessarily perturbative), and perturbative matrix elements describing the hard scattering of the partons. The parton distributions can be evolved from a particular scale to another. In the context of e+p interactions this may appear as a rather trivial assumption. However, factorisation is anticipated to be also applicable to hadron-hadron collisions. As an example, a Drell-Yan process has been schematically depicted in Fig. 8. It is certainly not evident that factorisation is valid for this process, since one hadron may influence the parton distribution of the other hadron prior to the hard interaction.

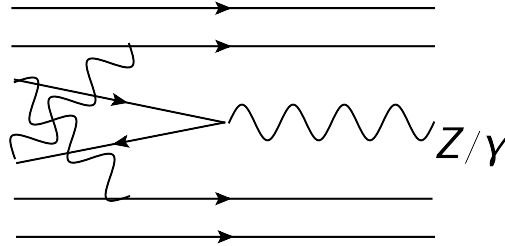


Figure 8: A schematic illustration of a Drell-Yan process, including higher order effects

5.1 COLLINEAR FACTORISATION

We start this section with reconsidering the result from eq. 52 on F_2/x that we obtained earlier:

$$F_2/x = \frac{\sigma^{\gamma p}}{\sigma^0} = \sum_q e_q^2 \int_x^1 \frac{d\tilde{\xi}}{\tilde{\xi}} \left(q(\tilde{\xi}) \left[\delta \left(1 - \frac{x}{\tilde{\xi}} \right) + \frac{\alpha_s}{2\pi} P_{qq} \left(\frac{x}{\tilde{\xi}} \right) \ln \left(\frac{Q^2}{k_{T,0}^2} \right) \right] + g(\tilde{\xi}) \left[\frac{\alpha_s}{2\pi} P_{qg} \left(\frac{x}{\tilde{\xi}} \right) \ln \left(\frac{Q^2}{k_{T,0}^2} \right) \right] \right). \quad (53)$$

We did not yet discuss how to treat the singularities that appear in the limit $k_{T,0}^2 \rightarrow 0$. We will apply the same technique that we introduced in chapter 3 to renormalise the coupling α_s : we *renormalise* the bare (unobservable) pdfs $q(x)$ and $g(x)$ by absorbing the divergent part into the *definition* of the pdf¹ at a scale μ :

$$\begin{aligned} q_i(x, \mu^2) &= q_i^0(x) + \int_x^1 \frac{d\bar{\xi}}{\bar{\xi}} q_i^0(\bar{\xi}) \left(\frac{\alpha_s}{2\pi} P_{qq} \left(\frac{x}{\bar{\xi}} \right) \ln \left(\frac{\mu^2}{k_{T,0}^2} \right) + \dots \right) \\ g(x, \mu^2) &= g^0(x) + \int_x^1 \frac{d\bar{\xi}}{\bar{\xi}} g^0(\bar{\xi}) \left(\frac{\alpha_s}{2\pi} P_{qg} \left(\frac{x}{\bar{\xi}} \right) \ln \left(\frac{\mu^2}{k_{T,0}^2} \right) + \dots \right). \end{aligned} \quad (54)$$

In terms of the *scale-dependent* pdfs the expression for F_2/x is regular:

$$\begin{aligned} F_2/x = \frac{\sigma^{\gamma p}}{\sigma^0} &= \sum_q e_q^2 \int \frac{d\bar{\xi}}{\bar{\xi}} \left(q(\bar{\xi}, \mu^2) \left[\delta \left(1 - \frac{x}{\bar{\xi}} \right) + \frac{\alpha_s}{2\pi} P_{qq} \left(\frac{x}{\bar{\xi}} \right) \ln \left(\frac{Q^2}{\mu^2} \right) \right] + \right. \\ &\quad \left. g(\bar{\xi}, \mu^2) \left[\frac{\alpha_s}{2\pi} P_{qg} \left(\frac{x}{\bar{\xi}} \right) \ln \left(\frac{Q^2}{\mu^2} \right) \right] \right). \end{aligned} \quad (55)$$

The above equations demonstrate the key ingredients of *collinear factorisation*; the collinear divergencies are factorised into (scale-dependent) pdfs and perturbative matrix elements at the (arbitrary) *factorisation scale* μ^2 . Collinear factorisation is derived in the limit where the intrinsic transversal momentum of the partons is neglected, since their longitudinal momentum is much larger. Thus, the kinematic domain of collinear factorisation is for not too small x .

The structure function is specific to a hadron, while the matrix elements are entirely general. The scale-dependent collinear pdfs $q_i(x, \mu^2)$ and $g(x, \mu^2)$ cannot be calculated perturbatively, since they are intrinsically non-perturbative³. Thus, the pdfs must be derived from experimental data.

Collinear factorisation has been proven for a variety of processes, i.e. the collinear divergencies can be absorbed consistently and the pdfs do not “cross talk” during the interaction:

- DIS processes
- Diffractive DIS processes, in which the proton interacts via colour-singlet exchange
- Drell-Yan production
- Single particle inclusive spectra; these are fragmentation functions

For other hadronic interactions at not too low x -values, collinear factorisation is assumed to hold. Experimental evidence seems to suggest this assumption is rather successful though.

¹ There are different schemes to absorb the divergence; the predictions for interactions are naturally independent of the scheme chosen
² The bare pdfs $q_i^0(x)$ and $g^0(x)$ may be thought of as a *counter-term for a composite operator*; it this perspective they are similar to the counter-terms encountered in the previous chapter, and similar normalisation conditions apply
³ Recently, interesting progress has been made on lattice-QCD to predict the structure functions from the forward Compton amplitude [26], although this novel method is currently in a preliminary phase

5.1.1 DGLAP Evolution

For the pdfs, which depend now on the arbitrary scale⁴ μ , we apply an analogous procedure as to the running coupling; we determine the pdf experimentally as a function of x for a given Q_0 value. The associated evolution equation to evolve the pdfs to a different scale Q^2 is the famous Dokshitzer Gribov Lipatov Altarelli Parisi equation (DGLAP) [27, 28]. The governing equation is:

$$\frac{\partial}{\partial \mu^2} F_2/x = 0. \quad (56)$$

Applying eq. 56 to eq. 55 and rewriting terms a bit, we obtain the following evolution equation:

$$\frac{d}{d \ln(\mu^2)} \begin{bmatrix} q_i(x, \mu^2) \\ g(x, \mu^2) \end{bmatrix} = \frac{\alpha_s}{2\pi} \begin{bmatrix} P_{qq}\left(\frac{x}{\xi}\right) & P_{qg}\left(\frac{x}{\xi}\right) \\ P_{gq}\left(\frac{x}{\xi}\right) & P_{gg}\left(\frac{x}{\xi}\right) \end{bmatrix} \otimes \begin{bmatrix} q_i(\xi, \mu^2) \\ g(\xi, \mu^2) \end{bmatrix}. \quad (57)$$

With the \otimes symbol a convolution of the form $\int_x^1 \frac{d\xi}{\xi}$ is implied.

Evidently, the evolution equation is more complex than the equation for the running coupling, since it is a set of coupled integro-differential equations. Thus, the evolution (usually) needs to be calculated numerically.

The observant reader may have noticed divergencies in the integral above, since P_{qq} and P_{gg} contain divergencies for $z \rightarrow 1$ and $z \rightarrow 0$, respectively. For the DGLAP equation we only need to focus on the first pole though⁵, which implies $x = \xi$. We ignored so far the virtual contributions (diagrams with a same final state as the diagrams that they are corrections to) to $\mathcal{O}(\alpha_s)$ to the amplitude for parton emission though. The contribution of the virtual correction can actually quite smoothly be calculated and cancels the divergence for $z \rightarrow 1$.

5.1.1.1 Solutions of the DGLAP equation

One assumption that we previously used to derive the DGLAP equation, is that x is not too small. Consequentially, DGLAP equations are typically used in a domain where the logarithm in $1/x$ does not need to be resummed. On contrary, except for the available phase-space there is no upper bound on Q^2 and the logarithms in Q^2 do need to be resummed.

The solution to the DGLAP equation can be approximated by considering only the emissions which are strongly ordered in k_T . For clarity, a parton ladder is depicted in Fig. 9; for this ladder we have $k_{T,1}^2 \ll k_{T,2}^2 \cdots \ll k_{T,N}^2 \ll Q^2$. To avoid any obscurity, we emphasise that not the DGLAP equation is strongly ordered in k_T ; the dominant part of the solution is.

⁴ Although the renormalisation scale is arbitrary per definition, for certain quantities (for example the QED coupling α) there are rather natural choices for fixing the renormalisation scale. For the strong coupling and collinear factorisation however, there is no unique choice

⁵ The pole for $z \rightarrow 0$ becomes relevant when $x \ll \xi < 1$. This falls outside the region for which DGLAP was constructed

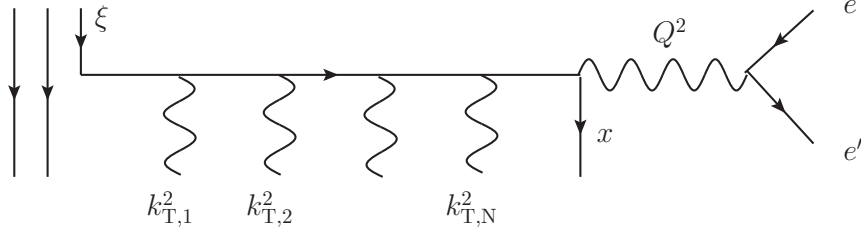


Figure 9: A schematic picture of a parton ladder. Solutions to the DGLAP equations are obtained by applying a strong ordering condition on the successive emissions: $k_{T,1}^2 \ll k_{T,2}^2 \cdots \ll k_{T,N}^2 \ll Q^2$

In Fig. 10 we display pdfs that were fitted to e+p data, evaluated at two different virtuality scales. At low x -values the gluon pdf clearly is dominant. With increasing the transversal resolution, the low- x gluon pdf also grows strongly. Both effects can easily be understood as a result of the increased phase-space for parton emission.

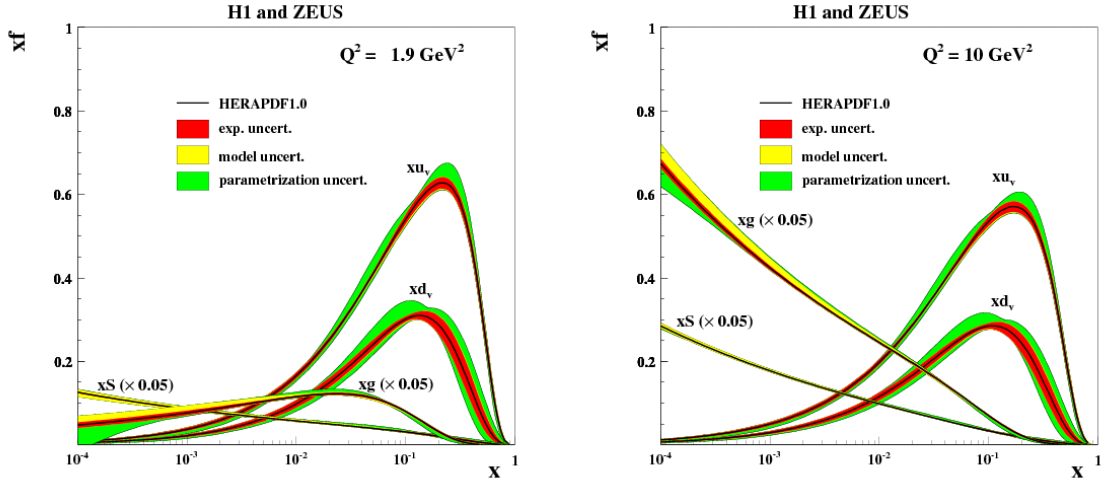


Figure 10: The parton distribution functions from HERAPDF1.0, extracted from fits to e+p data from the HERA and ZEUS experiment [29]. We observe the gluon distribution is dominant at low x -values, and grows strongly with Q^2

5.2 k_T -FACTORISATION AND GLUON SATURATION

The framework of collinear factorisation and the DGLAP evolution equations were all derived using the approximation that the intrinsic k_T and mass of the partons is neglected w.r.t. the large longitudinal momentum. Further, only logarithms in Q^2 need to be resummed. How-

ever, at low x eventually the longitudinal momentum becomes small, and this assumption is not realistic anymore. As an elementary example why the assumption becomes inconsistent, we may recompute the value of ξ (the longitudinal momentum fraction of the parton that enters the actual hard interaction), without neglecting the initial virtuality and outgoing mass of the parton anymore. For this simple situation already an inconsistency is found since $x \neq \xi$.

Therefore, k_T -factorisation is expected to describe the interactions instead at small x . The interactions are split into a k_T -dependent pdf (called an unintegrated parton density function ([updf](#))) at a certain x_0 -value, and hadron-independent perturbative matrix elements. The latter are derived for interactions between off-shell partons and also referred to as impact factors. The pdf can be evolved to $x' < x^0$ with an evolution equation in $\ln(1/x)$. The equations are derived solely for gluons, since these constitute the vast majority of the low- x partons (as can be observed in [Fig. 10](#)).

This section is ordered as follows: we start with a brief derivation of a general evolution equation in $\ln(1/x)$, which contains a non-linear term. We first discard the non-linear term, and elaborate the result to find an explicit solution for the linear evolution of the unintegrated pdf. This linear approximation however leads to a unitarity violation, which necessitates us to reconsider the non-linear reaction in the intermezzo. Lastly, we discuss the non-linear evolution equation and compare the linear and non-linear updfs. The equations are illustrated with the actual pdfs and their evolution, to which we will compare the key measurements presented in this thesis.

5.2.1 k_T -Factorisation in the dipole picture

There are two (nearly equivalent) perceptions on how a hadronic interaction at low x can be modelled. The Balitsky Kovchekov equation ([BK](#)) is derived in the dipole formalism and can be explained rather intuitively.

In the dipole formalism an incoming photon fluctuates into a $q\bar{q}$ colour dipole that interacts solely with the gluons from the hadron. The elastic forward process is depicted in [Fig. 11](#). The imaginary part of the *amplitude* of a forward elastic process can be related to the *probability* of a total inclusive reaction via the optical theorem, as explained in [appendix A.4](#). Therefore, the calculations focus rather on the amplitudes of the elastic processes instead of calculating probabilities directly, as was done for the QPM and collinear factorisation.

Further, it can be proven that the process can be factorised into photon-dipole overlap functions and the hadronic interaction, and that the dipole lifetime is much longer than the interaction time. The rapidity difference ΔY between the dipole and the target equals $\ln(1/x)$. The transversal position of the quark is depicted \mathbf{x} and \mathbf{y} for the anti-quark. We denote the amplitude $A_{dip.}$ for the dipole interaction with the gluons of the hadron with $D_Y(\mathbf{x} - \mathbf{y})$, and by translational symmetry we may equally well write $D_Y(\mathbf{r})$.

The interaction of the dipole with the hadron cannot be calculated from scratch, since the structure of the hadron is non-perturbative. It is of paramount importance to observe that although the interaction $D_Y(\mathbf{r})$ cannot be calculated, the *difference* between the interaction of

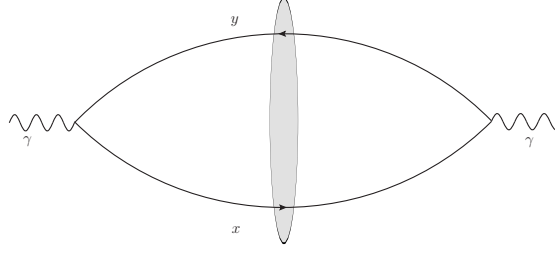


Figure 11: The forward elastic interaction of a photon with a hadron in the dipole formalism. The transversal position of the quark is depicted x and the anti-quark is at y . The hadron, which is highly Lorentz contracted in the dipole frame, is depicted with the grey blob

a dipole at Y and $Y + \Delta Y$ is calculable. The ΔY allows for a gluon emission, which we can calculate. To this purpose, we calculate the amplitude $D_{Y+\Delta Y}(r')$:

$$D_{Y+\Delta Y}(r') = D_Y(r') + \Delta Y (A_{virt.} + A_{real}) \quad (58)$$

In this equations, a small rapidity step is assumed and the contribution is approximated by a multiplication with ΔY .

The virtual contributions to the diagram in Fig. 11 at $Y + \Delta Y$ are given in the upper diagrams of Fig. 12, while the real emissions are depicted on the lower side. Surprisingly, an evolution equation can indeed be derived, since the amplitudes of the contributions can all be elegantly rewritten in terms of *new dipoles* $D_Y(r')$. For the virtual contributions we obtain:

$$A_{virt.} = 4\alpha_s D_Y(\mathbf{x} - \mathbf{y}) \int \frac{d\mathbf{z}}{(2\pi)^2} M_{\mathbf{xyz}}, \quad (59)$$

in which $M_{\mathbf{xyz}} = \frac{(\mathbf{x}-\mathbf{y})^2}{(\mathbf{x}-\mathbf{z})^2(\mathbf{y}-\mathbf{z})^2}$.

For the real emissions an approximation is made (the limit where the number of colours N_c is large): the gluon is envisaged to split into a $q\bar{q}$ dipole. This allows us to rewrite the amplitude solely in terms of new dipoles:

$$A_{real} = 4\alpha_s \int \frac{d\mathbf{z}}{(2\pi)^2} M_{\mathbf{xyz}} D_Y(\mathbf{x} - \mathbf{z}) D_Y(\mathbf{y} - \mathbf{z}). \quad (60)$$

Adding the virtual and real contributions, we obtain the the famous BK evolution equation in rapidity in spatial coordinates:

$$\frac{d}{dY} D_Y(\mathbf{x} - \mathbf{y}) = -\frac{\alpha_s}{2\pi} \int d\mathbf{z} M_{\mathbf{xyz}} (D_Y(\mathbf{x} - \mathbf{y}) - D_Y(\mathbf{x} - \mathbf{z}) D_Y(\mathbf{y} - \mathbf{z})). \quad (61)$$

We can Fourier transform eq. 61 to obtain the BK equation in momentum space (for a dipole with transversal momentum \mathbf{k} , emitting a gluon with \mathbf{q}):

$$\frac{d}{dY} D_Y(\mathbf{k}) = -\frac{\alpha_s}{2\pi} \int \frac{d\mathbf{q}^2}{\mathbf{q}^2} \left[\frac{\mathbf{q}^2 D_Y(\mathbf{q}) - \mathbf{k}^2 D_Y(\mathbf{k})}{|\mathbf{k}^2 - \mathbf{q}^2|} + \frac{\mathbf{k}^2 D_Y(\mathbf{k})}{\sqrt{4\mathbf{k}^4 + \mathbf{q}^4}} \right] - \alpha_s D_Y(\mathbf{k})^2. \quad (62)$$

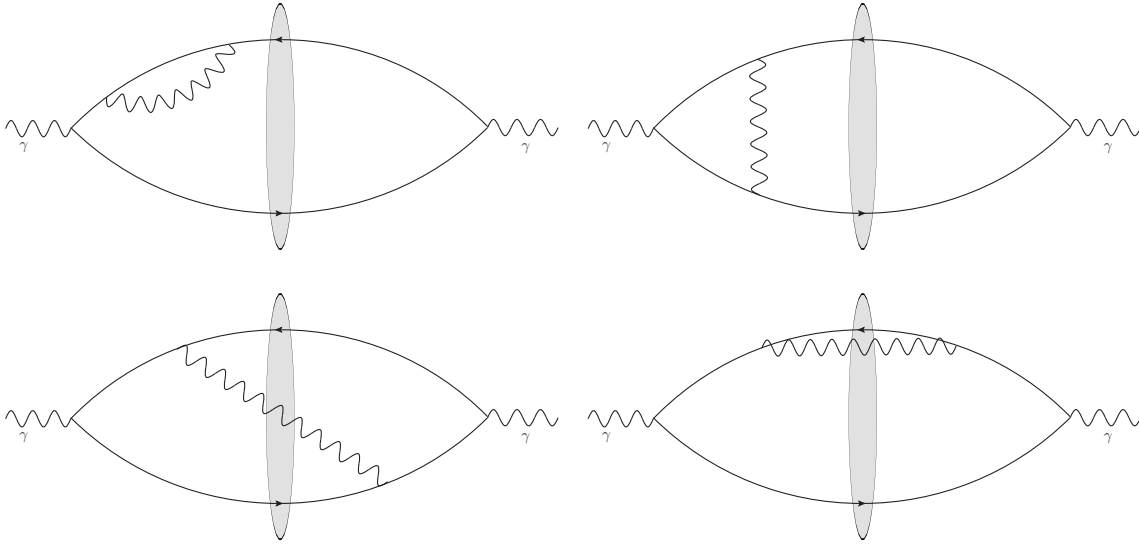


Figure 12: The diagrams representing the virtual (top) and real (bottom) contributions to the dipole

5.2.1.1 The orthogonality of collinear and k_T -factorisation

At this point a reflection on the final result in eq. 62 is in place. For the purpose of comparison, we may rewrite the BK equation more compactly as:

$$\frac{d}{dY} D_Y(\mathbf{k}) = K(\mathbf{k}, \mathbf{q}) \otimes D_Y(\mathbf{q}) - \alpha_s D_Y(\mathbf{q})^2, \quad (63)$$

in which the convolution implies an integral over \mathbf{q} . It is instructive to compare and contrast this result to eq. 57.

In many aspects, collinear and k_T -factorisation are rather orthogonal:

COLLINEAR FACTORISATION	k_T -FACTORISATION
<ul style="list-style-type: none"> • The evolution in <i>virtuality</i> is obtained by convolving the kernel with the pdf over the <i>longitudinal</i> splitting variable z • The virtual terms cancel the singularity for $z \rightarrow 1$ in the quark splitting function • A singularity in the k_T of the emitted parton is present and renormalised • A solution to the evolution equation is approximated by resumming the strongly ordered emissions in $\ln(Q^2)$, at moderate x 	<ul style="list-style-type: none"> • The evolution in <i>rapidity</i> is obtained by convolving the kernel with the pdf over the <i>transversal</i> splitting variable \mathbf{q} • The virtual terms cancel the singularity for $z \rightarrow 0$, which comes from the gluon splitting function. This is rather implicit in eq. 62, but can easily be found in different representations of the equation (we refer to [30]) • Potential singularities at $\mathbf{q} = 0$ and $\mathbf{q} = \mathbf{k}$ are actually canceled by the virtual terms, and no renormalisation is needed • An approximate solution to the evolution equation is obtained by resumming the strongly ordered emissions in $\ln(1/x)$, at moderate Q^2

Collinear and k_T -factorisation and the evolution equations also have various features in common though:

- For both equations the non-perturbative structure of the hadron has to be determined as an initial condition for the equation. For a collinear pdf, the degrees of freedom in virtuality below the renormalisation scale μ are integrated out. For the BK equation, the longitudinal degree of freedom for $x > x_0$ are usually integrated out. Various successful phenomenological initial conditions exist though for the latter.

- Both equations describe *simultaneously* the evolution of the pdf and the probability for parton emissions
- Ultimately, when for both equations the limit of large Q^2 and $1/x$ is taken, both results consistently deliver the DLL solution, which is very similar to the equation we derived from the soft bremsstrahlung law.

5.2.2 Linear rapidity evolution: the BFKL equation

We obtained an evolution equation in rapidity that contains a non-linear term. The evolution equation in which the non-linear term is simply discarded is the BFKL equation. It is anticipated to describe the rapidity evolution in the *dilute* regime, where the gluon density is not very high (we will elaborate this statement shortly).

The equation can be rewritten to describe the evolution of the updf instead of the evolution of the dipole⁶:

$$\frac{d}{dY}f(Y, \mathbf{k}) = \alpha_s \int_{\Lambda_{QCD}} \frac{d\mathbf{p}}{\pi} \frac{\mathbf{k}^2}{\mathbf{p}^2(\mathbf{k} - \mathbf{p})^2} \left(f(Y, \mathbf{p}) - \frac{f(Y, \mathbf{k})}{2} \right). \quad (64)$$

The unintegrated pdf is directly related to the collinear pdf as: $x\mathcal{G}(x, Q^2) = \int^{Q^2} \frac{d\mathbf{k}}{\pi\mathbf{k}^2} f(x, \mathbf{k})$. We illustrate the linear proton updf and its evolution, in Fig. 13. The initial conditions of the updf were obtained from a fit to e+p data.

This evolution equation is problematic though for two reasons:

- The lower bound of the integral is (manually) set to Λ_{QCD} ; the reason for this is that the equation otherwise diffuses in the small k_T^2 regime, which is non-perturbative.
- The above equation leads to a very rapid growth of the pdf with x . For a constant pdf as initial condition, the evolution is exponential:

$$f(Y, k) \propto e^{\alpha_s \omega_0 Y} = x^{-\alpha_s \omega_0} \approx s^{\alpha_s \omega_0} \quad (65)$$

in which ω is a positive constant.

Before discussing the non-linear evolution equation, we will outline in the intermezzo how the non-linear term accounts for both problems.

5.3 INTERMEZZO: UNITARITY VIOLATION AND GLUON SATURATION

The BFKL equation predicts an exponential growth of the gluon distribution in rapidity. This results in a total dipole-hadron cross section that grows approximately as a power law in the squared centre-of-mass energy s . It is known though, that the upper bound for the total hadronic cross section grows approximately logarithmic in s ; this is the famous Froissart bound[33]. Thus, the BFKL equation eventually leads to a unitarity violation, since the

⁶ This is accommodated by a Mellin transformation of the linear equation in spatial coordinates[31]

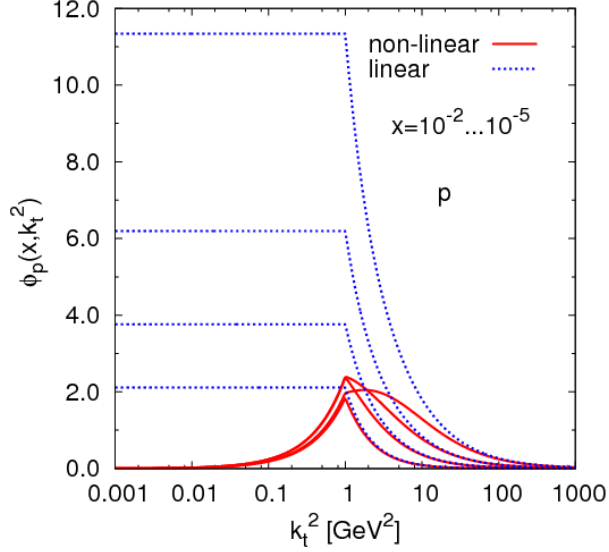


Figure 13: The unintegrated pdf [30], obtained by linear and non-linear fits to HERA data. The updf is depicted for $x = 10^{-2} \dots 10^{-5}$; the linear updf grows progressively with decreasing x , while the peak value of the non-linear updf shifts progressively to higher k_T values for decreasing x -values. The fast rise of the gluon distribution with increasing rapidity, and the non-triviality of modelling the k_T distribution below 1 GeV is manifest for the linear updf (the solution below 1 GeV is fixed by continuity). The increase of the mean value of the non-linear with increasing rapidity can be interpreted as the rise of the saturation scale. Below the saturation scale, the rise of the gluon density with k_T goes as k_T^2 , while above Q_s it is expected to behave as $1/k_T^2$ [32]

probability for an interaction of the dipole with the gluons becomes larger than the total interaction probability.

The solution to this problem is provided by the non-linear term in eq. 62. In the dipole picture, the term can be considered as the *simultaneous* interaction of both dipoles with the gluons of the hadron. In the hadron perspective however, the reaction represents the *recombination* of two hadronic gluons into one. Thereby, this self interaction effectively migrates gluons from low to higher x -values, and thus "tames" the exponential growth.

We briefly consider at which scales this process becomes important. The process only occurs when the *transversal* gluon density is sufficiently high. More quantitatively, the transversal area of a gluon when probing at a scale Q^2 is approximately $1/Q^2$. The transversal size of the hadron is given by πR_{had}^2 . Thus, the *saturation scale* Q_s^2 where the gluons transversally start to overlap, is defined by:

$$\frac{xg(x, Q^2)}{\pi R_{had}^2} \frac{1}{Q^2} \Big|_{Q^2=Q_s^2} \sim 1. \quad (66)$$

Rewriting the equation and using our initial result from eq. 65, we obtain as estimate for the saturation scale:

$$Q_s^2(x) \approx \frac{\alpha_s x g(x, Q_s^2)}{\pi R_{had}^2} \sim e^{\lambda Y} \quad (67)$$

We thus find that the saturation scale depends on x ; for an overview we refer to [32].

Further, we observe a dependence of the saturation scale on the type of hadron via the density xg and $1/R_{had}^2$. For a nucleus consisting of A nucleons the number of partons at a certain x, Q^2 coordinate grows linearly with A , while the transversal size is enhanced by a factor $A^{2/3}$. Therefore, the *nuclear* saturation scale $Q_{s,A}^2(x)$ is *enhanced* w.r.t. a nucleon by a factor $A^{1/3}$ (for a fixed x). For a lead ion ($A = 208$) this is a factor is six. This nuclear modification factor is called a nuclear *oomph factor*.

The saturation scale indicates the (gradual) change from a dilute to a dense regime. In the dense regime the exponential rise of the gluon density is tamed by the recombination reaction; it has been argued that the gluon density predicted by the BK equation grows approximately logarithmic in rapidity below Q_s^7 . Thus gluon saturation fulfils the very important task of rendering the theory finite.

5.3.1 The BK equation

Revisiting the BK equation, the important role of the non-linear term is manifest at this point. The initial condition for the equation is fitted to (usually) e+p data; we'll display results in chapter 8.

In Fig. 13 we display the non-linear gluon density for various x -values. A peak in the distribution is present; this indicates the saturation scale at the particular x -value. It is interesting and important to note that in the BK equation the saturation scale thus arises naturally, and is absolutely not artificially "put in by hand". We observe, as advocated, that saturation suppresses the gluons at k_T -values below the saturation scale (corresponding to large transversal sizes). Clearly, the saturation scale shifts to higher (more perturbative) k_T -values for smaller x ; since the gluon density grows with decreasing x , a smaller transversal size (higher k_T) is needed for the gluons not to overlap.

In the BK equation the problem with the diffusion is also not present anymore, since the saturation scale may be thought of as a scale below which colour neutrality is realised [32].

Previously, we emphasised the orthogonality and complementarity of the DGLAP and BK/BFKL equation. For the BFKL equation, this is entirely true. For the BK equation the situation is slightly more complex though, since the equation is non-local in x and k_T . Notably, the saturation scale and its evolution emerge naturally when evolving updfs with the BK equation. Furthermore, instead of evolving a k_T distribution in rapidity, the BK equation may also be used to evolve an x -dependent pdf in k_T . We will encounter different implementations of the BK equation in chapter 8.

⁷ This statement is only valid for a particular form of the gluon distribution (the William-Weizäcker distribution). Also, no reference or concrete derivation of this statement from [32] was found

The BK equation was first derived to leading order. A commonly used implementation is the running coupling BK equation (rcBK) equation [34], in which certain elements of the running coupling are absorbed in the evolution kernel. There is no unique manner to do this however, but arguments have been put forward to justify the current implementations [35]. The next-to-leading order BK equation [36] has also been derived, but it suffered from certain shortcomings. These have been recently overcome by a "collinearly-improved" BK equation [37]. One of the benefits from the last equation is that it predicts an evolution of the saturation scale that matches expectations based on experimental observations⁸.

5.4 BREAKDOWN OF FACTORISATION

The factorisation of hadronic interactions into pdfs and perturbative matrix elements has proven very successful, and a wealth of data has been successfully described by it. It should be noted however, that only for a few processes factorisation has been rigorously proven. For example, for Drell-Yan production with an additional parton emission no complete proof has been presented that indeed the universality of the pdfs is not broken. It may actually be expected, that the cross talk between pdfs can be expected to behave as $1/s^2$ in perturbation theory [38]. Further, in hadronic collisions more partons than just two may participate in the interaction. These mostly soft interactions can only be described by phenomenological models.

In fact, there are kinematic domains for which it is known that universality is actually broken. This means that different processes require their own pdf. These processes are usually described in terms of TMDs (transversal-momentum dependent parton distribution functions). An overview on the state-of-the-art concerning factorisation and TMDs can be found in [39].

5.5 SUMMARY

In this chapter, we factorised the interaction of a hadron into a hadron specific (u)pdf and perturbative matrix elements. We obtained two different factorisation schemes for different kinematic regions. We outlined how evolution equations to the different schemes are obtained. The equations and solutions were shown to be orthogonal in many aspects.

In the k_T -factorisation scheme a non-linear interaction term emerged, which is anticipated to result in an x -dependent saturation scale. The scale is enhanced (and more perturbative) in a heavy ion w.r.t. a nucleon. This scale describes the (gradual) crossover from a dilute to a dense regime. The term has been shown to be of major importance, and is the key topic of the experimental research of this thesis.

Various aspects that were discussed in this chapter have been summarised in Fig. 14. On the x -axis the evolution in virtuality is depicted, which may be interpreted as probing the proton on smaller transversal length scales. On the y -axis the rapidity evolution and the

⁸ The saturation scale behaves approximately as $Q_s(x) = e^{\lambda Y}$. The leading order BK equation predicted $\lambda \approx 1$, which contradicts experimental observations. The collinearly improved BK equation predicted $\lambda = 0.3$, which suits expectations better

increase in density is illustrated. In particular, we further observe that in the $\ln(Q^2), \ln(1/x)$ plane the saturation scale is a straight line.

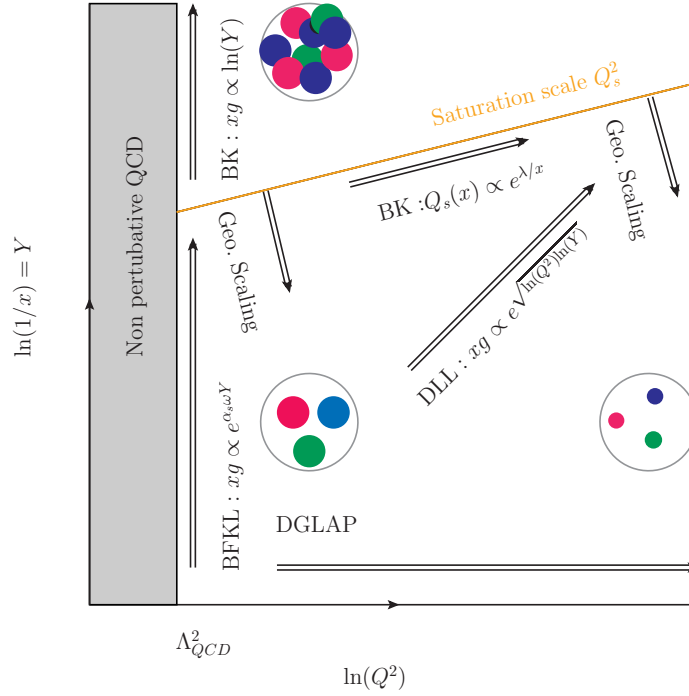


Figure 14: A schematic overview of the various evolution equations in the $\ln(Q^2), \ln(1/x)$ plane. It should be noted that the transition between BFKL (dilute regime) and BK (dense regime) evolution is expected to set in gradually. The saturation scale, of which the evolution is also described by the BK equation, has also been depicted; it becomes a straight line in this plane. The DLL solution is also indicated

Our discussion on hadronic interactions and evolution equations was focused so far on perturbative QCD. Occasionally we pointed out phenomenological strategies to estimate non-perturbative processes, but the emphasis was on reactions at scales where perturbation theory is applicable (as explained in chapter 3).

Historically, strong interactions were experimentally discovered well before the invention and experimental confirmation of QCD. Prior to QCD, these reactions were instead described by Regge-Gribov Theory (RGT) [40]. Although nowadays it is known that QCD is the fundamental theory to describe strong interactions, RGT is still very relevant since it provides a description of soft processes for which no perturbative calculations exist. For example, the total hadronic cross section is a quantity that is intrinsically non-calculable in perturbation theory, while RGT provides a satisfactory description of the experimental data over several orders of magnitude of \sqrt{s} .

The motivation for discussing RGT is bifold: at one hand it needs to be described as a background for our discussion on event generators in chapter 14. At the other hand, we also need to understand RGT before we can describe nuclear shadowing, which is a relevant nuclear phenomenon since the effects are similar to saturation in certain kinematical regimes.

6.1 REGGE-GRIBOV THEORY

The central concept of Regge theory is to rewrite the amplitude for an elastic hadronic interaction into a partial-wave decomposition as function of the *complex* orbital angular momentum l :

$$f_l(t) = \sum_{l=0}^{\infty} f_l(t)(2l+1)P_l(z), \quad (68)$$

in which $z = \cos(\theta)$. In this θ is the angle between the incoming and outgoing hadron.

Upon making certain assumptions on the analyticity of the scattering amplitude, it can be deduced that the amplitude obeys crossing symmetry (between the kinematic variables s and t). By using this identity it is found that $f_l(t)$ can be rewritten in terms of a function $\alpha(t)$ that contains poles:

$$f_l(t) = \frac{g_1(t)g_2(t)}{l - \alpha(t)}. \quad (69)$$

In this equation g_1 and g_2 are vertex functions. For a detailed discussion we refer to [41, 42].

Clearly, the function $f(t)$ has poles for $\alpha(t) = l$; these poles correspond to a *family* of exchanged particles with a particular spin. These families are referred to as Reggeons. The function $\alpha(t)$ may be expanded as $\alpha(t) = \alpha(0) + \alpha't$. A graph of the Reggeons is depicted in

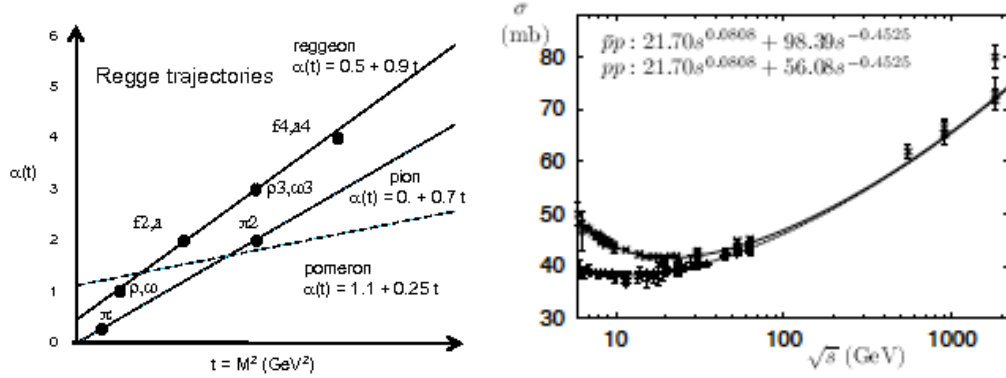


Figure 15: Left: two Reggeon trajectories (solid lines) together with measured resonances [43]. The Pomeron trajectory has been drawn with the dashed line. Right: the total p+p and p+p̄ cross section. The experimental data points have been fitted with the Regge equation for the total cross section. The fitted parameters are displayed in the graph [44]

Fig. 15 (left). We observe that various well-known resonances contribute to the Reggeons for $l = 0$ (pions etc.) and $l = 1$ (ω etc.).

6.1.1 The soft and hard Pomeron

We remember the optical theorem from our previous application in chapter 5: the imaginary part of the forward scattering amplitude can be related to the probability of an inclusive process (see also appendix A.4). It can be proven that the imaginary part of the amplitude of Regge exchange behaves approximately as:

$$\text{Im}(A(s, t)) \sim s^{\alpha(t)}, \quad (70)$$

in the limit of large s . Using the optical theorem we rewrite this to an equation for the total cross section σ_{tot} :

$$\sigma_{tot} \sim \frac{1}{s} s^{\alpha(t=0)} = s^{\alpha(t=0)-1}. \quad (71)$$

From Fig. 15 (right) we notice that indeed for small values of \sqrt{s} the total p+p and p+p̄ cross section decreases with \sqrt{s} . From 10 GeV onwards the p+p cross section increases with \sqrt{s} though. This cannot be accounted for by the Regge trajectories involving known particles, since these all have $\alpha(0) < 0.5$. To accommodate for this behaviour, a new Regge trajectory was introduced with vacuum quantum numbers: the soft Pomeron. By fitting σ_{tot} , the parameters of the soft Pomeron trajectory were determined, and an intercept $\alpha(0) = 1.08$ was found. The soft Pomeron trajectory has also been depicted in Fig. 15.

By including the soft-Pomeron contribution, a better description of σ_{tot} was obtained. Despite, data on the low- x and charm structure function required the introduction of another Pomeron with intercept ≈ 1.4 : this is called the hard Pomeron [45, 46]. The Pomeron trajectories do not contain any resonances; a Pomeron candidate in form of a resonance has never been observed.

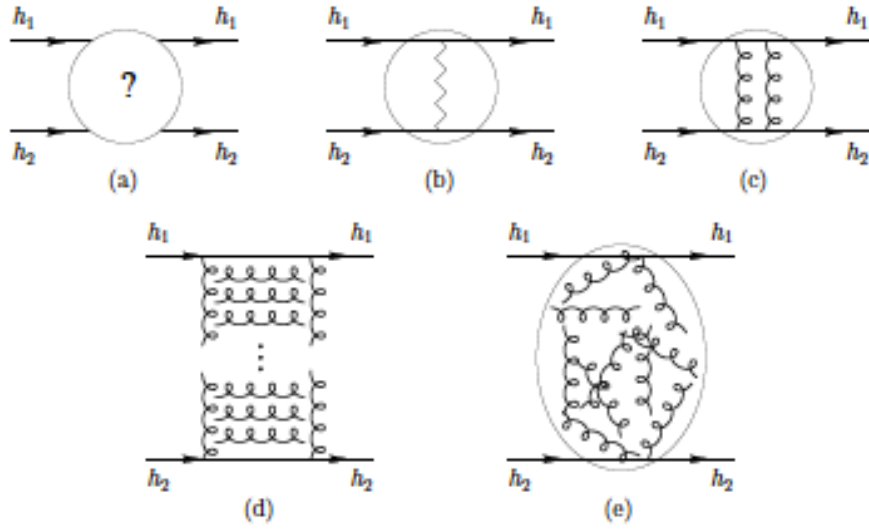


Figure 16: The Pomeron in perturbative QCD, in different levels of complexity [44]. The blob diagram, representing the unknown interaction, is given in diagram (a). In (b) the phenomenological Pomeron exchange is depicted. In (c) the Pomeron is envisaged as being due to two-gluon exchange; this exchange may accommodate for the vacuum quantum numbers of the Pomeron. In (d) a "Reggeised" Pomeron is depicted. This corresponds to the perturbatively calculable Regge trajectory of the gluons, including their self-interactions. Diagram (e) represents non-perturbative Pomeron exchange at small- t ; in this situation the partons only interact with the QCD vacuum fluctuations

When QCD emerged as the fundamental theory of the strong interactions, attempts were made to describe the Pomeron in terms of gluons. In Fig. 16 we depict the description of Pomeron exchange in QCD, in increasing levels of complexity. In (b) the phenomenological Pomeron exchange is depicted. In (c) the Pomeron is envisaged as being due to two-gluon exchange; this exchange may accommodate for the vacuum quantum numbers of the Pomeron. It was pointed out however that gluons are subject to self-interactions; in (d) a "Reggeised" Pomeron is depicted. This corresponds to the perturbatively calculable Regge trajectory of the gluons, including their self-interactions. The Reggeisation has been proven to all orders; a perturbative Pomeron represents an infinite number of diagrams in perturbative QCD. This Pomeron is also known as the BFKL Pomeron [47, 48].

A perturbative field theory based on Reggeon exchange was formulated [40]; we will encounter this theoretical description of hadronic interaction when describing event generators in chapter 14.

The last figure (e) represents non-perturbative Pomeron exchange for small- t interactions. In this situation the partons only interact with the QCD vacuum fluctuations, which we encountered previously in chapter 3.

Thus, we see that the *perturbative* Pomeron is actually well connected to our previous discussions on vacuum fluctuations in context of the strong coupling and the BFKL evolution equation.

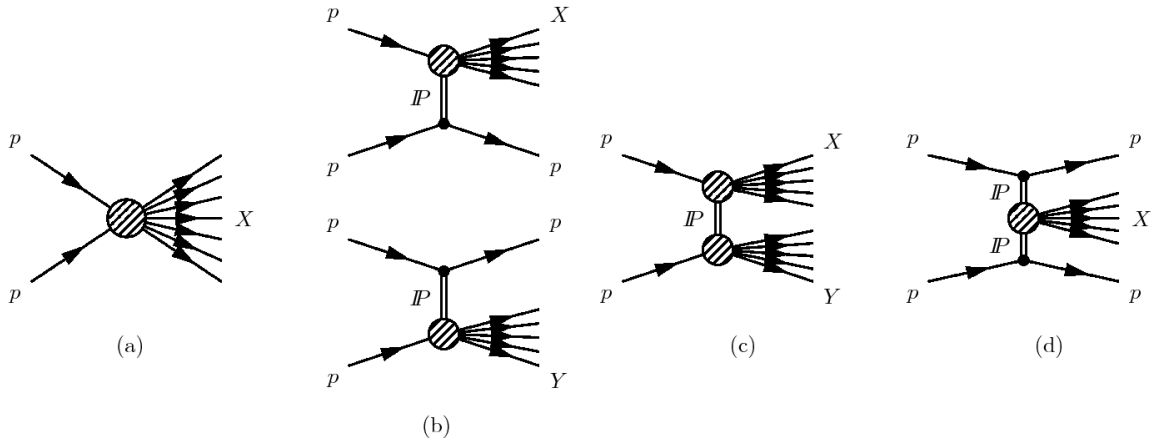


Figure 17: Diffractive event classification [49]. (a) Non-diffractive events. (b) Single-diffractive events, characterised by a rapidity gap. (c) Double-diffractive events, characterised by a rapidity gap. (d) Central diffractive events, which can be classified by multiple rapidity gaps

6.1.2 Diffractive event classification

We outlined that hadronic interactions can be mediated via Pomeron exchange. Events in which the Pomeron is emitted elastically are classified as diffractive events. Typically, such events can experimentally be distinguished by a rapidity gap. Since the exchanged particle is colour neutral, only the boosted fragments of the shattered hadrons are measured. Therefore, there is a detector region in pseudorapidity that is not struck by any collision products; this is known as a rapidity gap. These gaps are exponentially suppressed in hard interactions, and thus form an excellent observable to distinguish diffractive events.

In Fig. 17 we schematically depict various diffractive reactions. We can categorise single-diffractive (b), double-diffractive (c), and central-diffractive (d) events that all can, in principle, be experimentally discriminated via their characteristic topology.

6.2 NUCLEAR SHADOWING

As is well known, a nucleus consists of nucleons; a lead ion for example consists of 82 protons and 126 neutrons. In the most simplistic scenario, the interaction of a nucleus is plainly modelled as an incoherent superposition of nucleon interactions; a simple illustration of a proton-lead collision had been depicted in Fig. 18. For most purposes this is a far too simplistic approach though, and the nuclear structure function F_2^A differs from a superposition of nucleon structure functions in many aspects. It is beyond the scope of this thesis to denote and describe all these effects, predominantly since we are primarily interested in the low- x content of the nucleus.

Shadowing is a nuclear effect that is in particular important to our studies though, since it also suppresses the parton distribution at low- x values. It is thus anticipated to lead to a

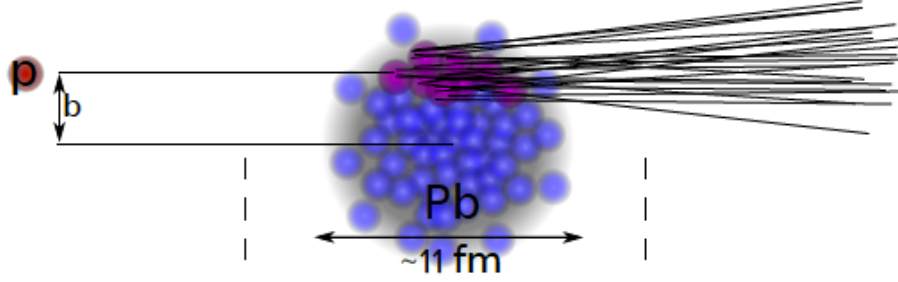


Figure 18: An illustration of a proton-lead collision [50]. The transversal distance between the incoming proton and the centre of the nucleus is denoted by the impact parameter b . The purple nucleons of the nucleus interact with the proton, and are called participants

similar effect as saturation. Since nuclear shadowing originates from Pomeron exchange, we briefly discuss it in this paragraph.

The interaction of a virtual photon with a nucleus in the dipole picture is depicted in Fig. 19 (left). We observe that there are two contributions to the amplitude in which the nucleon N_1 remains intact. The first single-step contribution comes from the upper diagram, in which only N_2 interacts. The two-step diagram is depicted in the lower diagram, in which the nucleon N_1 interacts elastically via Reggeon or Pomeron exchange. The amplitude of Reggeon exchange interferes constructively with the single-step amplitude, leading to anti-shadowing. This effect is mainly relevant for $0.1 \leq x \leq 0.2$. For Pomeron exchange the amplitudes add up destructively however, leading to shadowing.

The relative effect of shadowing and anti-shadowing on F_2^A has been depicted in Fig. 19 (right). We see that for low- x values, the effect is similar to the effect as expected from saturation, namely a relative suppression of F_2^A w.r.t. the nucleon, which is enhanced with decreasing x .

In [51] it is argued that shadowing is relevant for not too high parton densities. Thus, for a given x -value, it is anticipated that shadowing is relevant for higher virtualities than Q_s^2 . A quantitative estimate of both effects is beyond the scope of this work, although we will deploy event simulations based on both saturation and shadowing in chapter 14.

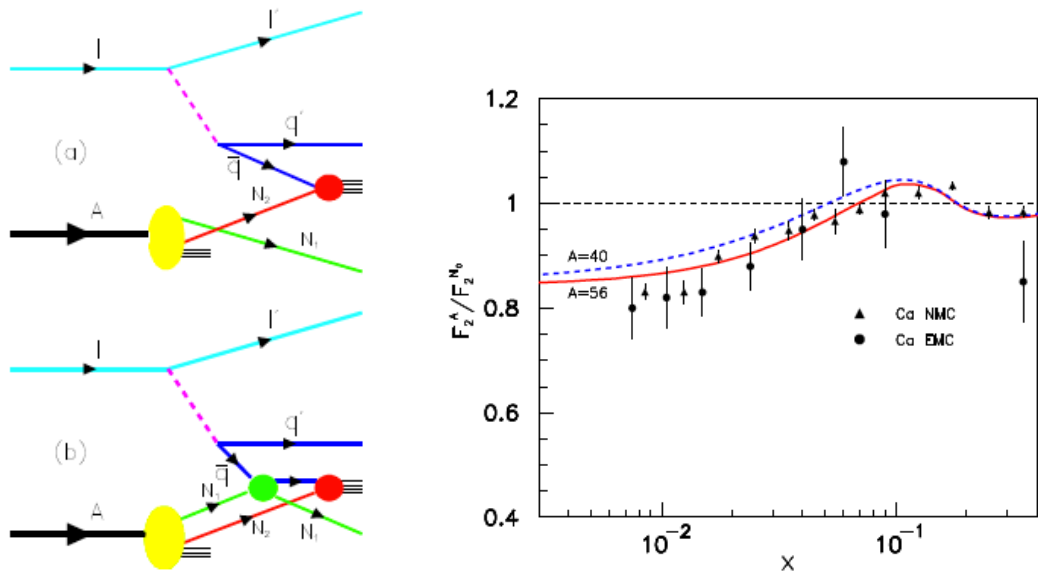


Figure 19: Left: the one-step (upper diagram) and two-step (lower diagram) contributions to lepton-nucleus scattering. The interference of the two-step amplitude is constructive for Reggeon exchange, leading to anti-shadowing at large- x . For Pomeron exchange the interference is destructive, leading to shadowing at low- x values. The effects on F_2^A have been depicted quantitatively in the right-hand graph. The figures are from [52]

FROM PARTONS TO JETS IN HADRONIC COLLISIONS

Up to this point, we have only discussed hadronic interactions in terms of parton-parton interactions. We discussed the equations that govern the evolution of parton densities and simultaneously describe the probability for n -parton emission. In real hadron-hadron collisions partons are not collided or measured directly though. The particles emerging from the interactions are solely hadrons; this is a consequence of confinement, which was discussed previously.

In a hadron-hadron collision many processes occur simultaneously, which we depict schematically in Fig. 20. In this section we briefly describe these processes. Although the emphasis of this thesis is on gluon saturation, a brief description of these processes is convenient to accurately interpret the data in subsequent chapters and complete the description of a hadronic collision. Also, we elaborate how the evolution equations enter the description of the collision and discuss the relevant experimental observables.

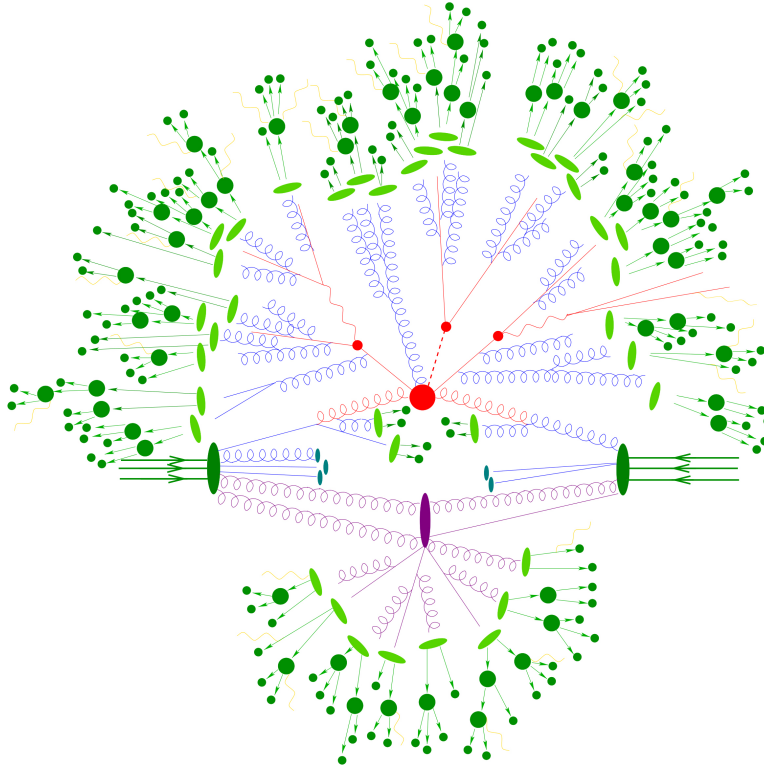


Figure 20: An illustration of a hadron-hadron collision [53]

7.1 QCD REACTIONS IN HADRONIC INTERACTIONS

Various reactions are depicted in Fig. 20, which we succinctly discuss below:

7.1.1 *The hard process*

The hard interaction is depicted in red in Fig. 20. This part of the interaction is calculated with perturbative matrix elements; the partons that enter the interaction are evolved to the scale on which the scattering occurs. The red dotted line indicates the hardest parton that emerges from the interaction.

7.1.2 *The underlying event*

The underlying event (UE) is essentially a collective name for all interactions that occur in addition to the hardest interaction. It is an active topic of interest at hadron colliders [54, 55]. It can be categorised into the three reactions described below, although it depends slightly on the definition whether or not initial and final state radiation are considered as part of the UE.

7.1.2.1 *Initial and final state radiation*

In Fig. 20 it can be observed that the partons entering the hard scattering emit partons themselves before (initial-state radiation) and after (final-state radiation) the interaction. These radiative emissions are described by the evolution equations that we discussed in the previous chapter. The observant reader also notices, that the lines entering the hard scattering only become red *after the last* emission. This explicitly illustrates the factorisation: the partons are evolved to a certain kinematic state (where the blue lines turn red) via parton emission, and for the particular kinematical configuration (the red lines), the perturbative matrix element is evaluated.

We have encountered explicit solutions for the evolution of *parton densities* in certain kinematic regions, for example the DLL solution of the soft bremsstrahlung law (eq. 44) and the solution to the BFKL equation (eq. 65). To calculate the number of *emitted partons* and their kinematics, certain evolution equations can be rewritten into equations with a Sudakov factor, which represents the no-branching (no-emission) probability [38]. This is also referred to as parton showering. Then the emissions can be simulated via Monte Carlo simulations. For the BK equation this is not possible, and the cross section for inclusive processes is approximated differently.

Thus, by studying different evolution equations, we can numerically generate predictions for various observables and compare these to experimental data.

7.1.2.2 *Multi-parton interactions and beam remnants*

In a hadron-hadron collision, soft non-perturbative interactions occur simultaneously to the hard scattering. These result in an energy density that is approximately uniform in rapidity.

This uniform density is perturbed by the hard scattering, multi-parton interactions (MPI) [56], and beam-remnant interactions.

The amount of these multiple soft and semi-hard MPI reactions depends strongly on the centrality of the collision, which is defined as the transversal separation between the colliding hadrons. An MPI reaction has been indicated schematically in purple in Fig. 20.

It should be noted that MPI is not trivial to combine with the concept of factorisation though, since after a parton is emitted from the hadron, the pdf of the hadron is not the same as before the interaction anymore. Various phenomenological models have been produced and tuned to experimental data. The current models provide a reasonably coherent picture of MPIs, for most observables the models are in $\approx 2\%$ level agreement with the data [54] [55]. There is certainly still room for improvements though.

The remainders of the hadrons that emitted a parton form the beam remnant (BR), indicated in blue in Fig. 20. This remnant itself may also initiate various interactions [57]. The beam remnant must interact with the hard partons via colour reconnection, since ultimately all final states must be colour neutral.

7.1.3 Hadronisation

So far we discussed the hadronic interaction up to the parton level. It was pointed out in chapter 3 though, that confinement prohibits free coloured objects to exist in Nature. Thus, all partons that emerge from the interaction hadronise. This means that particles are formed that are colour neutral, and consists of a fixed number of quarks¹. The hadrons are divided into two categories. Mesons consist of a quark and an anti-quark, and thus have a net baryon number of zero. Baryons are defined as particles that have a baryon number of ± 1 . Most baryons consist of three quarks². However, recently the pentaquark was discovered [58]; this rather exotic particle consists of four quarks and one anti-quark, and is thus formally also a baryon.

Hadronisation is a non-perturbative QCD process, and thus its description can only be approximated with phenomenological models. Various models exist, we refer (non-exhaustively) to the Lund string model [59, 60], and the independent jet model that is based on the Field-Feynman approach [61].

The Lund string model approximates the QCD potential between two partons to possess the behaviour of a string:

$$V(r) \approx kr, \tag{72}$$

in which k is the string constant, approximately 1 GeV/fm. As the two colour charges propagate away from each other, their momenta and invariant mass grow linearly until the string "breaks". Then the string is envisaged to split into a $q\bar{q}$ pair, and thus two new strings are generated. This process is iterated until all kinematical energy is depleted, and the remaining

¹ Searches are ongoing for final states consisting only of gluons, so called glueballs

² More precisely, the definition that a baryon constitutes of three quarks means that the total number of quarks minus the anti-quarks is three. These quarks are referred to as the valence quarks, while all other quarks of the baryon are called sea quarks

$q\bar{q}$ pairs are the colour neutral hadrons (for baryons the model is conceptually the same). The Lund string model reproduces certain features of hadronic collisions, for example the approximately constant energy density w.r.t. rapidity. It is implemented in various event generators to which we will compare our data later.

7.1.4 Jets

A parton that participates in the hard interaction or that is emitted as ISR or FSR, results in an experimental observable, provided its transversal momentum is large enough. The parton will radiate new partons itself. According to the soft bremsstrahlung law, these will be mainly soft partons, which thus are collimated w.r.t. their mother parton. Subsequently, these partons hadronise into final-state particles. Thus, a hard parton ultimately results in a stream of collimated particles propagating in the direction of the initial hard parton. The jet is experimentally observable.

To reconstruct the kinematics of the jet, its constituents must be identified w.r.t. the particles resulting from other processes. For this clustering algorithms are applied. Generally, these algorithms take a collection of four vectors as input and cluster these in $\eta - \phi$ space; the output is a new collection of four vectors, which represent the estimates of the kinematical properties of the jets. Usually a size parameter is given, i.e. the clustering algorithms will sum the particles in a cone with a certain radius in $\eta - \phi$.

Summarising, jets constitute an experimental observable that is sensitive to the processes on parton level. A good overview on existing clustering algorithms on the market and their performance can be found in [62].

8.1 INTRODUCTION

In this chapter we will briefly revise the experimental progress that has been made on studies of gluon saturation. We discuss (non-exhaustively) results on e+p, proton-proton, and hadron-nucleus collisions, at various centre-of-mass energies.

There are many experimental observables that possess sensitivity to parton evolution. Measurements of the inclusive structure function F_2 or inclusive particle spectra are opportune observables. Besides, certain more exclusive processes have been proposed with enhanced sensitivity. For example, angular correlations between di-hadrons in hadronic interactions provide an observable that is highly sensitive to evolution effects [63]. Models of hadronic interactions that include the radial dependence of the hadron may be used to predict exclusive processes in which the proton survives, such as exclusive vector meson production and deeply virtual Compton scattering (DVCS); a study can for example be found in [64]. Since this thesis is focussed on an inclusive measurement¹, we will restrict our discussion in this chapter mainly to the inclusive processes. The aim of this chapter is bifold: it should familiarise the reader with the translation of the theory discussed so far to experimental observables, and furthermore provide a context for the motivation of this thesis.

There are various saturation-based models that provide predictions for inclusive measurements [64–66]. We will focus on two implementations of the rcBK; this is the BK equation, in which certain higher order corrections due to the running coupling have been taken into account. We will discuss the rcBK equation in depth in chapter 14.

The implementation of the rcBK equation by Kutak Sapeta (KS) is of particular importance, since the *strength* of the non-linear term can be adjusted between absent (BFKL) and regular (BK) evolution. Further, we display results of the Albacete Armesto Milhano Quiroga-Arias Salgado (AAMQS) collaboration; since their implementation provides self consistent fits and descriptions to many inclusive measurements, this graciously serves as a common thread to portray the experimental results collected in three decades.

The final experimental results obtained in this thesis will be compared to predictions of the AAMQS and KS implementations.

8.2 RESULTS ON e+p COLLISIONS

At the HERA collider e+p scattering was studied at $\sqrt{s} = 320 \text{ GeV}$. The H1 and Zeus experiments measured the inclusive structure function [67] over several orders of magnitude in x and Q^2 ; the lowest x -values reached were around 10^{-6} . The measurements provided

¹ In this thesis the single-inclusive jet spectrum will be analysed, which is similar to the single-inclusive particle spectrum

important evidence for DGLAP evolution, as we displayed before in Fig. 6 (right). Also, the data revealed the fast rise of the gluon pdf at low x -values predicted by the authors of the BFKL equation.

The KS collaboration [30] confronted the rcBK equation with the HERA data. In their model, the initial condition was parameterised as an x -dependent pdf at a scale k_0 . This pdf was evolved to higher k_T -values using the rcBK equation. The evolution was performed with and without the non-linear term. The fit with the F_2 data is displayed in Fig. 21 (left). Clearly, the best $\chi^2/\text{d.o.f.}$ was obtained with the non-linear rcBK evolution equation, which converged to a value of 1.7. We will refer to this initial condition as the KS unintegrated pdf (KS-updf).

The AAMQS collaboration also analysed the HERA data with the rcBK equation [65]. The initial condition was given by the adapted GBW and MV models (a description and references may be found in [65]). These initial conditions represent a k_T distribution at a certain initial x -value x_0 . This distribution is evolved to lower x -values using the rcBK equation. Good fit results were obtained with $\chi^2/\text{d.o.f.}$ values of ≈ 1 , see Fig. 21 (middle). The initial conditions obtained by this collaboration are labelled as the AAMQS unintegrated pdf (AAMQS-updf).

The kinematic regime of the HERA data is regrettably too small to distinguish between the different initial conditions. Also, the estimate for Q_s^2 for the HERA data at $x = 0.01$ is $\approx 0.36 \text{ GeV}^2$; we display an AAMQS estimate of the saturation scale in Fig. 22 (right). Clearly, this value is close to Λ_{QCD}^2 . This invalidates a conclusive statement on the observation of saturation at HERA.

Nonetheless, the HERA data slightly favour the rcBK-oriented over DGLAP-based models. In [69] the stability of the DGLAP and rcBK fits to low- x data has been tested (with low- x it is generally meant that $x \leq 0.01$). The main conclusion is that overall the rcBK fits produce more stable results w.r.t. varying boundary conditions; for the DGLAP based fits a systematical offset between the low- x data and predictions sets in.

Concluding, the HERA data certainly provide a (non-decisive) hint that non-linear gluon dynamics at low- x may be realised in Nature.

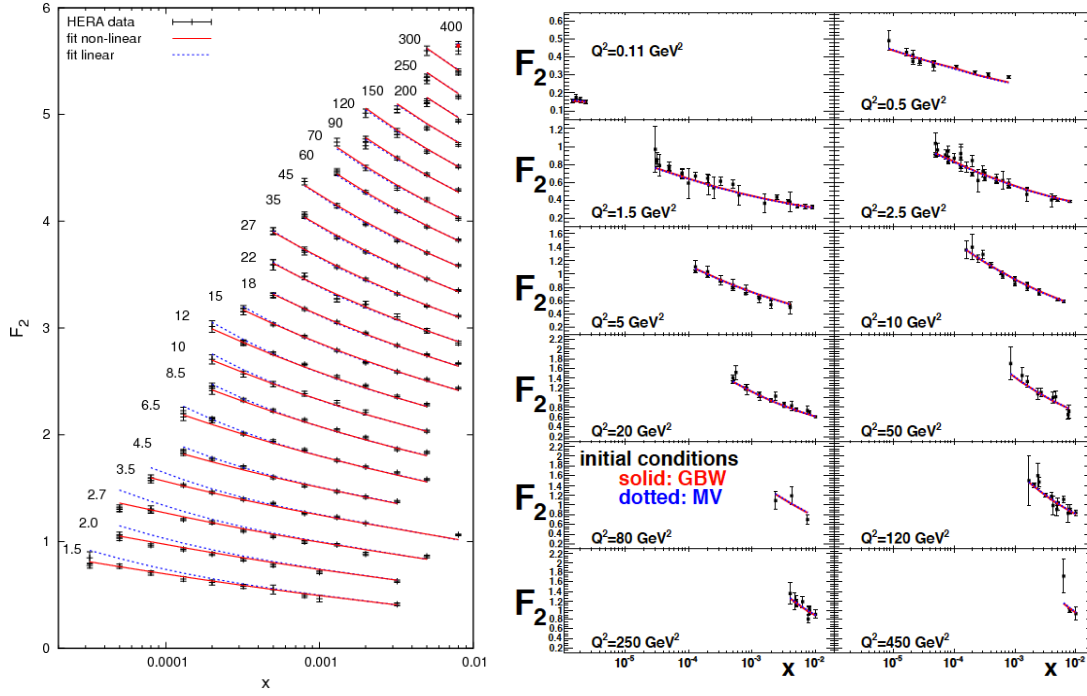


Figure 21: Hera data on F_2 with rcBK fits. Left: the linear and non-linear fits from the KS collaboration [30]. Right: the fit from the AAMQS collaboration [65]

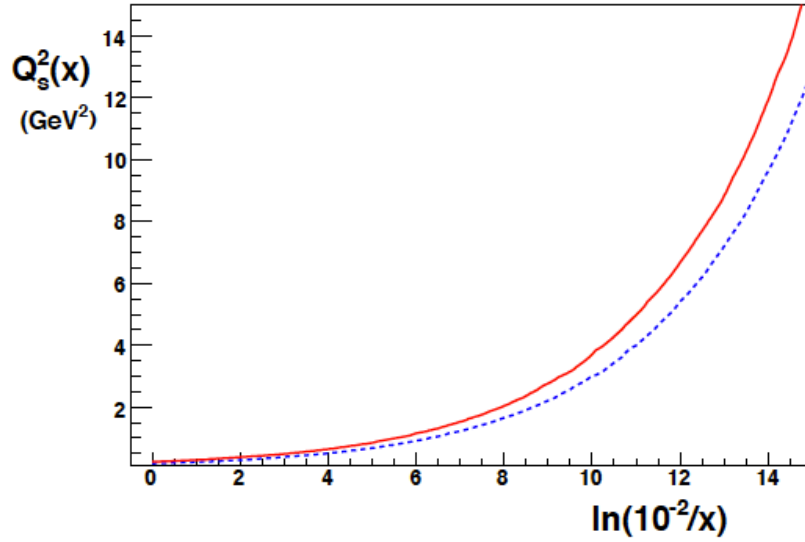


Figure 22: The saturation scale as extracted by the AAMS collaboration, for the GBW (red) and RV model (blue) [68]

8.3 RESULTS ON HADRON-HADRON COLLISION

8.3.1 Results from RHIC

The RHIC (relativistic heavy ion collider) generated p+p, Pb+Pb, and d+Au collisions at $\sqrt{s_{NN}} = 200$ GeV.

In Fig. 23 we display results on the inclusive forward p+p and d+Au spectra measured at RHIC [70], together with predictions based on the AAMQS fits to e+p data outlined above. The forward spectrum in d+Au is in particular sensitive to saturation, since for this observable the hard partons from the deuteron "probe" the glue distribution of the nucleus at low- x for which saturation is enhanced. For the d+Au collisions $x \geq 10^{-3}$ was reached.

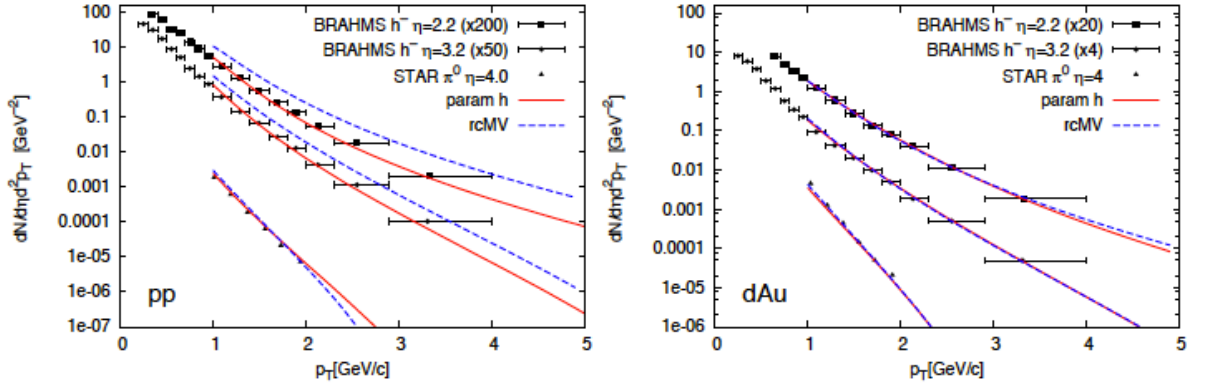


Figure 23: Forward particle spectra measured at the RHIC experiments together with various model predictions [70]. The fit indicated with h refers to a particular parameterisation as extracted by the AAMQS collaboration. Left: p+p collisions. Right: d+Au collisions

It can be observed that both parameterisations describe the data well, but the data do not allow for a clear distinction between the different initial conditions.

A complication arose when interpreting these data though. For the forward data, which are most sensitive to saturation effects, the projectile is probed at the kinematic limit $x \rightarrow 1$. For this situation, successful alternative explanations have been presented to the effects observed, such as parton energy loss [71]. This obscures the interpretation of the observed effects as being due to gluon saturation. This problem also persists for the RHIC di-hadron correlation studies [63].

Thus, the RHIC data certainly support an interpretation of hadronic interactions in terms of non-linear evolution models, but do not constitute an unambiguous observation of gluon saturation.

8.3.2 Results from TEVATRON and LHC

The Tevatron collided protons with anti-protons at $\sqrt{s} = 2$ TeV. The LHC program comprises p+p, p+Pb, and Pb+Pb collisions at a $\sqrt{s_{NN}}$ of maximally 13, 8, and 5 TeV, respectively. The

saturation scale is expected to be two to four times higher at the LHC than at RHIC. Thus, the LHC offers an excellent and unprecedented opportunity to stringently test hypotheses on saturation.

Various measurements of jet production in p+Pb collisions at $\sqrt{s_{\text{NN}}} = 5.02$ TeV at the LHC were performed. We (non-exhaustively) refer to a measurement of the ALICE collaboration [72], ATLAS [73], and CMS [74]. The LHCb collaboration measured Υ production and cold nuclear effects in p+Pb collisions [75]². We focus here on two particular studies, for which a comparison with predictions of the AAMQS implementation of the rcBK model is available. In Fig. 24 we display central-inclusive particle spectra in p+p collisions at $\sqrt{s} = 2$ (left) and 7 TeV (right). We observe that two of the initial conditions can be discarded based on the data, while the data again support the rcBK predictions with the other initial conditions. At the LHC values of $x \geq 10^{-4}$ are reached for central particle production, while TEVATRON probes at $x \geq 10^{-3}$. Thus, for these studies the sensitivity to saturation effects is rather limited. The AAMQS predictions have also been confronted with LHCf data on low- p_T ($\mathcal{O}(1 \text{ GeV})$) π^0 production at extremely forward rapidity ($8.8 \leq \eta \leq 10.8$) [77] and included in Fig. 24.

8.4 SUMMARY

Non-linear parton evolution models were confronted to a wealth of experimental results, for various collision types and kinematic configurations. The AAMQS and KS results provided a consistent description of the data. Further, it appears there is currently not a real competitive model or concept to describe all the data presented simultaneously. Also, a test of the stability of DGLAP and rcBK fits to e+p data seems to slightly favour the latter.

Despite, due to the reasons indicated (probing the projectile at the kinematic bound, and probing the proton close to the non-perturbative boundary), a definite claim on an observation of non-linear QCD appears not feasible at the moment [78], and different initial conditions cannot be distinguished well.

Many opportunities at the LHC exist though well beyond the result displayed here. In the subsequent part, we will motivate a measurement at the LHC with exceptional sensitivity to saturation, in an attempt to overcome the difficulties encountered above. Comparisons of the measurement to predictions of the models displayed in this chapter will be included.

² In particular, a measurement of charged particles in the central region [76] has been performed in p+p, p+Pb, and Pb+Pb collisions at $\sqrt{s_{\text{NN}}} = 5$ TeV. This is an excellent measurement to study saturation effects, although comparisons with AAMQS or KS predictions were not available at the time of writing

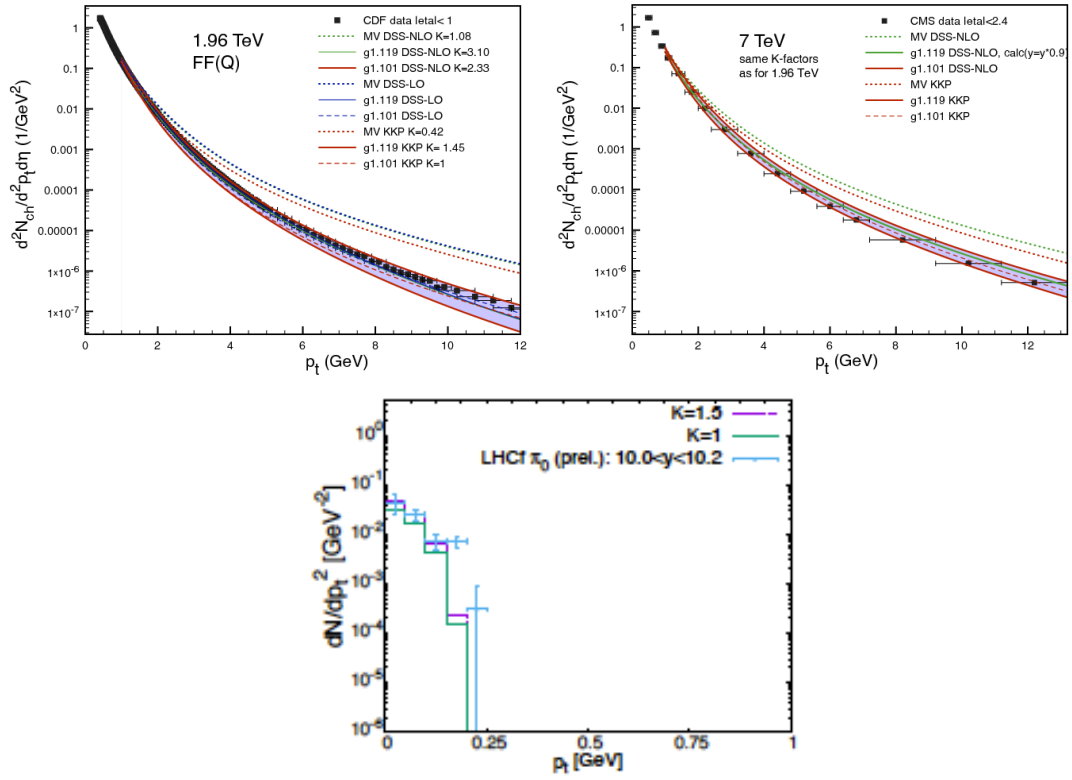


Figure 24: Central-inclusive particle spectra in p+p collisions at $\sqrt{s} = 2$ TeV (left, CDF) and $\sqrt{s} = 7$ TeV (right, LHC) [78]. Lower: the ultra-forward neutral pion p_T spectrum for $\sqrt{s} = 5.02$ TeV p+Pb collisions [77]. The rcBK predictions of the AAMQS collaboration have been included for various initial condition

Part II

THESIS HYPOTHESIS: AN UNPRECEDENTED EXPERIMENTAL SEARCH FOR SIGNALS OF SATURATION

The true sign of intelligence is not
knowledge but imagination

Albert Einstein

Investigating the hypothesis on the realisation of gluon saturation is of paramount importance for our fundamental understanding of Nature. Gluon saturation is expected to tame the exponential growth of the gluon pdf, and thus prevent the occurrence of a unitarity violation in the QCD description of hadronic interactions. Besides, gluon saturation is an important theoretical ingredient for formulating predictions on the initial state of heavy ion collisions. The latter constitute a core research program at the LHC. Also, cosmic-ray studies may directly benefit from improved modelling of the low- x content of hadrons (as was shown for the ultra-forward LHCf measurement in Fig. 24). Precision measurements of the Brout-Englert-Higgs boson may furthermore indirectly benefit from saturation studies, since the latter may constrain the uncertainty on the gluon pdf. Since gluon recombination is the dominant production mechanism of the scalar boson at the LHC, an improvement in the gluon pdf uncertainty would certainly not be a modest contribution.

These core arguments elucidate why, since non-linear parton evolution was hypothesised over two decades ago [27], saturation has been at the focal point of the theoretical and experimental community. So far, numerous papers have been presented on the topic. Models incorporating saturation have been confronted with a wealth of data, spanning nearly three decades of particle physics experiments. A central incentive for the recent proton-lead collisions at $\sqrt{s_{NN}} = 5$ and 8 TeV at the LHC is the search for signals of gluon saturation. Ambitions for the future include the foreseen construction of an electron-ion collider; a pivotal argument for this endeavour¹ is a precision measurement to distinguish between saturation and shadowing in a heavy ion, we refer in particular to the plot on page six of the EIC book [79]. The LHeC [80] would allow to study saturation in a proton.

Optimal sensitivity to probe gluon saturation may be achieved by measuring low- p_T jets in the forward direction. This statement can be motivated straightforwardly, since in a hard-parton interaction the x -value of the parton can, to leading

¹ The EIC estimated budget ranges from one to 1.5 billion US dollar

order, be reconstructed from the kinematical properties of the resulting jet via:

$$x = \frac{p_T e^{-|\eta|}}{\sqrt{s}}. \quad (73)$$

We succinctly derive the relation in appendix A.3 for completeness.

Concluding, forward low- p_T jets probe the hadron at low- x , where the effects of saturation are strongest. In Fig. 25 we depict the acceptances of the large LHC experiments, adapted to 5 TeV proton-lead collisions with the proton boosted in the negative direction; the acceptances are depicted in the proton-nucleon centre-of-mass system. The plot is complemented with the existing HERA measurements, and parameterisations of the saturation scale in a proton and lead ion are overlaid.

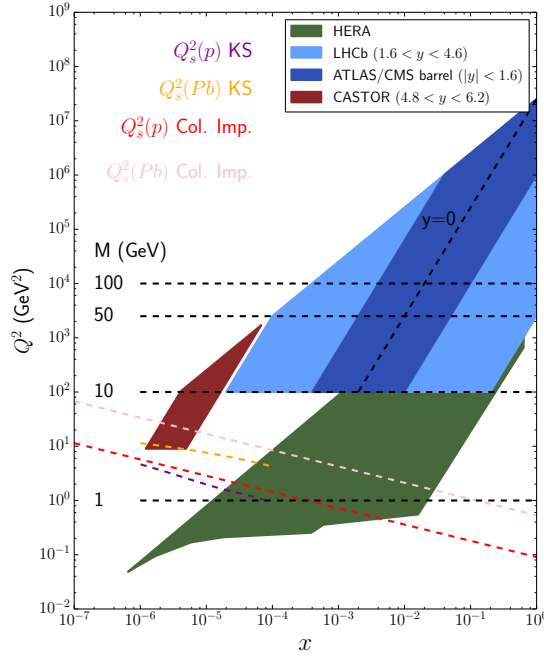


Figure 25: The acceptances of the large LHC experiments. These have been adjusted to the centre-of-mass system of a 5 TeV proton-lead collision, with the proton towards CASTOR. The kinematic regime of the HERA measurements is overlaid. The collinearly improved proton saturation scale has been parameterised as $Q_s(x) = ce^{\lambda/x}$. We fixed λ to 0.3 [37]. Given the slope parameter, we adjusted $Q_s^2(p)$ to 0.36 at $x = 0.01$ [68]. The nuclear saturation scale $Q_s^2(p)$ is enhanced with a factor $A^{1/3} = 5.9$ w.r.t. the proton saturation scale. The parameterisation of the Kutak-Sapeta (KS) saturation scales were obtained in a private communication

The CMS experiment at the LHC has been equipped with the CASTOR calorimeter, which extends the range in which jets can be measured (in the lab frame) to $-6.6 < \eta < -5.2$ (CASTOR is only installed at one side of the CMS experiment).

This calorimeter can measure very low p_T jets, the minimal p_T values presented in this analysis correspond to ≈ 3 GeV.

A study of jets in CASTOR in proton-lead collisions at the unrivalled centre-of-mass energies of the LHC thus possesses unique sensitivity to non-linear parton evolution. Evidently, such an analysis would overcome the adversities that obscured the conclusions in the HERA and RHIC analyses. The nuclear saturation scale for $\sqrt{s} = 5$ TeV p+Pb collisions in the CASTOR acceptance is expected to be around 10 GeV; this is well above the perturbative limit Λ_{QCD}^2 . Furthermore, a jet with a p_T of 3 GeV may be caused by a *hard* parton with an x -value of ≈ 0.15 . Thus, the fragmentation functions are not evaluated at the kinematic limit $x \rightarrow 1$. Concluding, the CASTOR single-inclusive jet spectrum constitutes indeed a very powerful observable to scrutinise hypotheses on saturation. Besides, since the jets probe a hadron at very low x , the results may signal the breakdown of collinear factorisation.

Given all the advantages and benefits of an analysis of jets in CASTOR in proton-lead collisions, such a study is on the other hand certainly not free of complications and obstacles. The CASTOR calorimeter was originally not designed to measure jets, which induces various afflictions (which will be extensively reviewed). In spite of various endeavours to study CASTOR jets in p+p collisions, this is the first CASTOR jet analysis that is in the process of submission to a journal. Given the experimental state-of-the-art, this thesis therefore targets two objectives: proving the experimental validity of CASTOR jets, and ultimately exploiting these to probe saturation.

Part III

THE EXPERIMENTAL SETUP

Calorimeters and their issues...

Hans van Haevermaet, FSQ-convenor

Up to this point we motivated why a measurement of very forward jets in high-energetic proton-lead collisions is highly sensitive to effects from non-linear QCD.

In this part we introduce the experimental setup, which is an indispensable background to the discussion of the actual measurement in the next part. There exists extensive documentation on both the LHC and CMS. Therefore, we aim at providing a general overview of the setup, and only focus in-depth on elements that are relevant to the analysis work of this thesis.

To this purpose, we start with a succinct introduction of the LHC and its experiments. This is followed by a chapter on the general concept and the architecture of the CMS detector. In it, we discuss two subsystems that are particularly relevant to our analysis. In the subsequent section the trigger and data-acquisition systems are introduced. Thereafter, we outline the reconstruction and simulation software of CMS, since we will use the software of CMS to extract the data and simulated event samples for this analysis.

The last chapter of this part is devoted to the CASTOR calorimeter, which is the key detector of this analysis.

THE LARGE HADRON COLLIDER

9.1 INTRODUCTION

Physicists have studied particle interactions for over a century. In Fig. 26 (left) modern accelerators and their centre-of-mass energies have been depicted.

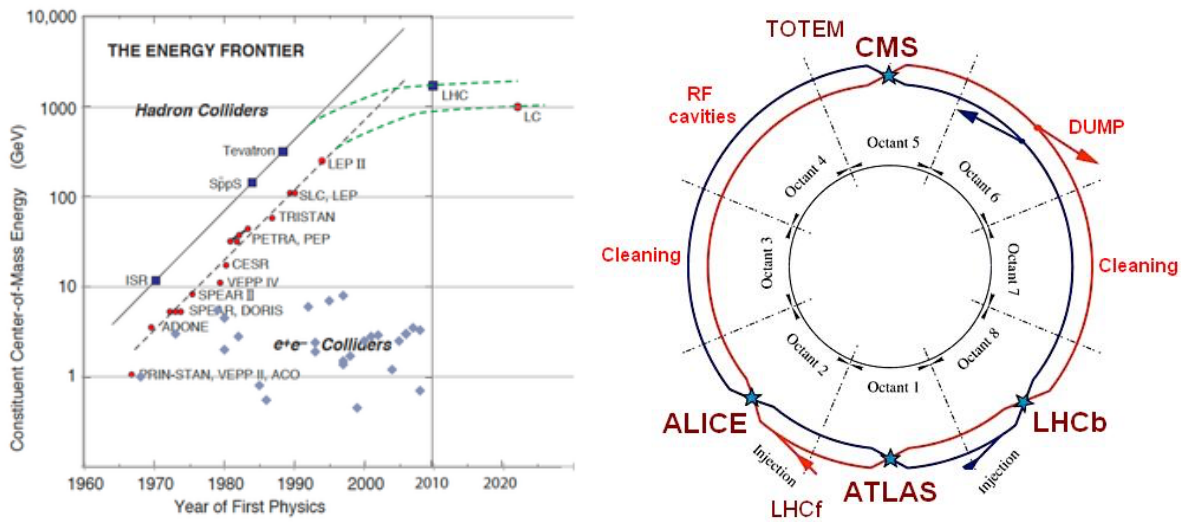


Figure 26: Left: a succinct history of modern particle accelerators and their centre-of-mass energies [81]. Right: an overview of the LHC collider and its experiments [82]

Discovering the Higgs boson was a key argument for the design of the Large Hadron Collider (LHC). To this purpose, the design centre-of-mass energy for p+p collisions is 14 TeV. The LHC is the largest accelerator (and machine in general) ever built. The tunnel of the accelerator has a circumference of 26.7 km, and is located near Geneva on the Swiss-French border. A large circumference is needed to keep the particles on their track by the Lorentz force, which is exerted on the particles by strong magnetic fields. Also, since the production of a Higgs boson is a very rare process, the accelerator was designed to deliver unprecedented amounts of luminosity (which we will describe in more details below).

A schematic overview of the LHC has been depicted in Fig. 26 (right). We observe that there are various experiments situated at four beam-interaction points at the LHC. The two largest, general-purpose experiments are ATLAS and CMS. ALICE is an experiment focussed in particular on heavy-ion physics. LHCb is specialised in b-quark physics and hadron-spectroscopy. It may be seen that two smaller experiments, LHCf and TOTEM, share the interaction point of ATLAS and CMS, respectively. TOTEM is an experiment optimised to

diffractive cross section measurements, while LHCf performs measurements of π^0 production in a phase-space relevant to cosmic ray physics.

9.2 DESIGN OF THE LARGE HADRON COLLIDER

In order to deliver stable beams (that can be used for physics analyses) to the experiments, the particle trajectories are bent by 1232 superconducting dipole magnets with a field strength of 8.3 T; an LHC magnet has been depicted in Fig. 27. The beams can be (de)focussed by 392 quadrupole magnets, which are distributed over the LHC ring. The beams revolve with a frequency of 11 245 Hz.

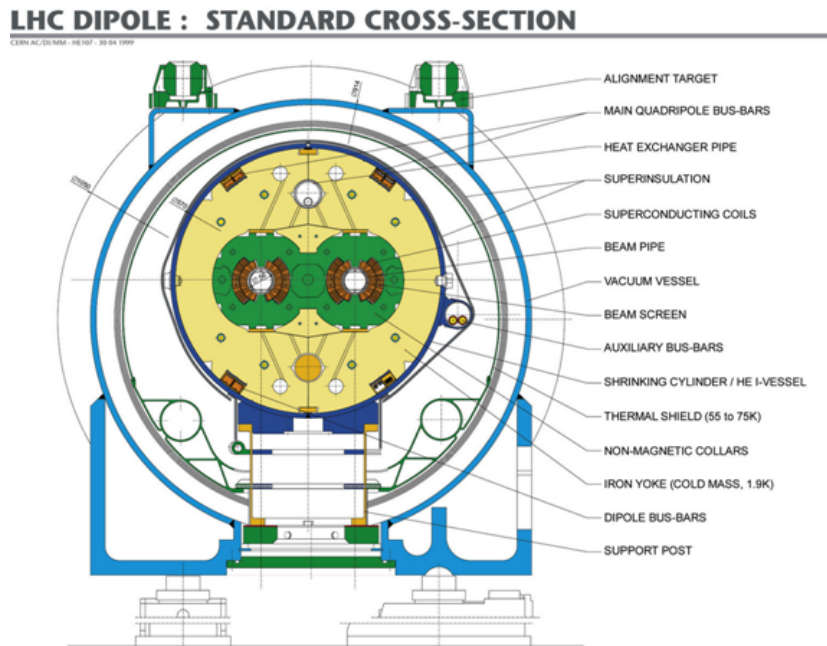


Figure 27: A schematic drawing of the design of an LHC magnet [83]

A maximally filled beam (at 7 TeV) possesses a kinematical energy of approx. 0.36 GJ. This is comparable with a 200 m long train at a velocity of 150 km/h. In the LHC tunnel this energy flows through a transversal area of the order of mm^2 , while at the interaction points this is reduced to square microns. Evidently, the energy of the beams constitutes a danger to the collider itself and the experimental infrastructure. Therefore, the beams possess a 900 m long abort gap in which no particles are situated that allows to abort and dump the beams in dedicated locations indicated in Fig. 26. Further information on the beam structure may be found at [84]. Eventually, all beams are dumped at the end of their lifetime, which is maximally 30 hours during collisions.

To maximise the luminosity that the LHC can deliver, a beam can be filled with 2808 bunches of particles (which are approx. 30 cm long). The bunches are minimally separated by 25 ns. The luminosity L , which was already formally described in chapter 1, describes how

many interactions two colliding beams can potentially produce. Intuitively, the number of collisions per unit of time and cross section (*instantaneous luminosity*) $\mathcal{L}_{\text{inst.}}$ can be understood more easily from its relation to the interaction rate r and the interaction cross section σ : $\mathcal{L}_{\text{inst.}} = r/\sigma$. The luminosity L can be obtained by integrating the instantaneous luminosity over the beam-interaction time. It should be noted that the value of $\mathcal{L}_{\text{inst.}}$ is not constant, but changes over time as the beam loses its brightness due to the collisions and beam-gas interactions. To optimise searches for the Higgs boson and other rare phenomena, $\mathcal{L}_{\text{inst.}}$ should be maximised. The design $\mathcal{L}_{\text{inst.}}$ of the LHC was $10^{34} \text{ cm}^{-2} \text{ s}^{-1}$, and this value was achieved in 2016¹.

For physics analyses it is of paramount importance to measure the luminosity precisely. To this purpose, two detectors are installed at both LHC rings. A Direct Current Current Transformer (DCCT [85]) measures the total Coulomb charge of the beam. The Fast Beam Current Transformer (FBCT [86]) measures the relative charges in the bunches. Their combined measurement delivers an accurate luminosity measurement.

9.3 PROTON-LEAD COLLISIONS AT THE LHC

In this section we outline the LHC beam operations during the p+Pb collisions that were delivered to CMS in January/February 2013.

The bunch spacing of these beams was 50 ns. It should be noted that the LHC magnets operate for both beams at the same field strength. The mass of the heavy ion is approx. $208 m_p$, while its charge equals $82 q_p$. As a result, the momentum per nucleon of the ion is $(82/208)$ times the momentum of the proton. Thus, at the LHC proton-lead beams possess asymmetric beam momenta. The protons were accelerated to 4.00 TeV, and consequently the energy per nucleon was 1.56 TeV.

Since the LHC experiments are generally not symmetric, the beam configuration is also important. During the first half of the data-taking campaign the proton travelled clockwise, and this direction is denoted p+Pb in this thesis. During the second half the beams were reversed (Pb+p). In Fig. 28 the integrated luminosity collection is depicted.

The actual luminosity delivered to the experiments may differ from the luminosity that the beams potentially can produce; this is also dependent on parameters such as the transversal separation between the beams². Therefore, the CMS experiment measures and monitors itself also the luminosity delivered to the experiment. To calibrate the luminosity measurement of CMS to the LHC measurement, van-der-Meer scans were performed for the proton-lead data taking campaign.

¹ It is foreseen to upgrade the LHC to a high-luminosity phase of the LHC (*HL-LHC*), with a target $\mathcal{L}_{\text{inst.}}$ that is factor 10 higher than the LHC

² For certain physics measurements the luminosity is deliberately scaled down by beam separation, since certain measurements cannot be performed when the event pileup is large

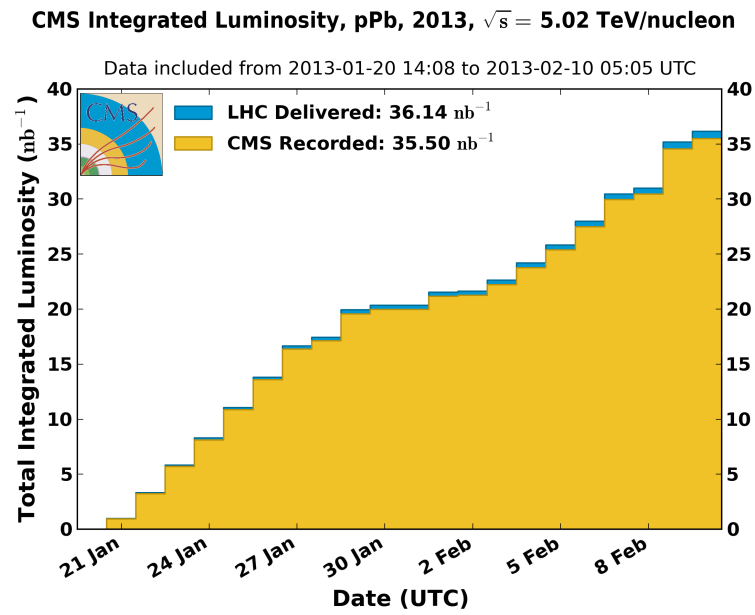


Figure 28: The integrated luminosity delivered to CMS during the 2013 proton-lead collision campaign [50]

10.1 INTRODUCTION

The CMS detector is a general-purpose detector, installed at the LHC ring in a cavern 100 m underground in France, near the village of Cessy. Its diameter is 15 m, its length 28 m, and the detector weighs approx. 14.000 tonnes. An overview of the design has been depicted in Fig. 29.

To meet the physics objectives that CMS was designed to pursue at least in the central region ($|\eta| \leq 2.5$) all particles emerging from the collisions are measured accurately for $p_T \geq 1$ GeV. Neutrinos are not measured directly, but their presence may be indirectly inferred via a measurement of the imbalance of the transversal momentum, referred to as missing E_T . The latter observable is not only necessary for measuring neutrinos but also accommodates searches for new (invisible) particles. Therefore, CMS was designed as an hermetic detector; almost all collision products are contained in the detector.

The CMS coordinate system is set up as follows. The x -axis points to the centre of the LHC ring, the y -axis points upwards, and the z -axis points to the west.

The central feature of CMS is a solenoid magnet, which is responsible for the homogeneous field of 3.8 T. The magnet is approx. 6 meters in diameter and 12.5 m long. The magnet is cooled by liquid helium and superconducting, such that 18000 Ampere currents may build up the magnetic field. Switching on and off the magnet happens in cycles (which generally take a day), and the number of cycles the magnet can make is limited. This has consequences for installation procedures, which require the magnet to be off.

CMS needs to determine the four-momenta of the particles and the primary vertices of the collision; i.e. the location where the hadrons collided. The latter is in particular important at the LHC due to the large number of multiple interactions per bunch crossing that may occur. Therefore, we start with outlining the general principles behind the design of CMS to accommodate for these demands.

Generally, three classes of particles can be distinguished that CMS needs to measure, which are electromagnetic particles, hadrons, and muons. Particles of these classes interact differently with a detector: electromagnetic particles can be absorbed by less material than hadrons, and hadrons need less material for full absorption than muons. To maximally exploit these response differences, CMS has been build in an onion-like shape, as may be inferred from Fig. 29. It is instructive to follow particles trajectories from the interaction point in the centre of the detector to its boundary, which has been depicted in Fig. 29 (bottom).

Firstly, CMS performs a measurement of all charged particles with $p_T \geq 1$ GeV using the tracker. This detector measures the track of charged particles, which exhibit a curvature due to the magnetic field that is present in the central region of CMS. From the curvature the 3-momenta of the tracks can be determined. Furthermore, the tracks allow to distinguish between the vertices. This constitutes a non-destructive measurement; the tracker aims to

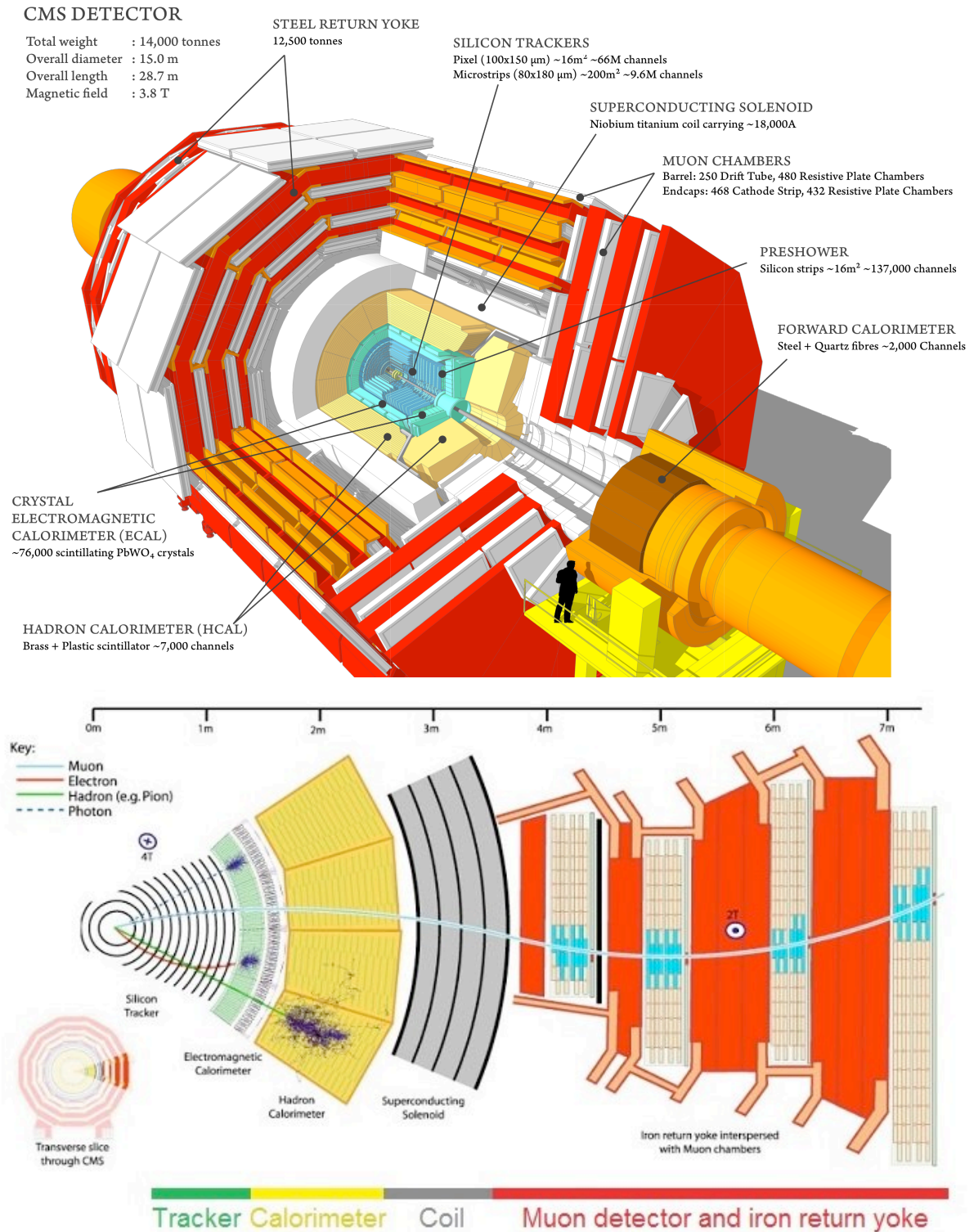


Figure 29: Top: a schematic picture of the CMS detector [87]. Bottom: a transversal view on the central part of the CMS detector, together with the trajectories of various particles [88]

minimally amend the kinematics of the particles, and to this purpose has a fixed material budget. One reason for this is that the tracker does not provide any information on the neutral particles, and therefore preferably amends their momenta minimally before their measurement¹.

Subsequently, the energy of the electromagnetic particles (photons and electrons/positrons) is destructively measured in the electromagnetic calorimeter (ECAL). ECAL consists of 62.000 lead-tungstate crystals. Due to its fine granularity and excellent performance the detector was pivotal in discovering the Higgs boson in the di-photon channel. Both the tracker and ECAL cover $|\eta| \leq 2.5$.

Outside of the ECAL, but still inside of the magnet, the hadronic calorimeter (HCAL) is situated. It extends from $R=1.77$ m to $R=2.95$ m. Hadronic particles deposit a fraction of their energy in the ECAL, but the major part is deposited in the HCAL. This calorimeter consists of brass interleaved with plastic scintillator plates. The HCAL covers $|\eta| \leq 3$. Outside of the magnet is another layer of HCAL, to catch the tails of the cascades of very highly energetic particles.

Muons (and neutrinos) are the only particles that are not fully absorbed at this point. Therefore, muon chambers are installed to measure their trajectory. Also, a return yoke is installed for the magnetic field, and the curvature of muons outside of the magnet is in opposite direction w.r.t. the inner region. Thereby, the muon chambers can determine the momentum of the muons from their curvature.

Thus, CMS optimally exploits the differences in the response of the particles. The combination of the measurements of the tracker, ECAL, and HCAL allows for an enhanced performance. Neutral hadrons can be identified as ECAL and HCAL clusters without a track pointing towards it. Further, the tracker allows to distinguish electron from photon deposits in ECAL. Particle-flow objects can be constructed, which optimally combine the information of the three subsystems. These objects are used in various analyses.

In the forward region CMS is complemented by the hadronic forward (HF) calorimeter, which extends the acceptance in the region $3 \leq |\eta| \leq 5$. Generally, the granularity of the subsystems is pragmatically adjusted to their installation location and requirements. Concluding, CMS has dedicated subsystems to measure all particles individually, and besides possesses hermetic coverage for missing E_T measurements.

The LHC environment imposes stringent demands on all CMS detectors. Collisions are delivered every 25 ns. To read out the detector and generate trigger signals at such high frequencies is challenging. The high luminosities delivered to CMS induce also another challenge, namely the sheer radiation load imposed on the detectors and electronics. Therefore, the CMS cylinder is longitudinally segmented in rings, which can be displaced. This facilitates access and maintenance of the most inner parts of the detector.

This chapter is organised as follows. We start with a slightly more in-depth discussion on the tracker and HF, which are in particular relevant to our analysis. The CASTOR detector, which is the key detector of this analysis, is discussed in a dedicated chapter. Further, we describe the trigger and data-acquisition systems of CMS, which facilitate a successful event

¹ Photons may occasionally convert in e^+e^- pairs, which allows for their reconstruction using the tracker

selection and recording at very high rates. We finish with a brief section on the software environment of CMS.

The design of CMS is described in great detail in [89] (this is the main resource for this chapter unless otherwise indicated).

10.2 THE CMS TRACKER

The CMS tracker measures the trajectory of charged particles to meet various important requirements. When multiple collisions occur during a bunch crossing, the tracker must be able to distinguish between these vertices, and assign all charged particles to their original vertex. The tracker is currently the only subsystem of CMS that can distinguish between multiple interactions per bunch crossing. Also, when particles produce a secondary vertex, this vertex must be identified. In particular b-quarks, which usually produce a displaced vertex, constitute an important observable that is necessary for many physics analyses. Furthermore, charged particles traversing the inner region of CMS have a bended trajectory due to the Lorentz force that is exerted on them by the magnetic field. The CMS tracker exploits this principle to measure the momentum of charged particles². Since our analysis relies on the identification of primary vertices we outline this subsystem below.

At the design luminosity of $10^{34}\text{cm}^{-2}\text{s}^{-1}$, the tracker will be traversed on average by a thousand particles each 25 ns. This results in a hit rate density of 1MHz/mm^2 at only 4 cm away from the beampipe.

To meet the requirements outlined above in the LHC collision environment, a tracker consisting of radiation-hard silicon was therefore designed, which is schematically depicted in Fig. 30. The tracker is 5.8 m long, and has a diameter of 2.5 m.

The tracker consists of two subsystems. The pixel detector is located most closely to the beam. It measures in three layers between 4.4 and 10.2 cm from the beampipe. It contains 66 million pixels to cope with the high intensities delivered.

The second part of the tracker is the strip tracker. It consists of 9.3 million silicon strips. Since this detector is located further away from the interaction point, strips instead of pixels suffice for an accurate measurement, although the silicon needs to be thicker than for the pixels. It measures in four barrel layers and disks, as can be seen in the TIB/TID regions. The outer region (TOB and TEC) is instrumented by six barrel layers and nine disks.

Overall, the tracker is composed of 200m^2 of silicon detectors that measure tracks in $|\eta| \leq 2.5$. To minimise its decay due to irradiation and the probability of a short-circuit due to water condensation, the tracker is maintained at -10° in dry air or nitrogen gas.

The full potential of the tracker becomes apparent in Fig. 31, in which multiple interactions in a bunch crossing were recorded. The tracker is capable of distinguishing between the collision products of 78 simultaneous interactions. The tracker was significantly upgraded in 2017 (the data used in this thesis were collected in 2013). The tracker will be fully replaced for the HL-LHC, which is scheduled for the period after 2025.

² It should be noted though, that in absence of the magnetic field, the vertex identification still functions, and also under these circumstances tracker information has been exploited for physics analyses

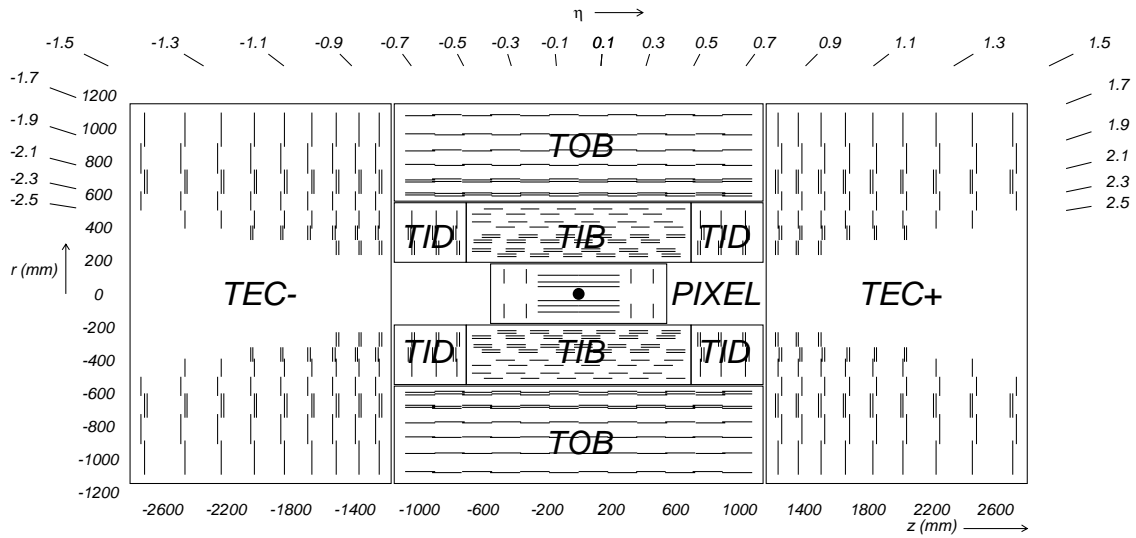


Figure 30: A detailed drawing of the CMS inner tracker system. The acronyms are given in the text. Each line denotes a layer of silicon [90]

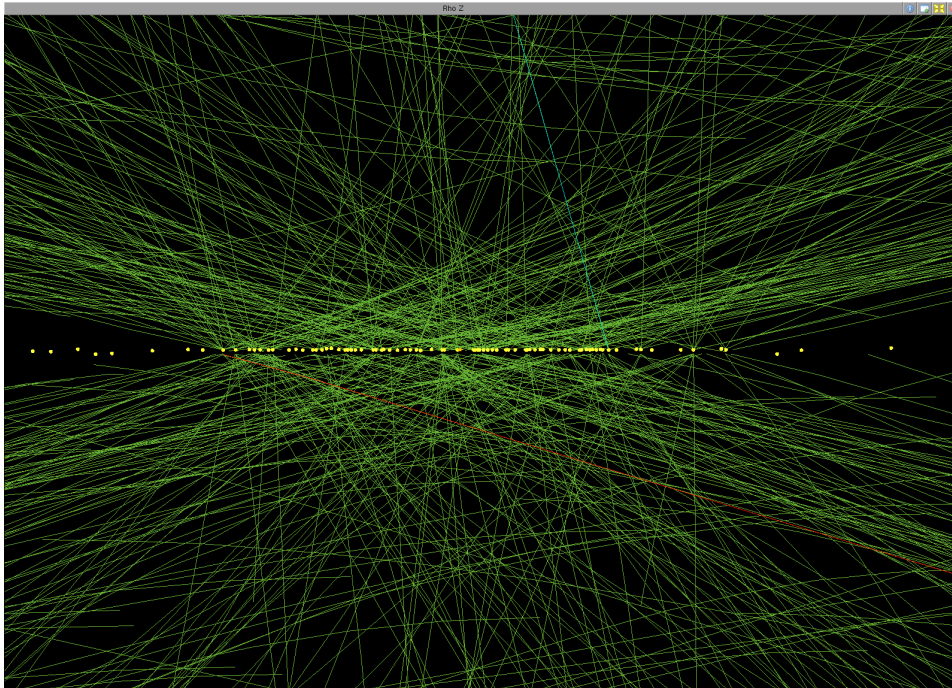


Figure 31: A bunch crossing with multiple collisions. The tracks reconstructed by the tracker are depicted in green. Overall 78 individual vertices could be reconstructed, which are indicated in yellow [91]

10.3 FORWARD INSTRUMENTATION

In this section we concisely introduce the forward detectors of CMS. Although we aim at providing a complete picture of the detectors, in our analysis only two forward detectors will actually be used: the HF calorimeters and CASTOR. Therefore, we will only discuss HF in detail, while a complete chapter is devoted to CASTOR.

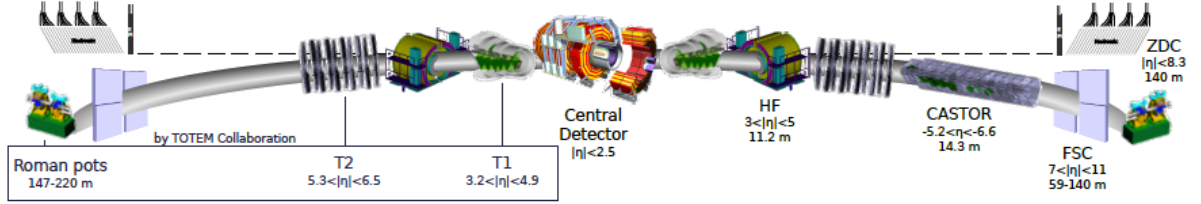


Figure 32: The forward detectors of the CMS and TOTEM collaborations, installed at the LHC interaction point five [50]

In Fig. 32 we depict the forward detectors of the CMS and TOTEM collaborations that share the LHC interaction point five; for completeness we briefly introduce the TOTEM detectors also. It may be seen that the HF calorimeters cover $3 \leq |\eta| \leq 5$. The CASTOR calorimeter, which is installed on one side only, covers $-6.6 < \eta < -5.2$ and is installed at 14 m from the interaction point. The TOTEM experiment has particle trackers (telescopes) located in the same η -regions. It should be noted, however, that in absence of a magnetic field, these tracking detectors can only measure track multiplicities, i.e., a momentum measurement cannot be performed³.

Further, CMS is equipped with Forward Shower Counters (FSC), which can measure at 59, 85, and 114 m away from the interaction point. These detectors are designed to measure interactions of diffractive particles that interact with the beam pipe. At 140 m from the interaction point the Zero-Degree calorimeters are installed (ZDC), which are designed to look for neutrons in heavy-ion collisions. These may emerge at zero degrees from the interaction point, since they are not deflected by the magnetic field back into the LHC beampipe. The ZDC response is correlated to the centrality of the heavy-ion collision.

It may further be seen that TOTEM symmetrically installed Roman Pot detectors at 147 and 220 m from the beampipe. These detectors are used for diffractive studies by tagging protons that have lost longitudinal momentum and thus are not kept on track by the magnets of the LHC. Recently the combination of the CMS and TOTEM experiments, united in the CT-PPS project [92], has opened up new phase-space to include the RPs in searches for anomalous quartic gauge field couplings, light-by-light scattering, and other interesting physics phenomena.

Furthermore, the LHC is equipped with Beam Pickup Timing for experiments (BPTX) detectors. For CMS, such counters are installed symmetrically at 175 m away from the

³ Although the combination of CASTOR energy deposits with T2 tracks would be very beneficial since they completely complement each others information, this option could not be pursued so far due to a lack of a reliable common CMS-TOTEM simulation

beampipe. These trigger on beam presence in CMS. By requiring coincidence between the signals, they are very well suited to serve as zero bias trigger, since these devices only reveal if a beam crossing occurred in the experiment, irrespective of whether an interaction took place. From the relative phase of the signals, the z -position of the interaction point can be determined.

We finish by mentioning that CMS is equipped with dedicated detectors to monitor the instantaneous luminosity, which are the Fast Beam Conditions Monitor (BCM1F) and the Pixel Luminosity Telescope (PLT). The hadronic forward calorimeter (to be discussed below) serves simultaneously as luminosity monitor and detector for physics analyses.

The remainder of this section is devoted to the HF detector, since we will crucially rely on its measurement for our event selection.

10.3.1 The HF calorimeter

The HF calorimeters complement the η -coverage of the central calorimeters. They are installed on one of the most radiation-harsh spots in the CMS cavern though; the radiation load in HF is on average seven times higher than in the central subsystems. Dedicated radiation-hard materials had to be used therefore for HF. The absorber consists of steel. Radiation-hard quartz fibres are guided through the steel. Particles traversing the fibres emit Cherenkov radiation, and the fibres guide the light outside the medium for amplification and analysis. Due to a higher-than-expected performance of the LHC, certain parts of HF had to be replaced already (before the moment initially scheduled); irradiation is certainly not a minor consideration for these detectors. HF is shielded from other external radiation by layers of steel, concrete, and polyethylene.

The calorimeter has been segmented in towers with a granularity of 0.175×0.175 in $\eta - \phi$ space. These towers consist of an EM section (located in front of the tower, with long fibres), and a hadronic section (at the back, with short fibres). This allows the distinction between electromagnetic and hadronic particles traversing the calorimeter (although the granularity is not as fine as the central ECAL detector). An HF channel has been depicted in Fig. 33.

The absolute scale of HF was determined in-situ by studying the $Z \rightarrow e^+e^-$ decay. Events were collected in which one of the electrons was measured by a central (calibrated) detector, while the other electron was incident on HF. The response was thus calibrated by reconstructing the resonance peak in the invariant mass spectrum. The hadronic calibration was performed by studying dijet events, with one jet in the central region and one jet in HF. By balancing the p_T of the jets, the HF response was calibrated. The general calibration procedure of jets in CMS may be revised in [93].

10.4 THE TRIGGER SYSTEM OF CMS

We explained before that the LHC delivers bunch crossings to CMS with a minimal time interval of 25 ns, which corresponds to a bunch crossing frequency of 40 MHz. Furthermore, per bunch crossing multiple interactions may occur, which potentially lead to high occupancy

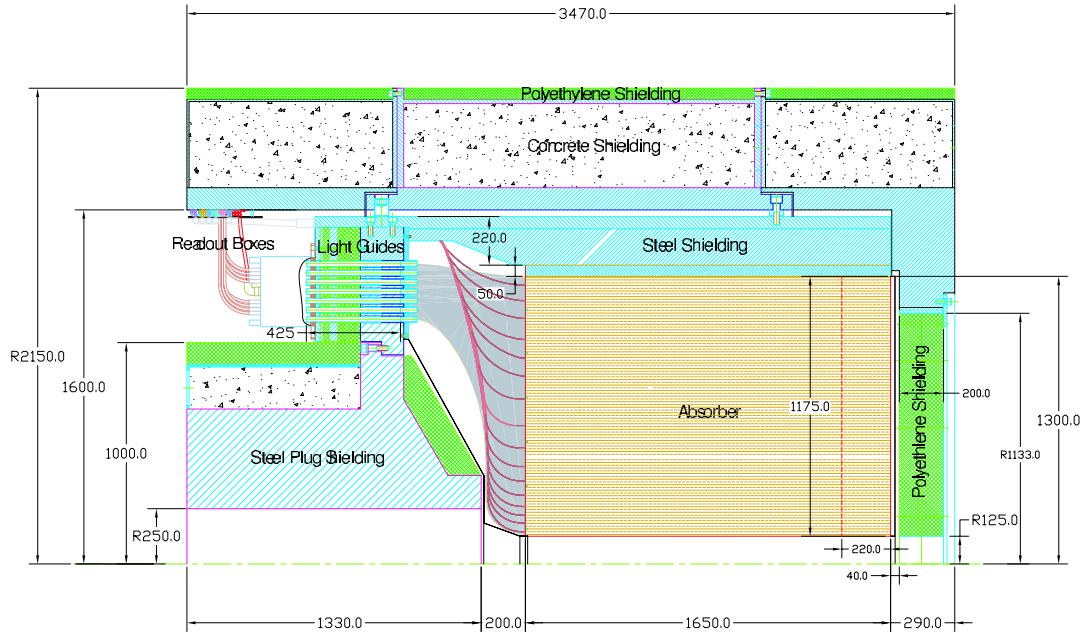


Figure 33: A schematic drawing of a channel from the HF detector [90]

numbers in the detector. It is neither possible to read out all channels of the detector at such a high frequency, nor feasible to store the data stream that this would lead to.

To bring the data flows in CMS to a manageable level while simultaneously not discarding events that may contain signatures of rare processes, such as Higgs boson production, CMS is equipped with a two-level trigger system. In a nutshell, bunch crossings occur at a frequency of 40 MHz, and the trigger system accommodates that complete events are stored at a rate of approx. 100 Hz. In this section we elaborate how the trigger and data acquisition system functions.

The trigger consists of two levels. The first level is referred to as the level-1 trigger (**L1 trigger**). This trigger analyses events from all bunch crossings, and reduced the rate from 40 MHz to approx. 100 kHz. It uses information of all subsystems except for the tracker; the latter is excluded, amongst others, due to its large number of channels. The L1 trigger makes use of custom-designed electronics such as Field Programmable Graphic Array (FPGA) and Application Specific Integrated Circuit (ASIC) chips, and configurable Lookup Tables (LUT). The L1 electronics are partially mounted directly on the detector elements itself, another part is located in a service cavern adjacent to the detector-cavern. Since the electronics of the L1 are directly mounted on the detector, this trigger does not need to completely read out the event. Thereby, the system is capable of repeating its function every 25 ns and analysing all bunch crossings.

The architecture of the L1 trigger is schematically depicted in Fig. 34. It can be seen that the trigger is build up of local, regional, and global triggers. The local trigger creates trigger primitives based on energy deposits in the calorimeters, and track or hit patterns in the muon stations. The regional trigger combines their information, and estimates what particle was responsible for the signal. The global calorimeter and muon trigger have the information of the entire subsystem to their disposal to construct jets or muons.

As may be seen in Fig. 34, the global trigger generates the final decision. At this phase the actual function of the trigger becomes active. Events are provided with a True or False value for various trigger bits, for example a trigger bit that specifies whether beams were present in the experiment (delivered by the BPTX devices), and a bit that specifies whether a high-energetic jet was present or not. The first bit may be referred to as a zero-bias bit, while the second bit is called a jet trigger. Naturally, the zero-bias bit will have a much higher rate than the jet trigger. Therefore, a factor that suppresses a fraction of a trigger rate (*prescale*) is applied to the zero-bias bit, i.e., for a certain predefined fraction of events with a True trigger outcome, the outcome is artificially, and randomly, turned to False. Thereby, the prescales allow to suppress the rate of events that have a low probability to contain a rare process; in this manner the output rate of the L1 GT can be brought down to a value of approx. 100 kHz, while simultaneously not discarding potentially interesting events.

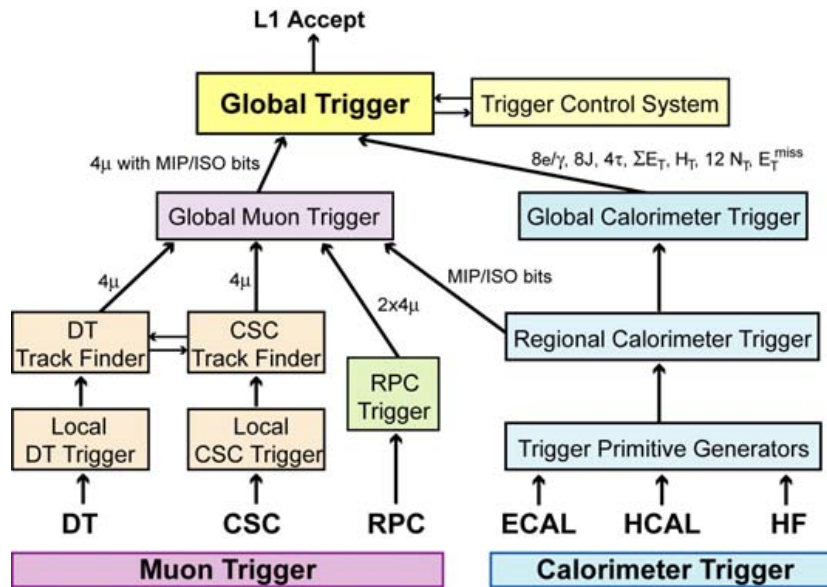


Figure 34: The architecture of the L1 trigger of CMS [90]

It should be noted that the GT only generates an *initial* decision. If the decision is positive, the complete detector is read out and the full detector information is sent to the high-level trigger (HLT) system, which makes the *final* decision, based on the full event information. If the GT outcome is negative the event is discarded.

The HLT analyses the event and generates the final decision whether the event is kept; a particular HLT algorithm is referred to as an HLT path. Since the HLT has the complete event information at its disposal, also dedicated b-quark triggers can be designed, which analyse the tracker information for displaced vertices. The HLT also applies prescales, thereby reducing the final rate at which events are stored to approx. 100 Hz. Since the HLT system analyses complete events at an input rate of approx. 100 kHz, the input data flow corresponds to 160 GB/s. This requires fast computation, which is facilitated by running 2500 CPU's in parallel.

We conclude by observing that the collision data of only 1 out of $\approx 5 \cdot 10^5$ bunch crossings can finally be stored. Therefore, it should be evident from this paragraph that for searches for rare processes the functionality of the trigger system is indispensable.

10.5 THE CMS DATA ACQUISITION

The CMS trigger system is completely embedded in the data-acquisition system (DAQ), which is responsible for saving the event information of all subsystems consistently to storage. Its general structure is displayed in Fig. 35.

The DAQ system must read out all channels synchronously. This is non-trivial, for example given the fact that the inner pixel layer is located only 4 cm from the interactions, while the outer detectors are 14 m away. Thus, there is a relative delay in the arrival of signal between different subsystems. This requires that all detectors are carefully synchronised, and the synchronisation needs to be repeated after each major interruption⁴.

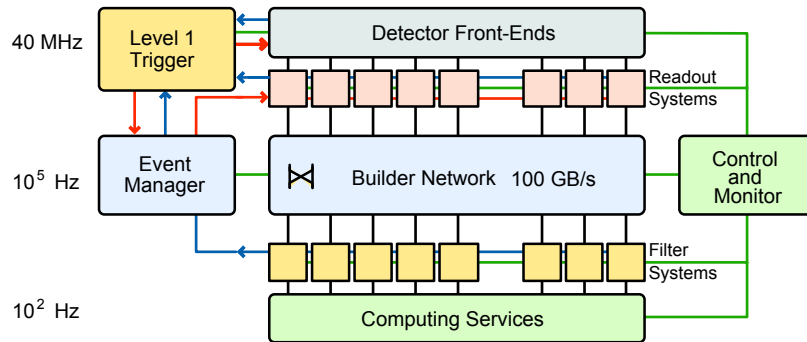


Figure 35: The architecture of the data-acquisition system of CMS [90]

However, also when the detectors are synchronised, the L1 trigger needs a time interval to process and analyse the events. This induced a latency of $3.2 \mu\text{s}$ between the actual recording of the event and the L1 decision to accept the event. Therefore, all subsystems are equipped with a front-end buffer (also referred to as a pipeline), which allows the temporary storage

⁴ The synchronisation is usually performed by comparing and matching the measured bunch-structure between different subsystems

of the signals until the L1 decision is ready. At this stage, all analog detector signals are digitised.

To facilitate a synchronised readout, the L1 accept is propagated to all the CMS subsystems by the Trigger Control and Distribution System (TCDS). Upon the arrival of the L1 accept, the Front End Drivers (FEDs) extract the event data from the front-end buffers and send it to the DAQ system. Thereafter, the event builder reconstructs a complete event from the data of the different subsystems. The event builder is also responsible for sending the event to the Computing Services above the surface, where the HLT farm analyses the event and makes the final decision.

10.5.1 Event storage

Every time the CMS DAQ is restarted, a new run number is generated. This allows to uniquely label the acquired data sets. We pointed out that for both the L1 and HLT phase a prescale can be applied to the L1 trigger bits and HLT paths, to maintain a sufficiently low event rate to the HLT farm and not overstrain the DAQ system. However, the rate of bunch crossings that result in a collision depends on beam and LHC configuration parameters, and is not constant in time (the beam loses its brightness with time evolution). Therefore, the trigger prescales are generally defined as function of the instantaneous luminosity, to accommodate for such changes. CMS defined a period during which the trigger prescales and trigger thresholds cannot be changed ([LumiSection](#)). It corresponds to 2^{20} orbits, which corresponds to 92 s.

Typically, CMS continuously collects data during eight to nine months per year. During such a prolonged period it may occur that subsystems are malfunctioning for a certain fraction of the data-taking period (or simply be switched off temporarily for safety reasons). However, for physics analyses it is absolutely vital to differentiate between luminosity sections that are suitable for the analysis and not. Therefore, CMS creates a dedicated file in which the run numbers and their good luminosity sections are stored ([JSON file](#)). Given an HLT path and a JSON file, the *effective* luminosity, which is corrected for prescales and discarded LumiSections, can be reconstructed with dedicated software tools from CMS. This quantity is necessary to correct measurements to cross-section levels.

After the HLT phase, the data output of CMS (under nominal conditions) is approx. 600 MB/s. Each event is streamed to a specific data partition, containing events obeying a specific L1 trigger or HLT path ([data stream](#)), and initially stored at the tier-0 computing centres at CERN and Budapest. Thereafter, the data are distributed via a dedicated network of high-bandwidth optical fibres to 13 tier-1 centres, which are globally distributed. These tier-1 centres distribute the data to 155 globally distributed tier-2 computer centres. The data distribution and access for end-point users is facilitated by the Worldwide LHC computing grid ([WLCG](#)) (usually abbreviated simply as the grid).

10.6 SOFTWARE AND SIMULATION

Up to this point we explained how events are selected and the storage procedure of the digital signals. The next step that is necessary to extract physics conclusions from this data, is to convert the tracker hits into tracks and (displaced) vertices, convert the calorimeter deposits into jets, distinguish electrons from photons etc. There are many different physics objects reconstructed in CMS, and each type needs its own reconstruction algorithm. Moreover, certain algorithms may rely on the information of multiple subsystems. For example, to distinguish an electron from a photon in the ECAL, one may infer whether there is a track pointing to the deposit. Also, for many physics analyses it is of crucial importance that the detector response is simulated properly; this is also accommodated in the CMS software.

Since we use both CMS collision data and simulated events in our analysis, in this section we present an overview of the software deployed by CMS. We start with a general overview of the reconstruction software. Thereafter, we discuss the simulation of events. We finish with discussing the tracker software, since our analysis relies on vertex identification. We present the CASTOR software and simulation in the dedicated CASTOR chapter. Our analysis relies also on HF, but the details of the differences in the simulation and reconstruction procedure between CASTOR and HF are beyond the scope of this thesis. The CMS software is heavily interfaced with ROOT, which is also used throughout this thesis to produce the results.

10.6.1 *Event reconstruction*

All the reconstruction software of CMS is contained in the CMSSW package. The algorithms are developed in C++ and steered via Python. CMSSW is interfaced with ROOT [94]. This is an open-source data analysis framework developed at CERN; it is used by many particle-physics experiments. CMSSW contains dedicated custom-build algorithms for reconstructing CMS data. Besides, many external software packages are interfaced to CMSSW, for example event generators and clustering algorithms. Together, these algorithms reconstruct the particle-level objects from the detector-level information.

For a proper event reconstruction, it is crucial to apply correct detector conditions in the reconstruction step. For example, the CMS response is not constant in time, but deteriorates under influence of irradiation, and the alignment may vary between different operation periods. Also, there have been data-taking periods during which the CMS magnet was off. Evidently, the reconstruction algorithms have to take the conditions of the detector at the moment of data taking into account when reconstructing the data. To this purpose, a set of files that specify the conditions of the detector at a certain data-taking period ([global tag](#)) is constructed and used in the reconstruction process.

10.6.2 *Detector simulation*

Many analyses in CMS (if not all) rely heavily on a proper event simulation. For the analysis of this thesis, for example, the simulation of the response of the CASTOR calorimeter is

particularly important, since the simulation will be used to correct the measurement back to an estimate on the particle-level.

The complete event-simulation chain can be performed consistently in the CMSSW framework. The procedure consists of various steps; we outline the workflow in a birds-eye view. First an event generator must be chosen to create the particle-level distributions. Thereafter, these particles are propagated through the detector volume using GEANT4 [95]. In this step, the detector response and its signal is estimated. Subsequently, the signals are digitised, and finally the reconstruction algorithms are applied.

A few words are in place though. Events are simulated for specific data sets. Due to the aforementioned changes in the detector condition, the conditions that the simulation tag specifies should optimally match the conditions that were present when the data were collected. Therefore, for the simulated events a global tag is also necessary, similar to the reconstruction of data. Furthermore, after the digitisation step, a simulated event must match a measured event, since for consistency the same reconstruction algorithms are applied to data and simulation.

We finish by pointing out that propagating an event completely through the detector using GEANT4 is a machine-intensive procedure, and the simulation of a statistically relevant event sample is usually distributed also over the WLCG.

10.6.3 Tracker software

As pointed out previously, all subsystems have their own, dedicated set of reconstruction algorithms. It is beyond the scope of this thesis to outline the complexity of the full reconstruction of, for example, a Z -boson in the di-muon channel (which generally involves combining information from all subsystems), because our analysis is simply not dependent on these high-level objects. In this section we succinctly discuss the track and vertex reconstruction though, since our analysis relies on proper vertex identification.

To construct tracks from the hits in the tracker, the hits need to be connected with a fitting routine. A complication in this procedure is the potential high multiplicity due to the multiple interactions per bunch crossing that may occur. This motivates the choice for the very fine granularity of the pixel detector which, as we demonstrated previously, even allows the identification of tracks and vertices when more than 70 collisions occur simultaneously.

Five kinematical parameters may be attributed to a track:

- The polar angle w.r.t. the beam pipe θ
- The azimuthal angle ϕ
- The transversal momentum p_T
- The transversal distance d_0 and longitudinal distance d_z between the vertex and the beam spot

The beamspot is defined using the three dimensional profile of the luminous region.

As a first step, seeds of these parameters are generated, based on two or three hits in the inner pixel detector. Thereafter, the tracks are extended transversally by the fit to include the hits from the outer tracker. The hits are added iteratively to the track, i.e., once a hit is added the track-parameters are updated. The process stops when the outer layer is reached or no more hits could be added. After the termination, a new fit is made to the candidate collection of hits to avoid a possible bias, and a cross check is performed by comparing the origin from the track with the estimated interaction vertex. For the latter purpose, naturally the procedure needs to be iterated.

When no more hits can be added to the track collection, a quality test is performed. From fits to the tracks a χ^2/ndof can be obtained, and cuts are placed on it. Also, cuts are placed on the five kinematic variables that we outlined before. Also, consistency checks are performed w.r.t. the interaction vertex. Tracks surviving the criteria are called high-purity tracks. Usually, physics analyses use the latter collection of tracks.

From the tracks the primary vertices are reconstructed, as well as secondary vertices (amongst others emerging from b-quark decays). A weight is calculated per track, based on the longitudinal distance between the point of closest approach to the beams pot. The primary vertex needs to be compatible with the majority of the tracks in the event. An adaptive vertex finding algorithm is used to this purpose [96].

11.1 INTRODUCTION

The CASTOR detector, which is the central detector of this analysis, is a calorimeter. Therefore, we provide in this chapter a concise introduction to the concepts of calorimetry and the key parameters for their characterisation. This should serve as a background to the subsequent chapter on CASTOR.

As was explained in the previous chapter on CMS, there exist various methods to measure kinematical properties of particles. All types of calorimeters have one feature in common though: they perform a destructive measurement, i.e., the particle is fully absorbed in the process of measuring it.

In a nutshell, a calorimeter functions as follows. A particle incident on the calorimeter starts to interact with the detector material. It loses its kinematical energy via various processes. This results in a cascade of secondary particles in the detector; this is referred to as a shower¹. This cascade is related to the energy of the incoming particle. Therefore, the art of calorimetry is to obtain an optimal estimate of this cascade.

We start with explaining how a particle incident on a calorimeter is converted into a cascade, and denote the differences between showers of various particle types. Thereafter, we introduce the experimental methods to detect and quantify the showers. Throughout the chapter various parameters that specify the key features of a calorimeter are explained also. The main reference for this chapter is the handbook of the Particle Data Group [15].

11.2 SHOWERS IN CALORIMETERS

In this section we will discuss the propagation of a high-energetic particle through a calorimeter. For simplicity, in this section we assume that the calorimeter consists of a single slab of a homogeneous medium.

When the particle traverses the medium, it loses its energy through many interactions of the particle with the atoms or molecules in the medium. The shower development is a stochastic process, and the shower can be described by statistical parameters. Many processes contribute to the energy loss of the incident particle. For a charged particle, these processes are ionisation and excitation of atoms (or molecules) in the medium, Bremsstrahlung, Cherenkov radiation, δ -rays, and possibly nuclear reactions. Photons interact via the photoelectric effect, Rayleigh scattering, Compton scattering, pair production, and photo-nuclear interactions. A part of the energy is also turned into heat. For precise definitions of these processes we refer to [15].

¹ In the past, therefore calorimeters were also referred to as shower counters

Electromagnetic showers (from electrons, positrons, and photons) can be well-described by QED. In Fig. 36 (left) an electromagnetic shower, "frozen" into a slab of plastic, is displayed. At low energies, the dominant contribution to the shower cascade comes from ionisation, while at high energies pair production and Bremsstrahlung provide the dominant contribution to the shower. Depending on the material, a part of the energy of the shower may be converted in scintillation or Cherenkov photons, which may be measured to estimate the kinetic energy of the incident particle².

For electromagnetic showers the radiation length X_0 is a macroscopic length scale, in which the particle deposits on average 63% of its energy in the medium. Naturally, each material has its own radiation length, which generally depends on the atomic number Z of the medium. The parameter X_0 can thus be used to estimate how much material is needed to fully contain the shower of electromagnetic particles.

The description of hadronic showers is more complicated due to the non-perturbative nuclear reactions. The most important nuclear contribution comes from spallation protons. These are protons that, upon a nuclear interaction of the incident particle, are separated from the nucleus of the atoms of the medium. These reactions generally do not result in measurable energy, i.e., the energy is not converted into photons and does not contribute to the calorimeter signal. This is referred to as invisible energy. The fluctuations in the *fraction* of invisible energy are (in energy ranges relevant at collider physics) substantial in comparison to the statistical shower fluctuations of an electromagnetic shower of the same energy.

A hadronic shower has also an electromagnetic component; it deposits a part of its energy via π^0 production, and the π^0 particles decay to two photons. This component fractionally grows with the energy of the incoming particle, and thus at large energies the invisible energy fluctuations become less important. The equivalent of X_0 for hadronic showers is the interaction length λ_I , which is defined as the average distance in which a hadron deposits 63% percent of its energy. Generally, for a given medium the interaction length is much larger than the radiation length.

Lastly, muons interact only very weakly with matter. To a good approximation, a muon behaves as a minimally ionising particle (MIP). As we will see, this property makes muons excellent particles to intercalibrate segments of calorimeters. The muon stopping power has been depicted in Fig. 36 (right), which also indicates at what kinematic domain the various processes are most relevant.

11.3 DETECTION MECHANISMS

We explained that particles deposit their energy in a medium via a shower, and that the amount of energy that is converted into observable energy is a stochastic process. In this section we discuss methods and strategies to characterise the energy of the particle incident on the calorimeter, which is its key purpose.

² There exist also calorimeters that do not make use of scintillation or Cherenkov photons, we will give an example of such a calorimeter below

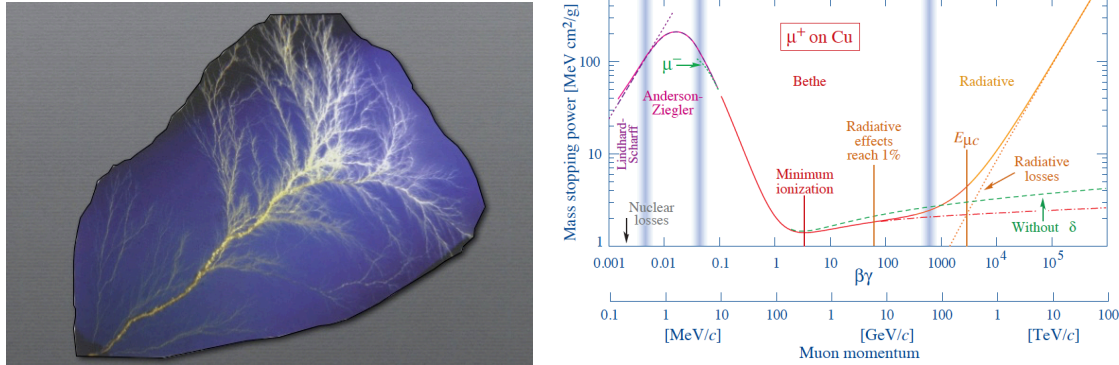


Figure 36: Left: shower development frozen in a slab of plastic [97]. Right: the stopping power of copper for muons, as function of the muon momentum [15]. It can be observed that different processes are dominant at different energies

Calorimeters are divided into homogeneous and sampling calorimeters. A homogeneous calorimeter consists of a single slab of a medium, in which usually the shower is fully contained. One may think of the lead-tungstate crystals of the EM calorimeter of CMS [89]; photons and electrons are fully absorbed in these crystals. These crystals are transparent, and the scintillation photons induced by the shower propagate to the rear of the transparent crystals. Here they are detected and amplified by avalanche photo-diodes. A homogeneous calorimeter has the advantage that the signal yield is relatively large, and thus the statistical uncertainty in the signal is relatively small.

A sampling calorimeter usually consists of slabs of material that absorb a fraction of the particles energy and create the shower; this is called the passive medium. This may be iron or tungsten, for example. This is interleaved with material that generates the actual signal, for example slabs of scintillating plastic. This is the active medium. Thus, the active medium "samples" the shower longitudinally. For a sampling calorimeter, an effective radiation and interaction length must be defined, which depends on the configuration of its various layers. For a sampling calorimeter inevitably a fraction of the shower does not contribute to the signal. Such calorimeters have the advantage though that geometrical properties of the shower may be inferred, which may allow for the identification of the incident particle. It may be noted that in a homogeneous calorimeter the medium performs both functions simultaneously: it both creates the shower, and generates the signal.

The different processes by which the incident particle loses its energy may be exploited to generate the signal. Scintillation (in the visible wavelength range also known as fluorescence), has as advantage that the light yield is relative large, but the process generally is relatively slow, $\mathcal{O}(200 \text{ ns})$. The light yield of Cherenkov radiation is lower, but the signal generation is much faster, $\mathcal{O}(10 \text{ ns})$. Another detection mechanism, which will be realised at CMS in the future, is a silicon-tungsten calorimeter; in this design the tungsten slabs are interleaved with silicon strips or pixels. The silicon is used to detect the charged particles of the shower.

Finally, it is important to distinguish between compensating and non-compensating calorimeters. As was indicated above, a fraction of the hadronic shower is invisible. This effect is

usually expressed in the π/e ratio (or another benchmark hadron such as a proton). This ratio reflects the difference in response of the calorimeter to pions and electrons of the same energy. For a non-compensating calorimeter, this factor will be (well) below one, and energy-dependent. The compensation for the difference in response has to be made after that the signal has been collected. Compensating calorimeters aim to correct for this difference instead by assembling the calorimeter from materials that suppress the contribution from the EM shower, and enhance hadronic contributions. Compensating calorimeters are always sampling calorimeters.

11.4 THE RESPONSE AND RESOLUTION OF CALORIMETERS

The response and resolution of a calorimeter may be tested by placing it in a testbeam. In such a setup, the incident energy of the particles is known and thus the response and resolution may be determined as function of the energy of the incident particle. When both electron and hadronic beams are available, the factor π/e may also be determined.

Typically, the relative energy resolution ρ is parameterised in terms of three parameters α , β , and γ as:

$$\rho(E) = \alpha \oplus \frac{\beta}{\sqrt{E}} \oplus \frac{\gamma}{E}. \quad (74)$$

As mentioned, the shower is stochastic in nature. Therefore, the natural statistical spread in the signal E is approx. \sqrt{E} . Thus, the contribution of the stochastic fluctuations to the *relative* resolution ρ is $1/\sqrt{E}$ (which leads to the remarkable property that ρ *improves* with energy). This term is represented by β . Other factors that may contribute to the resolution are leakage and noise. Noise becomes typically important at low energies of the incident hadron, and thus its relative contribution $\sim 1/E$ (represented by γ). Leakage effects on the other hand become important at high energies, and therefore their contribution is approximated by the constant α . Typically, the resolution of electromagnetic calorimeters is better than the hadronic detectors.

Preferably, the response of a calorimeter is linear in energy. Since the longitudinal profile of showers grows approximately logarithmic with the energy of the incoming particle, it is very important that the showers are fully contained in the calorimeter. Therefore, together with the resolution parameters, the (effective) radiation and interaction lengths are very important for specifying the potential of a calorimeter.

THE CASTOR CALORIMETER

12.1 INTRODUCTION

In this chapter we describe the CASTOR calorimeter, which is the key detector of our analysis. The performance of CASTOR during the operation period between 2015 and 2018 of the Large Hadron Collider (LHC RUN II) is outlined. Although our analysis focusses on data collected in 2013, we chose to discuss the performance during LHC Run II since the author was actively involved in all steps of the Run II data taking campaigns of CASTOR, ranging from installing the detector to the data analysis. We start with presenting CASTOR in a birds-eye view.

CASTOR is an electromagnetic-hadronic sampling Cherenkov calorimeter. The two tonnes weighing detector is installed at minus fourteen meters from the CMS interaction point at only 1 cm from the beam pipe, an illustration is depicted in Fig. 37. CASTOR can measure energy deposits, jets, and rapidity gaps in the range $-6.6 < \eta < -5.2$. No other calorimeter has been installed in this particular phase-space at the LHC.

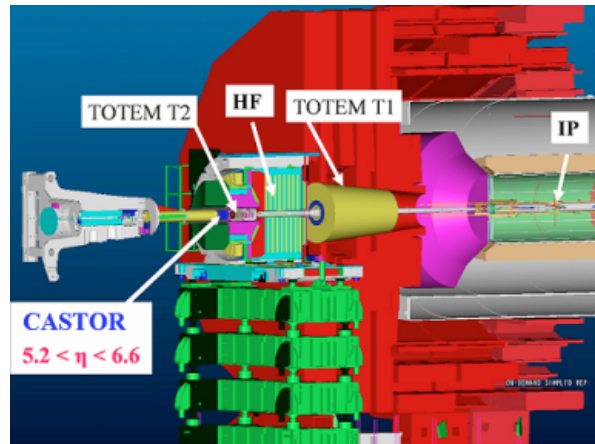


Figure 37: The location of CASTOR at CMS. The distance between the interaction point (IP) and CASTOR ≈ 14 m [98]

The key purpose of the detector is to measure the longitudinal shower development. Therefore, CASTOR is mechanically organised into two halves, see Fig. 38 (left) for an illustration of one half. A half consists of eight towers (occasionally referred to as a sector also). Each tower is longitudinally segmented into fourteen modules, this allows to search for strangelets and deeply penetrating objects [99]. Thus, CASTOR has 224 channels. We observe that CASTOR has only ϕ and no η -segmentation.

Each CASTOR channel consists of tungsten layers interleaved with quartz, see Fig. 38 (right). The photons of the Cherenkov cone are guided towards the PMTs, where the signal is amplified. Each channel is also equipped with an LED fiber that can illuminate the PMT for commissioning purposes. The two front channels of CASTOR contain half of the tungsten and quartz material of the other channels, allowing the distinction between electromagnetic (EM) and hadronic energy deposits. The other channels are referred to as hadronic channels. The tungsten in the electromagnetic (EM) sections correspond to 0.77 nuclear interaction lengths (corresponding to $20 X_0$), while the hadronic sections are 9.24 interaction lengths deep. Thus, the overall depth of CASTOR \approx ten nuclear interaction lengths. The choice for this design was partially motivated by the fast response, radiation hardness, and compactness of the materials. CASTOR is installed on approximately the most radiation-harsh spot of CMS.

In [100] the response and linearity of CASTOR was reviewed using test beams. The calorimeter was shown to have an excellent linearity. The parameter α and β from eq. 74 were found to have a characteristic value of 0.044 and 0.513 , respectively.

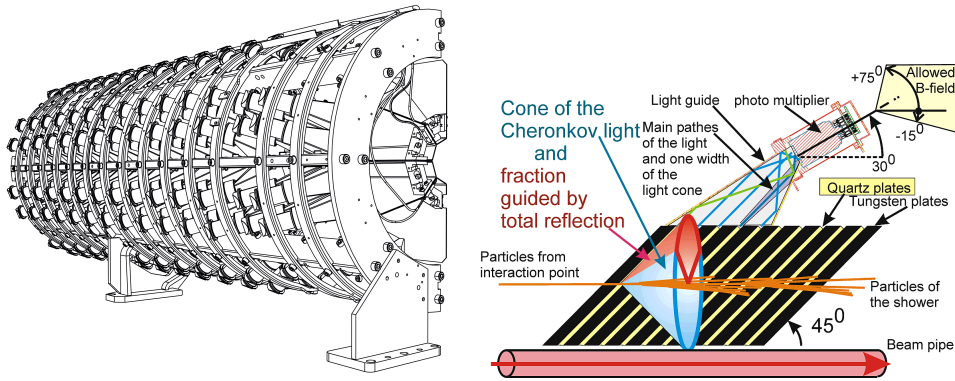


Figure 38: Left: schematic drawing of one CASTOR half. The diameter of CASTOR is roughly 0.6 m, its length approx [101]. 1.6 m. Right: schematic drawing of a CASTOR channel [102]

The Cherenkov photons are guided towards fine-mesh PMTs where the signal is amplified. Thereafter, the signals are compressed and prepared to be send to the central DAQ system of CMS. Fine-mesh PMTs, which have a relatively high resistance for magnetic fields, were chosen since the CMS magnetic field penetrates into CASTOR through air gaps in the B-field shielding¹. In one bunch-crossing time interval (typically 25 ns), the signal in a CASTOR channel is accumulated by a charge capacitor (CAP). In total each channel has four CAPS; the consecutive sampling allows for a measurement without deadtime. However, measurements revealed that the signal from one bunch crossing leaks a fraction of approx. 20% in the CAP of the next bunch crossing. The signal in a channel (called a RECHIT) is therefore reconstructed from the sum of two of these measurements (called a DIGI), and usually physics measurements are only performed for beams with 50 ns bunch separation. For each DIGI pedestal subtraction is performed with dedicated pedestal values per CAP; the pedestal is

¹ This shielding was adjusted to CASTOR during a late phase of the development of CMS, and the penetrating effect of the magnetic field through the air gaps could not be adjusted anymore in the short adaptation time

the mean signal value, for example due to the electronics, in absence of radiation (for CASTOR this means that no beams are present in the LHC machine).

Also, since CASTOR cannot assign a vertex to an energy deposit, the number of events per bunch crossing (*pileup*) may not exceed one for physics analyses. For certain analyses, for example a cross-section analysis including CASTOR [49, 103, 104], the pileup may need to be even lower to minimise the systematic uncertainty in the pileup-correction factor.

12.2 THE PERFORMANCE OF CASTOR DURING LHC RUN II

A key feature of measuring with the CASTOR calorimeter at the LHC, is that it usually needs to be reinstalled in its position for data taking prior to a particular campaign. During LHC Run II CASTOR was installed on three different occasions for data taking campaigns. Therefore, many aspects of the performance of CASTOR need to be reassessed; a straightforward example is the alignment.

In this section many aspects of the performance of CASTOR are revised, with emphasis on results relevant to the calibration of CASTOR. For an in-depth review on aspects such as the geometry and electronics we refer to [5]. We start with discussing the alignment, which imposes a non-negligible uncertainty on physics analyses. Next, we introduce the noise estimates of the CASTOR channels, which are improved w.r.t. LHC Run I. Thereafter we introduce the gain correction factors; together with the noise estimates these constitute key ingredients for the intercalibration of CASTOR. Penultimately, the procedure and results on the inter and absolute calibration are reviewed. We finish with comparing results from simulations to the real data.

12.2.1 Alignment and installation

We mentioned previously that CASTOR needs to be reinstalled for every data-taking campaign. The reason for this is the sheer radiation load in the particular spot in which CASTOR is installed, which is the highest of the whole CMS cavern. If CASTOR would be left in its position after its measurement, it would become so irradiated that its radioactivity would affect the measurements of other subsystems. It is anticipated that the electronics of CASTOR would also be damaged during the LHC high-luminosity runs. Besides, when ultimately the detector would need to be uninstalled, its radioactivity would pose a danger to the manpower disabling CASTOR.

The uncertainty in the alignment of CASTOR is a delicate ingredient of its performance due to its very forward installation location. In Fig. 39 (left) we display the propagated effect of a shift in the installation location on the η -acceptance and average energy measurement for $\sqrt{s} = 13$ TeV p+p collisions. We observe that an uncertainty in the alignment of 2 cm results in a shift in the overall energy measurement of $\approx 20\%$. For the measurement of an exponentially decaying spectrum this uncertainty may propagate into prohibitively large systematical uncertainties. Thus, various methods have been developed to obtain an estimate of the position of CASTOR with an acceptable uncertainty.

The position of CASTOR after installation is first measured w.r.t. fixed points in the cavern using laser targets²; this procedure is known as the survey. The installation and survey are always performed when the CMS magnet is off though. When the CMS magnet is ramped on, CASTOR becomes displaced. Therefore, the detector is equipped with various position sensors. The distance w.r.t. the beam-pipe can be measured using five infrared sensors per half and two potentiometers at the back. Two additional potentiometers measure the opening between the two halves, which can move separately.

These movements are carefully monitored with the sensors during the magnet ramp due to the close proximity to the beam-pipe; an interaction between the two-tonnes weighing detector and the delicate beryllium beam pipe would constitute a catastrophe to the LHC program. In Fig. 39 (right) we display the movements of CASTOR during a magnet ramp, as monitored by the infrared sensors.

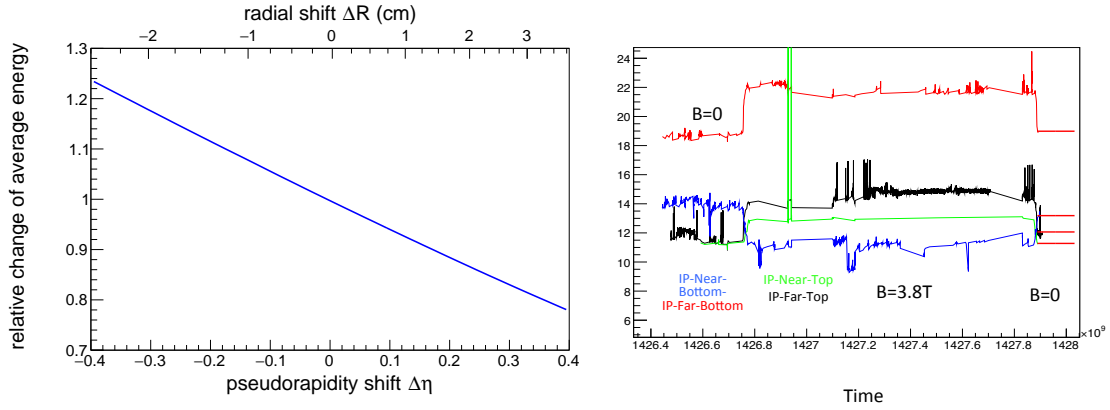


Figure 39: Left: a simulation of the impact of an offset of the position of CASTOR on the pseudorapidity acceptance and energy response [5]. Right: the distance of infrared position sensors at the interaction point side of CMS in mm w.r.t beam pipe during a full cycle of the magnet ramp. Near and Far indicate the different halves of CASTOR. The time span on the x -axis is of the order of a few days [5]

12.2.2 Noise and pedestal

The pedestal and noise of the CASTOR channels are estimated per channel by analysing a large set of events recorded in-situ in the absence of beams in the LHC. Those runs typically comprise around one million events. A pedestal spectrum, measured for the noisiest CAP of the channel of tower 12, module 12, is shown in Fig. 40. This pedestal spectrum is depicted for high voltage off (blue), 1500 V (purple), and 1800 V (black). The average data taking high voltage corresponds to ≈ 1500 V, where even for this noisy capacitor the noise probability is much below 1%.

² Until today, the position of CASTOR after installation has always been positively identified to be on the CMS minus side

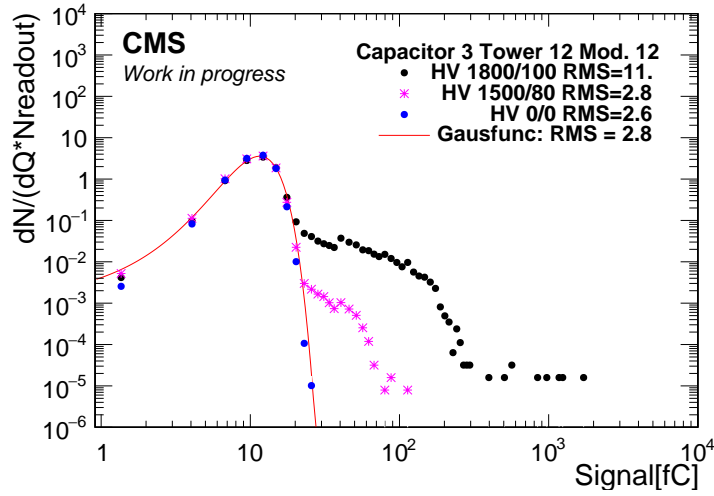


Figure 40: Pedestal charge spectrum for the noisiest capacitor of a typical CASTOR channel (tower 12, module 12) for various cathode and last dynode voltage settings. A Gauss fit to the data at 0 V is also shown.

The measurement without high voltage supplied to the PMT represents the purely electronic noise from the cables, the amplification, and the digitisation chain. After applying a voltage to the PMT, additional noise components start to contribute. The first shoulder corresponds to the thermal emission of single electrons from the PMT cathode. It can be seen that for the used fine-mesh PMTs single photoelectrons do not produce a clear peak but a rather smooth spectrum.

Signals of ion feedback start to become visible at very high voltages, but with a tiny noise rate of $< 10^{-4}$ per event. Ion feedback is a consequence of the non-perfect vacuum of the PMT tubes. Gas molecules may be ionised by the cascade. These charged ions subsequently traverse the tube in the opposite direction w.r.t. the cascade. This results in a second pulse that is dilated w.r.t. the original pulse; therefore the effect is also called afterpulsing. These constitute false signals. The maximum noise signals observed here correspond to ≈ 3000 fC, corresponding to ≈ 30 GeV of energy.

The peak of the Gaussian fit is used as the estimate of the pedestal value and is subtracted from all subsequent measurements. The width of the Gaussian (as opposed to the statistical standard deviation) is used to obtain the noise of a channel, since in particular for muon triggering a precise estimate of the noise is of paramount importance.

In Fig. 41 (top left) the distribution of the fitted value of the pedestal is shown, which on average is 11 fC. In the upper right plot the fitted width of the Gaussian is displayed, in the lower left plot the statistical RMS of the data. It can be seen that on average the statistical RMS overestimates the electronic noise by 17%, due to the aforementioned non-Gaussian tails due to thermal photons and ion feedback.

Comparing the statistical and fitted width has proven to be a useful method of identifying noisy or malfunctioning channels. In the lower right hand plot the distribution of the

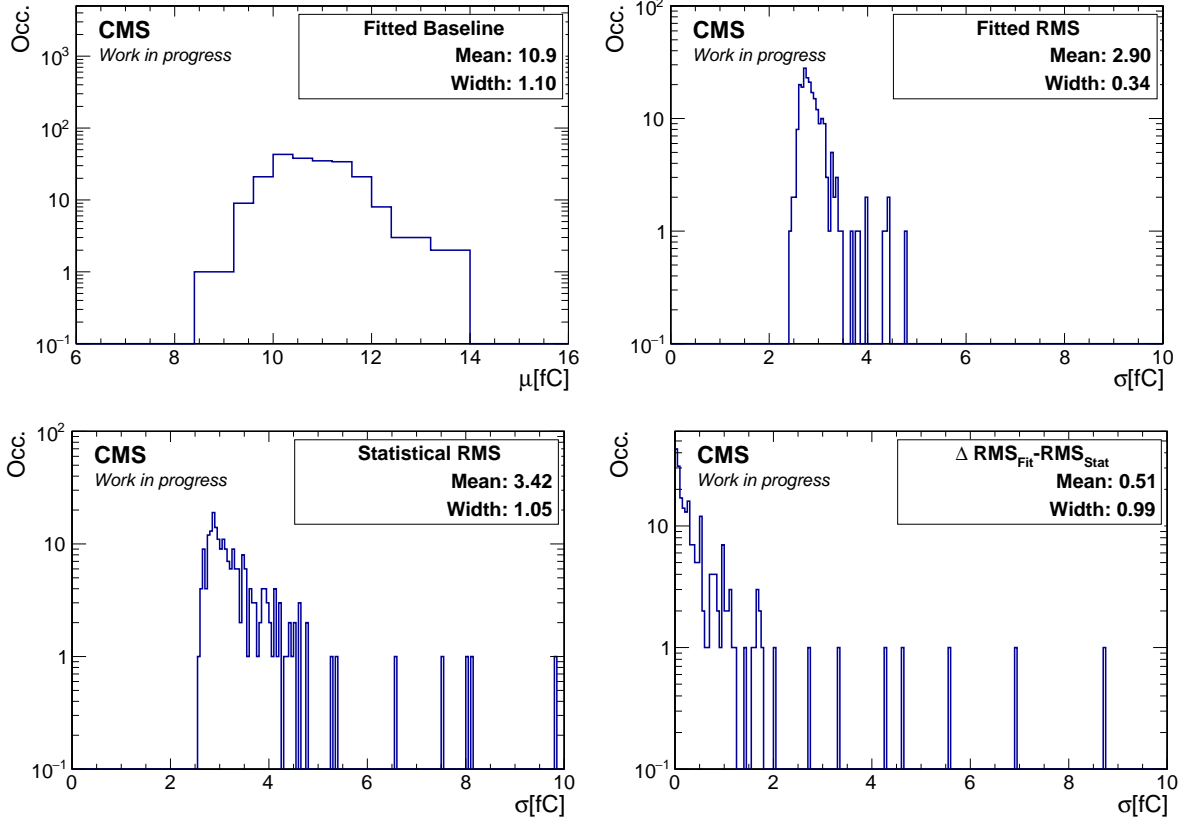


Figure 41: Overview of pedestal and variance measurements with 1500 V supplied to the PMTs. Two malfunctioning channels were not considered in this analysis. These data were recorded in 2015

difference of the statistical and fitted RMS per channel is displayed. From the distribution it can be inferred that a channel with a difference in excess of 2 fC is suspiciously noisy. These channels are subject to further inspection. Generally, if the difference is mainly caused by the very rare but very high signals from ion feedback the channel is still accepted for physics analyses, since the statistical probability of this noise is negligibly low. However, by using this method a few channels with a large contribution from thermal electrons were identified, which were masked for the online muon trigger, and occasionally altogether excluded for physics analyses.

12.2.3 Gain-correction factors

The intercalibration of CASTOR, which is discussed in the next paragraph, is performed with beam-halo muons. These deposit only small amounts of energy in the detector. In order to maximally distinguish these minute signals from the electronic noise, the muons are collected with CASTOR at its maximal gain settings (1800 V). To record physics events, maximal gain

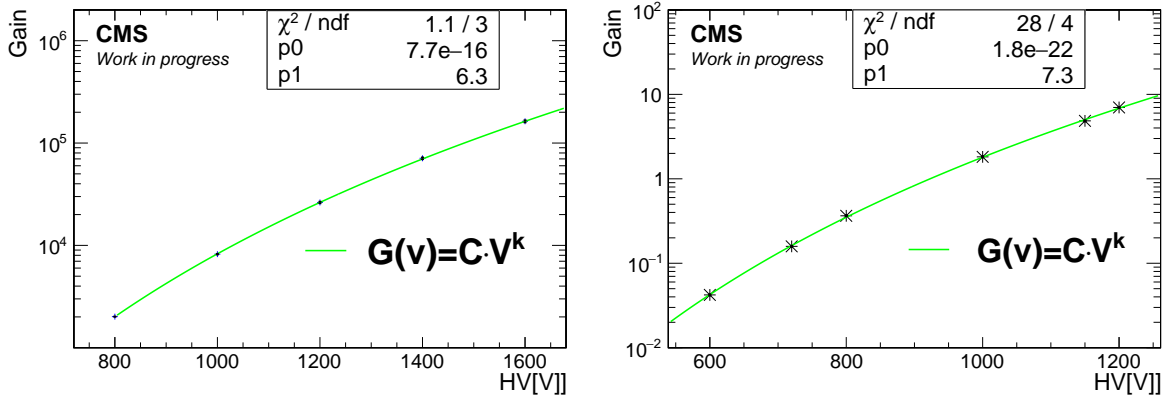


Figure 42: Left: response of the PMT of tower three module one during the characterisation to changing high voltage settings. Right: the response to physics events for the same channel. It should be noted the normalisation in this graphs is rather arbitrary; the signal strength on the right hand side corresponds to the pulse intensity of the laboratory measurements, while the left hand side signal strength corresponds to 5 TeV p+p collisions

settings are too high for the front channels of the detector, and custom gain recipes optimised to the dynamic range are applied instead. These recipes depend generally on the magnetic field configuration, but in particular also on the presence of heavy-ion collisions. In central lead-lead collisions the amount of energy that CASTOR needs to absorb and detect can become very large w.r.t. p+p collisions. The difference in gain settings between lead-lead and proton-proton collisions is therefore about a factor of 20.

Naturally, during physics data taking the PMTs are always operated at gains in the range where their signal-to-noise ratio is optimal.

Gain-correction factors are thus needed to transpose the intercalibration constants between the muon high voltage and the different physics recipes. Three different methods are available for this purpose. In this section we compare and contrast the different methods and their results.

One option is to rely on so-called dark-box PMT characterisation measurements performed in the laboratory prior to their installation in the experiment. Very precise data exists for $\approx 70\%$ of the PMTs, and these data even allow an estimate of the photon-gain³ of the PMT. However, potential ageing effects are not included. Also, the use of the results is limited since the measurements are not performed in-situ, and this restricts the usage to data sets recorded⁴ with $B \approx 0$ T. In Fig. 42 (left) the measurements and fit are depicted for a particular channel.

³ The photon-gain is the amplification factor from incident photons to the output signal (usually in fC). The electron gain only relates the number of photoelectrons to the output signal. These are related via the quantum efficiency of the PMT

⁴ It is rather exceptional that CMS recorded p+p collisions at $\sqrt{s} = 13$ TeV with its magnet off. This was due to a temporal deficiency of the cryogenic system

A second option is to use LHC MinBias high-pileup data, which is well suited to model the dependence of the electronic gain on the high Voltage. These events create strong signals in CASTOR and also such data are not used for CASTOR physics analyses. In 2016 a dedicated voltage scan was performed in such very realistic conditions.

These two methods have in common that the response of the channels was measured as a function of the high Voltage. This allowed to parameterise the gain by a fit of the form $c \cdot V^k$. The error in the constant c conveniently cancels in the calculation of the correction factor.

Finally, to complement the channels for which no characterisation or collision measurement are available, a statistical gain estimate is performed after CASTOR is installed in CMS using LED pulses. The statistical method evaluates the fluctuations observed in each channel as a response to the illumination of the cathode with LED pulses. The signal seen by a PMT for a LED pulse, S_{led} , is related to the PMT gain, g , and the number of photoelectrons, $N_{\text{p.e.}}$, according to $S_{\text{led}} = gN_{\text{p.e.}}$. Thus, the relative variance of S_{led} consists of a contribution from the gain fluctuations and from the Poissonian fluctuations of the conversion of photons to photoelectrons and is given by

$$\left(\frac{\sigma_{S_{\text{led}}}}{S_{\text{led}}}\right)^2 = \left(\frac{\sigma_{N_{\text{p.e.}}}}{N_{\text{p.e.}}}\right)^2 + \left(\frac{\sigma_g}{g}\right)^2 \approx \left(\frac{\sigma_{N_{\text{p.e.}}}}{N_{\text{p.e.}}}\right)^2 = \frac{1}{N_{\text{p.e.}}} = \frac{g}{S_{\text{led}}}. \quad (75)$$

It is assumed that the relative fluctuations of g are much smaller than the relative conversion fluctuations, and all effects of bandwidth limitations on the fluctuations are neglected. The gain is then estimated according to $g = \sigma_{S_{\text{led}}}^2 / S_{\text{led}}$.

For a full set of gain correction factors for all channels of the calorimeter typically the results of at least two of the methods described here must be combined.

Since some CASTOR physics data was collected only with the CMS magnet off, the results of the statistical method are compared to the other two methods with the CMS magnet on and off. In Fig. 43 (left) the weighted difference between the gain correction factors for muon-to-proton physics obtained by the characterisation and LED measurements for $B = 0$ is displayed. In Fig. 43 (middle) the correction factors for proton physics obtained from a voltage scan to physics events are compared to correction factors from LED measurements for $B = 3.8 T$. The comparison in Fig. 43 (right) is identical to the middle plot, except that the correction factors are for muon to heavy-ion physics. It can also be seen from the number of entries of the plots, that only for a fraction of the channels reliable measurements of two methods simultaneously are available⁵; especially the heavy-ion gain corrections motivate the simultaneous use of different methods.

The statistical properties of fits to these results reveal reasonable consistency between the methods. In particular, it should be noted that the statistical method, which has a broad range of applicability, clearly can be used irrespective whether a magnetic field is present or not. This is a very general result, of which the applicability extends to other subsystems utilising PMTs.

The uncertainties of gain correction factors derived from voltage scans and characterisation measurements ($\approx 1\%$) are significantly lower than the values obtained from the LED mea-

⁵ A lack of measurements by the statistical method is partially caused by a bad illumination fiber connected to tower one and two

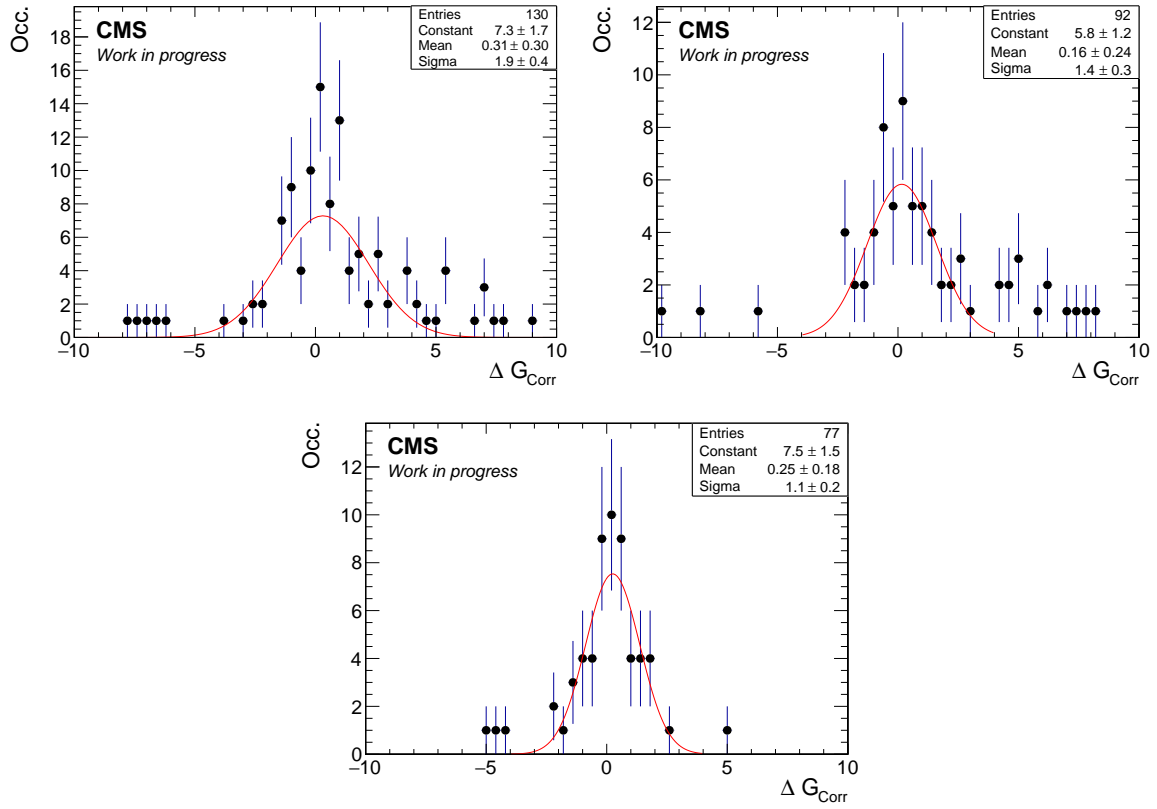


Figure 43: Distributions of the weighed difference, $\Delta G = (G_1 - G_2) / \sqrt{\sigma_{G_1}^2 + \sigma_{G_2}^2}$, between two sets of gain correction factors obtained by different methods. Left: muon HV to proton physics HV between LED and characterisation method at $B = 0$ T. Right: between LED and physics events analysis method at $B = 3.8$ T. Bottom: muon HV to heavy-ion physics HV between LED and physics events analysis method at $B = 3.8$ T.

surements ($\approx 17\%$). A plausible explanation for this may be, that for the LED gain-correction factors two measurements were simply divided, while for the other methods the gain was parameterised by a fit. This cancelation may also be achieved by fitting a high-voltage scan of LED measurements though, and it is expected similar precisions may be achieved.

12.2.4 Intercalibrating CASTOR using beam-halo muons

The LHC beam causes beam-halo muons. These muons propagate parallel to the beam-pipe and thus traverse the CASTOR towers longitudinally.

Per channel, a muon deposits approximately 1 GeV (as may be inferred from the propagation of muons through tungsten [15]). This energy loss is negligible for the high-energy muons of the LHC, and therefore these muons can to first order be approximated to behave as a Minimally Ionising Particle (MIP) in CASTOR. Muons may also deposit large amounts of energy via radiative reactions, but the contribution will on average be the same for all channels (if the muons shower, the shower will longitudinally be short since it is electromagnetic in nature). Thus, the response of CASTOR to isolated beam-halo muons can be exploited to intercalibrate the channels of CASTOR w.r.t. a reference channel. A clear advantage of this method is, that it can be applied in-situ (as opposed to using test-beam results for example), and all detector and magnetic field effects are automatically taken into account.

Isolated beam-halo muons are collected during periods in which beams are present in the LHC, while no collisions are generated yet. This occurs during the so-called interfill and circulating beam operation modes of the LHC. The majority of the muons is collected when the beams are injected into the LHC machine at a constant energy of 450 GeV. Therefore, the muon signal may not only be used for intercalibration purposes, but also serve as a constant probe to monitor the development of the calorimeter over its life time at the LHC.

To accomplish this, a dedicated level-1 hardware trigger was developed for CASTOR, which was activated during the circulating beam periods. A CASTOR tower is divided into three groups of four consecutive channels; the last two channels of CASTOR are not considered in the trigger due to hardware requirements. The online trigger demands one active tower, with minimally one channel per group above a five- σ channel-specific threshold, while simultaneously the rest of CASTOR is supposed to be below threshold. The channel-specific thresholds, which we carefully determined in section 12.2.2, are naturally of vital importance for the trigger to function properly. During these muon data taking periods, CASTOR was usually operated at optimal gains to maximally distinguish the minute muons signals from the noise. When a sufficient number of events was collected with maximal gains, another muon sample was collected with physics high-voltage settings for cross checks, if the installation period of CASTOR allowed for this.

After the online collection, further refinements are imposed offline. It is required that minimally five channels are above a 2- σ threshold in the active tower, while no more than five channels are above this threshold in the rest of the detector. Further, in the active tower there must be minimally one active channel in each group. Thereby, the trigger demand mimics the specific muon signature, while it simultaneously vetoes on hadronic activity, which may

pollute the muon signals. The intercalibration constant is obtained as the (statistical) mean signal value of the spectrum after the offline selection.

In Fig. 47 we display the noise (in red) and signal (black dots) distribution after the offline selection for a specific hadronic channel. The threshold has been indicated with the dotted

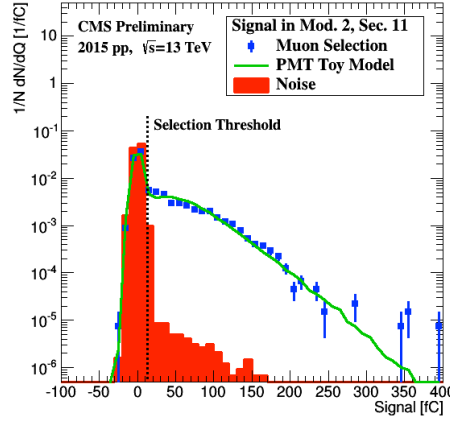


Figure 44: The signal spectrum of an EM module of CASTOR, after the offline muon selection for $B = 0\text{ T}$ [5]. The noise distribution is depicted in red, the signal is represented by the blue dots. The green line represents a tuned PMT model, which corresponds well with the measured muon signal. The threshold to distinguish noise from signal is depicted in black. The average number of photoelectrons of the PMT models $\langle N_{p.e.} \rangle$ is 0.58

line; evidently this is an important parameter. If the threshold is too high, one discards too many signal event, while a too low threshold results in many noise events. This can potentially lead to a high trigger rate that needs to be prescaled. Effectively, this leads to the recording of less signal events. A tuned PMT model has been overlaid in blue; clearly there is good agreement between the simulated and measured signal. Also, it may be observed that the muons do not produce a clear peak in the signal spectrum; this is due to the fact that in the amplification process in the PMT electrons may miss a dynode, which deteriorates the low-energy resolution. This behaviour is also well reproduced by the tuned model. Furthermore, from the tuned model it was found that the average number of photo-electrons ≈ 0.5 , which matches elementary expectations.

We will show in the validation section that the method establishes good results for the longitudinal intercalibration of the channels in a tower, while the transversal intercalibration is suboptimal. In the opinion of the author, it would be interesting to assess the potential of obtaining an estimate of the intercalibration constants of all channels by tuning a PMT model (as exemplarily displayed in Fig. 47), instead of working with the average value of the spectrum⁶.

⁶ A further investigation of this procedure would require a few more months of work, and is beyond the scope of this thesis

Lastly, it should be noted that the response of the modules in the middle of CASTOR (usually module six to eight) is badly affected by the magnetic field of CMS. The muon signals are minute, and thus these channels cannot be intercalibrated. Therefore, usually these channels cannot be used for physics analyses.

12.2.5 The absolute calibration of CASTOR

The absolute calibration of a calorimeter is an important parameter for specifying its performance. In this paragraph we discuss the determination of the scale that converts the signals in femto Coulomb (fC) to energy deposits in GeV (after the intercalibration is performed).

CASTOR is a non-compensating calorimeter. Since the response of a non-compensating calorimeter to electrons differs from the pions response, this difference needs to be accounted for. The response of CASTOR has been investigated using test beams [105], which have a known energy. Muons were used to intercalibrate testmodules, electrons to determine the absolute scale, and pions to determine the non-compensation factor $R_{\pi/e}$. The latter⁷ was found to be $\approx 50\%$. The detector was found to possess a good linearity and energy resolution.

However, the intercalibration constants and absolute scale from the test beam cannot be used directly for the measurement of p+p events, since, besides ageing effects, the magnetic field affects the calorimeter in a non-trivial way. The state-of-the-art method implemented to calibrate CASTOR in-situ is based on an extrapolation in η of the energy measured by the HF calorimeter (a nearby calorimeter, see chapter 10).

For a sample of MinBias $\sqrt{s} = 7$ TeV p+p collisions the total energy deposit in the first five modules of CASTOR was measured simultaneously with the energy in HF. These modules contain $\approx 75\%$ of the hadronic energy deposit in CASTOR. The η -dependence of the total energy in HF was determined and corrected to the particle level. An extrapolation from the HF measurement to the CASTOR acceptance was made. The uncertainty in the extrapolation was determined using extrapolations of nine different event generators that were normalised to the HF measurement, see Fig. 45. The extrapolation of the HF data together with models yield an estimate of the mean incident energy on CASTOR and its uncertainty.

A correction factor was determined, to correct the measured MinBias data for the non-compensation and leakage effects of CASTOR w.r.t. a pure electron beam:

$$R_{\text{MinBias}/e} = \frac{\sum E_\gamma + 0.75 \sum E_h R_{\pi/e}(E_h)}{\sum E_\gamma + \sum E_h}. \quad (76)$$

In this equation $R_{\pi/e}(E_h)$ is the (energy-dependent) non-compensation factor that was determined from test beams. The different generators are also used to determine an uncertainty on the correction factor $R_{\text{MinBias}/e}$, which is $\approx 5\%$. After applying this correction to the energy measurement of CASTOR, the measurement was equated to the HF-extrapolated energy on particle level to establish the absolute calibration, which was found to be 0.016 GeV/fC . This value is compatible with the value of the test beam measurements. This study was

⁷ The non-compensation factor is energy dependent, and asymptotically converges to unity in the limit of a hadron with infinite energy

performed at 7 TeV p+p collisions and the energy scale was corrected to different run periods [106]. The overall uncertainty of the energy scale of CASTOR is currently 15%. The different contributions are listed in table 1.

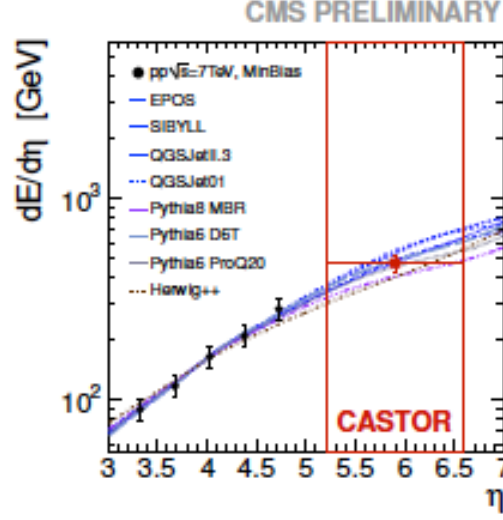


Figure 45: The energy deposit in HF with the model dependent extrapolations to the CASTOR acceptance [107]. The extrapolations were normalised to the HF measurement

Table 1: The various contributions to the systematical uncertainty in the energy scale of CASTOR.

Source of uncertainty	Value
HF energy scale	10%
Extrapolation and model dependence	10%
CASTOR non-compensation	5%
Total	15%

12.2.6 Simulation and validation

12.2.6.1 Simulation

The simulation of the CASTOR detector is fully incorporated in CMSSW, the software and simulation environment of the CMS experiment. In Fig. 46 we display a graph of the geometry of CASTOR in the simulation. The CASTOR halves can be moved independently in the simulation. The T2 telescope of the TOTEM experiment is located in front of CASTOR, and the LHC environment is displayed as well.

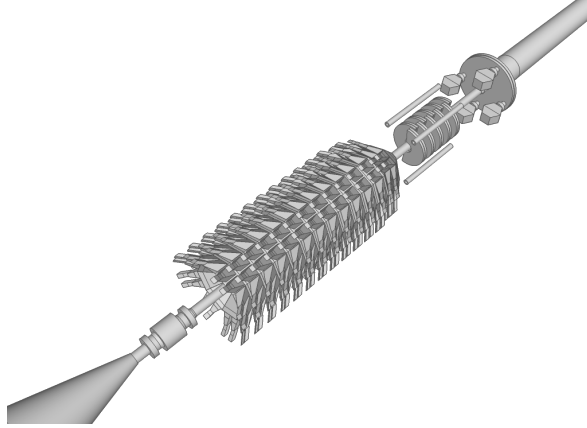


Figure 46: A visualisation of CASTOR in its installation location [5]. The T2 detector can be seen in front of the detector. The other materials belong to the LHC infrastructure

In the CMSSW framework, particles are propagated through the simulated detector volumes using GEANT4 [95]. The shower development inside the CASTOR volume, up to the generation of the Cherenkov photons in the sensitive volume, is also simulated by GEANT4. Thereafter, the number of photons is converted to a signal in fC in the PMT via analytical estimates. The simulation results match the longitudinal shower development in CASTOR well, but the overall energy deposit needs an additional correction factor though.

The propagation of particles through the CASTOR volume is rather time-consuming. For this purpose, a shower library was designed. The shower library essentially assigns an incident particle in a particular region of phase-space a certain energy deposit, taken randomly from earlier simulations in that particular phase-space region. Indeed, the shower library is maximally a factor 30 faster than a full simulation. Further, it is tuned and adjusted to the test beam data.

The shower library has a particular disadvantage though: the mapping between the incident particle and the specific region of phase space is currently only reliable when CASTOR is at its nominal position. Therefore, for the simulation of real physics events, for which the detector is displaced, the shower library is currently not suitable.

12.2.6.2 Validation

There are many distributions for which data and simulation can be compared to validate the simulation. Often the physics goals of the analysis determine which distributions are most relevant to look into. For a jet study the longitudinal shower development may be much more relevant than for a cross section measurement; for the latter the noise level correspondence between data and simulation on the other is hand very important.

We focus therefore on a comparison of the longitudinal and transversal profile of MinBias data and simulations for the 2015 $B = 0$ data, since these are very general results. For these data, all steps discussed above (improved noise study, gain correction factors, muon response analysis, and application and validation of the absolute scale) have been implemented to obtain the results. Moreover, in the absence of the magnetic field module six, seven, and eight

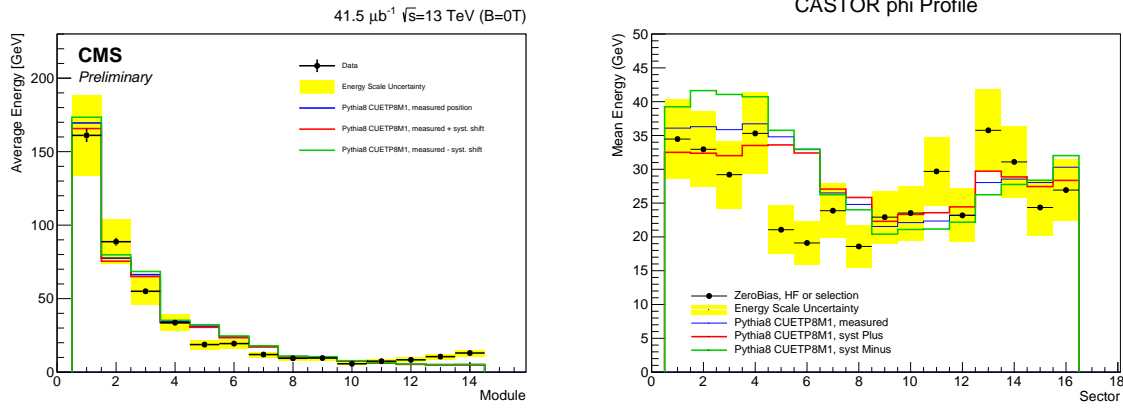


Figure 47: Profiles of MinBias p+p collision data with various event generators. Left: the z-profile of hadronic showers in CASTOR [108]. Right: the ϕ -profile [5]. The data were collected in 2015 at $B = 0$

could also be intercalibrated, which makes the longitudinal shape particularly interesting to study. Generally, the longitudinal shower shape is simulated consistently. For the last two modules, the intercalibration constants are clearly overestimated though. This is a consequence of the fact that these modules could not be incorporated into the online trigger. This problem could perhaps be circumvented by estimating the response of the channels via a fit or tuning procedure as in Fig. 47, instead of using the statistical average value.

We will display other validation results in the analysis chapter with an emphasis on jets, since these are more relevant to the particular analysis of this thesis.

12.3 SUMMARY AND OVERVIEW OF DATA-TAKING CAMPAIGNS

Various aspects of the performance of CASTOR during LHC Run II have been revised in this chapter. For most aspects of the performance, the uncertainties on the results have been proven to be not too large to extract physics conclusions from the data. The uncertainty on the energy scale however has proven prohibitive to draw physics conclusions for two studies of jets in CASTOR in p+p collisions at $\sqrt{s}=7$ and 13 TeV [109, 110]. Besides, preferably the energy scale would be fixed by a purely data-driven method, instead of the extrapolation used currently. Examples of a fully data-driven calibration are the reconstruction of the invariant mass of a known resonance or a jet balance study, in which one correlated a jet in CASTOR (with unknown p_T) to a central object with known kinematics. Such studies are notoriously difficult at CASTOR however.

A resonance study in the di-electron channel was pursued in the common CMS-TOTEM data set, constructing four-vectors from tracks in TOTEM and energy deposits in CASTOR. This study failed however, since the signal drowned in the π^0 background. Since no common simulation of CMS and TOTEM exist for this particular data set, a di-jet balance could not be pursued either. Such a study aims to minimise and quantise the residual data-simulation differences, for a review on the procedure we refer to the procedure applied to calibrate

central jets in CMS [111]. Evidently, a reliable simulation is needed for this in the first place. When the TOTEM tracker is not combined the simulation is accurate, but a CASTOR-only di-jet balance study is difficult due to the lack of η -resolution of CASTOR.

During LHC Run II CASTOR has successfully collected high-quality data for various collision configurations. The datasets and beam configurations are listed in table 2; for completeness the Run I campaigns have been listed also. One regrettable detail is, that CASTOR could only collect $\sqrt{s} = 13$ TeV data with the CMS magnet off. For all the data sets the offline corrections and constants have been determined, and the data are in a state ready for physics analyses. Furthermore, during LHC Run II CASTOR was equipped with a jet trigger, we refer to a conference report by the author for a brief review [112]. Thus, jet studies may exploit high-energy objects in CASTOR, which may be especially useful in studies correlating these jets to central objects. Furthermore, CASTOR managed to collect data at $\sqrt{s} = 5$ TeV for proton-proton, proton-lead, and lead-lead collisions, which allow for future nuclear modification studies.

A particularly interesting data set is the $\sqrt{s} = 5$ TeV p+p collisions data set. For these collisions, common data acquisition and trigger exchange with the TOTEM experiment was successfully realised, and one half of the T2 telescope located in front of CASTOR was functioning. In particular since TOTEM readout was forced by the CASTOR high-energy jet trigger, this data set allows for the construction of high-energy CASTOR-T2 jets. Also, for this data set, a common simulation likely is feasible, and first steps in this simulation direction have been taken already. The high-energy CASTOR-T2 jets may constitute the best chance to perform a data-driven calibration of at least one half of CASTOR.

These data are unique, since no other LHC experiment has such forward instrumentation, or is foreseeing this in its upgrades. Efforts are ongoing in a *CMS-legacy* project to store all data safely for future analysis endeavours.

The CASTOR data taking has up to the moment of writing resulted in published physics analyses on the forward underlying event [113], forward energy flow [114], and diffractive dissociative cross sections [49].

Table 2: Overview of the running periods of CASTOR during LHC Run I and II. The Run I proton-lead runs were taken with both the proton and ion towards CASTOR. For all Run II data sets, a high-energy jet trigger was active. The Run II proton-lead runs were only recorded in both directions at 8 TeV. The 13 TeV data set was recored at $B = 0$

year	centre-of-mass energy	colliding system
LHC Run I		
2009	0.9 TeV	proton-proton
2010	7 TeV	proton-proton
2011	7 TeV	proton-proton
2013	5.02 TeV	proton-lead
	2.76 TeV	proton-proton
	2.76 TeV	lead-lead
LHC Run I I		
2015	13 TeV	proton-proton
	5.02 TeV	proton-proton
	5.02 TeV	lead-lead
2016	5.02 TeV	proton-lead
	8 TeV	proton-lead

Part IV

DATA ANALYSIS

Essentially, Nature can serve saturation
as rare, medium, or well-done

In conversation with Krzysztof Kutak

The key objective of this part of the thesis is to address the hypothesis on gluon saturation. To this purpose, we will outline all the steps that are needed to analyse the inclusive CASTOR jet spectrum in $\sqrt{s} = 5$ TeV proton-lead collisions.

We start with outlining which data samples were used and how these were processed. This is followed by a description of the models for the event simulation and the simulation of the response of the CMS detector. Certain technical details, which are indispensable to render our final results reproducible but not directly relevant outside the CMS community, are included in an appendix⁸.

This is followed by a discussion on the event selection in chapter 15; an event selection has to be chosen carefully to comply optimally with the physics requirements of the analysis. Thereafter, the performance of the CASTOR detector during the specific data-taking period that is relevant to our analysis is introduced.

The next two chapters have a purpose in common, namely determining what the optimal jet radius for the detector and particle-level jets is. Therefore, we start with correlating jets on particle level to the underlying parton distribution in chapter 17. This does not only allow us to optimise the particle-jet radius, it allows us further to verify if forward low- p_T jets on particle level are correlated to the parton level at all. Since this is a pioneering study in this region of phase-space at the LHC, the latter needs to be examined prior to starting data analysis. This is followed by a chapter in which the jet radius for an optimal correlation between the particle-level jets and the CASTOR jets is examined. In this chapter we also outline how the jets are calibrated.

Subsequently, we proceed with motivating and reviewing the correction of the detector-level spectra to particle-level distributions in chapter 19. This procedure is described extensively for various reasons. Firstly, this procedure is challenging in particular for CASTOR jets, since CASTOR has no η -segmentation. Therefore, various cross checks are reviewed to obtain faith in the procedure.

Besides, a thorough review is necessary to understand the systematic uncertainty due to the correction in the final result, which is the dominant uncertainty in one of our final results. Thereafter, the various sources of systematic uncertainty that propagate in the final results are presented in chapter 21. Penultimately, the final results are presented. We interpret the results and conclude on the hypotheses in chapter 22, and reflect on the resulting implications. We finish with a concise summary of the thesis in English and Dutch.

8 This thesis has been requested as reference document by a research group working on CASTOR jet analyses

In this section the run selection and reconstruction of the proton-lead collision data are described, delivered to CMS at a centre-of-mass energy of $\sqrt{s_{NN}} = 5.02$ GeV in 2013. Throughout this document we will refer with p+Pb to collisions with the proton towards CASTOR, while Pb+p is for the reverse beam configuration.

The data of the HLT paths relevant for this analysis, which are defined in section 15, were streamed to a MinbiasUPC¹ dataset.

This dataset was processed with the reconstruction software of CMSSW. The correct CMSSW version and usage of a global tag guarantees that realistic conditions are used together with consistent reconstruction algorithms. The beams were delivered to CMS with 50 ns bunch spacing. Thus, the leakage of signal of CASTOR from a particular time slice in the next one is not affecting these data.

A subset of all runs is analysed for which the performance of CASTOR was already validated in [103]. The run numbers, together with their integrated luminosity and peak pileup, are given in appendix A.5.1. The peak pileup in these runs is 7.63%. We will show in chapter 20 that, if the data are analysed with an appropriate event selection, the pileup does not affect our results.

These runs were processed with the official golden JSON file² to select the correct luminosity sections.

The effective luminosity, in which the trigger prescale information was taken into account, was calculated. The final values for the effective integrated luminosities analysed in this thesis are 0.989 and 4.044 nb⁻¹ for p+Pb and Pb+p, respectively.

¹ UPC is an abbreviation for ultra-peripheral events. These are events in which the transversal distance between the hadrons is large w.r.t. the nucleus radius, and the participating hadrons do not split up

² The golden JSON file contains only luminosity sections for which all subsystems of CMS were operating adequately

There are two main objectives for simulating proton-lead collisions. Firstly, the data need to be corrected from the detector level to the particle level; the motivation and procedure are extensively reviewed in chapter 19. To this purposes, and to be able to assign a systematic uncertainty to the procedure, collisions are generated with three general-purpose event generators. Subsequently, the response of the detector to these collisions is simulated in the CMSSW framework. With general-purpose event generators is meant, that the results are supposed to be reasonably reliable in the phase-space where CMS can measure radiation (as opposed to certain models that are specifically designed to study physics in the forward region).

Another reason for simulating events is the physics interpretation of the final results. This purpose can also be subdivided still. One purpose is to verify if the event generators are consistent with the data, and if we can discriminate between the different physics assumptions upon which these are based. A measurement may also allow for a retuning of the event generators; for a variety of purposes, it is extremely important that these event simulations describe the data well.

Besides of comparing the predictions of the general-purpose generators to the data, we will generate predictions using two particular models that incorporate the rcBK equation. These models are dedicatedly targeted at interpreting the data in terms of non-linear QCD. Their predictions are of cardinal importance for addressing the central hypothesis of this thesis. We will not use these models to correct the data though, and therefore also not simulate the detector response to the events.

We start with describing the general-purpose event generators. This is followed by the specific rcBK-based models. We finish by quoting the sizes of the event samples and the cross sections of the generators.

14.1 GENERAL-PURPOSE EVENT GENERATORS

Events were generated with three general-purpose event generators: EPOS-LHC [115], HIJING [116], and QGSJETII-04 [117]. These generators do not include photon-induced events, and further HIJING does not include diffractive events. In chapter 15 we describe why and how such events are effectively suppressed in our analysis. Therefore, at this point there is no need for concern that photon-induced events are not included in our set of generators.

The CPU time needed to simulate events with a general-purpose event generator is generally negligible w.r.t. the time needed to simulate the response of the CMS detector to these events. For the latter, the computations were distributed and performed on the [WLCG](#), which is a worldwide network of computer clusters for data analysis and storage, and event simulation.

The response of the CMS detector was simulated using the CMSSW software. Simulation conditions that match the experimental conditions were implemented via a suitable global tag. Further, the alignment of CASTOR, and its pedestal and noise values were also adapted to the data-taking conditions. For technical details we refer to appendix A.5.2. The simulation of the response of CASTOR was performed with the GEANT4 full simulation configuration, which we refer to as Fullsim. To accommodate for the alignment uncertainty simulations were performed with CASTOR shifted maximally inwards and outwards with respect to the beampipe. The details are given in section 16.

14.1.1.1 Models based on Regge-Gribov theory

The EPOS-LHC and QGSJETII-04 event generators were partially designed to "bridge the gap" between collider and cosmic-ray physics¹, by simultaneously providing descriptions for both event classes. Both models, which we discuss below, are based on RGT.

14.1.1.1.1 EPOS-LHC

EPOS-LHC is a particular version of EPOS that was tuned to LHC data and released in 2014. EPOS is an acronym for:

- Energy conserving quantum mechanical multiple scattering approach, based on
- Partons and parton ladders
- Off-shell remnants
- Splitting of gluon ladders

A key feature of EPOS-LHC is that energy sharing and conservation is imposed on the multiple interactions, instead of considering these as independent. The interactions are split in hard and soft processes.

The soft interactions are modelled via Pomeron exchange. Hard interactions are modelled as the convolution of a soft pre-evolution, a DGLAP-based hard evolution, and standard leading order $2 \rightarrow 2$ QCD matrix elements. Saturation is envisaged to be caused by Pomeron-Pomeron self interactions, which lead to a modification of the x -dependence of the Pomeron amplitudes. However, it has been anticipated that this procedure overestimates the effects [119], and efforts are ongoing to develop a new version of EPOS. An interaction is schematically depicted in Fig. 48.

The parton ladders deposit their energy mainly in the central region of the detector, while the remnants rather fragment in the forward region. Hadronisation is implemented similarly to the LUND string model. Collective behaviour is implemented for high-density regions in the collision. The option exist to simulate a quark-gluon plasma (QGP) for phase-space

¹ Cosmic-ray events are interactions in the earth atmosphere between ultra-high energetic cosmic hadrons and (heavy) nuclei from the atmosphere. Due to the extremely high energies of the incident particles, ranging up to 10^{12} GeV, these events cannot be modelled with regular event generators for LHC energies such as PYTHIA [118]

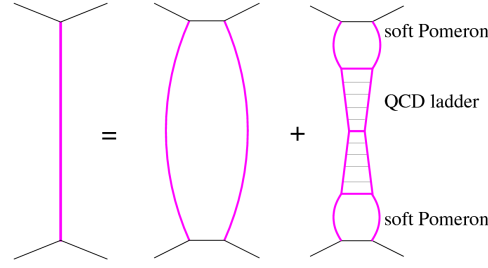


Figure 48: A schematic description of the modelling of soft and hard interactions in RGT-based models [120]

regions with a high energy density, together with a hydrodynamical model is implemented to evolve the QGP. Per default this option is not enabled however, since the time to generate a single event is approximately one day.

The differential cross section as a function of the diffractive mass follows $d\sigma/dM \propto 1/M^{2\alpha_{\text{diff}}}$, with $\alpha_{\text{diff}} = 1.05$.

14.1.1.2 QGSJETII-04

In QGSJETII-04 the hard and soft interactions are modelled similarly to EPOS-LHC. Pomeron self-interactions are included in QGSJETII-04, which accommodate for non-linear effects. Thereby, in QGSJETII-04 the effects of saturation and shadowing are encompassed in a self-consistent manner.

Similar to EPOS-LHC, the differential cross section as a function of the diffractive mass follows $d\sigma/dM \propto 1/M$. A QGP is not modelled.

14.1.2 HIJING

The HIJING event generator is based on collinear factorisation. It models its hard-QCD interactions via PYTHIA [118], which performs its parton evolution via DGLAP equations. The soft interactions are modelled via the Lund FRITIOF [121] and Dual Parton [122] model.

HIJING incorporates gluon shadowing, as outlined in chapter 6, via a modification of the nuclear pdf. Multiple interactions are modelled using a Glauber geometry (we refer to the literature on HIJING [116]). To correctly estimate the suppression as function of x , measurements of the nuclear modification of sea quark structure functions at moderate x are parameterised and fitted as function of the number of nucleons in the nucleus and x . The gluon nuclear modification at lower x values is obtained from an extrapolation of this function [123–125]; it is assumed that the shadowing effect for the gluons is the same as for the sea quarks. For other nuclear effects that were taken into consideration, for example the radial dependence of the shadowing effect, we refer to the paper [116] describing HIJING. The measurements of the nuclear modification and the fitted function is displayed in Fig. 49. We used HIJING version 1.383.

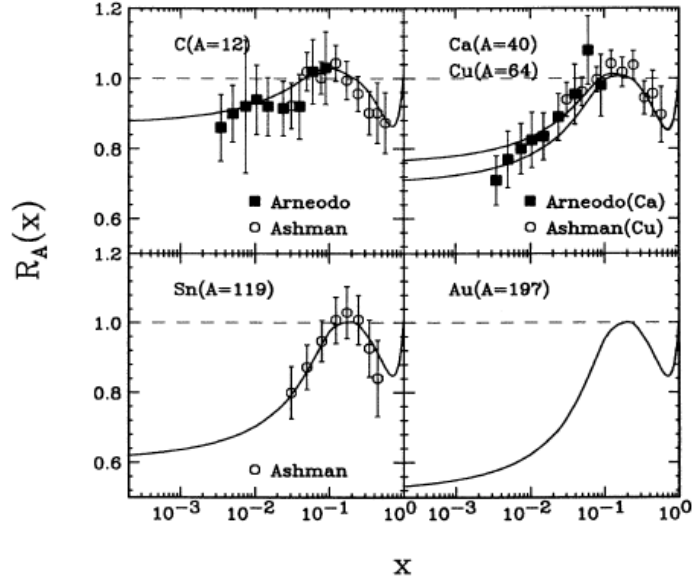


Figure 49: Nuclear modification of structure function from nuclear DIS data used by HIJING [126, 127]

14.2 HYBRID-FACTORISATION MODELS

We explained in chapter 5, that k_T -factorisation is expected to describe the interactions of the low- x content of hadrons. Here a brief note on nomenclature is in place though. Interactions in which two low- x partons participate (described by two updfs) is named k_T -factorisation (also called high-energy factorisation). The interactions of two soft partons usually leads to central production.

Forward processes are generally due to the interaction of a hard parton of hadron A with a soft parton of hadron B. The latter is here assumed to be a gluon. Hybrid factorisation is a specific factorisation scheme to generate analytical predictions for these processes [128, 129]. In hybrid factorisation the hard partons of hadron A are treated in the collinear framework and evolved using the DGLAP equations. The soft, off-shell gluons of hadron B are modelled using an unintegrated pdf that is evolved (for the models under consideration) by the rcBK equation.

The hybrid model is well-suited to generate predictions for p+Pb collisions (with the proton towards CASTOR), since for this beam configuration the dense regime of soft gluons of the heavy ion, where the non-linear QCD-effects are expected to be strongest, can be described with a updf and evolved using k_T -factorisation.

The reverse (Pb+p) is also possible, but we will see later that for this configuration the large underlying event and ion debris that is incident on CASTOR make such a study not very beneficial; we will elaborate this point later. Therefore, for the hybrid model predictions we will focus on p+Pb exclusively. We discuss two specific hybrid factorisation models below.

14.2.1 Hybrid factorisation with the Kutak-Sapeta unintegrated pdf

In the KS implementation of the hybrid model the cross section for $2 \rightarrow 1$ parton scattering is implemented as:

$$\frac{d\sigma}{dydp_T} = \frac{1}{2} \frac{\pi p_T}{(x_1 x_2 s)^2} \left[\sum_{q(\bar{q})} |\mathcal{M}_{g^* q(\bar{q}) \rightarrow q(\bar{q})}|^2 x_1 f_{q(\bar{q})/A}(x_1, \mu^2) \mathcal{F}_{g^*/B}^F(x_2, p_T^2, \mu^2) + |\mathcal{M}_{g^* g \rightarrow g}|^2 x_1 g_{g/A}(x_1, \mu^2) \mathcal{F}_{g^*/B}^A(x_2, p_T^2, \mu^2) \right]. \quad (77)$$

A concise introduction may be found in [130] and references therein.

In this equation f and g are the collinear quark and gluon pdfs for the hard partons. \mathcal{F}^F and \mathcal{F}^A are the unintegrated gluon distributions in the fundamental and adjoint representation, respectively. These were parameterised as a function of x at a scale k_0 . The parameters of the function were determined from fits to e+p data [30]. For the linear-QCD scenario a gluon density is implemented that follows from the extended BFKL equation [47, 48, 131], while for the non-linear case a BK gluon density [30, 132, 133] is used. For the collinear pdf the CTEQ10 NLO set was used [134]. We already displayed the difference between the linear and non-linear pdf previously in Fig. 13.

For our studies we need an unintegrated lead gluon distribution though. This was obtained by scaling the gluon density with a factor A (which is 208), and multiplying the non-linear term in the evolution equation by a factor $A^{1/3}$ (as motivated in section 5.3). We display the heavy-ion gluon pdf in Fig. 50².

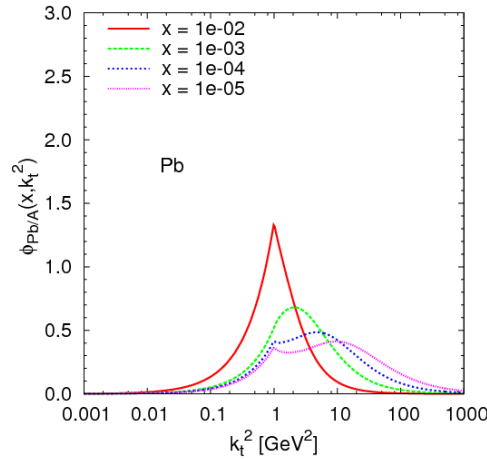


Figure 50: The nuclear updf as determined by Kutak-Sapeta [30]

² It is reassuring to compare the nuclear updf to the proton updf in Fig. 13, since we observe that indeed the nuclear saturation scale is enhanced for the nucleus

The matrix elements for the interaction of the off-shell gluons were modelled in KATIE [135], and hadronisation was modelled in CASCADE [136]³

The inclusive jet spectrum as function of the jet energy may be obtained from this equation as:

$$\frac{d\sigma}{dE} = \int_{y_{\min}}^{y_{\max}} dy \frac{d\sigma}{dy dp_T} \frac{1}{\cosh(y)}. \quad (78)$$

It should be noted that multi-parton interactions are currently not implemented in this model. Thereby, to a certain extend, this model is better suited to describe the leading particle jet spectrum instead of the inclusive jet spectrum.

A particularly relevant advantage and key motivation for this method is that in one framework consistent predictions can be generated using linear and non-linear QCD. Thereby the KS implementation of the hybrid model provides a mechanism to study the isolated effect of non-linear QCD on the forward single-inclusive jet spectra.

14.2.2 Hybrid factorisation in the AAMQS framework

The approach followed by the AAMQS collaboration to implement hybrid factorisation differs on various points from the KS implementation.

Firstly, as initial condition the dipole scattering amplitude was parameterised as a function of the dipole radius r at a certain initial value x_0 . In coordinate space the amplitude is given by:

$$N(r, x = x_0) = 1 - \exp \left[- \frac{(r^2 Q_{s,0}^2)^\gamma}{4} \ln \left(\frac{1}{r\lambda} + e \right) \right]. \quad (79)$$

We can relate the amplitude in coordinate space to the updf by a Fourier transform:

$$N(x, k_T) = \int d^2\vec{r} e^{-i\vec{k}\cdot\vec{r}} [1 - N(x, r)] \quad (80)$$

The amplitude was calculated to leading order in this framework. To obtain the nuclear pdf from the proton pdf the saturation scale is modified by the nuclear oomph factor. For the collinear pdf the CTEQ6 LO set was taken [137].

In this thesis we will study the MV (McLerran-Venugopalan) and the AAMQS initial conditions. The parameters of both sets were fitted to HERA data [65], and yielded a reduced $\chi^2 < 1.1$. In the MV model the anomalous dimension γ is simply set to one, while for the AAMQS parameterisation γ is a free parameter instead. Two slightly different parameterisations of the gluon distribution (labeled $g'01$ and $g'19$) are also used. The parameter γ controls the slope of the spectra, and $g'01$ is expected to have a slightly harder spectrum than $g'19$. Simultaneously, the $g'01$ fit has a 7% lower saturation scale $Q_{s,0}^2$ w.r.t. $g'19$. For the MV model γ equals 1 and the saturation scale is approx. 20% higher than in the AAMQS parameterisations.

³ Initial-state radiation is absorbed into the definition of the pdf in this setup. An initial investigation into the effect of final-state radiative corrections suggested that this effect plays a minor role at the low- p_T observables that are studied here

The equation for quark or gluon production in the hybrid framework is then given by:

$$\frac{d\sigma^{h_1 h_2 \rightarrow (q/g)X}}{dy d^2k} = \frac{K}{(2\pi)^2} \frac{\sigma_0}{2} x_1 f_{(q/g),h_1}(x, \mu^2) N_{(F/A),h_2}(x_2, k_T), \quad (81)$$

in which $f_{(q/g),h_1}(x, \mu^2)$ is the collinear pdf of quarks or gluon in hadron h_1 . The updf for hadron h_2 , $N_{(F/A),h_2}(x_2, k_T)$, is either in the adjoint (A, for gluons) or fundamental (F, for quarks) representation. The factor σ_0 comes from the implicit integration over the impact parameter; it carries the meaning of the transversal size of the hadron. The K -factor does not represent any calculations; it is just added to correct for higher-order and non-perturbative effects, and ideally it equals one. The evolution is performed using the rcBK kernel. Initial and final-state radiation are generated via the DGLAP equations in the evolution.

In the simulation multi-parton interactions were also taken into account. The hadronisation was performed via Lund string fragmentation as embedded in `PYTHIA`. A more detailed description of the event simulation may be found at [77].

Summarising, the KS implementation does not take multi-parton interactions into account, but has as advantage that the isolated effect of the non-linear term can be studied consistently. The AAMQS predictions can only be studied for non-linear parton evolution, but many effects have been included and the model has successfully described LHC p+Pb data. Thereby, we have two different, and rather orthogonal implementations of the hybrid factorisation model at our disposal to interpret the data and address the thesis hypothesis.

14.3 SIZES OF THE EVENT SAMPLES

The sizes and a few other characteristic properties of the event samples are listed in table 3, together with the respective cross sections of the generators. For the general-purpose event generators the cross sections were calculated using the CRMC package [138], while for the hybrid model these were calculated using `KATIE`. For the AAMQS models the measured proton-lead production cross section was used as determined by CMS [103].

Table 3: Event generators used in this analysis, together with the number of events generated and cross sections. With measured, inwards, and outwards position the position of CASTOR w.r.t. the beam pipe is indicated; the uncertainties are depicted in table 4. We observe that the cross sections for models simulated with KATIE are quite different from the other models. This is due to the fact that these cross sections do not denote the total proton-lead cross section (which is deployed to normalise the AAMQS predictions), but instead the cross section for the particular partonic interaction

Generator	N. evts. generated p+Pb	N. evts. generated Pb+p	σ (mb)
HIJING measured pos.	807436	848185	1811.90
HIJING inwards pos.	813520	757613	1811.90
HIJING outward pos.	812843	756143	1811.90
EPOS-LHC measured pos.	4157611	745213	2069.16
EPOS-LHC inwards pos.	813995	848112	2069.16
EPOS-LHC outward pos.	835886	889283	2069.16
QGSJETII-04 measured pos.	3257874	1513702	2191.03
QGSJETII-04 inwards pos.	3144576	1513702	2191.03
QGSJETII-04 outward pos.	2830911	1420771	2191.03
Kutak-Sapeta Linear	$3.4 \cdot 10^7$	-	11918.40
Kutak-Sapeta Nonlinear	$3.6 \cdot 10^7$	-	842.40
AAMQS g'_{01}	10^5	-	2061
AAMQS g'_{19}	10^5	-	2061
AAMQS MV	10^5	-	2061

We start this section with reviewing the physics requirements on our event selection. Thereafter, event selection parameters are defined that match these requirements optimally, and the agreement between data and simulation of these parameters is assessed. We conclude with summarising the selection parameters and their values.

This analysis aims to study forward jet production due to hard-parton interactions, which occur in non-diffractive hadronic collisions. In these interactions the incoming hadrons break up, and this allows for a relatively uncomplicated event selection.

However, in p+Pb collisions other processes also occur. The total p+Pb cross section consists for approx. 5% of photon-induced events. These are events in which the ion elastically emits a photon; the cross section for this process in p+Pb is approx. a factor 200 higher than in p+p collisions due to the large Coulomb charge of the nucleus. Furthermore, diffractive collisions also occur in p+Pb collisions. The aim of our event selection is, amongst others, to suppress the contribution of these interactions.

Another important constraint on the event selection is the size of the resulting event sample. Since CASTOR was not equipped with a jet trigger during the 2013 p+Pb data taking¹, the jet spectrum must be obtained from a zero or minimum-bias ([minbias](#)) event sample. Therefore, the maximal jet energy achievable in this analysis is limited by the sizes of the event samples.

15.1 ONLINE EVENT SELECTION

We choose the ZeroBias+PixelTrack HLT path for this analysis. This path is fed by an L1 zero-bias bit (which triggers on beam presence in CMS, as explained in chapter 10). Thereafter, the HLT path selects events that have minimally one pixel track with momentum above 0.4 GeV in the central tracker. This HLT path was chosen since it has a relatively low (luminosity-independent) overall prescale (3329) and is biased to hadronic non-diffractive events due to the pixel track requirement.

15.2 OFFLINE EVENT SELECTION

An offline event selection to effectively suppress photon-induced and diffractive events was constructed in a study on the inelastic cross section of proton-lead collisions at CMS [103]. In this study photon-induced events generated by STARLIGHT [139] were analysed, and a p+Pb event sample containing diffractive events generated by EPOS-LHC. An HF-AND selection was evaluated by requiring minimally one HF tower on the plus and minus side to be above a 4 GeV threshold. This selection suppressed the fraction of photon-induced

¹ During the 2016 p+Pb data taking at $\sqrt{s} = 5$ and 8 TeV a CASTOR jet trigger was successfully deployed

events to approx. $5 \cdot 10^{-5}$. After the HF-AND selection the EPOS-LHC sample contained 1.1% single-diffractive, 1.8% double-diffractive, and 0.5% central-diffractive events.

Since we use the same data set as the data set used in the inelastic cross section analysis [103], we adopt their event selection criteria. The residual effects from diffractive and photon-induced events can be expected to be very small w.r.t. the overall systematic uncertainty (which is minimally $\approx 20\%$).

In our analysis we apply the event selection to real and simulated events. It is therefore very important that there is good agreement between data and simulation in the distributions that we cut on. In Fig. 51 upper plots the HF-tower energy distribution is displayed for data and various event simulations, for events selected solely with the HLT ZeroBias+PixelTrack. We observe that from a cutoff of approx. 3 GeV onwards data and simulation are in good agreement. This allows us to deploy the HF-AND selection in this analysis.

Event pileup is not taken into account in the simulation. Although the peak pileup of the data runs selected is relatively low (maximally 7.63%), the effects must be minimised and assessed.

To mitigate the effects of pileup, we put a constraint on the number of vertices, which are constructed from tracks. Therefore, in Fig. 51 middle we first compare the p_T and p_Z distributions of the tracks. We observe good agreement between data and simulation, and thus we may place cuts on the vertex distributions.

In Fig. 51 lower plot the number of good primary vertices (GPV) per event in data and simulated events is displayed². In data and simulation events with up to five and four GPVs are present, respectively. The agreement between data and simulation is reasonable. Since the simulated events do not contain event pileup, we conclude that the additional vertices in simulation are due to vertex misidentification.

To minimise the effect of pileup in data only events with maximally one GPV are selected. It should be noted that no constraints are put on the number of vertices that do not survive the selection criteria for a GPV. In chapter 20 we will demonstrate that after our event selection the final result is independent of the instantaneous luminosity, and thus that event pileup is effectively mitigated. Furthermore, in section 19 we illustrate why this vertex requirement is preferred over, for example, exclusively demanding one GPV, in spite of the online demand of minimally one good pixel track. These vertex requirements are similar to the selections that were made for the CASTOR jet analysis at 7 TeV p+p collisions [109].

In addition, events are filtered by applying a no-beam-scraping filter. Upstream of the interaction point occasionally interactions occur between beam particles and the beampipe, and beam-gas interactions take place due to gas ions polluting the LHC vacuum; these events are removed by the filter.

The efficiency of the HLT ZeroBias+PixelTrack path w.r.t. our offline selection was evaluated by studying the occurrence of the path in a pure zerobias event sample to which the offline selection criteria were applied. The efficiency was found to be 100 and 99% in data and simulation, respectively. This effect is very small w.r.t. other sources of systematic uncertainty, and not further taken into consideration.

² A GPV is a vertex which is not fake, has minimally four degrees of freedom, the z-coordinate must be within 15 cm of the CMS centre, and the distance in the transversal plane w.r.t. the CMS centre cannot exceed 2 cm

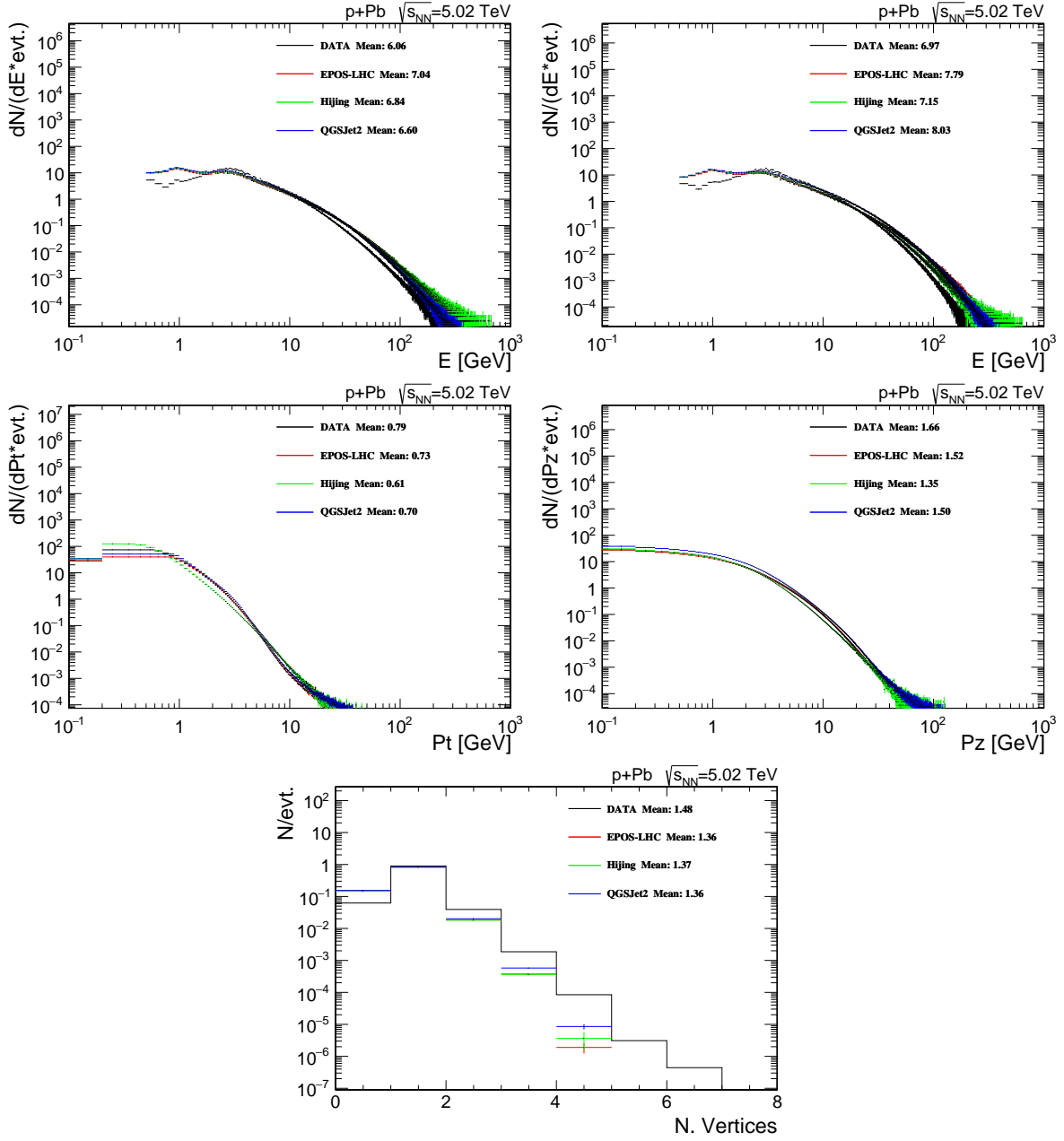


Figure 51: Distributions of observables used for the offline event selection for ZB+PixelTrack events in data and simulation. Top: the energy distribution in HF-calotowers. Middle: the p_T and p_z distribution of tracks. Bottom: the number of GPVs in data and simulation

15.3 SUMMARY OF THE EVENT SELECTION

Summarising, we select events online with the ZeroBias+PixelTrack HLT path. Offline these are subsequently filtered on beam-scraping events. An HF-AND requirement is imposed with a tower threshold of 4 GeV, and maximally one GPV is allowed.

This event selection complies with the various demands outlined, and we can consistently apply the selection to real and simulated events.

In this chapter we briefly discuss the performance of CASTOR during the 2013 p+Pb data taking campaign. We focus non-exhaustively on the specific elements that are relevant to the systematic uncertainty of our jet analysis; for a broader overview we refer to chapter 12.

16.1 ALIGNMENT

The general alignment procedure has been outlined in section 12.2.1. For the 2013 p+Pb data taking period, a method was available in addition to the survey and position sensor procedure to obtain the alignment of CASTOR, since common data taking with the TOTEM experiment [140] was achieved.

The T2 telescope of TOTEM is located in front of CASTOR. By extrapolating T2 tracks to CASTOR and correlating these with isolated EM energy deposits the in-situ position of CASTOR was determined by an independent method [141]. The graph with the location of incidence of the extrapolated TOTEM tracks is depicted in Fig. 52 (left). This method is only available when common data-taking is possible, which in practice is rather exceptional.

The final positions of the two CASTOR halves were determined by combining the T2 measurement with the global fit to the survey and position sensor data. The numbers with their uncertainties are given in table 4. It should be noted that the halves do not overlap when both halves are shifted towards the beam-pipe within their uncertainty (which is not necessarily true for other CASTOR data taking campaigns). This allows to shift the CASTOR halves inwards and outwards w.r.t. the beam-pipe in simulations to evaluate the maximal systematic uncertainty due to the alignment.

Table 4: The position of CASTOR during the 2013 p+Pb data taking with the systematic uncertainty. The values are given in mm. The position is quoted w.r.t. the nominal position of CASTOR that is defined as (0.0)

Coordinate	Value	Uncertainty
NEAR half		
x	13.87	2.02
y	-8.09	3.73
FAR half		
x	-5.18	2.34
y	-4.17	3.61

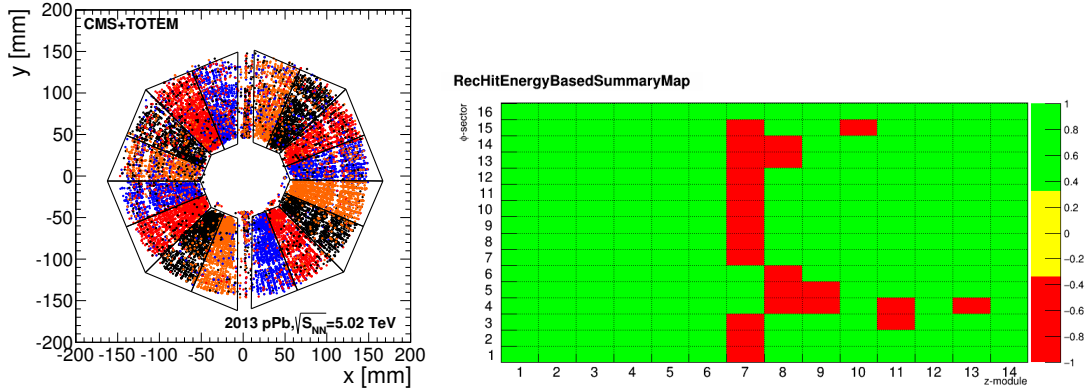


Figure 52: Left: a "tomography" of CASTOR, using the correlation between isolated EM electron tracks in the TOTEM tracker and isolated EM energy deposits in the EM sections of CASTOR [141]. Right: the map of the bad channels of CASTOR (in red) during the 2013 data-taking campaign [98]

16.2 BAD CHANNELS

During the 2013 data taking CASTOR had only bad channels in module 7, 8 and higher. A map of the channels of CASTOR is depicted in Fig. 52 (right). Despite of the fine-mesh PMTs the channels located in module 7 and 8 are strongly affected by the magnetic field of CMS and not used. Since the majority of the energy of the showers is contained in the front (defined as the first 5 channels), the bad channels generally play a minor role in the 2013 data taking. The bad channels are masked in both data and simulation.

16.3 SUMMARY

It is worth to point out that the 2013 p+Pb data set is qualitatively one of the best data sets recorded with CASTOR. There are no bad channels in the front which is very opportune for various physics analyses. The alignment is relatively well understood and cross checked by the T2 measurement; the successful combination of CASTOR-T2 data combination has established itself in this campaign. Regrettably, since no common simulation was available in CMSSW version 5, a combined CASTOR-T2 physics analysis has not yet been achieved, but from the data perspective there appear to be no obstacles.

17.1 INTRODUCTION

We pointed out previously that no publication exists for jets in hadronic collisions in this very forward phase space. In this section we investigate the correlation between the particle-level jets and the underlying parton-level jets. If such a correlation does not exist in the p_T region assessable in data, a study of forward jets may not allow us to investigate the thesis hypothesis. Therefore, we determine if there is a p_T cutoff from which value onwards the parton level distribution is correlated to the particle level, and optimise the correlation w.r.t. the particle jet radius (for this particular study we may work as well with correlations in p_T instead of energy). It is crucial to investigate these questions and optimise the parameter-space *prior* to unfolding the data, since the latter is a rather complex and labour-intensive operation. Also, the cutoff is necessary to interpret the final results.

We start with specifying the event generator that we used for this study, discuss the definition of the particle and parton level that we adopt, and explain the event selection. In the results section we display distributions on the spatial and p_T correlation and state the key numbers we obtained. Finally, we conclude on the optimal particle jet radius.

17.2 EVENT GENERATION AND SELECTION, AND JET COLLECTIONS

We generated and analysed one million PYTHIA8 [142] p+p events with $\sqrt{s} = 5.02$ TeV. The CMS Pythia8-4c tune [143] was applied. To enrich the sample we imposed $10 \leq \hat{p}_T \leq 30$. The event scale \hat{p}_T denotes the p_T exchange of the hardest parton interaction of the collision.

We define the particle level as all particles that have no subsequent decay vertex anymore. The partons are defined as all outgoing particles of a subprocess, just before the hadronisation sets in¹. This allows us to define the following jet collections:

- **Particle jets:** we cluster all particles in the event using the anti- k_T clustering algorithm [144]. We select all particle jets that have their jet-axis in the CASTOR acceptance ($-6.6 < \eta < -5.2$)
- **Parton jets:** we cluster all partons in the event using the anti- k_T algorithm. We select parton jets that have their jet-axis in CASTOR

We can pick various radii for the anti- k_T jet with radius R ($ak(R)$). We investigate the sensitivity of the correlations by picking $R = 0.3, 0.5$, and 0.7 (it may be instructive to observe that partons can be thought of as parton jets in the limit of $R \rightarrow 0$).

We select events by cutting on the p_T of the particle jet collection. We only accept events with a single particle jet above the p_T cutoff. We apply p_T cutoffs of 1, 3, and 5 GeV.

¹ This is accommodated by checking whether the particle is a parton and has PYTHIA8 status flag 62 or 63 activated

Thereafter, we correlate the particle jet to our final parton jet collection. In this correlation study we will refer to the object above the cutoff as the leading object for brevity (but we implicitly mean that the object is leading only in the Castor acceptance, and we additionally demand that it is the only object above the cutoff).

17.3 RESULTS

We first inspect results on the spatial correlation. We define the distance $\Delta R(\phi, \eta)$ between a particle and parton jet as:

$$\Delta R(\phi, \eta) = \sqrt{\Delta \eta^2 + \Delta \phi^2}. \quad (82)$$

In Fig. 53 the distributions of $\Delta R(\phi, \eta)$ for the leading particle jet with all parton jets are displayed.

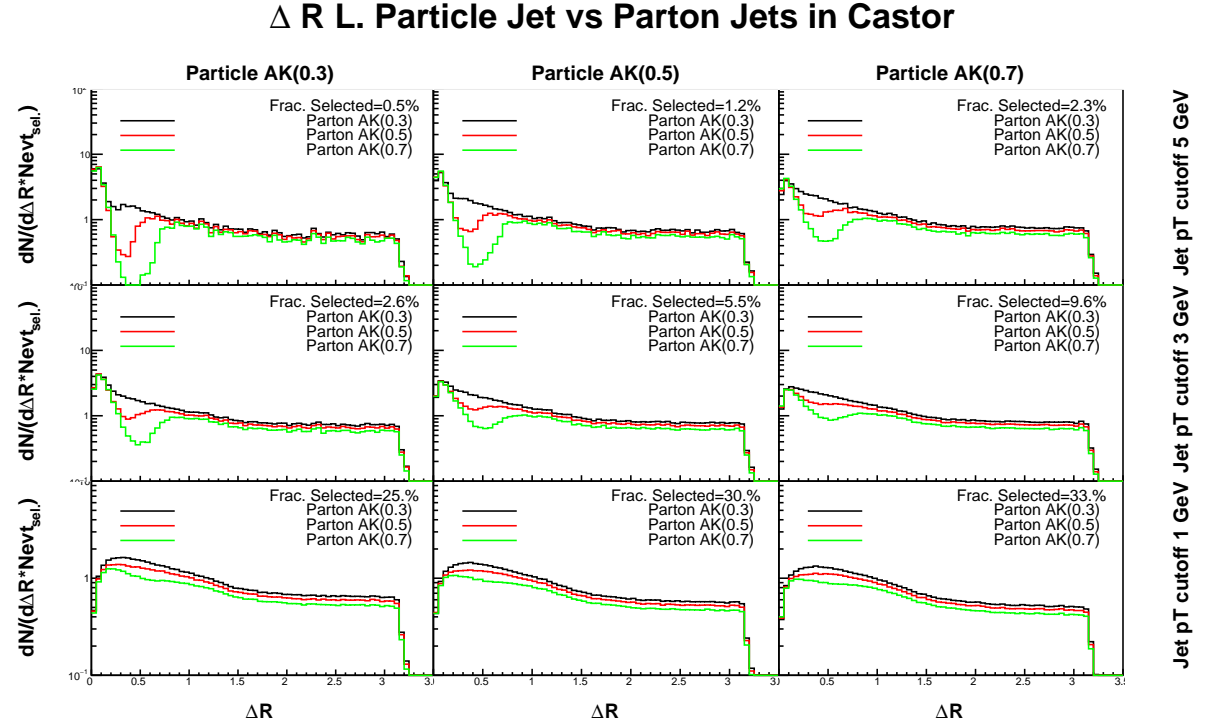


Figure 53: The ΔR distribution of the leading particle jet with all parton jets as function of the particle jet p_T cutoff for various combinations of jet radii. The fraction of events passing the p_T cutoff is also displayed

Before interpreting the graphs, let us briefly consider how the ΔR distribution of two completely uncorrelated parton and particle jet collections would look like. For such distributions $\Delta \phi$ would look flat on its domain. The domain of $\Delta \eta$ is restricted to $0 \leq \Delta R \leq 1.4$ (with its minimum at 1.4). Further, one can expect the distribution to fall off around $\Delta R = 0$ due to the boundary of the jet area. Only one parton jet can be located in the vicinity of the particle jet while multiple jets may be located at larger values of ΔR .

In Fig. 53 we note that for a p_T cutoff of 1 GeV the ΔR distribution is approx. flat from $\Delta R=1.4$ onwards, while for smaller ΔR the distribution rises. The distributions drop for ΔR small w.r.t. the jet radius. Thus, we conclude that for a p_T cutoff of 1 GeV the parton jets are not correlated to the particle jets.

For a p_T cutoff of 3 GeV onwards we observe a peak (instead of a dip) at $\Delta R = 0$. Further, we observe that the jet area around $\Delta R = 0$ stays depopulated. This is again an effect of the parton jet area and its boundary (and since the distributions are correlated now the effect is more pronounced than for the p_T cutoff of 1 GeV). We conclude that the particle jets are spatially correlated with the parton-jet distribution. The correlation increases progressively with the p_T cutoff.

Particle jets with a small radius that are selected with the same p_T cutoff as jets with a large radius lead to effectively harder objects (which may also be inferred from the fraction of events that pass the cutoff). This explains why these jets possess a stronger correlation.

We continue with investigating the energy and p_T correlation. We would like to correlate the p_T of the leading particle jet to the closest parton jet, but simultaneously veto on events for which the jets lie too far apart. From Fig. 53 we conclude that a tight jet matching criterium would be $R_{cut} = 0.1$, while $R_{cut} = 0.25$ would suffice as a loose criterium.

We define (the relative) Δp_T and ΔE as:

$$\Delta p_T = \frac{p_T^{\text{partonjet}} - p_T^{\text{particlejet}}}{p_T^{\text{particlejet}}}; \quad \Delta E = \frac{E^{\text{partonjet}} - E^{\text{particlejet}}}{E^{\text{particlejet}}}. \quad (83)$$

In Fig. 54 we depict Δp_T for the leading particle jet for the tight matching criterium. The shapes look, as expected, approximately Gaussian, and the dependence on the jet radii matches geometrical expectations. The symmetry of the Gaussians is approximately best for equal parton and particle jet radii.

In Fig. 55 we display the width of the p_T distributions of Fig. 54, which can be thought of as a relative resolution ρ . Despite the fact that jets with a small radius correspond to effectively harder objects, the p_T correlation is best for $R_{jet} \geq 0.5$ (for both the particle and parton jet radii). In Fig. 56 we depict the same distribution for the energy of the particle and parton jets, for which analogue conclusions hold.

In table 5 various key numbers are summarised as a reference for both the loose and tight matching criterium. As expected, there is a trade-off between these criteria: the resolution deteriorates for the loose selection, while we obtain a larger fraction of correlated events.

Particle jet cut	$\rho p_T(t)$	$\rho E(t)$	$\rho p_T(l)$	$\rho E(l)$	% Sel.	% Cor.(t)	% Cor.(l)	$N_{Const.}$
$p_T \geq 3 \text{ GeV}$	30%	25%	30%	30%	5.5%	1.6%	3.8%	5
$p_T \geq 5 \text{ GeV}$	15%	15%	21%	22%	1.2%	0.58%	1.0%	5.9

Table 5: Key numbers obtained on the relative resolution ρ , the fraction of selected and correlated events, and the number of constituents for $p_T \geq 3 \text{ GeV}$. All numbers are for a parton and particle jet radius of 0.5. The tight and loose matching criterium are indicated with (t) and (l), respectively

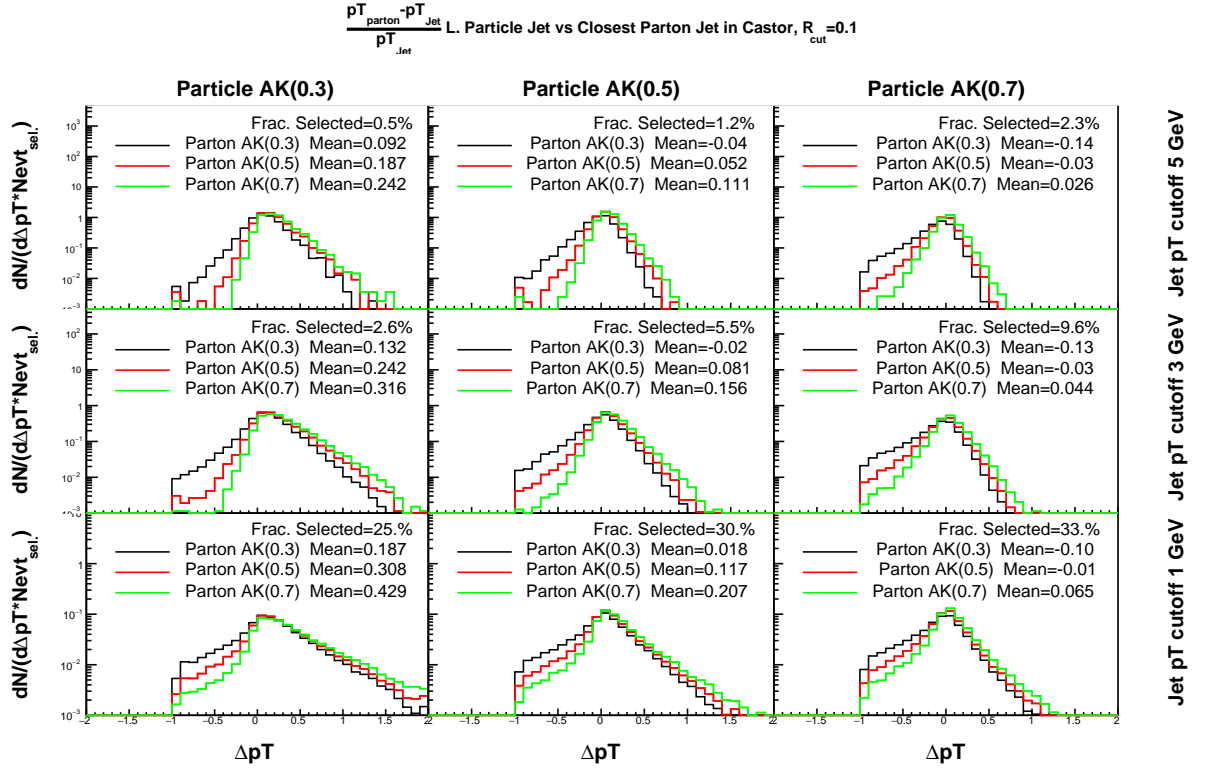


Figure 54: The Δp_T distribution of the leading particle jet with the closest parton jet as function of the particle jet p_T cutoff for various combinations of jet radii

17.4 CONCLUSIONS

The very forward particle and parton jets are correlated from a p_T cutoff of 3 GeV onwards, and thus a study of CASTOR jets indeed possesses sensitivity to the underlying parton distribution. Jets with $R=0.5$ and 0.7 correlate approximately equally well, while a jet radius of 0.3 is clearly not preferable. The correlation is optimal for equal parton and particle jet radii.

The relative p_T and energy resolution ρ is around 25(15)% for a particle jet p_T cutoff of 3(5) GeV, a tight matching criterium ($R_{\text{cut}} \leq 0.1$), and a parton and particle jet radius of 0.5 , as may be found in table 5. For a loose matching criterium the p_T resolution for these cutoffs are 30 and 21%, respectively.

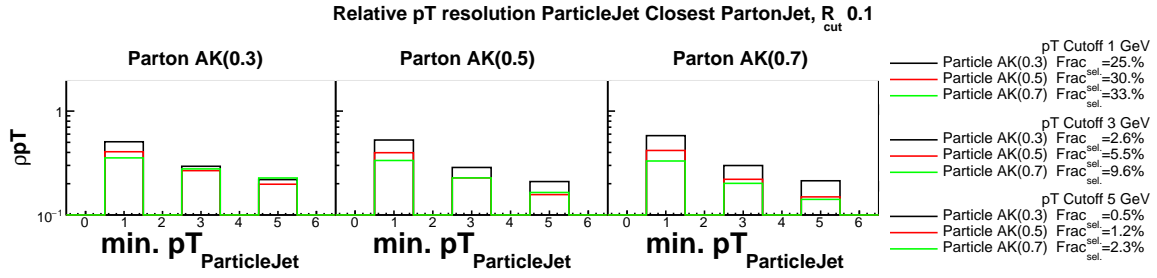


Figure 55: The ρp_T distribution of the leading particle jet with the closest parton jet as function of the particle jet p_T cutoff for various combinations of jet radii

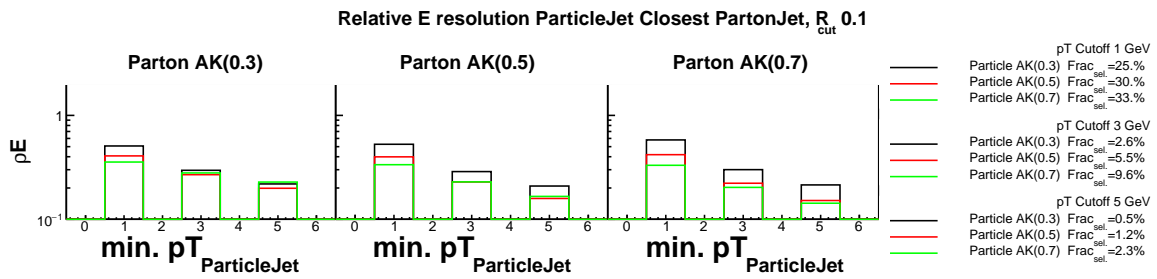


Figure 56: The ρE distribution of the leading particle jet with the closest parton jet as function of the particle jet p_T cutoff for various combinations of jet radii

18.1 INTRODUCTION

The central calorimeters of the CMS experiment have a fine granularity, which allows clustering of jets in both η and ϕ . This results in excellent spatial, momentum and energy resolution. Also, the central jets may be calibrated in various data-driven manners, and residual data-simulation corrections can be derived.

We emphasise that CASTOR, which has no η resolution, was originally not designed to measure jets. The design, with its 14-fold longitudinal segmentation, was rather optimised to measure anomalous showers in Pb+Pb collisions.

In this section all necessary preparations are outlined to successfully analyse the CASTOR jet spectrum. We start with explaining how the CASTOR jets are constructed from the raw CASTOR data. This is followed by a section on jet identification; we may classify jets in CASTOR as hadronic, EM, or undetermined. For the hadronic jets we derive a set of calibration functions, and optimise the final choice of the jet radii on detector and particle level. We finish the section with a validation study, i.e. we verify the correspondence between data and simulation in a jet distribution.

18.2 CONSTRUCTING CASTOR JETS

The energy measurement of all channels in a CASTOR tower are summed to a total tower energy. In this step the bad channels are masked. Thereafter, the towers are zero-suppressed (which means that towers below a certain threshold are simply discarded). These towers are clustered with the anti- k_T algorithm into CASTOR jets, that have their η -coordinate (approximately) fixed to the geometrical centre of the tower.

18.2.1 CASTOR jet identities

A CASTOR jet may consist of energy deposits in multiple channels; thus a CASTOR jet has geometrical properties besides of the total amount of energy. This allows us to define various identities of CASTOR jets:

- $\text{width}^2 = \frac{\sum_{\text{tower}} (\varphi_{\text{tower}} - \varphi_{\text{jet}})^2 E_{\text{tower}}}{E_{\text{total}}}$
- $\text{Depth } \langle z \rangle = \frac{\sum_{\text{chan.}} z_{\text{chan.}} E_{\text{chan.}}}{E_{\text{total}}}$
- $\sigma_z^2 = \frac{\sum_{\text{chan.}} (z_{\text{chan.}} - \langle z \rangle)^2 E_{\text{chan.}}}{E_{\text{total}}}$
- $E_{\text{tot}}, E_{\text{had}}, E_{\text{EM}}$: total, hadronic, and EM jet energy

- E_{hot} : energy of the hottest channel in the jet
- N_{tower} : number of towers in a jet
- ϕ : weighed azimuthal angle of a jet

18.2.2 CASTOR jet radius

There are various arguments in favour of a radius parameter of 0.5 for the CASTOR and particle jets. The jet-energy scale, which we will determine below, matches testbeam results optimally for $R = 0.5$. Further, it is preferable to pick the jet radius on particle and detector level symmetrically to avoid certain systematic effects. We saw previously that particle jets with $R \geq 0.5$ correlate well to the parton level, so the choice of 0.5 is supported by our previous study. Furthermore, for the particular case of proton-lead collisions, the underlying event contribution may be larger than in proton-proton collisions. Thus, $R = 0.5$ is clearly preferable¹ over $R = 0.7$.

18.3 DISCRIMINATING HADRONIC CASTOR JETS

Hadronic particles that deposit their energy in CASTOR suffer from non-compensation, and this effect is energy dependent. Thus, the energy of the hadronic jets needs a correction on top of the absolute scale of EM particles, which we obtained in chapter 12.

Dedicated simulations of electron and pion showers indicate that showers in CASTOR may be identified as either EM, hadronic, or undetermined in nature, by applying cuts on the jet identities. In this section we outline how the jet identification is performed. The following cuts were determined to discriminate between hadronic and EM jets [145]:

A JET IS HADRONIC IF THE FOLLOWING THREE CONDITIONS ARE *not* MET:

- The jet does have both $\langle z \rangle > -14450$ mm and $E < 175$ GeV
- The jet does have both $\langle z \rangle > -14460$ mm and $E > 175$ GeV
- The ratio of energy in the EM channels to the total energy exceeds 95%

A JET IS EM IN NATURE IF THE FOLLOWING CONDITIONS *are* MET:

- Minimally 45% of the energy of the jet comes from a single channel
- Minimally 90% of the energy of the jet originates from the EM channels
- The width of the jet does not exceed 11.5°
- The jet meets maximally one of the requirements per pair listed below:

¹ The choice was not evident on beforehand. For example, in Pb+Pb collisions jets with $R = 0.3$ are also deployed, since the underlying event can be very large in central Pb+Pb collisions

- $\sigma_z > 30$ mm and $E < 75$ GeV
- $\sigma_z > 40$ mm and $E > 75$ GeV
- $\langle z \rangle < -11450$ mm and $E < 125$ GeV
- $\langle z \rangle < -11460$ mm and $E > 125$ GeV

These cuts are not complete though: certain jets may be neither EM nor hadronic. These jets are labelled as undetermined.

In Fig. 57 we display the five jet identity distributions for data and simulation that are used to identify the nature of the jets. The distributions are for events that pass the event selection criteria. The models were simulated with the Fullsim option. We observe reasonable agreement between the simulations and the models. In particular, the distribution of the width is slightly wider for data than simulations.

18.4 CALIBRATING CASTOR JETS IN DATA AND SIMULATION

In this section we briefly summarise the jet calibration procedure for the hadronic jets. First we discuss a matching procedure to obtain the response of CASTOR to the particle-level jets. Thereafter, we explain how calibration functions are derived from the response. We finish with validating the procedure; to this purpose we compare various distributions of CASTOR jets in data to simulations.

18.4.1 Matching CASTOR jets to particle jets

To obtain the response of CASTOR to particle-level jets, we must first define the latter. On generator level, generally all particles that are not in a partonic state are accepted and are clustered into particle jets. Neutrinos, and μ and τ leptons are ignored though (the CMS `genparticlesforJets` collection was used. We give the precise definition in appendix A.6). We cluster these particles into jets using the `ak(0.5)` jet algorithm. This jet definition holds for all particle jets that are used in the context of simulating CASTOR.

Our objective is to estimate the response for the most energetic CASTOR jet of the event. To this purpose, we follow a procedure as was followed in [146]. Since CASTOR jets do not contain η -information except for acceptance requirements, the particle-level jets are only matched in ϕ to the CASTOR jet. We only matched jets that are maximally a distance of 0.2 apart.

Thereafter, the response was determined if the particle jet was isolated and contained. With contained is meant that the particle-level jet was fully contained in the CASTOR acceptance; in practise this means that the jet-axis must be in $-6.1 \leq \eta \leq -5.7$.

In Fig. 58 (top) we schematically depict the containment requirement. A jet pair is isolated if except for the matched particle jet no other generator particles contribute to the CASTOR jet. The isolation requirement is illustrated in the left-bottom plot of Fig. 58. A proper isolated and contained jet pair is depicted in the right-bottom plot of Fig. 58.

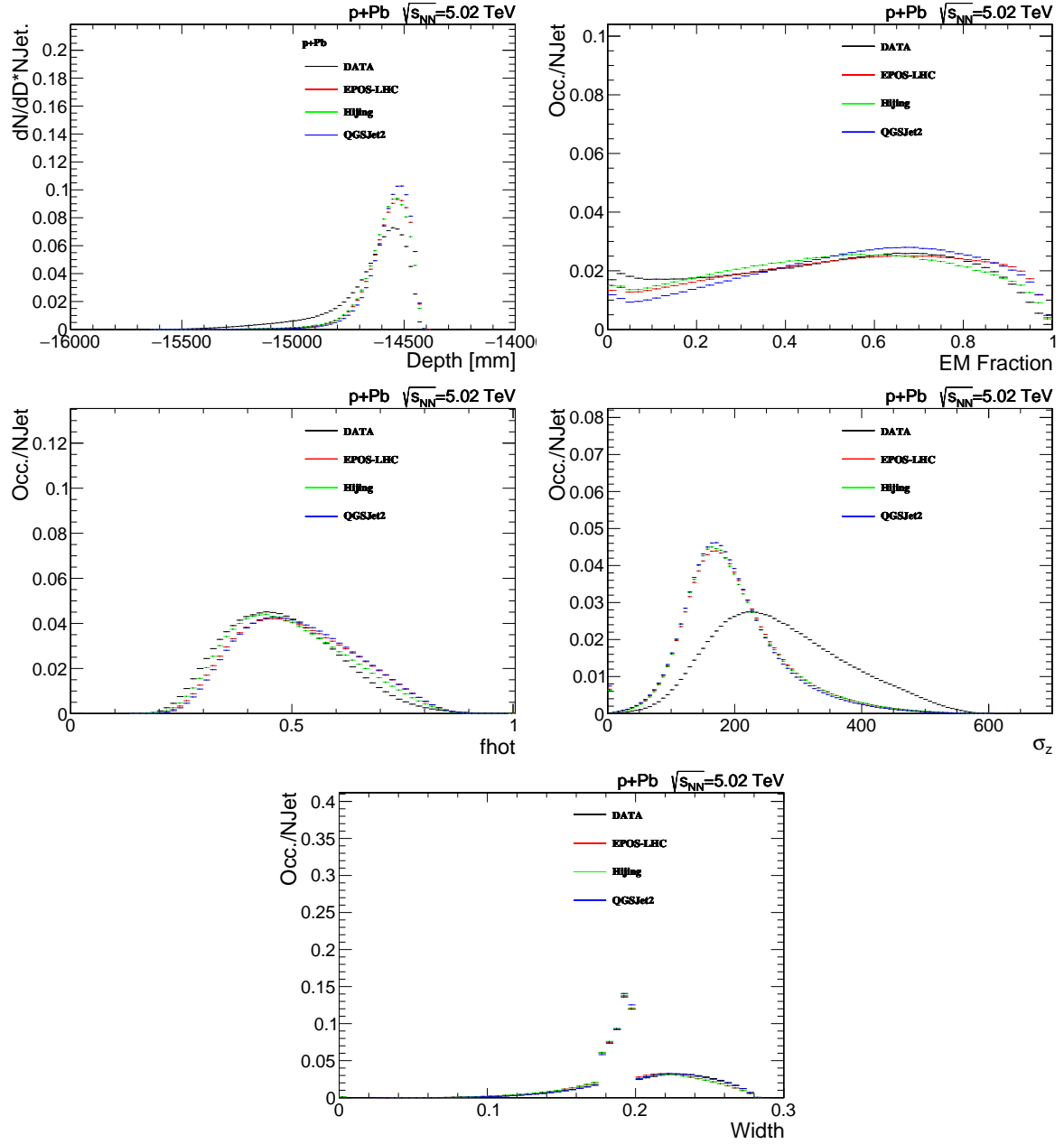


Figure 57: The jet identity distributions that are used in data and simulation to determine whether a jet is hadronic. The distributions are for events that pass the event selection

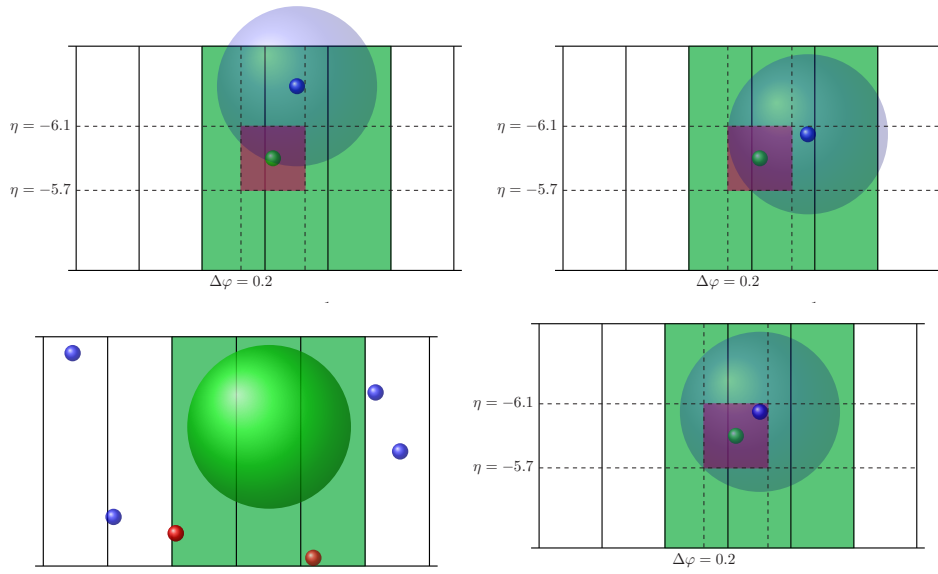


Figure 58: Illustration of the jet matching. The CASTOR jet is indicated with the green area in $\eta - \phi$ space, the centre is represented with the green dot. The particle jet is displayed as a circle with the blue dot in its centre. Top: the containment criterium. In the top left plot the particle jet partially falls outside the η -acceptance of CASTOR. In the top right plot the jet is separated by more than 0.2 in ϕ from the CASTOR jet centre. Bottom left plot: illustration of the isolation criterium. There are particles contributing to the CASTOR jet that do not belong to the particle jet (the green circle). Bottom right: a proper match between a CASTOR jet and a particle jet. The illustrations are from [146]

18.4.2 Parameterising the calibration function

To realistically determine the response of CASTOR to particle-jets, p+p collisions at $\sqrt{s} = 7$ TeV were simulated and analysed. A good summary, including the closure test of the procedure, may be found at [147] (CMS-restricted access) or [146].

For these isolated and contained jet pairs, the relative energy response was obtained as function of the CASTOR jet energy. The energy-dependent response was successively used to parameterise a calibration function of the form:

$$C_{Calib.}(E_{Meas.}) = \alpha + \beta \cdot \text{Log}(\gamma + E_{Meas.}). \quad (84)$$

It is important at this point to clarify the reason for distinguishing between the calibration of jets in real and simulated events. The response of CASTOR can be simulated either with its shower library or with the full GEANT4 simulation. Since the shower library is dedicatedly tuned to test-beam data [100], calibration functions derived with the shower library simulation can be applied to the jets from data.

To correct the CASTOR jet spectrum to a particle-jet spectrum (motivated and described in section 19), simulations with CASTOR at its data-taking position are required. Regrettably, the shower library does not function for CASTOR at a displaced position, and therefore the Fullsim option had to be used for this purpose. The response from the full simulation is approx. 20% lower than the shower-library response. Therefore, another set of calibration functions was derived to calibrate jets in Fullsim modus.

The parameters for the Fullsim and shower-library calibration functions that were used in this analysis are given in table 6.

Table 6: The constants for the calibration functions for hadronic CASTOR jets for shower library and Fullsim simulations. The function description is given in eq. 84

Generator	
Shower library constants	Parameter value
α	2.39
β	-0.0812
γ	1000
Fullsim constants	
α	2.07
β	-0.0761
γ	1000

18.4.3 The relative response of jets in CASTOR

In this section, we verify the calibration functions for the p+Pb simulations.

Before these calibration functions could be used in software version 5_3_32, a minor adjustment still needed to be implemented, because the calibration functions were derived for simulations in software version 4_X_Y. A change in the simulation software (on the DQZ value, which parameterises the transport of light through the quartz of CASTOR) between 4_X_Y and 5_3_32 forced us to introduce an overall (well known) energy-correction factor of magnitude 1/1.1 to retain consistency with the Fullsim calibration functions derived in 4_X_Y. This factor is not absorbed in table 6, since these calibration functions are only applied to hadronic jets, while the aforementioned overall correction factor applies to all jets instead.

In Fig. 59 we validate the relative response to hadronic, EM, and all CASTOR jets in p+Pb collisions before and after calibration. From an inspection of the location of the EM and hadronic peak after calibration we infer that the calibration functions appear to function correctly.

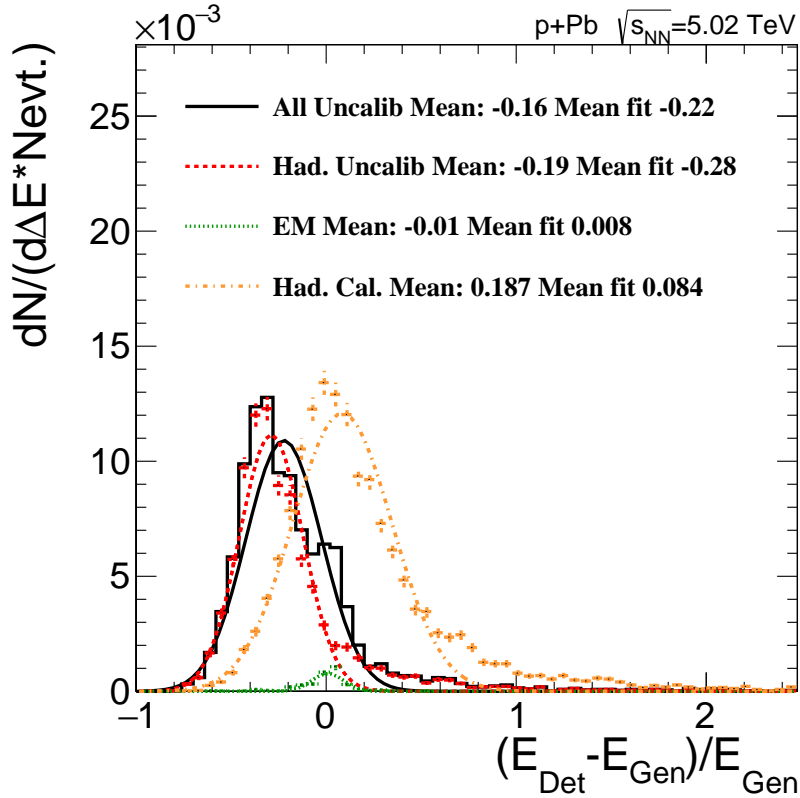


Figure 59: The response of CASTOR jets in simulated p+Pb collisions before and after the application of calibration functions, together with Gaussian fits. We observe that after the calibration the peak of the hadronic jets corresponds well to the electromagnetic-jet peak

18.5 VALIDATION OF CASTOR JETS

Before analysing the CASTOR jet spectrum, we validate the correspondence of a basic distribution of CASTOR jets in data and simulation. To this purpose, we propagate already certain systematic uncertainties to the distributions. An explanation can be found in chapter 20.

In Fig. 60 we display the number of CASTOR jets per event normalised to the cross section for p+Pb (left) and Pb+p (right) collisions, after the event selection was applied. For p+Pb we see a progressive offset between data and simulation with increasing jet multiplicity, but the offset appears not significant due to the large systematical uncertainties. For the Pb+p collisions we observe that the deviations between simulations and data are comparable to the deviations between the models.

We conclude that after applying the event selection and calibration functions, there is sufficient agreement between the validation distributions in data and simulation to trust the procedures followed.

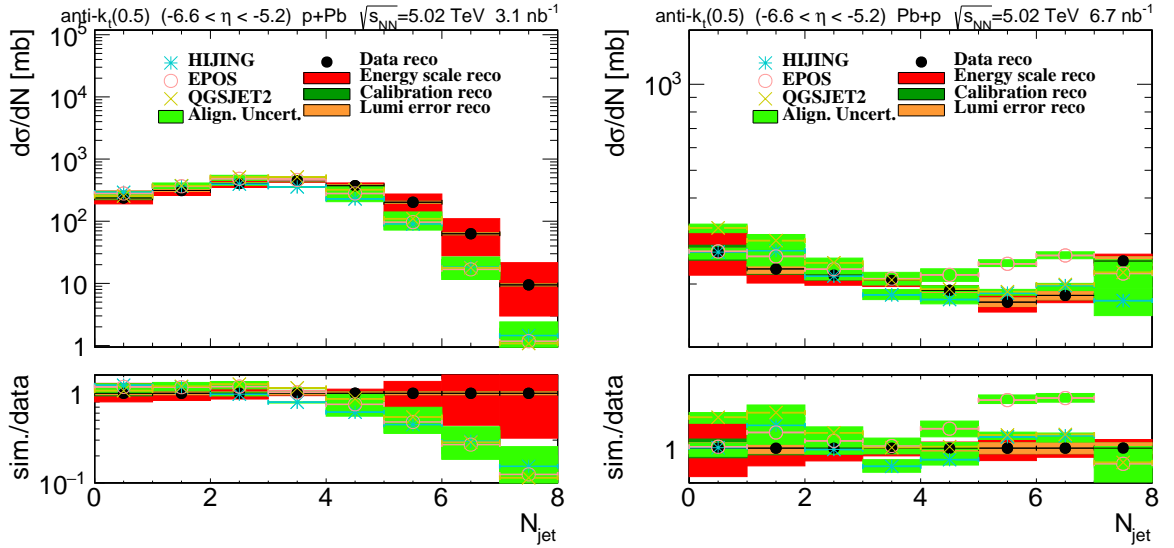


Figure 60: The multiplicity of CASTOR jets per event in data and simulation, after application of the event selection and calibration functions. Left: p+Pb collisions. Right: Pb+p collisions

19.1 INTRODUCTION AND MOTIVATION FOR UNFOLDING

In this chapter the correction of the measured CASTOR jet spectrum to a particle-level jet spectrum is discussed. We start with a concise introduction and motivation.

Correcting the measurement to the particle level generalises the result by removing all detector effects. This allows future models to be tested straightforwardly to the measurement; to compare new models in the (far) future to the uncorrected CASTOR jet spectrum may at a certain moment become difficult due to the complications arising with simulating a detector with the dimensions of CMS. Furthermore, interpreting the discrepancies between the measurement and models is less complicated when potential detector effects do not have to be taken into consideration. In particular, it is convenient to correct the data to the particle level for generator tuning. Besides, it facilitates the comparison of measurements between different experiments.

There are various manners in which the correction can be performed; the most straightforward approach is to simply divide the particle-level spectrum by the detector-level spectrum to obtain the correction factors; for certain measurements such a bin-by-bin correction suffices.

Unfolding is instead a rather complex mathematical operation to perform the correction. To correct the CASTOR jets to the particle level unfolding is needed though for various reasons. The CASTOR jet spectrum is exponentially decreasing with energy, while the bin size we intend to use will not be large w.r.t. the jet-energy resolution (JER) of CASTOR (we will assess the effective JER in detail below). The combination of these features of the energy spectrum result in non-negligible migrations between bins.

Provided that the simulation describes the detector well, unfolding can account for these jet migrations and all other detector effects by means of the response matrix, and miss and fake spectra ([ResponseObject](#)); we will define the construction of the response object precisely in section 19.3.1. In a birds eye view, the response matrix parametrises the response of the detector to the particle jets. The principle is quite similar to the procedure applied for the calibration of CASTOR, except that we do not impose containment or isolation constraints on the jet matching. The miss and fake-jet spectra allow to compensate for the effects of unmatched jets without an effect or cause, respectively.

The spectrum of detector-level jets is related to the particle jets as:

$$E_{\text{det,all}} - E_{\text{det,fake}} = (E_{\text{part,all}} - E_{\text{part,miss}}) \times \bar{M}_{\text{resp.}} \quad (85)$$

In this equation $\bar{M}_{\text{resp.}}$ is the response matrix. All detector (particle) level jets are denoted with $E_{\text{det,all}}$ ($E_{\text{part,all}}$), while the miss (fake) spectra are given by $E_{\text{part,miss}}$ ($E_{\text{det,fake}}$).

Clearly, if for a particular generator the response matrix, particle spectrum, fakes, and misses are known, the detector-level spectrum can trivially be computed from the particle-level spectrum.

For our purpose we need the inverse procedure though. If the response matrix is sufficiently smooth and diagonal, the matrix may be inverted. Then the procedure can be inverted trivially to obtain the correction of the detector level to the particle level. Indeed, for certain measurements this may constitute a straightforward solution

However, performing the correction by inverting the response matrix may neither be trivial nor deliver the desired result for at least two reasons:

- The inverse of $\bar{M}_{\text{resp.}}$ may not exist
- Correcting a measurement back to the particle level using the inverse of $\bar{M}_{\text{resp.}}$, provided it exists, will provide the minimal log likelihood (MLL) solution. This solution can be proven to be unbiased [148]. However, this solution is very sensitive to statistical fluctuations of the input spectrum. This may result in large fluctuations between the bins and large statistical uncertainties, which compromises the resolution of the final result to distinguish between different physics models. Thus, this is not necessarily the preferred solution

There exist various *regularised* unfolding techniques though, which can circumvent these problems. Since unfolding is a complex procedure, various parameters and cuts will emerge in defining the phase-space of the response object and tuning the unfolding procedure. The emphasis of this chapter is therefore on the optimisation of these parameters and the consistency of the procedure rather than the final unfolded result itself.

A major difficulty for unfolding CASTOR jets is the relatively high miss and fake-jet fractions. The lack of η -resolution of CASTOR makes the matching of particle level to detector-level jets unconventionally hard, resulting in relatively large miss and fake-jet fractions. These fractions propagate in the model uncertainty of the unfolding procedure, and thus must be kept minimal. Therefore, throughout this chapter the role of miss and fake jets is slightly emphasised.

This chapter is organised as follows: we start with defining and optimising an unambiguous definition of the event selection on particle level. This is followed by a section dedicated to the construction of the response object, in which we also tune its various parameters. Thereafter, we discuss the method and procedure to unfold the data to the particle level, and perform consistency tests on the results. In the validation section we perform a final consistency check on our procedure. In the summary section the steps are succinctly summarised, together with the final values that we obtained for all parameters that were introduced.

19.2 EVENT SELECTION ON PARTICLE LEVEL AND EVENT-MATCHING RESULTS

We motivated and outlined in chapter 15 the event selection on detector level. In this section we describe the event selection on particle level and review the consequences of our event-

selection criteria. There are two main reasons why an unambiguous and well-chosen particle-level event selection is necessary.

Reproducibility is the first argument; we unfold the data to the particle level such that data of other experiments and future models may be compared smoothly with the corrected measurement. For the latter purpose, it is absolutely necessary to adopt the same particle-level event definition as used in our unfolding procedure. Secondly, the detector-level event selection was optimised to a non-diffractive, hadronic event selection, as outlined in chapter 15. To correct a CASTOR jet spectrum from such events back to a non-diffractive, hadronic particle-level spectrum (and to avoid for example correcting non-diffractive events from data back to diffractive particle-level events), the selection on particle level must be chosen consistently. To optimise the particle-level criteria the simulated events are categorised in four classes in this analysis:

- Good events, for which both the detector and particle-level requirements are met
- Miss events, which only meet the particle-level requirements
- Fake events, which only meet the detector-level requirements
- Bad events, which meet neither detector nor particle-level requirements

The bad events are simply discarded from further consideration, and the treatment of the good events is discussed in the next section.

The key objective of the optimisation is to keep the miss and fake-event fractions as low as possible, since the detector and particle-level jets in the fake and miss events will not be matched (as explained in the section below), but their jets will be added to the fake and miss-jet spectra, respectively. Hence, these events will contribute to the systematic uncertainty in the model dependence of the unfolded result.

Also, ideally the miss and fake events balance each other. The number of non-diffractive, hadronic particle-level events $N_{\text{part.}}$ can be reconstructed from the detector-level events $N_{\text{meas.}}$ with a correction factor:

$$N_{\text{part.}}/N_{\text{meas.}} = (1 - F_{\text{fake}})(1 + F_{\text{miss}}). \quad (86)$$

In this equation F_{fake} is the fraction of good detector-level events that are fake, and F_{miss} is the fraction of good particle-level events that are miss. If the correction factor is far from unity, large corrections need to be applied to the measured spectrum. These potentially induce large systematic uncertainties in the final results.

Summarising, a particle-level event definition must be found that optimally complies with the detector-level definition. The following definition was adopted:

- Events that have a particle in the HF-PLUS and HF-MINUS acceptance with a minimal energy of 4 GeV
- Events that have a charged particle in the tracker acceptance with a minimal p_T of 0.4 GeV

Results on the event matching are given in Fig. 61. We observe that the miss and fake fractions are of the order of a few percent. Furthermore, the correction factor $(1 - F_{\text{fake}})(1 + F_{\text{miss}})$ deviates 3% from unity. To first-order approximation these deviations are small w.r.t., for example, the energy-scale uncertainty¹. We conclude that the event-selection criteria on particle and detector level comply reasonably well.

As part of the optimisation procedure different sets of detector and particle-level event definitions were pursued. The HF-AND requirement was always used in these selections though, to ensure cancellation of the photon-induced and non-diffractive events. For example, we also selected events that have exclusively one vertex on detector level. A variety of particle-level event definitions was evaluated against this detector-level selection, but all led to much higher miss and fake fractions and larger deviations of the correction factor from unity. A possible explanation could be that the centre-of-mass system in p+Pb collisions is boosted w.r.t. the lab frame. This boost factor on the collision products perhaps enhances the fraction of events with a charged particle in the tracker region, while no good primary vertex could be reconstructed.

Our choice for the event selection provided optimal event-matching results, and was thus chosen for the unfolding procedure.

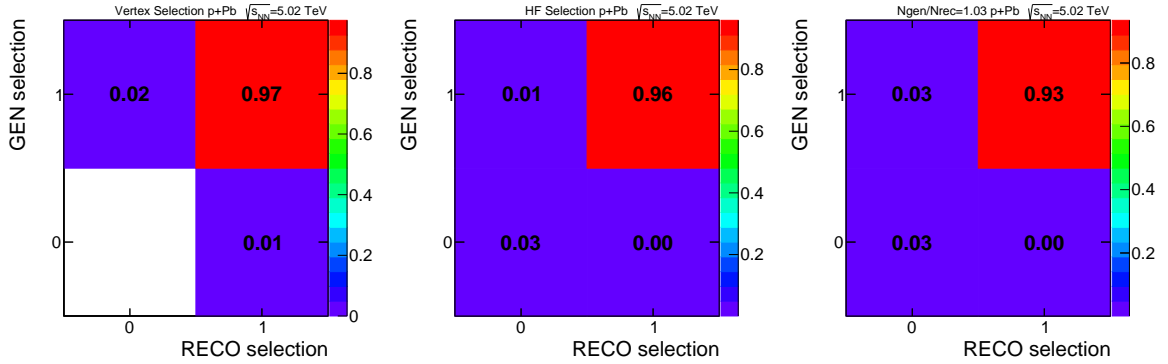


Figure 61: Event-matching outcome for events selected with the ZB+PixelTrack HLT path. Success (failure) is indicated with 1 (0). Left: the vertex-matching outcome. The vertex demand on particle level consists of requiring a charged particle in the tracker acceptance. It can further be derived that events with more than one good primary vertex without particle-level activity in the tracker do not occur, as expected. Middle: the matching of the HF-AND requirement on particle and detector level. On particle level minimally one particle with $E \geq 4$ GeV in the HF+ and HF- acceptances was demanded. Right: the overall event-matching outcome. The correction factor $(1 - F_{\text{fake}})(1 + F_{\text{miss}})$ is also depicted

¹ Care must be taken with such arguments though, since we do not yet know if the miss and fake events are biased to a certain jet energy

19.3 CONSTRUCTING AND OPTIMISING THE RESPONSE OBJECT

Since we have defined an event definition at particle and detector level, we can start to construct the response object. For the good events we match detector to particle-level jets to infer the response of CASTOR. This procedure depends on various matching parameters; therefore we optimise these parameters such that the miss and fake-jet fractions are minimal.

We will work per default with HIJING to unfold the data, since this model describes the data optimally (as we will demonstrate in chapter 21).

19.3.1 Matching jets

For all matched events a collection of CASTOR and particle-level jets is defined that contain jets above an energy cutoff $E_{\text{cutR.O.}}$. A priori it is not clear what an optimal acceptance for the particle-level jets is. Therefore, we accept particle jets of which the jet axis lie in the CASTOR acceptance extended by $\Delta\eta$.

From the collection of CASTOR jets the hottest jet is selected. The distance $|\phi_{\text{det.}} - \phi_{\text{part.}}|$ between all jets from the particle-jet collection and the CASTOR jet is computed. All particle jets for which $|\phi_{\text{det.}} - \phi_{\text{part.}}| \leq \Delta\phi$ are put into a candidate collection. From the candidate particle jets the hottest jet is selected and matched to the CASTOR jet. The bin of the two-dimensional response matrix that corresponds to the energies of the matched particle and detector jet is filled, and the jets are removed from their respective collections. If the CASTOR jet could not be matched to any particle jet, this jet is added to the fake-jet distribution. This procedure is consecutively repeated, in order from hottest to coolest CASTOR jet. After all CASTOR jets have been considered, the remaining particle jets are added to the miss-jet distribution. We prioritise matching the highest energetic jets, since these have the highest probability not to be miss or fake.

For the fake events all detector-level jets are added to the fake distribution, and all particle-level jets of the miss events are added to the miss spectrum.

We need to optimise the values of $\Delta\eta$ and $\Delta\phi$. In Fig. 62 (p+Pb) and 63 (Pb+p) we display the response matrix of the matched jets for a set of $\Delta\eta$ and $\Delta\phi$ values. Clearly, the matrices are most slim and diagonal for $\Delta\eta = 0$ and $\Delta\phi = 0.5$. The fact that the matrices are diagonal provides also further confirmation that the calibration procedure for the jets has the desired effect on the simulated events.

We continue with investigating the dependence of the fakes and misses on $\Delta\eta$ and $\Delta\phi$. In Fig. 64 (p+Pb) and 65 (Pb+p) the miss jets and the ratio of miss jets to all particle jets is depicted for a set of $\Delta\eta$ and $\Delta\phi$ values. The contributions from miss and matched events are stacked. The $\Delta\eta$ and $\Delta\phi$ dependencies comply with geometrical expectations.

It can be observed that miss events contribute significantly for small $\Delta\eta$ for Pb+p. For this setup the high-energy miss jets are solely due to miss events, but their fraction is very low, approx. 1%. Further, we observe that the miss fraction grows progressively with decreasing jet energy. Naturally, a very high-energetic jet is more likely to be successfully matched than a very low-energetic particle jet, of which the effect on detector level may easily be merged into another jet. Our jet-matching procedure itself is biased to matching the high-energetic

jets first; thus the shape of the miss-jet spectrum can be well-accounted for. For the fake jets depicted in Fig. 66 (p+Pb) and 67 (Pb+p) similar conclusions can be drawn. Fake events do not add significantly to the fake-jet spectrum though for any setup. Clearly, $\Delta\phi = 0.5$ results in the smallest miss and fake-jet fractions. This further matches expectations since we also picked a jet radius of 0.5.

We finish this paragraph with concluding that $\Delta\phi = 0.5$ and $\Delta\eta = 0$ constitute an optimal choice for creating the response object.

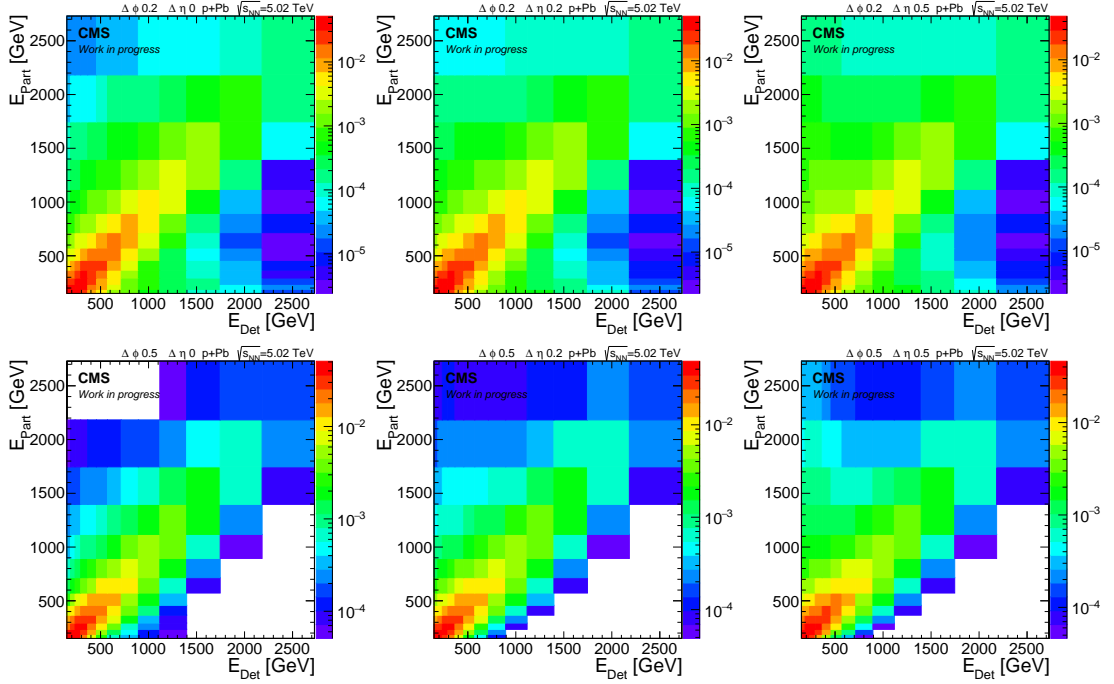


Figure 62: The response matrices for a set of $\Delta\eta$ and $\Delta\phi$ values. On the x -axis the CASTOR jet energy is depicted, on the y -axis is the particle-level jet energy, for p+Pb collisions. The graphs are normalised to the total number of matched-jet pairs

19.3.2 Balancing fake and miss jets

In this section we optimise the value of $E_{\text{cutR.O.}}$, the lower bound for the energy of the jets in the spectrum and response object. Preferably, the expected number of unfolded jets $N_{\text{unf.}}$ equals the number of measured jets $N_{\text{meas.}}$, since then the unfolding algorithm only needs to migrate jets instead of adding or subtracting these (which potentially deteriorates the model dependence of the procedure). Similarly to eq. 86, we define F_{miss} as the fraction of miss jets w.r.t. all jets from the good particle-level events, while F_{fake} is the fraction of fake CASTOR jets w.r.t. all jets from the good detector-level events. We relate the number of unfolded jets $N_{\text{unf.}}$ to $N_{\text{meas.}}$ via:

$$N_{\text{unf.}}/N_{\text{meas.}} = (1 - F_{\text{fake}})(1 + F_{\text{miss}}). \quad (87)$$

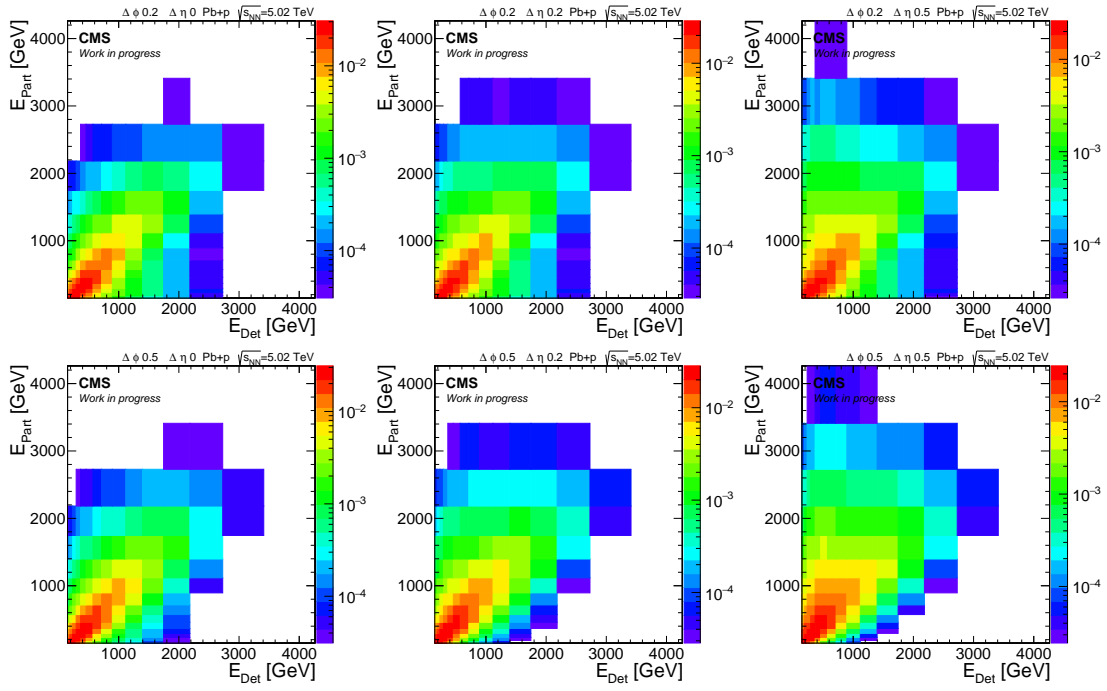


Figure 63: The response matrices for a set of $\Delta\eta$ and $\Delta\phi$ values. On the x -axis the CASTOR jet energy is depicted, on the y -axis is the particle-level jet energy, for Pb+p collisions. The graphs are normalised to the total number of matched-jet pairs

Thus, preferably the correction factor $(1 - F_{\text{fake}})(1 + F_{\text{miss}})$ is (close to) unit.

Naturally, the correction factor strongly depends on the parameters $\Delta\eta$, $\Delta\phi$, and $E_{\text{cut,R.O.}}$. Since we already established that $\Delta\eta = 0$ and $\Delta\phi = 0.5$ are the optimal setup parameters for this analysis, we tune $E_{\text{cut,R.O.}}$ by optimising the correction factor $N_{\text{unf.}}/N_{\text{meas.}}$. In Fig. 68 the correction factor is depicted as function of the setup parameters. We tuned the energy cutoff to 150 GeV, for which we obtain for both p+Pb and Pb+p simultaneously a good value for the correction factor; only the factor for Pb+p is 4% off w.r.t. unity. The latter is not evident, since p+Pb and Pb+p possess a different dependence of the correction factor w.r.t. the cutoff.

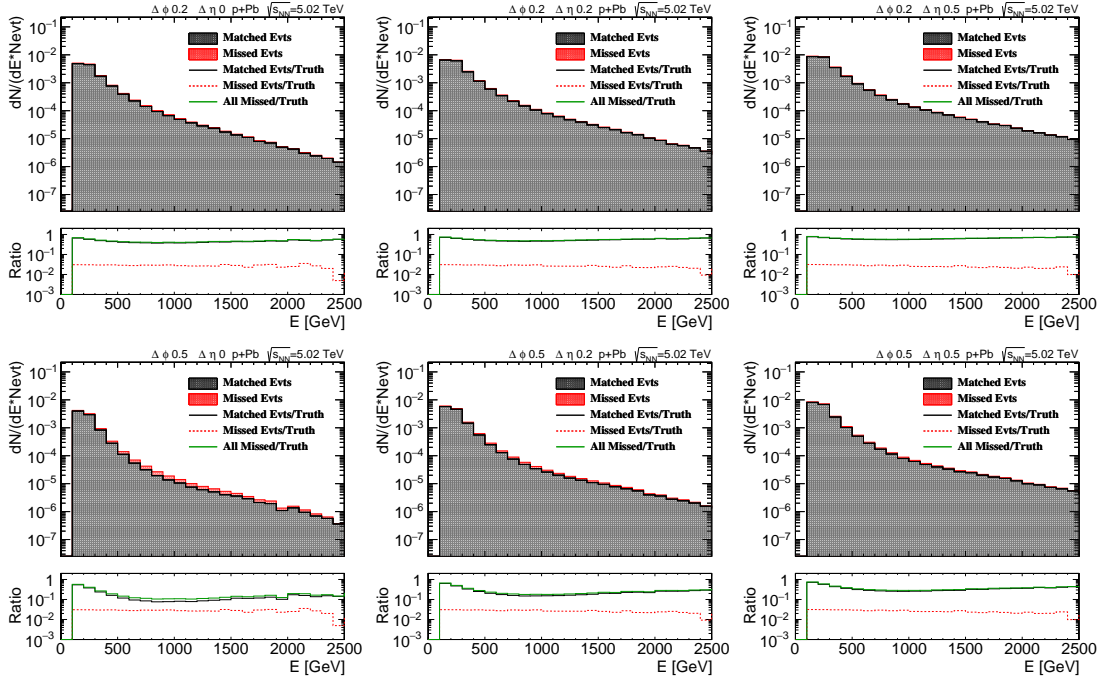


Figure 64: The miss jets and the ratio of miss to all particle jets as function of jet energy for a set of $\Delta\eta$ and $\Delta\phi$ values for p+Pb collisions

All the parameters that were needed to create and define the phase-space for the response object are thus outlined and optimised at this point.

19.4 UNFOLDING THE INCLUSIVE CASTOR JET SPECTRUM

There are various methods that use the response object to unfold a measured spectrum to an estimated particle-level distributions. In this section we start with a brief motivation for the method of our choice. Thereafter, we use the method to unfold the measured CASTOR spectrum. Various consistency checks are performed on the result to validate that the procedure works as expected. Furthermore, this will allow us to optimise certain parameters of the method.

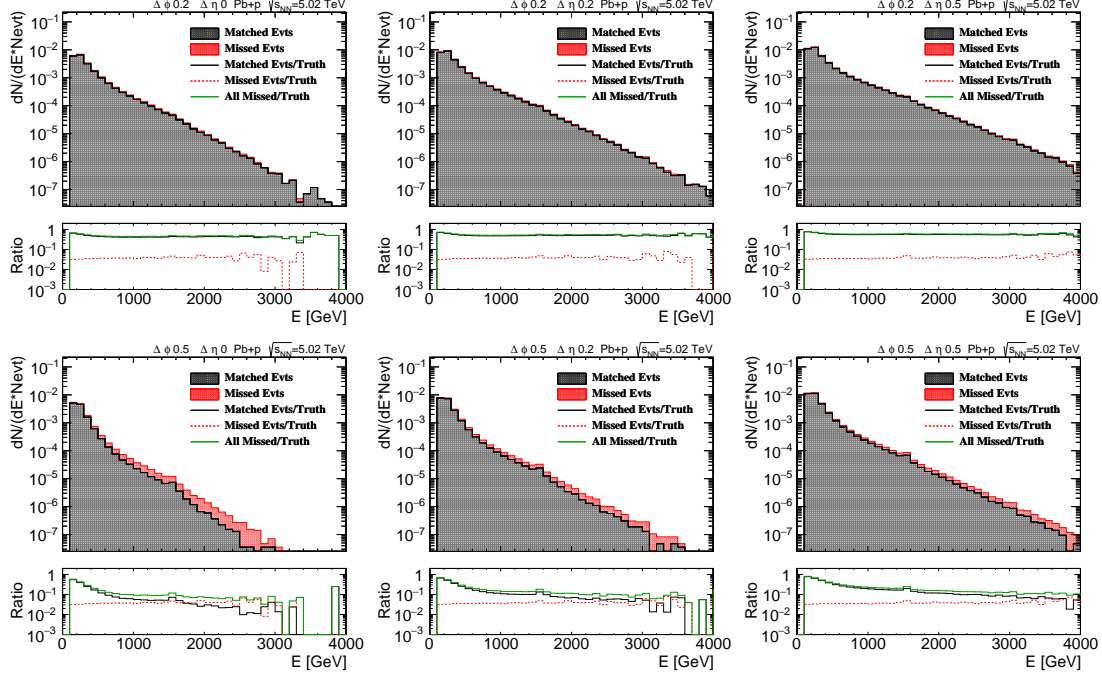


Figure 65: The miss jets and the ratio of miss to all particle jets as function of jet energy for a set of $\Delta\eta$ and $\Delta\phi$ values for Pb+p collisions

19.4.1 Unfolding the spectrum iteratively

We start with analysing if regularised unfolding is needed, as opposed to straightforwardly inverting the response matrix. To this purpose, we evaluate the condition number of the response matrix. This number is indicative whether the response matrix can be inverted, and if much regularisation is needed to approach the MLL solution. This number is calculated as $\sigma_{\max}/\max.(0, \sigma_{\min})$, in which σ_{\max} and σ_{\min} are the maximal and minimal singular value of the response matrix. The condition number was found to be of the order of 10^3 and 10^5 for p+Pb and Pb+p, respectively.

These numbers are relatively large, i.e. the number is typically $\mathcal{O}(10)$ for response matrices that can straightforwardly be inverted and do not need regularisation. We refer to [148] and the (restricted) concise, informative website of the CMS statistics committee on unfolding [149]. This large number can be attributed to the fact that the response matrices are rather broad, which in turn is a consequence of the transversal leakage of CASTOR. This indicates that for Pb+p regularised unfolding is definitely needed. Besides, for Pb+p the matrix could not be inverted.

For p+Pb unregularised unfolding was investigated by directly inverting the response matrix. The unfolded spectrum, as could have been readily anticipated, yielded large statistical fluctuations and uncertainties though, which blur the resolution of the final result to distin-

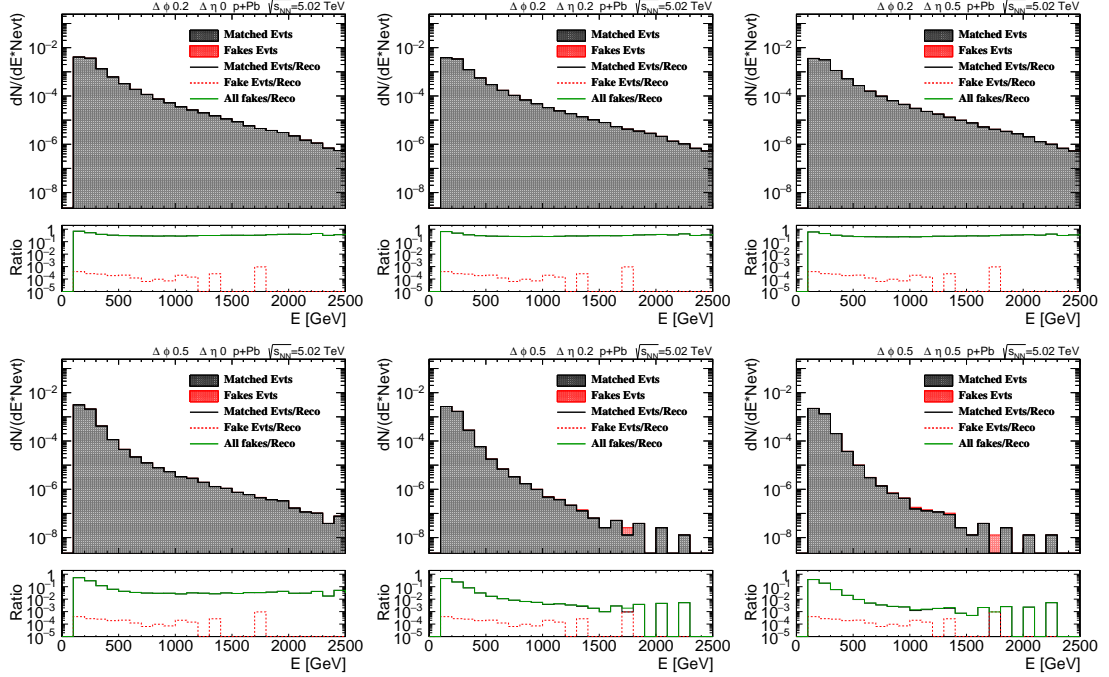


Figure 66: The fake jets and the ratio of fake to all detector jets as function of jet energy for a set of $\Delta\eta$ and $\Delta\phi$ values for p+Pb collisions

guish between different physics models. Regularised unfolding is thus needed for both p+Pb and Pb+p.

Unfolding may actually be considered to be a research topic in its own right, and there exist various methods that can accommodate for the problems we outlined. It is beyond the purpose of this thesis to present a detailed overview; an introduction may be found in [148]. The d’Agostini iterative procedure [150] is a Bayesian unfolding technique that computes the particle-level spectrum via an iterative procedure². The condition number gives an indication about the number of iterations needed to converge to the MLL solution. Thus, the procedure allows to select an intermediate solution for which the bias can be shown to be acceptable, while simultaneously the sensitivity to statistical fluctuations is diminished. Therefore, the Bayesian unfolding technique was chosen. We utilised the implementation from ROOUNFOLD [151].

This method also introduces a new parameter N_{Bayes} , which represents the number of Bayesian iterations for the unfolding. For the condition numbers under consideration, it is not uncommon to need $\mathcal{O}(10^3)$ iterations to reach the MLL solution. In contrast, for analyses in which the condition number is small ($\mathcal{O}(1)$) usually four iterations suffice.

In the two subsections below we test whether we can consistently apply the method on the CASTOR data, and optimise the unfolding parameters. Although we already optimised $\Delta\eta$,

² This technique is quite frequently used in high-energy physics analyses

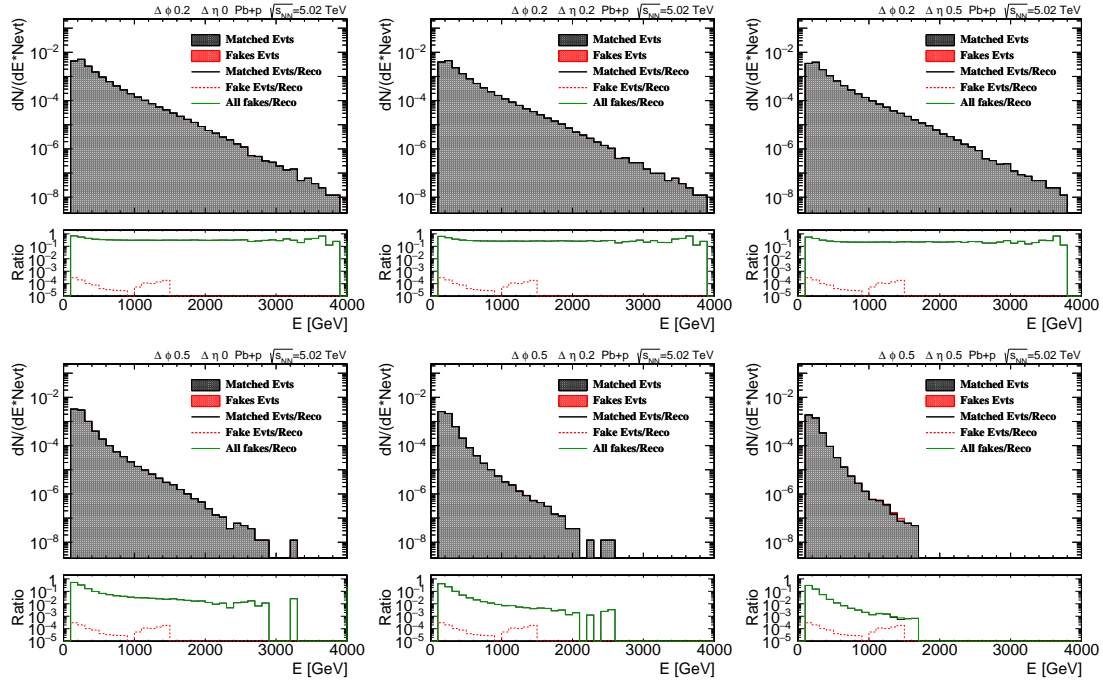


Figure 67: The fake jets and the ratio of fake to all detector jets as function of jet energy for a set of $\Delta\eta$ and $\Delta\phi$ values for Pb+p collisions

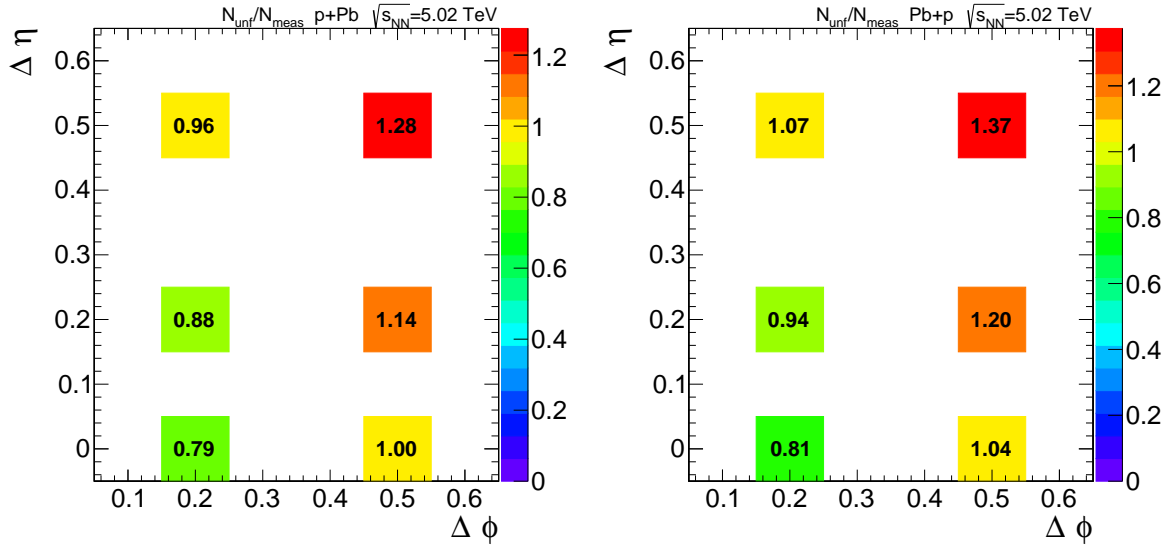


Figure 68: The correction factor is depicted as function of the setup parameters for a set of $\Delta\eta$ and $\Delta\phi$ values for an energy cutoff of 150 GeV. Left: p+Pb collisions. Right: Pb+p collisions

$\Delta\phi$, and $E_{\text{cut}_{\text{R.O.}}}$, we will perform the unfolding for different $\Delta\eta$ and $\Delta\phi$ values to validate our preliminary choice.

19.4.2 The backsmeared spectrum

In this section we analyse the dependencies of the unfolding by studying the backsmeared spectrum. After unfolding the data we may successively apply the reverse operation, i.e. we smear the unfolded spectrum back with the response matrix and add the fake jets. We can compare this backsmeared spectrum to the original CASTOR spectrum that we started out with. In Fig. 69 the data and backsmeared spectra are displayed for various values of N_{Bayes} . We observe that above 600 GeV the backsmeared spectrum appears to be consistent with the original spectrum after sufficient iterations.

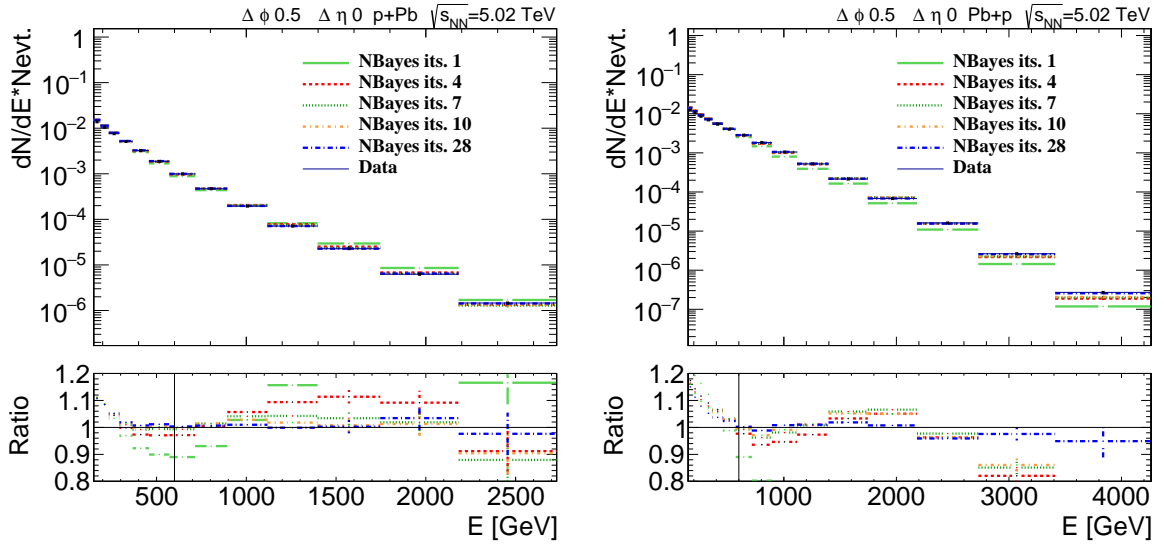


Figure 69: The data spectrum with the backsmeared spectra for various numbers of Bayesian iterations for p+Pb (left) and Pb+p (right) collisions. The vertical line in the ratio plot indicates from which energy onwards the χ^2/N_{dof} is calculated.

In Fig. 70 the χ^2/N_{dof} between the measured and backsmeared distribution is displayed for p+Pb and Pb+p. The description of how to properly take the covariances into account in the calculation of the χ^2/N_{dof} is for brevity presented in appendix A.7. The convergence is optimal for small $\Delta\eta$ and $\Delta\phi = 0.5$. Although we biased the unfolding already via $E_{\text{cut}_{\text{R.O.}}}$ to this configuration, this nonetheless constitutes a convenient reassurance that indeed our initial choice appears to be correct. Furthermore, from Fig. 70 we learn that for the p+Pb spectrum the χ^2/N_{dof} converges to ~ 2 for all setups with $\Delta\phi = 0.5$, which is encouraging for our confidence in the procedure. For Pb+p the value converges to ≈ 10 , which is acceptable.

The minimal number of iterations needed is 10 for p+Pb and 28 for Pb+p. This number is somewhat larger than conventional in CMS jet analyses, but can absolutely be justified given the high condition numbers of the response matrices.

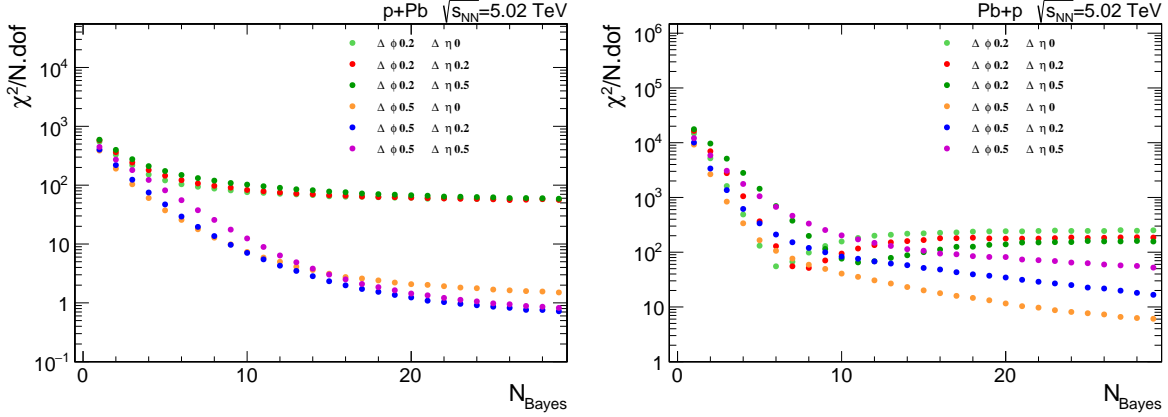


Figure 70: The χ^2/N_{dof} between the data and backsmearred distribution as function of the number of Bayesian iterations for p+Pb (left) and Pb+p (right) collisions

In the calculation of the χ^2/N_{dof} only bins with $E \geq E_{\text{cut,spec.}}$ were taken into account. It is of paramount importance to note that the unfolding is done with spectra and a response object with lower bound $E_{\text{cut,R.O.}}$. Only *after* that the unfolding and backsmearing was performed, the cutoff $E_{\text{cut,spec.}}$ was applied. The cutoff $E_{\text{cut,spec.}}$ was varied until a minimal value was found for which an acceptable χ^2/N_{dof} was obtained³. This was achieved for $E_{\text{cut,spec.}} = 600$ GeV. One reason for placing this cutoff is that the miss and fake-jet fractions are below 10 and 5% from this cutoff onwards, respectively.

Since this value corresponds reasonably well to the p_T -cut of 3 GeV, below which the particle jets are not correlated to the parton level anymore, the effect of this cutoff on the physics message of the analysis is conveniently limited. The cutoffs are indicated as a vertical line in the ratio plot of Fig. 69. In the paragraph below is analysed why this spectrum cutoff $E_{\text{cut,spec.}}$ is substantially higher than $E_{\text{cut,R.O.}}$.

19.4.2.1 The effect of migrations on the spectrum cutoff

In this section we review the energy range of migrations over the cutoff $E_{\text{cut,R.O.}}$ that can be expected, to provide an explanation for the aforementioned high cutoff $E_{\text{cut,spec.}}$.

In the previous section we introduced a lower cutoff $E_{\text{cut,R.O.}}$ for the response object. Jets below the cutoff can migrate over it, and thus a dependence is introduced on the shape of the jet spectrum below the cutoff. Concretely, the shape of the data spectrum below the cutoff may be different from the shape in simulations, but the response object is ignorant on this. As a result, the unfolding cannot compensate for the difference in migrations over the cutoff between data and simulation. We prefer to discard the part of the unfolded spectrum that is potentially affected by this effect from the final result.

We investigate which part of the spectrum is affected by the migrations of jets over the 150 GeV cutoff. Both the JER and the exponential shape of the spectrum are of importance;

³ We specify a minimal value, since the analysis loses discriminative power if we unnecessarily discard data

since the CASTOR jet spectrum falls off exponentially, the migration of a small jet fraction from a low to a high-energy bin can still significantly modify the content of the high-energy bins, and thus deteriorate the *effective* JER.

The relative JER at 150 GeV is approx. 25%. Initially, one would therefore expect only small contributions above a three- σ cutoff, which would be located around 250 GeV. But many particle jets also suffer from transversal leakage. Since CASTOR has no η -segmentation, no distinction can be made between for example a 150 GeV particle jet that deposits all its energy in CASTOR, and a 300 GeV particle jet incident on the edge of CASTOR and only depositing half of its energy. This effectively leads to a deteriorated JER; in Fig. 71 the mean and width of the energy of the matched particle jets is displayed per bin of CASTOR jet energy. We observe that for the lowest energy bin the width is 100 GeV, in contrast to the approx. 40 GeV that one would expect from just the JER. As can be seen in Fig. 71, a three- σ cutoff would effectively influence bins up to approx. 700 GeV. Below this value, the spectrum can be significantly affected by model-dependent migrations.

In the previous paragraph, we found that the backsmeared data spectra behave consistently from approx. 600 GeV onwards. Therefore, we conclude here that the value of 600 GeV of $E_{\text{cut,spec.}}$ can be well accounted for by the effective deterioration of the JER of CASTOR due to transversal leakage.

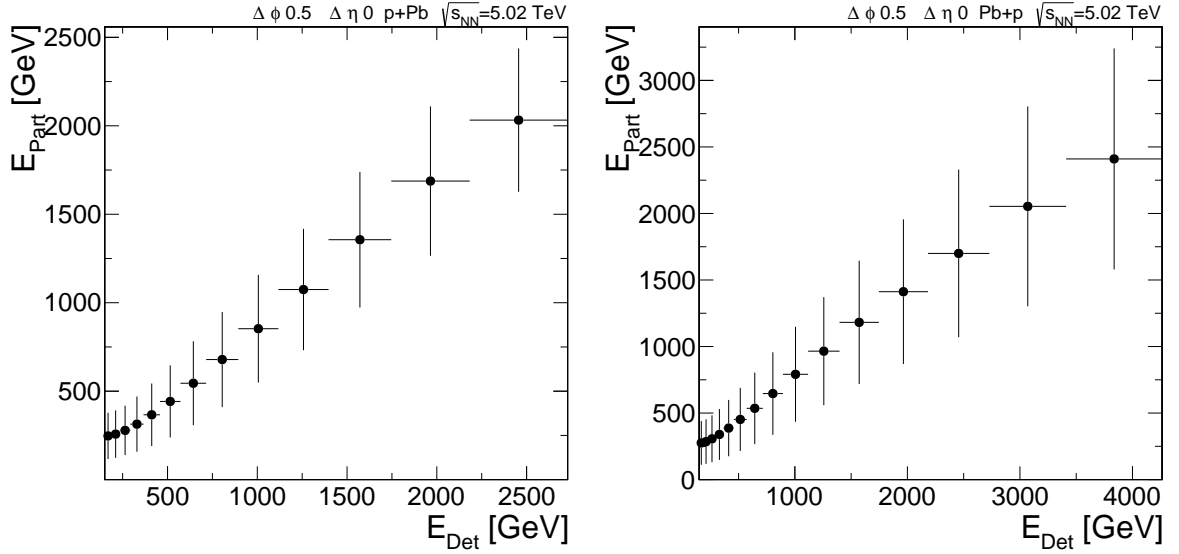


Figure 71: The mean and width of the energy of the matched particle jets per bin of CASTOR jet energy, for p+Pb (left) and Pb+p (right) collisions. The mean is the actual value of the symbol, and the width is depicted by the error bar

19.4.3 Convergence of the unfolded spectrum

In principle, the phase-space of the response object, the number of iterations N_{Bayes} for the unfolding, and the cutoff $E_{\text{cut,spec.}}$ above which the effect of migrations over $E_{\text{cut,r.o.}}$ is miti-

gated have been analysed and optimised at this point. We may deploy another test on the convergence in N_{Bayes} of the unfolded spectrum though.

In Fig. 72 we display the χ^2/N_{dof} for unfolded data, calculated between distributions with N and $N+1$ Bayesian iterations. We observe that after 28 iterations the p+Pb spectrum only changes with 1% of the statistical uncertainty (averaged over the bins), while for Pb+p still changes of 10% occur. These changes were checked not to be caused by a single (or a few) bins. Since deviations of 10% of the statistical uncertainty will be shown to be small w.r.t. the final systematic uncertainties, it was chosen to unfold the final results with 28 Bayesian iterations.

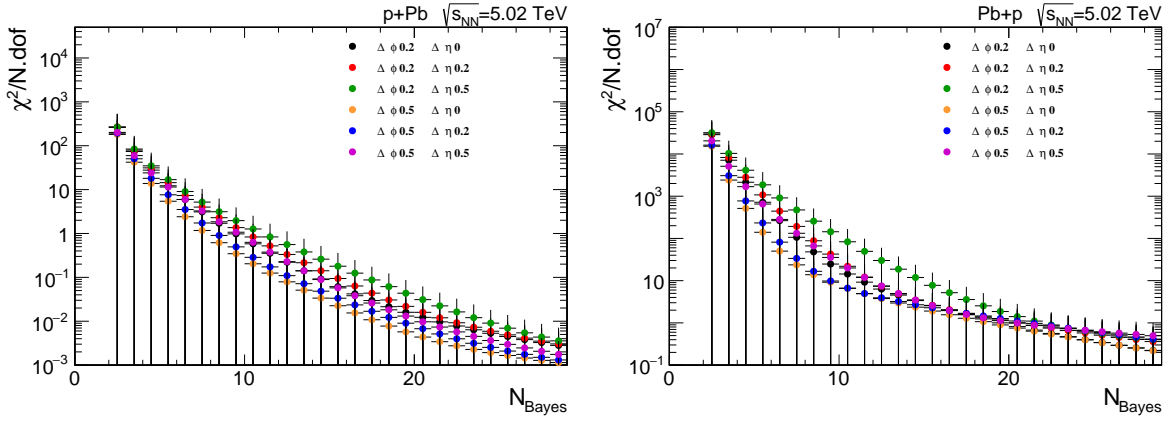


Figure 72: The χ^2/N_{dof} for unfolded data, calculated between distributions with N and $N+1$ Bayesian iterations. Results are displayed as a function of the number of Bayesian iterations for p+Pb (left) and Pb+p (right) collisions

19.5 THE MODEL DEPENDENCE IN THE FINAL UNFOLDED SPECTRUM

Even when we only consider the unfolded spectrum from energies onwards that are not affected anymore by $E_{\text{cutR.O.}}$, still a model dependence enters the unfolding. In this section we assess the cause and magnitude of the effect.

The unfolding can correct the shape of the input jet distribution via the matched jets. However, the (scaled) miss and fake-jet spectra are only added and subtracted, respectively. Different event generators lead to different miss and fake spectra, for which the unfolding does not compensate. The misses and fakes are only fully correct for the model that they belong to.

To estimate the consequences of this effect, in Fig. 73 (left) we unfold and backsmear an EPOS-LHC CASTOR jet spectrum with a response object that was filled with an independent EPOS-LHC event sample. We observe that after just a few iterations the backsmear spectrum matches the original spectrum well, which confirms again that the procedure was implemented properly. In Fig. 73 (right) we display the unfolded spectrum divided by the input particle-jet spectrum. Again, we observe that the unfolding produces consistent results.

It is rewarding to perform the same test with two different event generators. In Fig. 74 (left) we display a HIJING spectrum that was unfolded by an EPOS-LHC response object, divided by the particle-jet spectrum of HIJING. We observe deviations up to 50%. Since the detector simulation is identical for both generators and the unfolding procedure is sane, the deviations have to be mainly attributed to the different fake and miss-jet spectra.

In Fig. 74 (right) we unfold and backsmear a HIJING spectrum with an EPOS-LHC response object. We observe that the results are reasonably consistent. Here it is anticipated that the misses and fakes have canceled out, since both are once subtracted and added in the procedure.

The result in Fig. 74 indicate that a model dependence of $\approx 50\%$ can be expected in the unfolded data due to the model dependence in the procedure; this is also roughly observed in the next chapter (we refer to table 8).

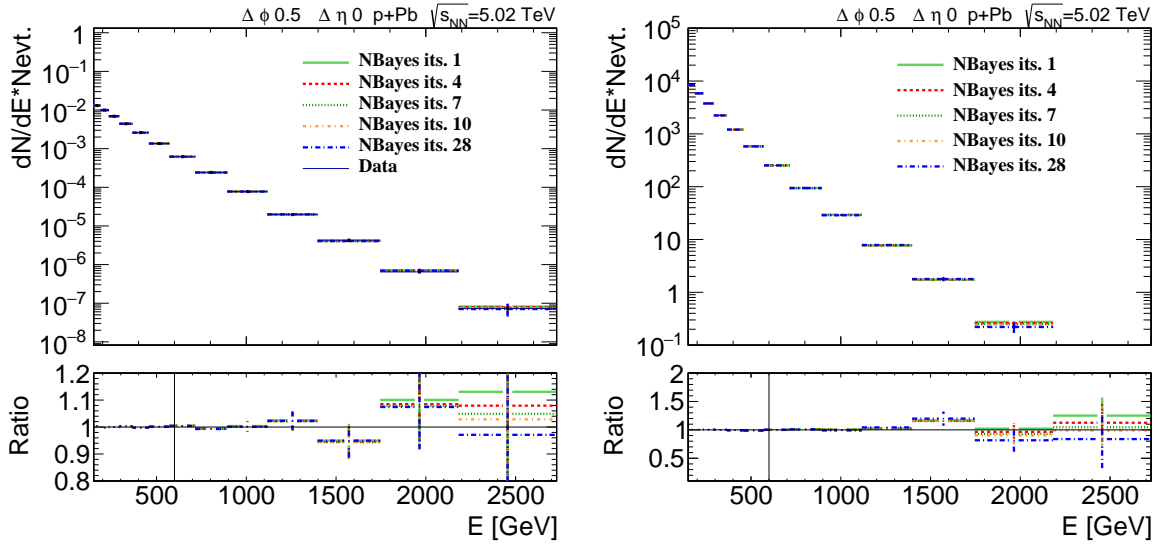


Figure 73: Left: the unfolded and backsmear EPOS-LHC CASTOR jet spectrum together with the CASTOR jet spectrum. Right: the unfolded EPOS-LHC CASTOR jet spectrum together with the input EPOS-LHC particle-jet spectrum. The unfolding and backsmearing was performed with a response object that was filled with an independent EPOS-LHC event sample

19.6 VALIDATION: THE BOTTOM-LINE TEST

The results that were discussed so far indicate that the unfolding procedure is delivering solid results. There exists another sanity check that we may impose on our results though, which is the bottom-line test (BLT).

The principle behind the BLT is that the agreement between a model and the data cannot be improved by the unfolding procedure. As a consequence, the χ^2/N_{dof} between a model and the data in the smeared space (on detector level) cannot be worse than the same quantity

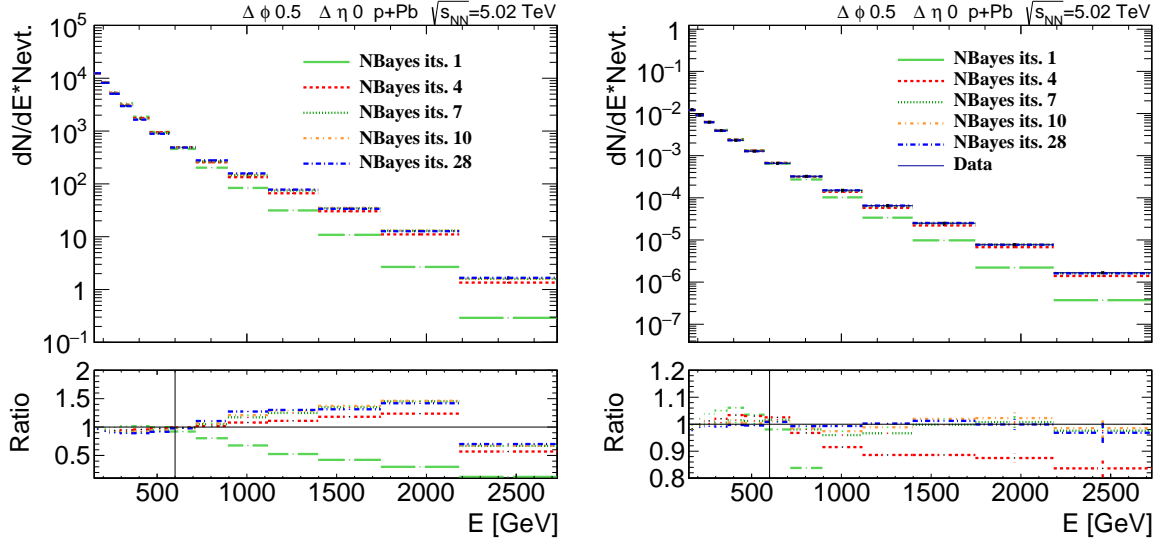


Figure 74: Left: the unfolded HIJING CASTOR jet spectrum together with the HIJING particle-jet spectrum. Right: The unfolded and backsmeared HIJING CASTOR jet spectrum together with the input HIJING CASTOR-jet spectrum. The unfolding was performed with EPOS-LHC

in the unfolded space. Put differently, we cannot enhance our resolution to reject models by changing from the smeared to the unfolded space.

Mathematically, the χ^2 in the smeared space may be expressed as:

$$\chi_{\text{smeared}}^2 = (\mathbf{y} - \mathbf{b} - \mathbf{K}\lambda')^T \mathbf{V}_y^{-1} (\mathbf{y} - \mathbf{b} - \mathbf{K}\lambda'). \quad (88)$$

In this equation \mathbf{y} are the values of the backsmeared data, and \mathbf{b} denotes the background. In our procedure the background is simply the fake-jet spectrum. The response matrix is denoted by \mathbf{K} . It acts on λ' , which contains the values of the model on particle level. Lastly, \mathbf{V}_y^{-1} denotes the covariance matrix of the data.

To calculate the value of χ^2/N_{dof} the number of degrees of freedom is needed. Usually, this equals the number of bins. Here a complication arises though. If substantial regularisation is needed, the true N_{dof} may actually be different from the number of bins. Instead, it can be estimated from computing the effective rank of \mathbf{S} , which is given by:

$$\mathbf{S} = \mathbf{K}\mathbf{J}\mathbf{J}^T\mathbf{K}^T. \quad (89)$$

In this equation \mathbf{J} is the error-propagation matrix.

The effective rank of \mathbf{S} may be calculated as its number of singular values that are non-zero. A cross check revealed that the effective rank actually corresponded to the number of bins. The latter could thus be safely used throughout this analysis.

The χ^2/N_{dof} in the unfolded space was calculated using a similar equation:

$$\chi_{\text{unfold}}^2 = (\hat{\lambda} - \lambda')^T \mathbf{V}_{\hat{\lambda}}^{-1} (\hat{\lambda} - \lambda'), \quad (90)$$

in which $\hat{\lambda}$ represents the unfolded data, $V_{\hat{\lambda}}^{-1}$ is the inverse of the covariance matrix in the unfolded space, and λ' contains the model predictions.

The BLT was obeyed for p+Pb for 100 Bayesian iterations, while 700 iterations were needed for Pb+p. Thus, with a sufficiently large number of iterations the BLT can be obeyed.

A careful inspection of the final result for 28 and 100 (p+Pb) or 700 (Pb+p) iterations revealed only relatively small, insignificant differences. Therefore, it was ultimately decided to use the minimal amount of regularisation necessary for convergence of the final results, which was 28 iterations.

We conclude that the unfolding procedure is implemented properly, and may be applied to the CASTOR jet spectra.

19.7 SUMMARY: PROCEDURE AND PARAMETERS FOR UNFOLDING

Before listing the final parameters and their values, it may contribute to the clarity of this chapter to succinctly retrace our steps.

Our objective was to correct our measurement back to the particle level. We started with defining an event selection on the particle level that optimally complies with the detector-level selection. To correct the data to the particle level, a response object was constructed. The parameters were optimised by the symmetry of the response matrix, and the balance between and minimisation of the miss and fake-jet fractions.

We found that the condition numbers of the response matrices are rather high, which ultimately can be attributed to the lack of η -resolution of CASTOR. This implies that the unfolding needs substantial regularisation, which is facilitated by the iterative Bayesian unfolding method.

The χ^2/N_{dof} between the data and the backsmeared distribution converges to acceptable values after 28 iterations. Furthermore, it was found that a reliable result could only be obtained when a cutoff on the final results was applied of approx. 600 GeV⁴. We also demonstrated that this high cutoff can be well-accounted for by the lack of η -resolution of CASTOR.

Furthermore, we reviewed the model dependence of the unfolding procedure by unfolding different models with each other. This confirmed again that our implementation is sane, but also gave rise to some caution: systematic uncertainties of the order of 50% may be expected in the final result due to the model dependence of the unfolding procedure.

As a final validation test we imposed the BLT on our data. We found that the test can indeed be obeyed, provided that we apply a large number of iterations. Our overall conclusions is that the unfolding procedure can indeed be applied to correct the CASTOR jets to the particle level.

We finish this section with stating in table 7 all parameters and their values that are relevant for creating the response object and unfolding the data, together with a brief parameter description. These are the parameters that are used for creating the final unfolded spectra and evaluating the systematic uncertainties in the next section.

⁴ This value conveniently corresponds approx. to the 3 GeV p_T -cutoff below which the jets are not correlated to the parton-level processes anymore

Table 7: All parameters relevant for filling the response matrix and unfolding the data together with a brief description and their final value

parameter	description	final value
Response object		
$\Delta\eta$	Extension of η -acceptance for particle jets	0
$\Delta\phi$	Max. distance in ϕ between particle and CASTOR jets	0.5
$E_{\text{cutR.O.}}$	Lower jet-energy cutoff for filling response object	150 GeV
Unfolding		
$E_{\text{cutspec.}}$	Lower spectrum cutoff for final results	600 GeV
N_{Bayes}	Number of Bayesian iterations for unfolding	28

In this section we describe the various sources of systematic uncertainty that propagate in the final results.

At this point we can clearly motivate why we will present results both on detector and particle level. At one hand the unfolding generalises the results for comparisons with future models and other experiments, as indicated in the previous chapter. At the other hand we already learned that substantial model uncertainties may propagate in the particle-level spectrum due to the unfolding procedure. The model uncertainty is absent for the results on detector level, and therefore these results have an enhanced resolution to distinguish between simulations of *existing* event generators¹.

We start this chapter with a concise list of the sources of systematic uncertainty that were considered in this analysis. As pointed out in the introduction, one of the objectives of this analysis is to partially cancel out certain systematic uncertainties in the ratio $p\text{+Pb}/\text{Pb+}p$. Therefore, as an example the propagation of the model uncertainty is discussed in detail to illustrate the interference effects that occur. Penultimately, we demonstrate that the event selection effectively mitigates the effects of pileup. We finish the section with discussing the spectra on particle and detector level with all uncertainties added cumulatively, and provide a table with the numerical values of the systematic uncertainties for the lowest and highest energy bin that $p\text{+Pb}$ and $\text{Pb+}p$ have in common.

20.1 SOURCES OF SYSTEMATIC UNCERTAINTY

The following sources of systematic uncertainty were taken into consideration in this analysis (approx. ordered in significance):

- **Energy scale uncertainty.** The energy scale of CASTOR is only known to 15% accuracy. Therefore, CASTOR jet spectra were constructed for which the energy scale was varied by $\pm 15\%$ and successively unfolded.
- **Model dependence.** Training the response object with different event generators (EPOS-LHC, HIJING, and QGSJETII-04) leads to different results for the unfolded distribution. This is mainly caused by the different miss and fake distributions, since the unfolding cannot compensate for this. Since it was found that HIJING describes the data best (as can be inferred from chapter 21), HIJING was used as default event generator to estimate the systematic uncertainties.
- **Alignment.** The position of CASTOR is known with limited precision; the uncertainties are given in table 4. Therefore, HIJING events were simulated with the CASTOR halves

¹ We like to emphasise that for such a comparison the detector response to the events must be simulated, for which the WLCG infrastructure is needed

shifted inwards and outwards w.r.t. the beam-pipe. Response objects were created for these simulations and used to unfold the data.

- **Jet-calibration uncertainty.** The parameters used for the jet identification have been proven to function well in simulated events. To account for residual differences between data and simulation, data spectra were also constructed without jet identification. For these samples all jets were treated as hadronic jets and calibrated.
- **Luminosity uncertainty.** The integrated luminosity is known for the p+Pb and Pb+p run with a precision of 3.4 and 3.6% [152], respectively. We (conservatively) add these uncertainties to an uncertainty of 5% in the p+Pb/Pb+p ratio.
- **Pileup.** It was found that the CASTOR jet spectrum for the 2013 proton-lead data was independent of the instantaneous luminosity after our event selection. Thus, pileup is effectively mitigated and not contributing to the results of this analysis.

The total systematic uncertainty was obtained by adding the individual sources of uncertainty in quadrature.

20.2 UNCERTAINTY PROPAGATION BY AN EXAMPLE: THE MODEL DEPENDENCE

In Fig. 75 the propagation of the uncertainty in the model dependence of the particle-level spectra is exemplary depicted, for p+Pb (left), Pb+p (middle), and p+Pb/Pb+p (right). The data were unfolded with HIJING (depicted DATA), EPOS-LHC (depicted plus-shifted), and QGSJETII-04 (depicted minus-shifted). For the uncertainty a record is kept per bin of the shift in the plus and minus direction. If, for a particular bin, the two displacements lead to a shift in the same direction (for example the last bin of the p+Pb distribution), the maximal shift is taken as uncertainty and symmetrised in absolute magnitude. The interference effects of this can be seen in the one-but-last bin of the ratio plot. The upper bound is much larger than the lower bound of the uncertainty, while the individual uncertainties for p+Pb and Pb+p behave rather smooth.

20.3 TESTING THE PILEUP-SAFENESS OF THE EVENT SELECTION

Although only events with zero or one vertex were selected, event pileup can still occur. An event with a vertex may be accompanied by an event without a proper vertex (for example a diffractive event). The energy of these events can potentially be summed up, which would compromise the measurement.

In Fig. 76 the CASTOR jet spectrum is depicted for events selected from ten different instantaneous luminosity bins, which approximately sample the instantaneous luminosity range of our data. If pileup events would lead to a contribution to the spectrum, the spectrum would possess a dependence on the instantaneous luminosity. Since no dependence on the latter is observed, we conclude that pileup does not play a role after the event selection.

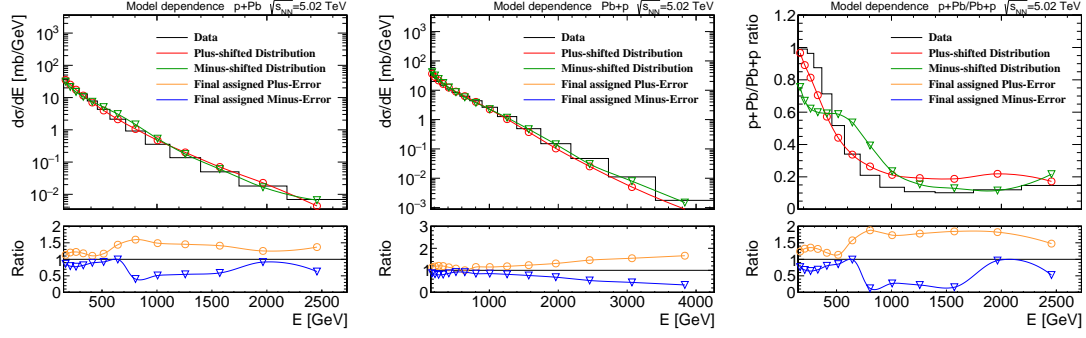


Figure 75: The CASTOR jet spectra on particle level, unfolded with a response object created with HIJING, EPOS-LHC, and QGSJETII-04. These are labelled as DATA, Plus-shifted, and Minus-shifted, respectively. In the ratio plot the final value of the uncertainty is depicted. The plots are for p+Pb (left), Pb+p (middle), and p+Pb/Pb+p (right)

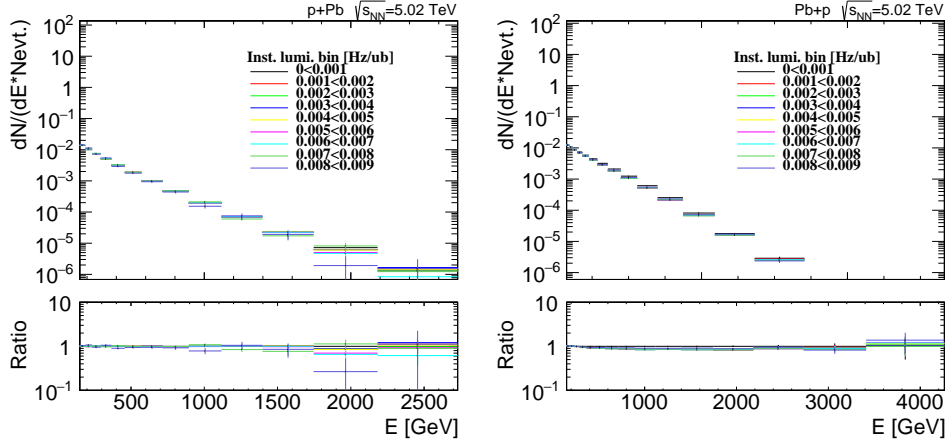


Figure 76: The CASTOR jets spectra for p+P (left) and Pb+p (right) collisions for different instantaneous luminosity bins

20.4 THE FINAL SPECTRA WITH ALL UNCERTAINTIES ADDED CUMULATIVELY

In Fig. 77 the final particle-level spectra with their systematic and statistical uncertainties are depicted for p+Pb (left), Pb+p (middle), and p+Pb/Pb+p (right).

For p+Pb and Pb+p, the dominant uncertainty in the spectra is caused by the energy-scale uncertainty. For p+Pb/Pb+p, this uncertainty largely cancels out and the model uncertainty is dominant instead.

For p+Pb the calibration uncertainty is small compared to the corresponding uncertainty in Pb+p. This can be explained by the fact that the fraction of EM jets in Pb+p data is an order of magnitude higher than in the p+Pb data. For Pb+p the energy scale uncertainty becomes large after 3 TeV; we observe that the lower bound of the uncertainties extends to negative values.

For the ratio p+Pb/Pb+p it is rewarding to observe that uncertainty cancelation indeed occurs significantly. The most significant uncertainty in the ratio is the model dependence instead of the energy-scale uncertainty. This could have been anticipated, since this is an uncertainty mainly caused by misses and fakes, and relatively independent for p+Pb and Pb+p.

In table 8 we state the numerical values of the systematic uncertainties on particle level for the lowest and highest bin. The magnitude of the uncertainties in the p+Pb and Pb+p spectra are reasonably comparable to p+p CASTOR jet analyses [109, 110], while the p+Pb/Pb+p distribution has an appreciably improved resolution to distinguish between different physics models.

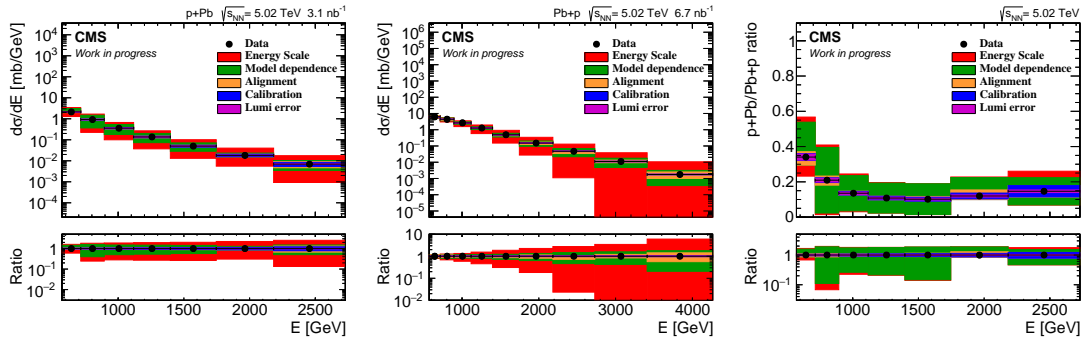


Figure 77: The final unfolded spectra with the systematic and statistical uncertainties for p+Pb (left), Pb+p (middle), and p+Pb/Pb+p (right)

In Fig. 78 we display the final detector-level spectra with their systematic and statistical uncertainties for p+Pb (left), Pb+p (middle), and p+Pb/Pb+p (right). The uncertainties on detector level are reasonably comparable to those on the particle-level, except that the model dependence is absent. For the ratio p+Pb/Pb+p this is particularly important, and this distribution relatively is in excellent shape to verify the general-purpose event generators. It can further be observed that the lower-bound of the x -axis is lower than for the unfolded spectra, since the cutoff $E \geq E_{\text{cut,spec}}$ did not need to be applied.

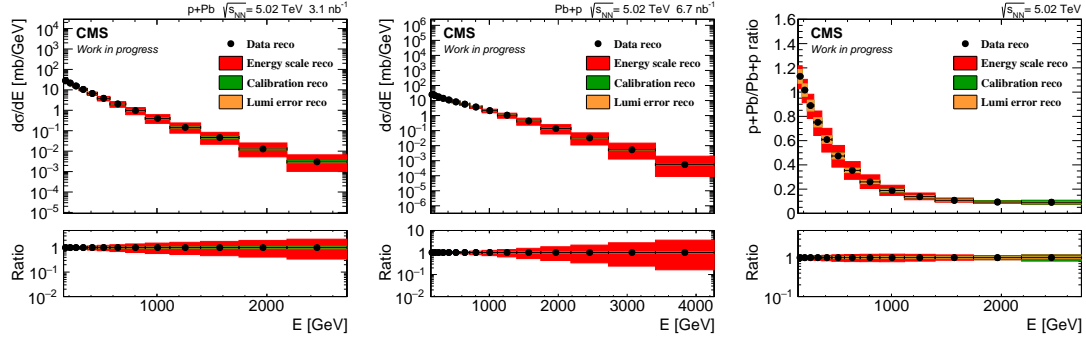


Figure 78: The energy spectra of CASTOR jets normalised to the cross section. Left: p+Pb. Middle: Pb+p. Right: the ratio p+Pb/Pb+p

Table 8: The contribution of various sources to the systematic uncertainty in the particle-level spectra. The results are quoted for the lowest and highest common energy bin for the p+Pb, Pb+p, and p+Pb/Pb+p spectra. The overall number is also quoted.

Source of uncertainty	p+Pb		Pb+p		p+Pb/Pb+p	
	600 GeV	2.5 TeV	600 GeV	2.5 TeV	600 GeV	2.5 TeV
Energy scale	+2% -2%	+145% -71%	+6% -6%	+170% -82%	+5% -7%	+57% -9%
Model dependence	+14% -14%	+37% -37%	+13% -13%	+46% -46%	+24% -24%	+48% -48%
Alignment	+3% -3%	+24% -24%	+3% -6%	+49% -24%	+10% -6%	+4% -6%
Jet identification	+1% -1%	+22% -22%	0% 0%	0% 0%	+1% -1%	+21% -21%
Total	+15% -14%	+153% -87%	+15% -16%	+177% -98%	+27% -26%	+77% -54%

RESULTS

In this chapter we compare the final unfolded differential cross sections to model predictions as function of jet energy for p+Pb and Pb+p collisions, and the ratio p+Pb/Pb+p. The ratio may initially be expected to yield a data-driven signal for saturation, i.e., a signal that we may interpret independently of any model.

The effect of saturation is strongest in the p+Pb collisions, for which the low- x gluons of the heavy ion are probed with the hard partons of the proton. This effect is much weaker for the Pb+p collisions, for which the hard partons of the ion probe the soft partons of the proton instead. Therefore, initially one would expect that a suppression in the low-energy part of the p+Pb/Pb+p ratio could be interpreted as a data-driven indication of saturation.

However, there are various reasons why this simplified picture does regrettably not apply to our measurement. First, it should be noted that for all our results the η -selection was made in the laboratory frame. This frame is boosted w.r.t. the centre-of-mass frame in opposite directions for the p+Pb and Pb+p collisions. Therefore, different centre-of-mass frame acceptances are compared; the Lorentz boost results in a shift in the η -acceptance of 0.87 between p+Pb and Pb+p, respectively. As a result, in the ratio p+Pb and Pb+p we convolute the effects of saturation with the x -dependence of the proton and nuclear pdf. This boost may turn a depletion at low energy instead into an enhancement.

It would therefore be preferable to correct the jet spectra back to the centre-of-mass frame. This would allow to study the ratio of only the jets that are in a common acceptance region. Indeed, if all components of the four vector of the jet are determined, the correction is a well-defined operation. Regrettably, the η -coordinate of the CASTOR jets is only defined by acceptance requirements. Thus, instead of correcting individual jets from the laboratory frame to the centre-of-mass frame, the only option is to correct the spectrum itself instead. The correction factors for this procedure can only be estimated using a model. In Fig. 79 we display the factors for correcting the ratio p+Pb/Pb+p to the centre-of-mass frame for three models; it may be observed that these are very model dependent though. Therefore, such a correction is not feasible; this is ultimately a consequence of the lack of η -resolution of CASTOR.

Another effect that obscures the interpretation, is that the jet clustering algorithm picks up contributions from the heavy ion beam remnant in the Pb+p collisions. This effect manifested itself already in the detector-level distributions that we encountered in the previous chapters, in which jets with energies up to 4 TeV were present. Subtle effects from non-linear parton evolution are expected to drown in the large debris contribution. Lastly, the hard-parton pdf of a heavy ion is subject to various nuclear effects. This further diffuses the symmetry between p+Pb and Pb+p collisions.

Concluding, although the p+Pb/Pb+p ratio may profit from the cancelation of certain systematical uncertainties, a data-driven interpretation of the ratio in terms of saturation is obscured by other effects.

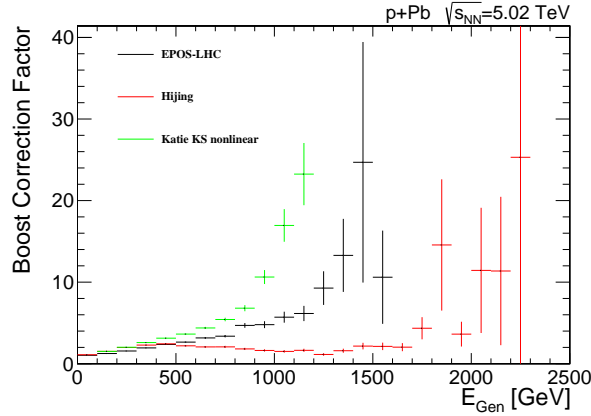


Figure 79: The correction factor to correct the ratio p+Pb/Pb+p for the boost. The correction factors were obtained by dividing p+Pb/Pb+p in the lab frame by the same result in the centre-of-mass frame. The correction factor is displayed for EPOS-LHC, HIJING, and the KATIE KS non-linear model

21.1.1 RESULTS ON P+PB COLLISIONS

We start with reviewing the results on the p+Pb collisions. In Fig. 80 (left) we compare the data to the predictions of the KATIE program, which was interfaced with the KS linear and non-linear pdf. These are labelled KATIE KS linear and KATIE KS non-linear, respectively. For KATIE KS non-linear a band has been added to the result that indicates a variation of the saturation strength between 50 and 100%. The linear and non-linear predictions do not describe the data accurately. The linear results describe the normalisation of the data better than the non-linear predictions. The non-linear spectrum is harder, and describes the shape of the data better instead. The effect of saturation on the jet spectrum is indeed very substantial; at the lowest jet energies saturation depletes the spectrum by an order of magnitude, while at the highest jet energies the linear and non-linear results appear to converge. The difference between the linear and non-linear predictions is also resolvable by the data at low energies, i.e., the data uncertainties are smaller than the model differences.

In Fig. 80 (right) we display the AAMQS predictions for different unintegrated pdfs¹. We labelled these as MV, g'01, and g'19. Further, we reviewed the MV model with the MPI option off. At low jet energies all predictions resemble each other quite well. Here the effect from saturation is expected to be strongest, and the models underestimate the data by approx. an order of magnitude. This may indicate a too strong suppression due to saturation. The models describe the data at high energies. The MV model with MPI off provides the hardest spectrum, and the g'01 spectrum is slightly harder than g'19; this complies with expectations from the parameterisation (we refer to chapter 14 and [65]). It can be seen that switching MPI off results in a slightly harder spectrum; this effect is not yet fully understood. The

¹ The graph that is prepared for publication in a journal combines a subset of the AAMQS and KATIE KS results. The graph can be found in appendix A.1

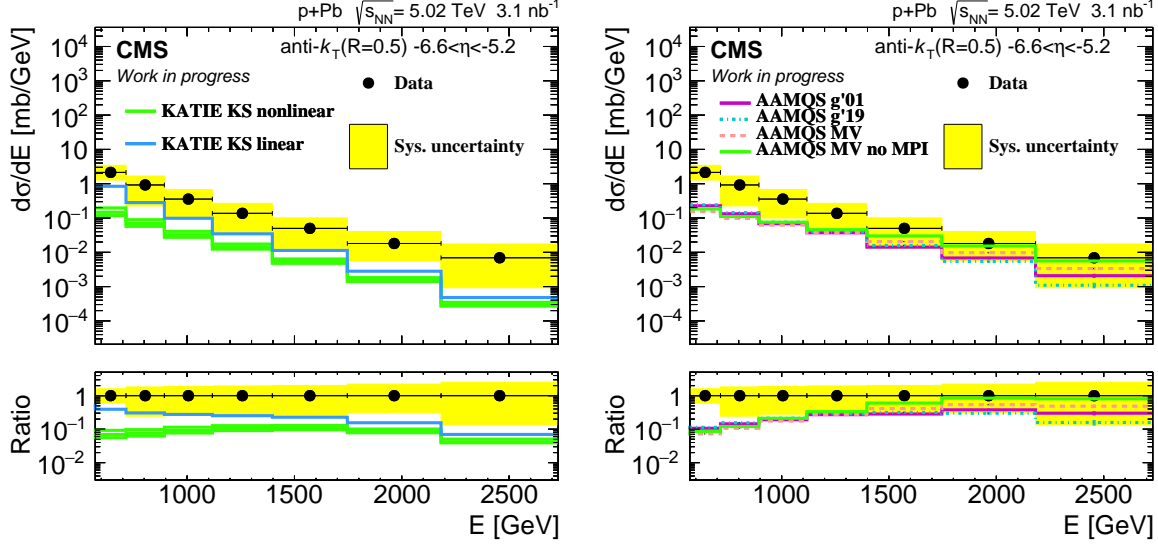


Figure 80: The stable-particle level differential jet energy cross section for p+Pb. Left: results from data are compared to predictions by KATIE. Right: results from data are compared to predictions by AAMQS

data favour the MV model without MPI, but the differences between the models cannot be decisively resolved by the data.

Although both the KS and AAMQS collaboration exploit the rcBK equation in the framework of hybrid factorisation, their predictions are quite different. The KS model uses off-shell matrix elements, while the AAMQS predictions were generated using on-shell scattering amplitudes derived in the Colour Glass Condensate framework.

In Fig. 81 (left) we compare the data to the predictions of EPOS-LHC, HIJING, and QGSJETII-04. We observe that HIJING provides a good description of the data. This favours an approach based on DGLAP-based parton showers, combined with nuclear shadowing. The EPOS-LHC model describes the low energy part of the data still, where the saturation effects are strongest. But both the EPOS-LHC and QGSJETII-04 spectra are too soft and underestimate the high energy region by more than two orders of magnitude. For EPOS-LHC a possible reason for the suppression of the hard component is discussed in [119], and improvements in the description of the data are expected in future releases.

21.2 RESULTS ON PB+P COLLISIONS

In Fig. 81 (right) we depict the data for Pb+p collisions with the reverse beam configuration (in which the ion propagates towards CASTOR), together with predictions from EPOS-LHC, HIJING, and QGSJETII-04. It can be seen that jets with energies up to 4 TeV are present; this clearly illustrates that the jet algorithm picks up contributions from the ion debris. Both EPOS-LHC and HIJING describe the data reasonably well, but their normalisation is a bit too low. The QGSJETII-04 model yields a too soft spectrum.

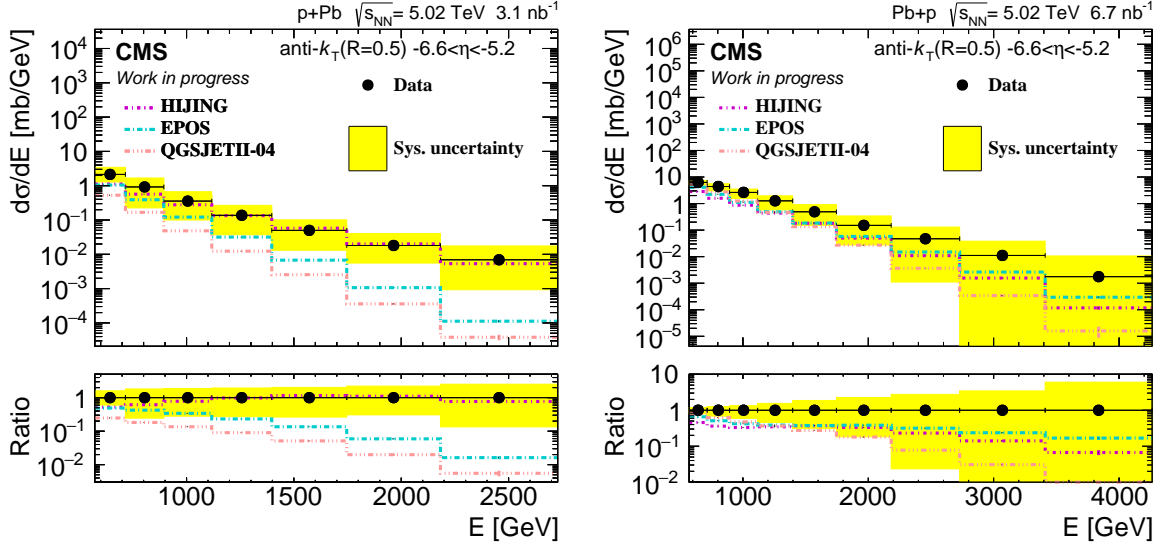


Figure 81: The stable-particle level differential jet energy cross section for p+Pb (left) and Pb+p (right). Results from data are compared to predictions by EPOS-LHC, HIJING, and QGSJETII-04

21.3 RESULTS ON THE RATIO P+PB/PB+P

Finally, in Fig. 82 we display the data and predictions for the ratio p+Pb/Pb+p. None of the models describe the data over the full range. We observe that HIJING describes the shape best, but has a too high normalisation. This can be attributed to the underestimation of the Pb+p spectrum. This offset is significant in the ratio plot; this is a clear virtue of the error cancelation. The EPOS-LHC model describes the low energy part of the ratio well. It underestimates the high energy part though, which is caused by the too soft p+Pb spectrum. Finally, QGSJETII-04 describes the shape of the data better than EPOS-LHC, but its normalisation is worse. This can also be attributed to its too soft p+Pb spectrum.

21.4 RESULTS ON DETECTOR LEVEL

In this section we compare the measurement on detector level to simulations for EPOS-LHC, HIJING, and QGSJETII-04. Results are displayed in Fig. 83 for p+Pb (left) and Pb+p (right) collisions, while the ratio p+Pb/Pb+p is displayed in Fig. 84. For these results, the alignment uncertainty has been assigned to the models.

These results are limited in their predictive power; we refer to our discussion in chapter 19. The motivation to display these results resides in their enhanced resolution to distinguish between the simulated models, since the model uncertainty is absent.

For the p+Pb spectra most conclusions are similar to the results on particle-level. However, it can be seen that EPOS-LHC underestimates the low-energy region more severely than in the unfolded data. For the Pb+p spectrum the conclusions are also analogue to the particle-level

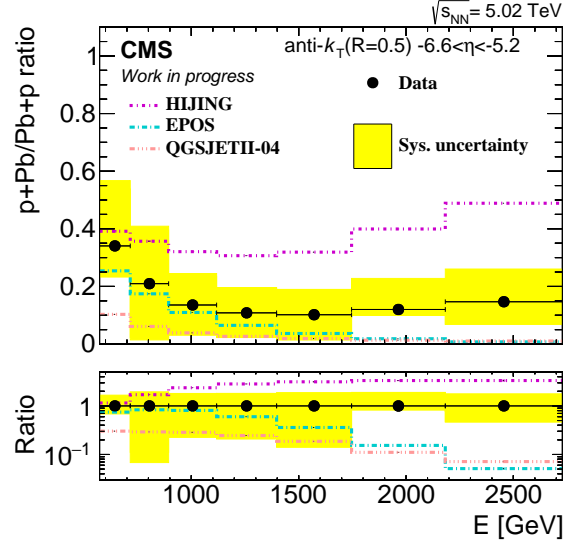


Figure 82: The stable-particle level differential jet energy cross section for the ratio of cross sections in p+Pb and Pb+p. Model predictions are included for EPOS-LHC, HIJING, and QGSJETII-04

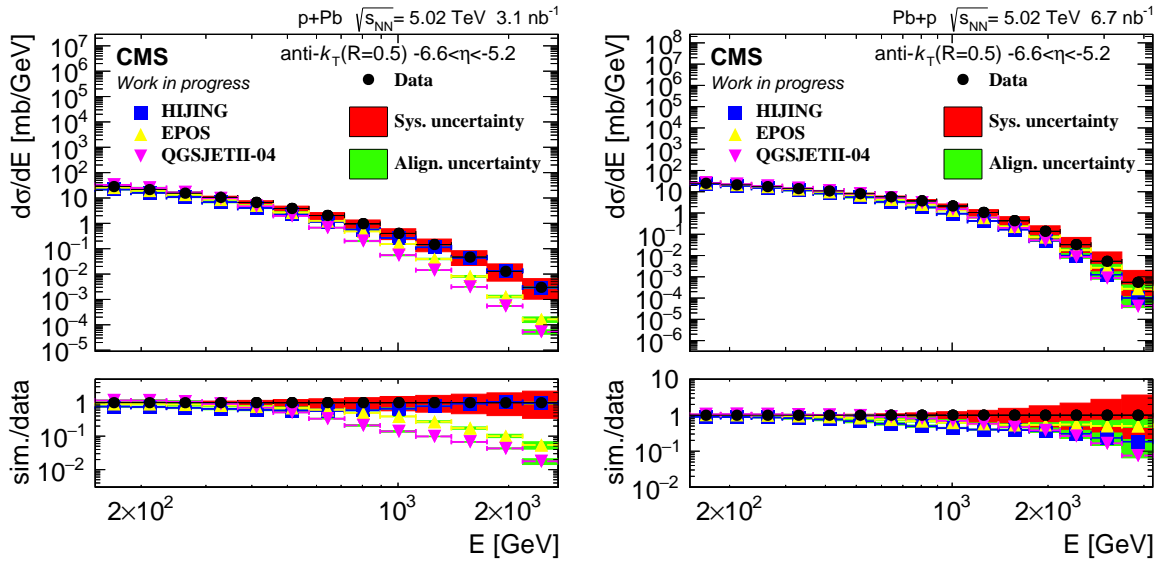


Figure 83: The detector level differential jet energy cross section for p+Pb (left) and Pb+p (right). Results from data are compared to predictions by EPOS-LHC, HIJING, and QGSJETII-04

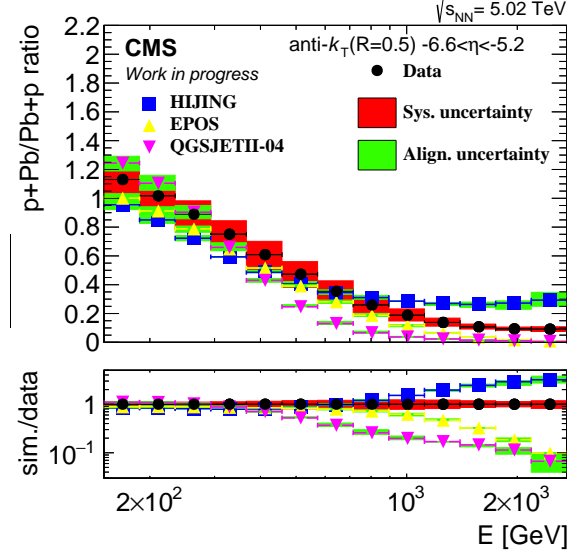


Figure 84: The detector level differential jet energy cross section for the ratio of cross sections in p+Pb and Pb+p. Model predictions are included for EPOS-LHC, HIJING, and QGSJETII-04

result, although the underestimation of HIJING w.r.t. the data is a bit more prominent than for the unfolded data.

Finally, from the ratio $p+Pb/Pb+p$ in Fig. 84 we learn that both EPOS-LHC and QGSJETII-04 completely underestimate the ratio, which could not be resolved as clearly in the particle-level result.

CONCLUSIONS

The key purpose of this thesis is to assess the hypothesis whether gluon saturation is realised in Nature. Furthermore, we aim to analyse whether the k_T or collinear factorisation framework describes the parton dynamics at small- x . Addressing these hypotheses using jets in CASTOR also constitutes an experimental milestone, since it serves as a proof of principle for more complex studies involving CASTOR jets.

To this purpose, we presented a measurement in an unprecedented kinematical domain of differential cross sections as function of jet energy for p+Pb and Pb+p collisions, and the ratio p+Pb/Pb+p. These results were obtained using the CASTOR calorimeter in the laboratory pseudorapidity range $-6.6 < \eta < -5.2$.

From the KATIE KS-linear and non-linear results we learned that the low-energy region of the p+Pb spectrum is potentially highly sensitive to saturation effects; here the linear and non-linear predictions differ over an order of magnitude. The KATIE KS non-linear and AAMQS saturation models underestimate the data by approx. an order of magnitude in this region, while the EPOS-LHC and QGSJETII-04 models, which are based on Regge-Gribov theory and incorporate saturation via different approaches, are clearly too soft. The latter is visible with an enhanced resolution in the detector-level distributions. Concluding, none of the saturation models describe this region of the data.

The HIJING model, which uses DGLAP-based parton showers and nuclear shadowing for the gluon pdf, provides an accurate description of the p+Pb spectrum, while none of the models based on k_T -factorisation can describe all aspects of the data.

Furthermore, we obtained various findings on the specific models that were used in this analysis. The shape of the Pb+p spectrum is reasonably well described by HIJING and EPOS-LHC, while QGSJETII-04 is too soft. The enhanced resolution of the ratio p+Pb/Pb+p, in particular on detector level, further allowed us to conclude that HIJING significantly underestimates the normalisation of the Pb+p spectrum, while the underestimation of EPOS-LHC and QGSJETII-04 of the low-energy part of the p+Pb spectrum can be resolved more significantly.

The differences between the KATIE KS-non-linear and AAMQS predictions are substantial at large jet energies. A first estimate of the influence of the MPI reactions, which are absent in the KATIE KS-non-linear model, suggested only a very moderate effect on the AAMQS predictions. Thus, the differences must rather emerge from the scattering amplitudes, which are derived in the colour glass condensate framework for the AAMQS model, while the KATIE KS-non-linear model uses off-shell matrix elements instead.

The underestimation of the AAMQS model of the low-energy part of the spectrum could perhaps partially be explained by its K -factor, which fixes its normalisation. This K -factor is expected to incorporate higher-order effects that were not taken into account in the model, and ideally it is unitary. The offset of an order of magnitude between the p+Pb data and the model appears rather large to be plainly absorbed in the K -factor though. More importantly, the shape of the AAMQS spectra appears not to be favoured by the data.

A possible explanation for the success of HIJING is that the nuclear shadowing was fixed by fitting its parameterisation to nuclear DIS data. The AAMQS and KS model do not rely on any nuclear data instead, and start from more elementary principles. For EPOS-LHC a future release is expected to improve the spectrum, which is currently too soft.

This analysis aims to overcome the limitations of previous analyses, since the anticipated saturation scale is well above the perturbative limit and the hard partons of the projectile are not probed at the kinematic limit. A clear limitation of the analysis is the lack of η -resolution of CASTOR though, since this prevents the measurement to be corrected from the laboratory frame to the centre-of-mass system.

The saturation-based models, given their current state-of-the-art, are not supported by the data. This implies that gluon saturation is either not realised by Nature in this part of the phase-space, or that the effects are modelled incorrectly. A model with DGLAP-based parton showers and a particular model of nuclear shadowing successfully describes various features of the data. This suggest that collinear factorisation is still applicable to this kinematic domain, and that shadowing effects on the nucleon level potentially explain the observations, instead of parton-level effects. The latter suggestion would need further scrutinisation though, in particular since the shadowing effects enter via a fit to DIS data.

This implies that saturation effects would be absent in p+p collisions of the same centre-of-mass energy, and that their jet-energy spectra can be described in the framework of collinear factorisation. Naturally, these implications have far-reaching consequences for the unitarity violation that we discussed in section 5.3. Furthermore, these results establish CASTOR jets as an experimental reality, and thus that these can also be used for more complex studies.

Certain reviews and clarifications concerning the models would be beneficial for interpreting the data. The differences between the AAMQS and KATIE KS-non-linear predictions deserve further attention. Speculatively, a model based on full NLO BK calculations may provide a better description of the data. All ingredients appear to be ready: the NLO matrix elements have been calculated, and in [153] the collinearly-improved NLO-BK equation is given¹. A linearised version of the AAMQS model could perhaps describe the p+Pb data, and provide an alternative to HIJING based on k_T -factorisation.

Also, a precise estimate of the effect of nuclear shadowing in this part of the phase-space would be illuminating.

In 2015, a p+p dataset was recorded at $\sqrt{s} = 5$ TeV by the CMS experiment, including CASTOR. A clear experimental priority would be to add the jet spectra for these collisions.

Various other analyses involving CASTOR can be thought of to further unveil the role of gluon saturation. It is expected that potential effects of saturation are stronger in the centre of the nucleus than in its peripheral region. The centrality is correlated to the transversal separation of the ion and projectile, and can be measured by using for example the HF detectors. An interesting extension of the analysis would therefore be a study of the spectrum as function of the centrality of the collision, for example we refer to [73]. Furthermore, a study of dijets in CASTOR, possibly combined with a veto on jets in the central acceptance, would

¹ In a private communication with theoretical experts, it was understood though that the differences between LO and NLO BK calculations are expected to be $\mathcal{O}(10\%)$, and thus not capable of explaining the discrepancy between the saturation models and the data

possess an enhanced sensitivity to saturation effects compared to the inclusive spectrum. A study of Mueller-Navelet jets with one jet in CASTOR² (or in particular a study of the ratio Mueller-Navelet jets over inclusive dijets, for which the energy scale uncertainty potentially would cancel) would possess an enhanced sensitivity to distinguish between collinear and k_T -factorisation.

The modelling of nuclear shadowing could be further investigated. In 2017 Xe+Xe collisions were delivered by the LHC. Speculatively, a complementary study of CASTOR jets in p+Xe collisions would allow to probe the A -dependence of nuclear shadowing.

A more involving improvement would be to enhance the uncertainty in the energy scale of CASTOR. This would potentially allow, for example, to distinguish between the different parameterisations of the AAMQS collaboration in the high-energy region of the p+Pb spectrum. The p+p dataset at $\sqrt{s} = 5$ TeV was recorded with common data taking with the TOTEM experiment, and furthermore trigger signals from a CASTOR high-energy jet trigger were exchanged. Therefore, this dataset allows to combine CASTOR and T2 data and construct particle-flow jets. These objects would have a well-defined η -coordinate and p_T value. Speculatively, CASTOR-T2 particle-flow jets would therefore allow to calibrate the p_T of a CASTOR jets w.r.t. a central object in the CMS detector. An initial analysis of CASTOR-T2 flowjets is presented in appendix A.8.

² Mueller-Navelet jets are jet pairs above a certain p_T threshold that have the largest rapidity separation of all jets in the event

SUMMARY

To our best understanding, there exist four fundamental forces in Nature. One of these is QCD, which is a non-Abelian $SU(3)$ residual gauge symmetry of the Standard Model Lagrangian. Quarks are fundamental matter fields, and QCD binds the quarks into composite particles that are hadrons.

The force carrier (the quantum) of QCD is the gluon. Due to the self-interactions of the gluons, the coupling strength of QCD becomes strong for length scales larger than approx. the proton radius. Therefore, QCD *confines* the quarks into colour-neutral hadrons.

Since the QCD coupling becomes strong for large distance scales, no perturbative predictions can be made about the structure of hadrons. Therefore, the interaction of a hadron is *factorised* into a non-perturbative long-distance part that is called a pdf, together with short-distance partonic matrix elements. The structure function is bound to the particular hadron, while the perturbative partonic matrix elements are entirely general. The strength of the factorisation approach resides in the fact that the structure of a particular hadron needs to be measured only once, and can thereafter be used to generate predictions for different observables or collision types.

A relatively clean method to experimentally extract the pdf of a hadron is deep inelastic scattering, in which we probe the hadron structure with a lepton. For this type of collisions, two particularly relevant kinematical variables can be determined from the outgoing lepton. One is the x -value; to first order this corresponds to the longitudinal momentum fraction of the struck quark. The other observable is the virtuality Q^2 . In a particular frame, this may be thought of as the squared transverse momentum exchange between the electron and the hadron, and thus as the transverse resolution by which we probe the hadron.

To describe the hadronic interactions in various kinematical regimes, different approximations are made. For *collinear* factorisation, it is assumed that the partons do not carry any intrinsic transverse momentum. These parton densities are typically measured at a particular virtuality Q_0^2 as a function of x . The density may be evolved to higher virtualities using the DGLAP equations; solutions of these equations resum large logarithms in Q^2 . In a birds-eye view, the kinematical region of collinear factorisation is therefore large transverse scales and not too small x -values.

The complementary kinematical domain is found at moderate transverse scales and small x -values. In this regime collinear factorisation is expected to be inapplicable for mainly two reasons. Firstly, the intrinsic transverse momentum of the partons cannot be neglected w.r.t. the small longitudinal momentum anymore. Furthermore, to evolve parton densities at small x the logarithms in $1/x$ rather than Q^2 need to be resummed. k_T factorisation takes both effects into account, and the experimental input is an *unintegrated* pdf; this usually is a k_T distribution at an initial scale x_0 . The evolution equation to evolve the updf to lower x -values is the BFKL equation.

However, the BFKL equation predicts an exponential growth in $1/x$ of the gluon density, leading to a unitarity violation. A hypothesised solution to this problem is a *non-linear* extension of the BFKL equation, called the BK equation.

At low x -values, the density of gluons becomes large. Simultaneously, a gluon occupies a transverse area of size $\approx 1/Q^2$. Thus, it is anticipated that *recombination reactions* occur when the collective area of the gluons at a certain scale Q^2 starts to exceed the area of the hadron, by which the gluons effectively migrate to higher x -values. The non-linear reactions tame the evolution speed, and are expected to set in at low x -values and small virtualities.

The BK equation leads to a dynamically generated hadron-specific *saturation scale* $Q_s^2(x)$, which describes the virtuality where the recombination reactions set in as function of x . In a heavy ion the saturation scale is expected to be larger than in a proton by a factor $A^{1/3}$, which is approx. six for lead ions. Therefore, the saturation effects are more pronounced in lead than a proton.

Saturation has been at the focal point of the QCD community for over two decades. Previous analyses found hints for saturation, but the interpretation of the results was diffused by various effects.

In a hadron-hadron collision the interaction of a hard (high- x) parton from one hadron with a soft parton from the other results in one or more forward jets. Therefore, forward low- p_T jets constitute a sensitive observable to saturation effects. In this thesis we review the hypothesis on gluon saturation by studying very forward low- p_T jets in proton-lead collisions at $\sqrt{s_{NN}} = 5$ TeV at the CMS experiment. The collisions were delivered to CMS in 2013 by the Large Hadron Collider. Furthermore, an analysis of forward low- p_T jets may also allow to assess whether collinear factorisation is still applicable at very low- x .

The CMS experiment is a general purpose detector. It has an onion-like structure that allows the experiment to identify and measure all particle species emerging from the hadronic collisions. The analysis presented in this thesis benefitted from three subsystems in particular: the central tracker (for vertex identification), the forward hadronic calorimeters (for selecting events with a hard partonic interaction), and the very forward CASTOR calorimeter, which is the key detector of the analysis.

CASTOR is a Cherenkov sampling hadronic calorimeter; it consists of tungsten plates as absorber, interleaved with quartz plates that generate the Cherenkov radiation. It is located on one side of the CMS experiment only, and measures in $-6.6 < \eta < -5.2$, which is unrivalled at the LHC. It has a 16-fold transversal and 14-fold longitudinal segmentation. However, CASTOR has no η -segmentation. Substantial contributions to both the online and offline conditions and performance of CASTOR during the LHC Run 2 were presented, and a significant contribution to the data taking campaign of CASTOR to collect the p+p and Pb+Pb collisions at $\sqrt{s} = 5$ TeV was made.

Measurements of differential inclusive forward jet cross sections as function of the jet energy in proton-lead collisions at $\sqrt{s_{NN}} = 5$ TeV were presented. All results were corrected to the particle level, which is accomplished via unfolding. Since the lack of η -segmentation complicates the procedure, extensive tests were performed to comprehend and validate the final results. For the same reason the measurements were presented in the laboratory η -range $-6.6 < \eta < -5.2$. Beam configurations with either the proton (p+Pb) or ion (Pb+p)

towards CASTOR were studied. The ratio $p\text{Pb}/\text{Pb}+p$ was also presented, for which certain systematical uncertainties (approximately) cancel.

To test the hypothesis on gluon saturation, two specific saturation models were confronted with the $p\text{Pb}$ data, in which we probe the soft gluons of the ion with the hard partons of the proton. From the KATIE KS model, we learned that the $p\text{Pb}$ spectrum is potentially indeed very sensitive to saturation; the linear and non-linear predictions differ by an order of magnitude in the low energy part of the spectrum. All saturation models underestimate the data by approx. an order of magnitude in this region. The KATIE linear model has furthermore a too soft spectrum, while the KATIE non-linear model describes the shape of the data reasonably well.

The AAMQS models describe only the high-energy part of the spectrum, and clearly have a wrong shape. EPOS-LHC and QGSJETII-04, which incorporate a phenomenological approach to gluon saturation, evidently have a too soft spectrum. The HIJING model on the other hand, which utilises DGLAP-based parton showers and nuclear shadowing, provides a good description of the $p\text{Pb}$ spectrum.

Further, we compared also the predictions of EPOS-LHC, HIJING, and QGSJETII-04 to the $\text{Pb}+p$ spectrum. This spectrum is dominated by the ion debris though, in which subtle saturation effects drown. The $p\text{Pb}/\text{Pb}+p$ ratio was studied also, which has an enhanced resolution w.r.t. the $p\text{Pb}$ and $\text{Pb}+p$ spectra. A purely data-driven interpretation of the ratio in terms of saturation is complicated though, since besides the ion debris the $p\text{Pb}$ and $\text{Pb}+p$ measurements correspond to a different η -acceptance in the proton-ion centre-of-mass frame. None of the models is able to describe all aspects of the data presented.

Since it is estimated that for the $p\text{Pb}$ setup $Q_s^2 \approx 16 \text{ GeV}^2$ (well above the perturbation scale) and that the hard partons causing these jets carry approx. $x = 0.25$ (well below the kinematic limit $x \rightarrow 1$), the effects that blurred the interpretation of previous analyses are not present in this analysis.

The saturation-based models, given their current state-of-the-art, are not supported by the data. This implies that gluon saturation is either not realised by Nature in this part of the phase-space, or that the effects are modelled incorrectly. A model with DGLAP-based parton showers and a particular model of nuclear shadowing successfully describes various features of the data. This suggests that collinear factorisation is still applicable to this kinematic domain, and that shadowing effects on the nucleon level potentially explain the observations, instead of effects on the parton level.

This analysis not only addresses the hypothesis on gluon saturation and k_T -factorisation, but also aims at establishing the experimental viability of CASTOR jets. Thereby, the results aim to pave the way for further CASTOR jet analyses. From the many new and unprecedented opportunities, the most evident extension of this analysis would be a complementary study of the CASTOR jet spectrum in the $\sqrt{s} = 5 \text{ TeV}$ $p+p$ collisions.

Voor zover momenteel bekend is, bestaan er vier fundamentele krachten in de Natuur. Een van deze krachten is QCD (Quantum Chromo Dynamica). QCD is een niet-Abelse $SU(3)$ residueel eik symmetrie van de Standaard Model Lagrangiaan. In deze Lagrangiaan zijn de quarks fundamentele massa velden, die door QCD in samengestelde deeltjes worden gebonden die hadronen heten.

Het krachtdeeltje (ook wel het kwantum) van QCD is het gluon. Door de zelf-interacties van de gluonen wordt de koppeling van QCD sterk voor afstand schalen groter dan ongeveer de afmeting van een proton. Dit leidt ertoe, dat quarks alleen in kleur-neutrale hadronen voorkomen.

Aangezien de koppeling sterk is voor afstand schalen van ongeveer de grootte van een hadron, is het niet mogelijk perturbatieve berekeningen en voorspellingen te maken van de structuur van hadronen. Om die reden wordt de interactie van een hadron *gefactoriseerd* in een niet-perturbatief deel dat een parton distributie functie (pdf) wordt genoemd, samen met partonische matrix elementen. De structuur functies zijn hadron-specifiek, terwijl de perturbatieve matrix elementen, die de interacties van partonen op kleine afstand schalen beschrijven, juist geheel algemeen zijn. Daarom is de kracht van factorisatie, dat de structuur functies van een hadron slechts eenmaal gemeten dienen te worden. Hierna kan de pdf gebruikt worden om voorspellingen te genereren voor specifieke interacties van het hadron, in verschillende collisie scenarios.

Een relatief zuivere manier om de pdf's te meten is door zogenaamde Diepe Inelastische Verstrooiingen te meten; in deze interacties meten we de structuur van een hadron met behulp van een lepton (bijvoorbeeld een elektron). Voor dit type botsing kunnen twee specifieke kinematische observabelen worden gedefinieerd m.b.v. een meting van het uitgaande lepton. Een is de Bjorken- x ; bij benadering correspondeert x met de longitudinale momentum fractie van het quark dat interageert. De andere observabele is de virtualiteit Q^2 . In een speciaal frame kan de virtualiteit voorgesteld worden als het kwadraat van de transversale momentum uitwisseling tussen het lepton en het hadron. Daarom kan de virtualiteit wel vergeleken worden met de *transversale resolutie* waarmee het hadron bestudeerd wordt.

Om de hadronische interacties in verschillende kinematische regimes te beschrijven, moeten verschillende aannames gemaakt worden. Voor *collineaire factorisatie* neemt men aan dat de partonen geen intrinsiek transversaal momentum hebben. Deze parton distributie functies worden typisch gemeten op een referentie schaal Q_0^2 als functie van x , en de functie kan naar hogere virtualiteiten *geëvolueerd* worden m.b.v. de DGLAP vergelijkingen. Oplossingen van deze vergelijkingen hersommen logaritmen in Q^2 . Samenvattend kan dus gesteld worden dat collineaire factorisatie typisch van toepassing is op collisies met grote transversale momentum schalen, bij niet te lage x -waarden.

Het complementaire kinematische domein bestaat uit kleine transversale momentum schalen en zeer lage x -waarden. In dit kinematisch regime wordt verwacht dat collineaire factorisatie

niet toepasbaar is door voornamelijk twee redenen. Ten eerste kan bij lage x waarden het intrinsieke transversale momentum van de gluonen niet meer verwaarloosd worden t.o.v. het lage longitudinale momentum. Ten tweede dienen voor de evolutie niet de logaritmen in Q^2 maar in $1/x$ gehersommeerd te worden. k_T -factorisatie brengt beide effecten in rekening, en de experimentele input is een niet-geïntegreerde pdf; doorgaans is dit een k_T -distributie op een initiële schaal x_0 . De evolutie vergelijking om de pdf te evolueren naar lagere x -waarden is de BFKL vergelijking.

De BFKL vergelijking voorspelt echter een exponentiële groei van de gluon density in $1/x$, wat tot een unitariteitsschending leidt. Een hypothetische oplossing voor dit probleem wordt geleverd door een *niet-lineaire* uitbreiding van de BFKL vergelijking, genaamd de BK vergelijking.

Bij lage x waarden wordt de gluonen dichtheid in een hadron hoog. Tegelijkertijd schaalt de karakteristieke transversale oppervlakte van een gluon met $1/Q^2$. Daarom wordt verondersteld dat *fusie-reacties* plaats vinden wanneer het collectieve oppervlak van de gluonen bij een zekere schaal Q^2 groter wordt dan het oppervlak van het betreffende hadron zelf. Door dit veronderstelde effect *migreren* gluonen van een lage naar een hogere x -waarde. Door dit effect remmen de fusie reacties dus de groei in $1/x$. Deze reacties worden typisch verwacht bij lage x en Q^2 waarden.

De BK vergelijking leidt tot een dynamisch gegenereerde *saturatie schaal* $Q_s^2(x)$. Deze schaal beschrijft de virtualiteit waarbij de fusie reacties relevant worden als functie van x . Deze schaal is hadron-specifiek; in een loodkern wordt verwacht dat deze hypothetische schaal ongeveer een factor zes groter is dan in een proton. Men verwacht dus, dat de effecten van de fusie reacties sterker zijn in een loodkern (of een andere zware atoomkern) dan in een proton.

De hypothetische saturatie van de gluonen dichtheid staat al tientallen jaren volop in de belangstelling van de deeltjes fysica gemeenschap. Verscheidene analyses van collisies vonden aanwijzingen voor saturatie, maar een eenduidige interpretatie was doorgaans niet mogelijk om uiteenlopende redenen. In een hadronische interactie lijdt de interactie van een hard parton (met een hoge x waarde) van een hadron met een zacht parton van het andere hadron tot een of meerdere voorwaartse jets. Daarom vormen voorwaartse jets met een laag transversaal momentum een observabele die sensitief is voor effecten van gluon saturatie.

In deze thesis testen we de hypothese m.b.t. gluon saturatie door een studie van zeer voorwaartse jets met een laag transversale momentum in proton-lood botsingen met $\sqrt{s_{NN}} = 5$ TeV met het CMS experiment. De botsingen werden door de Large Hadron Collider geleverd in 2013. Bovendien staat een dergelijke analyse ook toe om te testen of collineaire factorisatie nog van toepassing is bij lage x waarden.

De CMS detector is georiënteerd op een algemeen fysica programma; de detector wordt gebruikt voor metingen van allerhande fenomenen zoals de productie van Higgs deeltjes, zoektochten naar nieuwe deeltjes, en bijvoorbeeld studies van QCD effecten. De detector heeft een cilindrisch gelaagde structuur, die het experiment in staat stelt om alle deeltjes die uit een botsing komen te identificeren en hun kinematica te meten. De analyse die in deze thesis besproken wordt was afhankelijk van drie sub-detectors in het bijzonder: de centrale tracker (voor de identificatie van collisie-vertexen), de hadronic-forward calorimeters (voor

het selecteren van botsingen met een harde, partonische interactie), en de zeer voorwaartse CASTOR detector; deze detector speelt een sleutelrol in onze meting.

CASTOR is een longitudinaal gesegmenteerde hadronische Cherenkov calorimeter. De detector bestaat uit wolfram platen die dienen om de invallende hadronen te absorberen. Deze worden afgewisseld met kwarts platen, die de Cherenkov radiatie genereren. CASTOR is gesitueerd aan enkel een zijde van het CMS experiment, en meet collisie producten in $-6.6 < \eta < -5.2$; daarmee is CASTOR uniek bij de LHC. CASTOR heeft een 16-voudige transversale en 14-voudige longitudinale segmentatie. De detector heeft echter geen η -segmentatie. Verscheidene substantiële bijdragen aan het online en offline functioneren van CASTOR werden gepresenteerd. Ook werd een significante bijdrage geleverd aan de campagne om CASTOR data van proton-proton en lood-lood botsingen met $\sqrt{s} = 5 \text{ TeV}$ te verzamelen in 2015.

Als finaal resultaat werden metingen van de differentiële inclusieve werkzame doorsnede voor jet productie als functie van de jet energie in proton-lood botsingen met $\sqrt{s_{NN}} = 5 \text{ TeV}$ gepresenteerd. Alle resultaten werden gecorrigeerd voor detector effecten. Om de data correct te corrigeren werd een speciale numerieke ontvouwingstechniek toegepast. Aangezien het gebrek aan η segmentatie de procedure compliceert, werden verscheidene tests uitgevoerd om de finale resultaten te valideren. Om dezelfde reden zijn de resultaten gepresenteerd in het laboratorium stelsel in plaats van het massa-middelpunts stelsel. Zowel deeltjesbundel configuraties waarbij het proton (p+Pb) of ion (Pb+p) naar CASTOR gericht was werden bestudeerd. Ook de ratio p+Pb/Pb+p werd geanalyseerd, waarvoor bepaalde systematische onzekerheden grotendeels wegvallen.

Om de hypothese m.b.t. gluon saturatie te testen werden twee specifieke saturatie modellen met de p+Pb data geconfronteerd. Voor deze configuratie worden de harde partonen van het proton gebruikt om de zachte gluonen van het ion te meten. Het KATIE KS model bevestigt dat de data potentieel inderdaad zeer sensitief zijn voor saturatie effecten; het lineaire en niet-lineaire model verschillen ongeveer een orde van grootte in het lage energie deel van het spectrum. Alle saturatie modellen onderschatten de data met een grootte orde in deze regio. Daarnaast heeft het KATIE lineaire model een te zacht spectrum, terwijl het niet-lineaire spectrum de data goed beschrijft.

De AAMQS modellen beschrijven alleen het hoge-energie deel van het spectrum, en de vorm van de spectra beschrijven de data evident niet. Twee andere modellen, EPOS-LHC en QGSJETII-04, die beide een fenomenologische implementatie van saturatie bevatten, voorspellen beiden een te zacht spectrum. Het HIJING model daarentegen, wat berust op DGLAP-gebaseerde parton evolutie en shadowing effecten, die zich op nucleon in plaats van parton niveau afspelen, geven een goede beschrijving van het proton-lood spectrum.

Voorts vergeleken we de voorspellingen van EPOS-LHC, HIJING, en QGSJETII-04 met het Pb+p spectrum. Dit spectrum wordt echter gedomineerd door de brokstukken en resten van het ion. Dit geeft een dusdanig grote bijdrage aan het signaal, dat verwacht wordt dat subtiële effecten van saturatie hierdoor overstemd worden en niet zichtbaar zijn. De ratio p+Pb/Pb+p werd ook bestudeerd. De ratio heeft een verbeterde resolutie t.o.v. de individuele p+Pb en Pb+p spectra.

Hoewel zeer wenselijk, is het echter lastig om een conclusie te trekken puur op grond van de data. Enerzijds komt dit door de ion overblijfselen. Anderzijds corresponderen de p+Pb

en Pb+p meting met verschillende η -acceptanties in het mass-middelpunts stelsel, waardoor verschillende effecten verweven raken in het eindresultaat. Geen van de modellen is in staat alle aspecten van de data te beschrijven.

De modellen gebaseerd op saturatie, gegeven hun huidige staat van dienst, beschrijven de data niet. Dit impliceert dat gluon saturatie of niet door de Natuur gerealiseerd wordt in dit kinematisch gebied, of dat de effecten niet correct gemodelleerd worden. Een model gebaseerd op collineaire factorisatie en een specifieke implementatie van nucleaire shadowing beschrijft de p+Pb data goed. Dit suggereert dat collineaire factorisatie nog steeds goed toepasbaar is in dit kinematische domein, en dat effecten op nucleon in plaats van parton niveau potentieel de metingen kunnen verklaren.

Deze analyse beschouwd niet alleen de hypothese m.b.t. gluon saturatie en collineaire versus k_T factorisatie, maar tracht ook, door middel van een eerste publicatie, de bruikbaarheid van CASTOR jets te bewijzen voor fysica analyses. Daarmee effent de analyse ook de weg voor toekomstige CASTOR jet analyses. Er zijn bijzonder veel mogelijkheden voor uitbreidingen. De meest voor de hand liggende optie zou een referentie meting van het CASTOR jet spectrum in proton-proton botsingen bij een massa-middelpunts energie van $\sqrt{s} = 5$ TeV zijn.

Part V

APPENDIX

APPENDICES

A.1 RESULTS ON P+PB COLLISIONS PREPARED FOR JOURNAL SUBMISSION

In chapter 21 we presented our main results. However, only a subset of the KATIE and AAMQS predictions was selected for the final figure in the draft paper. This figure has been depicted below for completeness.

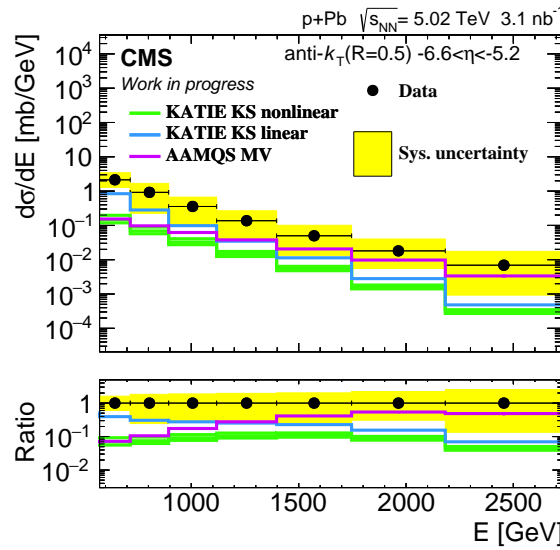


Figure 85: The stable-particle level differential jet energy cross section for p+Pb. Results from data are compared to predictions by KATIE and AAMQS

A.2 GLOBAL SYMMETRIES OF THE STANDARD MODEL

Besides of the local gauge symmetries, the Standard Model Lagrangian also possesses certain *approximate* global symmetries, which we discuss (non-exhaustively) in this appendix. A general discussion may for example be found in [17].

Two approximate $U(2)$ symmetries are realised, one per chiral state of the quarks. These symmetries would be exact in the limit of massless quarks. These symmetry groups work on the weak doublets of the Lagrangian. The groups can be decomposed into $SU(2) \times U(1)$.

Two linear combinations of $SU(2)_L \times SU(2)_R$ form the vector and axial symmetry. The associated Goldstone bosons are the charged and neutral pion. Currently, it is known though that the pions are not fundamental particles; they are mesons and constitute of two quarks.

The pions are responsible for the force that keeps the nucleons in a nucleus together instead of being driven apart by their Coulomb charge.

The $U(1)$ vector symmetry induces baryon number conservation. The conserved current is given by $\bar{\psi}\gamma^\mu\psi$. The $U(1)$ axial symmetry is a symmetry of the classical Lagrangian density, but this symmetry is broken when the Lagrangian is quantised and thus (even approximately) not realised in Nature. Classically, the symmetry would induce a conserved current of the form $\bar{\psi}\gamma^\mu\gamma^5\psi$.

A.3 KINEMATICS IN DIS SCATTERING

In this section we start with further outlining certain kinematical relations that were straightforwardly used in the thesis without a derivation or motivation.

A.3.1 The virtuality versus the transversal scale

We start with a review of the relation between the transversal scale (p_T) and virtuality Q^2 in an e+p collision.

The following relations can be deduced:

$$\begin{aligned} Q^2 &= 2E_e E'_e (1 - \cos(\theta')) = 2E_e E'_e \sin^2(\theta'/2) \\ y &= 1 - \frac{E'_e}{E_e} \cos(\theta/2)^2 \\ p_{T,e} &= E' \sin(\theta) = 2E' \sin(\theta/2) \cos(\theta/2) \end{aligned} \tag{91}$$

In this equation all quantities labelled with e refer to the electron, and the primed variables denote kinematical quantities of the outgoing electron in the laboratory frame. We refer to chapter 4 for the definitions of the other variables.

Thus, it follows that

$$Q^2 = \frac{p_{T,e}^2}{1 - y} \tag{92}$$

Thus, we observe that the virtuality Q^2 does not *equal* the transversal scale. The virtuality rather specifies the *maximal* p_T that the electron can have, under the kinematical condition that $y = 0$. The latter occurs when the electron does not transfer any longitudinal momentum.

A.3.2 Deriving the longitudinal momentum fraction from x , \sqrt{s} , and p_T

We stated in the hypothesis that $x = \frac{p_{T,e}^{-|\eta|}}{\sqrt{s}}$. We elaborate this statement.

We recall the definition of the rapidity y , which equals the pseudorapidity η for massless particles:

$$\eta = \frac{1}{2} \log \left(\frac{1 + \beta}{1 - \beta} \right). \quad (93)$$

We consider two massless hadrons with $p_Z = \pm E$. In a collision, two partons may interact, which carry a momentum fraction x_1 and x_2 . The η -value of this system w.r.t. the lab frame is then given by:

$$\eta = \frac{1}{2} \log \left(\frac{x_1}{x_2} \right). \quad (94)$$

We may rewrite $\frac{1}{2} \log \left(\frac{x_1}{x_2} \right) = \log \left(\sqrt{\frac{x_1}{x_2}} \right)$.

Thus we obtain:

$$e^\eta \sqrt{x_1 x_2} = x_1. \quad (95)$$

We observe that $x_1 x_2$ can be related to the total centre-of-mass energy S , via the parton centre-of-mass energy s via:

$$x_1 x_2 = \frac{s}{S}. \quad (96)$$

Thus, if we assume that all the parton centre-of-mass energy is converted to p_T of the outgoing particles, we obtain the desired result:

$$x = \frac{p_T e^{-|\eta|}}{\sqrt{s}}. \quad (97)$$

What we learn from the derivation, is that again the p_T sets only a limit: the above equation denotes a minimum for x , since a part of the parton centre-of-mass energy may have also been converted into longitudinal momentum.

A.4 THE OPTICAL THEOREM

The probability for any interaction between an initial and final state in QFT is contained in the S -matrix. It can be proven that the scattering matrix is *unitary* [17]: $SS^\dagger = 1$. This matrix can be decomposed into a trivial part (no interaction takes place), and the transition matrix T that prescribes the interactions, via $S = 1 + iT$. It follows that

$$-i(T - T^\dagger) = T^\dagger T. \quad (98)$$

We imagine a scattering process of initial states k_1, k_2 to p_1, p_2 . The states have momentum k'_1, k'_2 and p'_1, p'_2 , respectively. The transition matrix is related to the scattering amplitude \mathcal{M} via a momentum-conserving delta function:

$$(2\pi)^4 \delta^4(k'_1 + k'_2 - (p'_1 + p'_2)) \mathcal{M}(k_1, k_2 \rightarrow p_1, p_2) = \langle p_1, p_2 | T | k_1, k_2 \rangle. \quad (99)$$

For notational convenience, we absorb the delta function in the definition of scattering amplitude and obtain:

$$\mathcal{M}(k_1, k_2 \rightarrow p_1, p_2) = \langle p_1, p_2 | T | k_1, k_2 \rangle. \quad (100)$$

The unitarity of the S -matrix can be exploited to derive the optical theorem. We sandwich eq. 101 between the initial and final states, and insert a resolution of the identity of the form $1 = \sum |q\rangle \langle q|$ in the right-hand side:

$$-i(\langle p_1, p_2 | T | k_1, k_2 \rangle - \langle p_1, p_2 | T^\dagger | k_1, k_2 \rangle) = \sum_q \langle p_1, p_2 | T^\dagger | q \rangle \langle q | T | k_1, k_2 \rangle. \quad (101)$$

We can rewrite the equation in terms of scattering amplitudes:

$$-i(\mathcal{M}(k_1, k_2 \rightarrow p_1, p_2) - \mathcal{M}^*(p_1, p_2 \rightarrow k_1, k_2)) = \sum_q \int dq' \mathcal{M}(k_1, k_2 \rightarrow q) \mathcal{M}^*(p_1, p_2 \rightarrow q). \quad (102)$$

For an elastic and forward scattering amplitude, the initial state $|k_1, k_2\rangle$ equals the final state $\langle p_1, p_2|$. Inserting this special condition in eq. 102, we finally obtain the desired optical theorem:

$$2\text{Im}(\mathcal{M}(k_1, k_2 \rightarrow k_1, k_2)) = \sum_q \int dq' |\mathcal{M}(k_1, k_2 \rightarrow q)|^2 \quad (103)$$

Concluding, the optical theorem relates the imaginary part of the forward elastic scattering amplitude to the total cross section for the initial state to scatter into any state q .

A.5 TECHNICAL ANALYSIS INFORMATION

In this appendix we quote certain technical details that are relevant for reproducibility of the analysis.

A.5.1 Data analysis

The MinbiasUPC dataset, which contains the events that we analyse, is located at `/hidata/HIRun2013/PAMinBiasUPC/RECO/PromptReco-v1/`.

The dataset was processed with the reconstruction software of CMSSW version 5_3_8_patch2. The reconstructed data set was thereafter analysed within the framework of CMSSW version 5_3_32 using the conditions from Global Tag GR_R_53_V21.

The run numbers that were used in this analysis are depicted in table 9. These runs were processed with the official golden JSON file to select the correct luminosity sections; the file may be found on the LXPLUS servers of CERN at:

`/afs/cern.ch/user/m/mnguyen/public/pPbJSON/Cert_210676-211631_HI_PromptReco_Collisions13_JSON_v2.txt`.

The effective luminosity was calculated using the lumicalc software, which can be found at:

<https://cms-service-lumi.web.cern.ch/cms-service-lumi/brilwsdoc.html>

Table 9: Runs numbers used in this analysis, together with the integrated luminosity and peak pileup

Run number	Integrated luminosity (nb^{-1})	Peak pileup (%)
Proton to CASTOR (p+Pb)		
210885	1.15	6.28
210998	0.50	4.57
211000	0.34	3.03
211001	0.11	2.31
211032	1.04	4.95
Total (5)	3.13	-
Beam reversal, ion to CASTOR (Pb+p)		
211256	1.03	7.11
211371	0.55	6.68
211390	0.84	6.34
211460	0.95	7.83
211532	1.13	7.31
211538	1.19	7.36
211607	1.04	7.63
Total (7)	6.71	-
overall (12)	9.84	-

A.5.2 Event simulation

The response of the CMS detector was simulated in CMSSW version 5_3_32 with Global Tag STARHI53_V27. In the simulation the alignment of CASTOR, its baseline, and its noise were also adapted to the data-taking conditions, although this information does not reside in the Global Tag. Manual adjustments have to be made in the simulation code to insert the correct conditions for CASTOR (a technical explanation is provided in [154], but this source is only accessible to CMS members).

A.6 GENERATOR-LEVEL PARTICLES FOR JETS

On generator level, generally all particles that are not in a partonic state are accepted and clustered into particle jets. The decay products of resonances, neutrinos, τ , and μ leptons are ignored though. The CMSSW collection "genparticlesforjets" was used. The precise definition of this class can be found at:

https://github.com/cms-sw/cmssw/blob/09c3fce6626f70fd04223e7dacebf0b485f73f54/RecoJets/Configuration/python/GenJetParticles_cff.py

The pdg codes can be reviewed at:

<http://pdg.lbl.gov/2007/reviews/montecarlo.pdf>

A.7 CALCULATION OF THE χ^2/N_{DOF} BETWEEN THE BACKSMEARED AND DATA SPECTRUM

In this section we succinctly outline the procedure to calculate the χ^2/N_{dof} between the data and the backsmeared spectrum.

- The following ingredients are needed for the calculations:
 - S_{dif} : the vector of the bin-to-bin difference between the data and backsmeared spectrum
 - The covariance matrix V
- To calculate S_{dif} :
 - We subtract the fakes from the data spectrum
 - We unfold the data spectrum E_{Reco} to E_{gen} (we do not add misses)
 - We calculate the best estimate of the backsmeared spectrum: $E_{\text{BackSmear}} = R \circ E_{\text{gen}} + E_{\text{fake}}$, which R is the response matrix
 $\rightarrow S_{\text{dif}} = E_{\text{Reco}} - E_{\text{BackSmear}}$
- The calculation of the covariance matrix V is more involving and requires a Monte-Carlo simulation:
 - We need $\approx 10^4$ *perturbed* backsmeared distribution $E'_{\text{BackSmear}}$. To this purpose:
 - * We generate a Poissonian perturbed response object R' (not to be mistaken with the response matrix, we explain the calculation below)
 - * We poissonian perturb the fake spectrum to obtain E'_{fake} (we first scale to the proper number of events and then apply the perturbation)
 - * We obtain: $E'_{\text{BackSmear}} = R' \circ E_{\text{gen}} + E'_{\text{fake}}$
 - We calculate $E'_{\text{BackSmear}}$ 10^4 times, to obtain an average $\bar{E}'_{\text{BackSmear}}$
 - We generate 10^4 matrices $V_{i,j}^n = ((E')_{\text{BackSmear},i}^n - \bar{E}'_{\text{BackSmear},i}) \times ((E')_{\text{BackSmear},j}^n - \bar{E}'_{\text{BackSmear},j})$

- From $V_{i,j}^n$ we calculate an average matrix \bar{V} .
- We add the data to the diagonal of the matrix (which can be perceived as the statistical error on the data squared)
- We invert the matrix (this turned out always possible in our calculations)
- We apply a cutoff of 600 GeV to our vectors and matrices, since our objective is to obtain the χ^2/N_{dof} for $E > 600$ GeV
- Finally, we calculate the χ^2/N_{dof} via matrix multiplication: $\rightarrow \chi^2/N_{\text{dof}} = S_{\text{dif}} \circ V^{-1} \circ S_{\text{dif}}/N_{\text{Bins}}$

The generator and detector-level jets, together with the response matrix M , constitute the response object. The perturbed response object R' , which is needed for the perturbed backsmearing, is calculated as follows:

- First, we need a perturbed data and generator spectrum:
 - We obtain the matched generator and detector-level spectra as a one-dimensional projection from the response matrix. We apply Poissonian perturbations to the spectra
 - We add perturbed fakes to the perturbed matched detector-level spectrum to obtain the perturbed data spectrum
 - We add perturbed misses to the perturbed matched generator-level spectrum to obtain the perturbed generator spectrum
 - We perturb the elements of the response matrix to obtain M'
- From these three objects we obtain the perturbed response object R'

A.8 CASTOR-T2 FLOWJETS

In this thesis, we have been confronted at various points with the disadvantages due to the lack of η -resolution of CASTOR. As a result, the CASTOR jets do not have a p_T -value, and cannot not be corrected back to the centre-of-mass frame for the asymmetric p+Pb collisions. Another consequence is the relatively large model uncertainty on our final results on particle level; this uncertainty is even dominant in the ratio p+Pb/Pb+p.

Common data taking with the CMS and TOTEM experiment was achieved in 2013. The data of CASTOR and T2 were successfully merged and correlated. This allowed to derive the alignment of CASTOR in-situ with an independent method, we refer to Fig. 52.

We investigated the potential of combining the CASTOR deposits and T2 tracks into flow-jets, since such jets would potentially overcome the adversities mentioned above. To this purpose we created FlowObjects, consisting of CASTOR sectors and primary T2-tracks¹:

- We consider a CASTOR sector above threshold

¹ These are tracks with a high probability to emerge from a primary p+Pb collision

- We count the incident primary T2 tracks in front of the sector
 - No Track: we keep the default η and ϕ of the sector
 - One track: we update the sectors coordinates with η and ϕ of the track
 - multiple tracks: we update the coordinates of the sector with the mean η and ϕ of the tracks
 → We observe that not all sectors may be updated
- We run an anti- k_T (R) cluster algorithm on the FlowObjects
 - Updated FlowJet: flow jet with at least 1 primary T2 track towards it
 - Complete FlowJet: all sectors of jet Updated
- An updated or complete FlowJet *does* have both a p_T and η coordinate.

We illustrate a CASTOR-T2 flowjet (for a jet radius of 0.7) in Fig. 86. We observe the presence of sectors that are (not) updated. The final CASTOR jet is indicated in black, while the FlowJet is in red. We observe substantial differences between these jets, for example the CASTOR jet contains four and the FlowJet only three sectors.

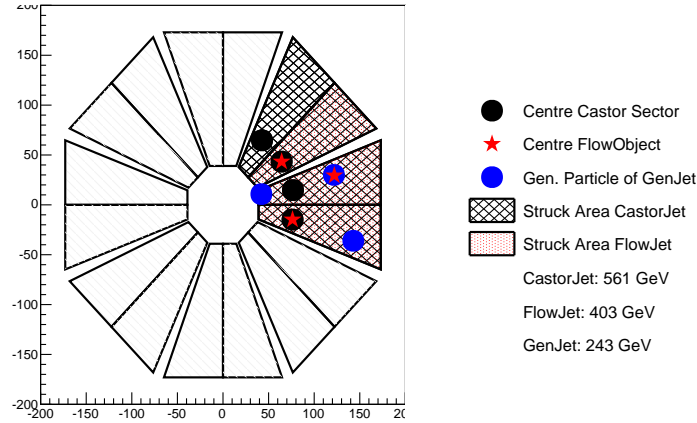


Figure 86: An schematic illustration of a CASTOR jet and CASTOR-T2 FlowJet

A simple generator-only study was pursued to obtain a first-order estimate of the benefits of T2 tracks on the p_T resolution of the CASTOR jets. This study was conducted as follows:

- We generated 5 TeV collisions with Pythia. We cluster the energy in the CASTOR acceptance into CASTOR sectors
- We use the η and ϕ coordinates of the *charged* particles in the T2 acceptance as T2 Tracks

- We update the CASTOR sectors as outlined above
 → By this means we simulate the effect of clustering, transversal leakage and the invisibility of neutral particles

The resolution of the CASTOR jets and FowJets was investigated, by comparing their kinematical properties to the generator jet collection. We found that the p_T resolution of CASTOR jets w.r.t. updated (complete) flowjets improved from 43 to 32 (20)%. Thus, the resolution improves dramatically by adding the T2 track information.

Ultimately, an analysis of CASTOR-T2 FlowJets could not be completed. The CMS objects for the common dataset are reconstructed in CMSSW software version 5_3_X (we refer to chapter 10). Regrettably, the TOTEM collaboration did not port their software to this particular version of the CMS software. Ultimately, as a consequence this analysis could not be pursued, while the data appear to be in excellent shape.

The author was heavily involved in successfully collecting a common CASTOR-T2 dataset in 2015 in $\sqrt{s} = 5$ TeV p+p collisions. This dataset is reconstructed in CMSSW version 7_1_X, and in this dataset the TOTEM software is available. Regrettably, these data came too late (and unexpected) to be included in this thesis still.

BIBLIOGRAPHY

- [1] *Very forward inclusive jet cross sections in p+Pb collisions at $\sqrt{s_{NN}} = 5.02$ TeV.* Tech. rep. CMS-PAS-FSQ-17-001. Geneva: CERN, 2017. URL: <https://cds.cern.ch/record/2258273>.
- [2] Merijn H. F. van de Klundert. “Very forward inclusive jet cross sections in p+Pb collisions at $\sqrt{s_{NN}} = 5.02$ TeV at CMS.” In: *PoS DIS2017* (2018), p. 045.
- [3] “Results on CASTOR Performance during LHC Run 2.” In: CMS-DP-2016-006 (2016). URL: <http://cds.cern.ch/record/2133152>.
- [4] Merijn H F Van De Klundert. “Performance of the CASTOR calorimeter at CMS during Run II of LHC.” In: CMS-CR-2016-156 (2016). URL: <http://cds.cern.ch/record/2203099>.
- [5] *In review: The CASTOR very forward calorimeter of CMS. To be published in JINST.*
- [6] Merijn H F Van De Klundert. *SOFT QCD AT ATLAS AND CMS*. Tech. rep. CMS-CR-2017-121. Geneva: CERN, 2017. URL: <https://cds.cern.ch/record/2263388>.
- [7] *The figure was obtained from:* <https://commons.wikimedia.org/w/index.php?curid=5970403>.
- [8] *The figure was obtained from:* <http://www.u-tokyo.ac.jp/content/400021545.jpg>.
- [9] *The figure was obtained from:* <http://static.newworldencyclopedia.org/thumb/0/00/Interactions.png/400px-Interactions.png>.
- [10] CMS Collaboration. “Study of vector boson scattering and search for new physics in events with two same-sign leptons and two jets.” In: *Phys. Rev. Lett.* 114.CMS-SMP-13-015 (2014), 051801. 27 p. URL: <https://cds.cern.ch/record/1957133>.
- [11] ATLAS collaboration. “Measurement of $W^{\pm}W^{\pm}$ vector-boson scattering and limits on anomalous quartic gauge couplings with the ATLAS detector.” In: *Phys. Rev. D* 96.CERN-EP-2016-167 (2016), 012007. 34 p. URL: <https://cds.cern.ch/record/2230988>.
- [12] Vardan Khachatryan et al. “Measurement of electroweak production of two jets in association with a Z boson in proton-proton collisions at $\sqrt{s} = 8$ TeV.” In: *Eur. Phys. J. C* 75.2 (2015), p. 66. DOI: [10.1140/epjc/s10052-014-3232-5](https://doi.org/10.1140/epjc/s10052-014-3232-5). arXiv: [1410.3153](https://arxiv.org/abs/1410.3153) [hep-ex].
- [13] Georges Aad et al. “Observation of a new particle in the search for the Standard Model Higgs boson with the ATLAS detector at the LHC.” In: *Phys. Lett. B* 716 (2012), pp. 1–29. DOI: [10.1016/j.physletb.2012.08.020](https://doi.org/10.1016/j.physletb.2012.08.020). arXiv: [1207.7214](https://arxiv.org/abs/1207.7214) [hep-ex].
- [14] Serguei Chatrchyan et al. “Observation of a new boson at a mass of 125 GeV with the CMS experiment at the LHC.” In: *Phys. Lett. B* 716 (2012), pp. 30–61. DOI: [10.1016/j.physletb.2012.08.021](https://doi.org/10.1016/j.physletb.2012.08.021). arXiv: [1207.7235](https://arxiv.org/abs/1207.7235) [hep-ex].

- [15] K. A. Olive et al. "Review of Particle Physics." In: *Chin. Phys.* C38 (2014), p. 090001. DOI: [10.1088/1674-1137/38/9/090001](#).
- [16] A. C. Aguilar, D. Binosi, and J. Papavassiliou. "Gluon and ghost propagators in the Landau gauge: Deriving lattice results from Schwinger-Dyson equations." In: *Phys. Rev. D* 78 (2008), p. 025010. DOI: [10.1103/PhysRevD.78.025010](#). arXiv: [0802.1870 \[hep-ph\]](#).
- [17] Michael E. Peskin and Daniel V. Schroeder. *An Introduction to quantum field theory*. Reading, USA: Addison-Wesley, 1995. ISBN: 9780201503975, 0201503972. URL: <http://www.slac.stanford.edu/~mpeskin/QFT.html>.
- [18] David Griffiths. *Introduction to elementary particles*. 2008. ISBN: 9783527406012.
- [19] R. C. Walker et al. "Measurements of the proton elastic form-factors for $1\text{-GeV}/c^2 \leq Q^2 \leq 3\text{-GeV}/c^2$ at SLAC." In: *Phys. Rev. D* 49 (1994), pp. 5671–5689. DOI: [10.1103/PhysRevD.49.5671](#).
- [20] A. F. Sill et al. "Measurements of elastic electron - proton scattering at large momentum transfer." In: *Phys. Rev. D* 48 (1993), pp. 29–55. DOI: [10.1103/PhysRevD.48.29](#).
- [21] M. Breidenbach, J. I. Friedman, H. W. Kendall, E. D. Bloom, D. H. Coward, H. DeStaebl, J. Drees, L. W. Mo, and R. E. Taylor. "Observed Behavior of Highly Inelastic Electron-Proton Scattering." In: *Phys. Rev. Lett.* 23 (16 1969), pp. 935–939. DOI: [10.1103/PhysRevLett.23.935](#). URL: <https://link.aps.org/doi/10.1103/PhysRevLett.23.935>.
- [22] M. Derrick et al. "Measurement of the F2 structure function in deep inelastic e+p scattering using 1994 data from the ZEUS detector at HERA." In: *Z. Phys.* C72 (1996), pp. 399–424. DOI: [10.1007/BF02909169](#), [10.1007/s002880050260](#). arXiv: [hep-ex/9607002 \[hep-ex\]](#).
- [23] Jorge Casalderrey-Solana and Carlos A. Salgado. "Introductory lectures on jet quenching in heavy ion collisions." In: *Acta Phys. Polon.* B38 (2007), pp. 3731–3794. arXiv: [0712.3443 \[hep-ph\]](#).
- [24] D. P. Barber et al. "Discovery of Three Jet Events and a Test of Quantum Chromodynamics at PETRA Energies." In: *Phys. Rev. Lett.* 43 (1979), p. 830. DOI: [10.1103/PhysRevLett.43.830](#).
- [25] Guido Altarelli and G. Parisi. "Asymptotic Freedom in Parton Language." In: *Nucl. Phys.* B126 (1977), pp. 298–318. DOI: [10.1016/0550-3213\(77\)90384-4](#).
- [26] A. J. Chambers, R. Horsley, Y. Nakamura, H. Perlt, P. E. L. Rakow, G. Schierholz, A. Schiller, K. Somfleth, R. D. Young, and J. M. Zanotti. "Nucleon Structure Functions from Operator Product Expansion on the Lattice." In: *Phys. Rev. Lett.* 118.24 (2017), p. 242001. DOI: [10.1103/PhysRevLett.118.242001](#). arXiv: [1703.01153 \[hep-lat\]](#).
- [27] V. N. Gribov and L. N. Lipatov. "Deep inelastic e p scattering in perturbation theory." In: *Sov. J. Nucl. Phys.* 15 (1972). [*Yad. Fiz.*15,781(1972)], pp. 438–450.

- [28] Yuri L. Dokshitzer. "Calculation of the Structure Functions for Deep Inelastic Scattering and $e^+ e^-$ Annihilation by Perturbation Theory in Quantum Chromodynamics." In: *Sov. Phys. JETP* 46 (1977). [Zh. Eksp. Teor. Fiz.73,1216(1977)], pp. 641–653.
- [29] F. D. Aaron et al. "Combined Measurement and QCD Analysis of the Inclusive $e^+ p$ Scattering Cross Sections at HERA." In: *JHEP* 01 (2010), p. 109. DOI: [10.1007/JHEP01\(2010\)109](https://doi.org/10.1007/JHEP01(2010)109). arXiv: [0911.0884](https://arxiv.org/abs/0911.0884) [hep-ex].
- [30] Krzysztof Kutak and Sebastian Sapeta. "Gluon saturation in dijet production in p-Pb collisions at Large Hadron Collider." In: *Phys. Rev. D* 86 (2012), p. 094043. DOI: [10.1103/PhysRevD.86.094043](https://doi.org/10.1103/PhysRevD.86.094043). arXiv: [1205.5035](https://arxiv.org/abs/1205.5035) [hep-ph].
- [31] K. Kutak and A. M. Stasto. "Unintegrated gluon distribution from modified BK equation." In: *Eur. Phys. J. C* 41 (2005), pp. 343–351. DOI: [10.1140/epjc/s2005-02223-0](https://doi.org/10.1140/epjc/s2005-02223-0). arXiv: [hep-ph/0408117](https://arxiv.org/abs/hep-ph/0408117) [hep-ph].
- [32] Javier L. Albacete and Cyrille Marquet. "Gluon saturation and initial conditions for relativistic heavy ion collisions." In: *Prog. Part. Nucl. Phys.* 76 (2014), pp. 1–42. DOI: [10.1016/j.ppnp.2014.01.004](https://doi.org/10.1016/j.ppnp.2014.01.004). arXiv: [1401.4866](https://arxiv.org/abs/1401.4866) [hep-ph].
- [33] Marcel Froissart. "Asymptotic Behavior and Subtractions in the Mandelstam Representation." In: *Phys. Rev.* 123 (3 1961), pp. 1053–1057. DOI: [10.1103/PhysRev.123.1053](https://doi.org/10.1103/PhysRev.123.1053). URL: <https://link.aps.org/doi/10.1103/PhysRev.123.1053>.
- [34] Ian Balitsky. "Quark contribution to the small- x evolution of color dipole." In: *Phys. Rev. D* 75 (2007), p. 014001. DOI: [10.1103/PhysRevD.75.014001](https://doi.org/10.1103/PhysRevD.75.014001). arXiv: [hep-ph/0609105](https://arxiv.org/abs/hep-ph/0609105) [hep-ph].
- [35] Javier L. Albacete and Yuri V. Kovchegov. "Solving high energy evolution equation including running coupling corrections." In: *Phys. Rev. D* 75 (2007), p. 125021. DOI: [10.1103/PhysRevD.75.125021](https://doi.org/10.1103/PhysRevD.75.125021). arXiv: [0704.0612](https://arxiv.org/abs/0704.0612) [hep-ph].
- [36] Ian Balitsky and Giovanni A. Chirilli. "Next-to-leading order evolution of color dipoles." In: *Phys. Rev. D* 77 (2008), p. 014019. DOI: [10.1103/PhysRevD.77.014019](https://doi.org/10.1103/PhysRevD.77.014019). arXiv: [0710.4330](https://arxiv.org/abs/0710.4330) [hep-ph].
- [37] E. Iancu, J. D. Madrigal, A. H. Mueller, G. Soyez, and D. N. Triantafyllopoulos. "Resumming double logarithms in the QCD evolution of color dipoles." In: *Phys. Lett. B* 744 (2015), pp. 293–302. DOI: [10.1016/j.physletb.2015.03.068](https://doi.org/10.1016/j.physletb.2015.03.068). arXiv: [1502.05642](https://arxiv.org/abs/1502.05642) [hep-ph].
- [38] R. Keith Ellis, W. James Stirling, and B. R. Webber. "QCD and collider physics." In: *Camb. Monogr. Part. Phys. Nucl. Phys. Cosmol.* 8 (1996), pp. 1–435.
- [39] R. Angeles-Martinez et al. "Transverse Momentum Dependent (TMD) parton distribution functions: status and prospects." In: *Acta Phys. Polon. B* 46.12 (2015), pp. 2501–2534. DOI: [10.5506/APhysPolB.46.2501](https://doi.org/10.5506/APhysPolB.46.2501). arXiv: [1507.05267](https://arxiv.org/abs/1507.05267) [hep-ph].
- [40] V. N. Gribov. "A REGGEON DIAGRAM TECHNIQUE." In: *Sov. Phys. JETP* 26 (1968). [Zh. Eksp. Teor. Fiz.53,654(1967)], pp. 414–422.
- [41] T. Regge. "Introduction to complex orbital momenta." In: *Nuovo Cim.* 14 (1959), p. 951. DOI: [10.1007/BF02728177](https://doi.org/10.1007/BF02728177).

- [42] Eugene Levin. “Everything about Reggeons. Part 1: Reggeons in ‘soft’ interaction.” In: (1997). arXiv: [hep-ph/9710546](#) [[hep-ph](#)].
- [43] Nicol Cartiglia. “Measurement of the proton-proton total cross section at 2, 7, 8 and 57 TeV.” In: *Proceedings, 32nd International Symposium on Physics in Collision (PIC 2012): Strbske Pleso, Slovakia, September 12-15, 2012*. 2013, pp. 55–64. arXiv: [1303.2927](#) [[hep-ex](#)]. URL: <https://inspirehep.net/record/1223517/files/arXiv:1303.2927.pdf>.
- [44] Otto Nachtmann. “Pomeron physics and QCD.” In: *Proceedings, Ringberg Workshop on New Trends in HERA Physics 2003: Ringberg Castle, Tegernsee, Germany, September 28-October 3, 2003*. 2004, pp. 253–267. DOI: [10.1142/9789812702722_0023](#). arXiv: [hep-ph/0312279](#) [[hep-ph](#)].
- [45] P. V. Landshoff. “The Total cross-section at the LHC.” In: *Acta Phys. Polon.* B39 (2008), pp. 2063–2094. arXiv: [0709.0395](#) [[hep-ph](#)].
- [46] J. R. Cudell. “The Total Cross Section at the LHC: Models and Experimental Consequences.” In: *Elastic and Diffractive Scattering. Proceedings, 13th International Conference, Blois Workshop, CERN, Geneva, Switzerland, June 29-July 3, 2009* (2009), pp. 42–47. arXiv: [0911.3508](#) [[hep-ph](#)]. URL: <https://inspirehep.net/record/837249/files/arXiv:0911.3508.pdf>.
- [47] E. A. Kuraev, L. N. Lipatov, and Victor S. Fadin. “The Pomeron singularity in Nonabelian Gauge Theories.” In: *Sov. Phys. JETP* 45 (1977). [*Zh. Eksp. Teor. Fiz.* 72,377(1977)], pp. 199–204.
- [48] I. I. Balitsky and L. N. Lipatov. “The Pomeron singularity in Quantum Chromodynamics.” In: *Sov. J. Nucl. Phys.* 28 (1978). [*Yad. Fiz.* 28,1597(1978)], pp. 822–829.
- [49] Vardan Khachatryan et al. “Measurement of diffraction dissociation cross sections in pp collisions at $\sqrt{s} = 7$ TeV.” In: *Phys. Rev. D* 92.1 (2015), p. 012003. DOI: [10.1103/PhysRevD.92.012003](#). arXiv: [1503.08689](#) [[hep-ex](#)].
- [50] Colin Baus, Johannes Blümer, Günter Quast, and Ralf Ulrich. “Measurements in the Forward Phase-Space with the CMS Experiment and their Impact on Physics of Extensive Air Showers.” Presented 17 Apr 2015. 2015. URL: <http://cds.cern.ch/record/2109249>.
- [51] Eugene Levin. “An Introduction to pomerons.” In: *High energy physics. Proceedings, LAFEX International School, Session C, Workshop on Diffractive Physics, LISHEP’98, Rio de Janeiro, Brazil, February 16-20, 1998*. 1998, pp. 261–336. arXiv: [hep-ph/9808486](#) [[hep-ph](#)].
- [52] Stanley J. Brodsky, Ivan Schmidt, and Jian-Jun Yang. “Nuclear antishadowing in neutrino deep inelastic scattering.” In: *Phys. Rev. D* 70 (2004), p. 116003. DOI: [10.1103/PhysRevD.70.116003](#). arXiv: [hep-ph/0409279](#) [[hep-ph](#)].
- [53] S. Sekula. *Representation of a proton collision event*. URL: [cooleysekula.net](#).

- [54] Morad Aaboud et al. “Measurement of charged-particle distributions sensitive to the underlying event in $\sqrt{s} = 13$ TeV proton-proton collisions with the ATLAS detector at the LHC.” In: *JHEP* 03.CERN-EP-2016-28 (2017), p. 157. DOI: [10.1007/JHEP03\(2017\)157](https://doi.org/10.1007/JHEP03(2017)157). arXiv: [1701.05390](https://arxiv.org/abs/1701.05390) [hep-ex].
- [55] Albert M Sirunyan et al.. “Measurement of the underlying event activity in inclusive Z boson production in proton-proton collisions at $\sqrt{s} = 13$ TeV.” In: CMS-FSQ-16-008. CMS-FSQ-16-008-003 (2017). Submitted to JHEP. All the figures and tables can be found. URL: <https://cds.cern.ch/record/2292613>.
- [56] Markus Diehl, Daniel Ostermeier, and Andreas Schäfer. “Elements of a theory for multiparton interactions in QCD.” In: *Journal of High Energy Physics* 2012.3 (2012), p. 89. ISSN: 1029-8479. DOI: [10.1007/JHEP03\(2012\)089](https://doi.org/10.1007/JHEP03(2012)089). URL: [https://doi.org/10.1007/JHEP03\(2012\)089](https://doi.org/10.1007/JHEP03(2012)089).
- [57] T. Sjostrand and Peter Z. Skands. “Multiple interactions and beam remnants.” In: *Physics at TeV colliders. Proceedings, Workshop, Les Houches, France, May 26-June 3, 2003*. 2004. arXiv: [hep-ph/0401060](https://arxiv.org/abs/hep-ph/0401060) [hep-ph].
- [58] Roel Aaij et al. “Observation of $J/\psi p$ Resonances Consistent with Pentaquark States in $\Lambda_b^0 \rightarrow J/\psi K^- p$ Decays.” In: *Phys. Rev. Lett.* 115 (2015), p. 072001. DOI: [10.1103/PhysRevLett.115.072001](https://doi.org/10.1103/PhysRevLett.115.072001). arXiv: [1507.03414](https://arxiv.org/abs/1507.03414) [hep-ex].
- [59] Bo Andersson, G. Gustafson, G. Ingelman, and T. Sjostrand. “Parton Fragmentation and String Dynamics.” In: *Phys. Rept.* 97 (1983), pp. 31–145. DOI: [10.1016/0370-1573\(83\)90080-7](https://doi.org/10.1016/0370-1573(83)90080-7).
- [60] B. Andersson, G. Gustafson, and C. Peterson. “A semiclassical model for quark jet fragmentation.” In: *Zeitschrift für Physik C Particles and Fields* 1.1 (1979), pp. 105–116. ISSN: 1431-5858. DOI: [10.1007/BF01450386](https://doi.org/10.1007/BF01450386). URL: <https://doi.org/10.1007/BF01450386>.
- [61] R. D. Field and R. P. Feynman. “A Parametrization of the Properties of Quark Jets.” In: *Nucl. Phys.* B136 (1978), p. 1. DOI: [10.1016/0550-3213\(78\)90015-9](https://doi.org/10.1016/0550-3213(78)90015-9).
- [62] Matteo Cacciari, Gavin P. Salam, and Gregory Soyez. “FastJet User Manual.” In: *Eur. Phys. J.* C72 (2012), p. 1896. DOI: [10.1140/epjc/s10052-012-1896-2](https://doi.org/10.1140/epjc/s10052-012-1896-2). arXiv: [1111.6097](https://arxiv.org/abs/1111.6097) [hep-ph].
- [63] Cyrille Marquet. “Forward inclusive dijet production and azimuthal correlations in p(A) collisions.” In: *Nucl. Phys.* A796 (2007), pp. 41–60. DOI: [10.1016/j.nuclphysa.2007.09.001](https://doi.org/10.1016/j.nuclphysa.2007.09.001). arXiv: [0708.0231](https://arxiv.org/abs/0708.0231) [hep-ph].
- [64] Amir H. Rezaeian, Marat Siddikov, Merijn Van de Klundert, and Raju Venugopalan. “Analysis of combined HERA data in the Impact-Parameter dependent Saturation model.” In: *Phys. Rev.* D87.3 (2013), p. 034002. DOI: [10.1103/PhysRevD.87.034002](https://doi.org/10.1103/PhysRevD.87.034002). arXiv: [1212.2974](https://arxiv.org/abs/1212.2974) [hep-ph].

- [65] Javier L. Albacete, Nestor Armesto, Jose Guilherme Milhano, Paloma Quiroga-Arias, and Carlos A. Salgado. “AAMQS: A non-linear QCD analysis of new HERA data at small- x including heavy quarks.” In: *Eur. Phys. J. C* 71 (2011), p. 1705. DOI: [10.1140/epjc/s10052-011-1705-3](#). arXiv: [1012.4408 \[hep-ph\]](#).
- [66] Krzysztof J. Golec-Biernat and M. Wusthoff. “Saturation effects in deep inelastic scattering at low Q^2 and its implications on diffraction.” In: *Phys. Rev. D* 59 (1998), p. 014017. DOI: [10.1103/PhysRevD.59.014017](#). arXiv: [hep-ph/9807513 \[hep-ph\]](#).
- [67] H. Abramowicz et al. “Combination and QCD Analysis of Charm Production Cross Section Measurements in Deep-Inelastic ep Scattering at HERA.” In: *Eur. Phys. J. C* 73.2 (2013), p. 2311. DOI: [10.1140/epjc/s10052-013-2311-3](#). arXiv: [1211.1182 \[hep-ex\]](#).
- [68] Javier L. Albacete, Nestor Armesto, Jose Guilherme Milhano, and Carlos A. Salgado. “Non-linear QCD meets data: A Global analysis of lepton-proton scattering with running coupling BK evolution.” In: *Phys. Rev. D* 80 (2009), p. 034031. DOI: [10.1103/PhysRevD.80.034031](#). arXiv: [0902.1112 \[hep-ph\]](#).
- [69] J. L. Albacete, J. G. Milhano, P. Quiroga-Arias, and J. Rojo. “Linear vs Non-Linear QCD Evolution: From HERA Data to LHC Phenomenology.” In: *Eur. Phys. J. C* 72 (2012), p. 2131. DOI: [10.1140/epjc/s10052-012-2131-x](#). arXiv: [1203.1043 \[hep-ph\]](#).
- [70] H. Fujii, K. Itakura, Y. Kitadono, and Y. Nara. “Forward particle productions at RHIC and the LHC from CGC within local rcBK evolution.” In: *J. Phys. G* 38 (2011), p. 124125. DOI: [10.1088/0954-3899/38/12/124125](#). arXiv: [1107.1333 \[hep-ph\]](#).
- [71] B. Z. Kopeliovich, J. Nemchik, I. K. Potashnikova, M. B. Johnson, and I. Schmidt. “Breakdown of QCD factorization at large Feynman x .” In: *Phys. Rev. C* 72 (2005), p. 054606. DOI: [10.1103/PhysRevC.72.054606](#). arXiv: [hep-ph/0501260 \[hep-ph\]](#).
- [72] Jaroslav Adam et al. “Measurement of charged jet production cross sections and nuclear modification in p-Pb collisions at $\sqrt{s_{NN}} = 5.02$ TeV.” In: *Phys. Lett. B* 749 (2015), pp. 68–81. DOI: [10.1016/j.physletb.2015.07.054](#). arXiv: [1503.00681 \[nucl-ex\]](#).
- [73] Georges Aad et al. “Centrality and rapidity dependence of inclusive jet production in $\sqrt{s_{NN}} = 5.02$ TeV proton-lead collisions with the ATLAS detector.” In: *Phys. Lett. B* 748 (2015), pp. 392–413. DOI: [10.1016/j.physletb.2015.07.023](#). arXiv: [1412.4092 \[hep-ex\]](#).
- [74] Vardan Khachatryan et al. “Measurement of inclusive jet production and nuclear modifications in pPb collisions at $\sqrt{s_{NN}} = 5.02$ TeV.” In: *Eur. Phys. J. C* 76.7 (2016), p. 372. DOI: [10.1140/epjc/s10052-016-4205-7](#). arXiv: [1601.02001 \[nucl-ex\]](#).
- [75] Roel Aaij et al. “Study of Υ production and cold nuclear matter effects in pPb collisions at $\sqrt{s_{NN}} = 5$ TeV.” In: *JHEP* 07 (2014), p. 094. DOI: [10.1007/JHEP07\(2014\)094](#). arXiv: [1405.5152 \[nucl-ex\]](#).
- [76] Vardan Khachatryan et al. “Charged-particle nuclear modification factors in PbPb and pPb collisions at $\sqrt{s_{NN}} = 5.02$ TeV.” In: *JHEP* 04 (2017), p. 039. DOI: [10.1007/JHEP04\(2017\)039](#). arXiv: [1611.01664 \[nucl-ex\]](#).

- [77] Javier L. Albacete, Pablo Guerrero Rodrez, and Yasushi Nara. "Ultraforward particle production from color glass condensate and Lund fragmentation." In: *Phys. Rev. D* 94.5 (2016), p. 054004. DOI: [10.1103/PhysRevD.94.054004](https://doi.org/10.1103/PhysRevD.94.054004). arXiv: [1605.08334](https://arxiv.org/abs/1605.08334) [hep-ph].
- [78] Javier L. Albacete, Adrian Dumitru, Hirotugu Fujii, and Yasushi Nara. "CGC predictions for p + Pb collisions at the LHC." In: *Nucl. Phys. A* 897 (2013), pp. 1–27. DOI: [10.1016/j.nuclphysa.2012.09.012](https://doi.org/10.1016/j.nuclphysa.2012.09.012). arXiv: [1209.2001](https://arxiv.org/abs/1209.2001) [hep-ph].
- [79] A. Accardi et al. "Electron Ion Collider: The Next QCD Frontier." In: *Eur. Phys. J. A* 52.9 (2016). Ed. by A. Deshpande, Z. E. Meziani, and J. W. Qiu, p. 268. DOI: [10.1140/epja/i2016-16268-9](https://doi.org/10.1140/epja/i2016-16268-9). arXiv: [1212.1701](https://arxiv.org/abs/1212.1701) [nucl-ex].
- [80] J L Abelleira Fernandez et al. "A Large Hadron Electron Collider at CERN Report on the Physics and Design Concepts for Machine and Detector." In: *Journal of Physics G: Nuclear and Particle Physics* 39.7 (2012), p. 075001. URL: <http://stacks.iop.org/0954-3899/39/i=7/a=075001>.
- [81] The figure was obtained from: <https://en.wikipedia.org/w/index.php?curid=42671919>.
- [82] The figure was obtained from: https://www.lhc-closer.es/taking_a_closer_look_at_lhc/0.lhc_layout.
- [83] The graph of the LHC dipole magnet was obtained from: <http://cds.cern.ch>.
- [84] Information on the LHC beams was obtained from: https://edms.cern.ch/file/445762/3/Vol3_Chap2_v4.pdf.
- [85] P Odier, M Ludwig, and S Thoulet. "The DCCT for the LHC Beam Intensity Measurement." In: CERN-BE-2009-019 (2009). URL: <https://cds.cern.ch/record/1183400>.
- [86] D. Belohrad, P. Odier, S. Thoulet, and S. Longo. "Mechanical design of the intensity measurement devices for the LHC." In: Beam diagnostics and instrumentation for particle accelerators. Proceedings, 8th European Workshop, DIPAC 2007, Venice, Italy, May 20-23, 2007 (2007), pp. 253–255. URL: <http://web.lib.cern.ch/abstract?CERN-AB-2007-026>.
- [87] The overview graph of the CMS experiment was obtained from: <https://cms.cern/>.
- [88] The graph of the intersection of the CMS experiment was obtained from: http://cylindricalonion.web.cern.ch/sites/cylindricalonion.web.cern.ch/files/users/achintya/particles_bending.gif.
- [89] S. Chatrchyan et al. "The CMS Experiment at the CERN LHC." In: *JINST* 3 (2008), S08004. DOI: [10.1088/1748-0221/3/08/S08004](https://doi.org/10.1088/1748-0221/3/08/S08004).
- [90] S. Chatrchyan et al. "The CMS Experiment at the CERN LHC." In: *JINST* 3 (2008), S08004. DOI: [10.1088/1748-0221/3/08/S08004](https://doi.org/10.1088/1748-0221/3/08/S08004).
- [91] A Holzner. "78 reconstructed vertices in event from high-pileup run 198609." CMS Collection. 2012. URL: <https://cds.cern.ch/record/1479324>.
- [92] M. Albrow et al. "CMS-TOTEM Precision Proton Spectrometer." In: CERN-LHCC-2014-021, TOTEM-TDR-003, CMS-TDR-13 (2014).

- [93] Vardan Khachatryan et al.. “Jet energy scale and resolution in the CMS experiment in pp collisions at 8 TeV.” In: *JINST* 12.CMS-JME-13-004. CERN-PH-EP-2015-305. CMS-JME-13-004 (2016), Po2014. 92 p. URL: <https://cds.cern.ch/record/2198719>.
- [94] R. Brun and F. Rademakers. “ROOT: An object oriented data analysis framework.” In: *Nucl. Instrum. Meth.* A389 (1997), pp. 81–86. DOI: [10.1016/S0168-9002\(97\)00048-X](https://doi.org/10.1016/S0168-9002(97)00048-X).
- [95] S. Agostinelli et al. “Geant4 a simulation toolkit.” In: *Nuclear Instruments and Methods in Physics Research Section A: Accelerators, Spectrometers, Detectors and Associated Equipment* 506.3 (2003), pp. 250–303. ISSN: 0168-9002. DOI: [http://dx.doi.org/10.1016/S0168-9002\(03\)01368-8](http://dx.doi.org/10.1016/S0168-9002(03)01368-8). URL: <http://www.sciencedirect.com/science/article/pii/S0168900203013688>.
- [96] Wolfgang Waltenberger. “Adaptive Vertex Reconstruction.” In: CMS-NOTE-2008-033 (2008). URL: <https://cds.cern.ch/record/1166320>.
- [97] Richard Wigmans. *Calorimetry*. International Series of Monographs on Physics. Oxford University Press, 2017. ISBN: 9780198786351.
- [98] *The CASTOR website (restricted) can be found at:* <https://twiki.cern.ch/twiki/bin/view/CMS/CASTOR>.
- [99] A. L. S. Angelis and A. D. Panagiotou. “CASTOR: A dedicated detector for the detection of centauros and strangelets at the LHC.” In: *J. Phys. G* 23 (1997), pp. 2069–2080. DOI: [10.1088/0954-3899/23/12/032](https://doi.org/10.1088/0954-3899/23/12/032).
- [100] Xenofon Aslanoglou et al. *Performance studies of the final prototype for the CASTOR forward calorimeter at the CMS experiment*. Tech. rep. CMS-NOTE-2008-022. Geneva: CERN, 2008. URL: <https://cds.cern.ch/record/1127566>.
- [101] Igor Katkov. “Physics with the CMS forward CASTOR calorimeter.” In: CMS-CR-2011-008 (2011). URL: <http://cds.cern.ch/record/1322141>.
- [102] Peter Götlicher. “Design and test beam studies for the CASTOR calorimeter of the CMS experiment.” In: *Nuclear Instruments and Methods in Physics Research Section A: Accelerators, Spectrometers, Detectors and Associated Equipment* 623.1 (2010). 1st International Conference on Technology and Instrumentation in Particle Physics, pp. 225 – 227. ISSN: 0168-9002. DOI: <https://doi.org/10.1016/j.nima.2010.02.203>. URL: <http://www.sciencedirect.com/science/article/pii/S0168900210004882>.
- [103] Vardan Khachatryan et al. “Measurement of the inelastic cross section in proton-lead collisions at $\sqrt{s_{\text{NN}}} = 5.02$ TeV.” In: *Phys. Lett. B* 759.CMS-FSQ-13-006. CERN-PH-EP-2015-210. CMS-FSQ-13-006-003 (2015), 641. 22 p. URL: <https://cds.cern.ch/record/2052029>.
- [104] *Measurement of the inelastic proton-proton cross section at $\sqrt{s} = 13$ TeV*. Tech. rep. CMS-PAS-FSQ-15-005. Geneva: CERN, 2016. URL: <https://cds.cern.ch/record/2145896>.
- [105] X. Aslanoglou et al. “Performance studies of prototype II for the CASTOR forward calorimeter at the CMS experiment.” In: *The European Physical Journal C* 52.2 (2007), pp. 495–506. ISSN: 1434-6052. DOI: [10.1140/epjc/s10052-007-0380-x](https://doi.org/10.1140/epjc/s10052-007-0380-x). URL: <https://doi.org/10.1140/epjc/s10052-007-0380-x>.

- [106] “CASTOR very forward calorimeter performance in 2013 data in pPb and pp collisions.” In: *CMS-DP-2013-035* (2013). URL: <https://cds.cern.ch/record/1632684>.
- [107] “Measurement of the pseudorapidity and centrality dependence of the very forward energy density in PbPb collisions at $\sqrt{s}=2.76$ TeV.” In: *CMS-PAS-HIN-12-006* (2012). URL: <https://cds.cern.ch/record/1472732>.
- [108] “Measurement of the energy distribution in the very forward direction at 13 TeV with CMS.” In: *CMS-PAS-FSQ-16-002* (2016). URL: <https://cds.cern.ch/record/2145374>.
- [109] “Measurement of the very forward inclusive jet cross section in pp collisions at $\sqrt{s} = 7$ TeV.” In: *CMS-PAS-FSQ-12-023* (2016). URL: <https://cds.cern.ch/record/2146008>.
- [110] “Measurement of the very forward inclusive jet cross section in pp collisions at $\sqrt{s} = 13$ TeV with CMS.” In: *CMS-PAS-FSQ-16-003* (2016). URL: <http://cds.cern.ch/record/2146006>.
- [111] “Jet Energy Corrections determination at 7 TeV.” In: *CMS-PAS-JME-10-010* (2010). URL: <https://cds.cern.ch/record/1308178>.
- [112] Merijn H F Van De Klundert. *Performance of the CASTOR calorimeter at CMS during Run II of LHC*. Tech. rep. CMS-CR-2016-156. Geneva: CERN, 2016. URL: <https://cds.cern.ch/record/2203099>.
- [113] Serguei Chatrchyan et al. “Study of the underlying event at forward rapidity in pp collisions at $\sqrt{s} = 0.9, 2.76$, and 7 TeV.” In: *JHEP* 04 (2013), p. 072. DOI: [10.1007/JHEP04\(2013\)072](https://doi.org/10.1007/JHEP04(2013)072). arXiv: [1302.2394](https://arxiv.org/abs/1302.2394) [hep-ex].
- [114] Albert M Sirunyan et al. “Measurement of the inclusive energy spectrum in the very forward direction in proton-proton collisions at $\sqrt{s} = 13$ TeV.” In: *JHEP* 08 (2017), p. 046. DOI: [10.1007/JHEP08\(2017\)046](https://doi.org/10.1007/JHEP08(2017)046). arXiv: [1701.08695](https://arxiv.org/abs/1701.08695) [hep-ex].
- [115] T. Pierog, Iu. Karpenko, J. M. Katzy, E. Yatsenko, and K. Werner. “EPOS LHC: Test of collective hadronization with data measured at the CERN Large Hadron Collider.” In: *Phys. Rev. C* 92.3 (2015), p. 034906. DOI: [10.1103/PhysRevC.92.034906](https://doi.org/10.1103/PhysRevC.92.034906). arXiv: [1306.0121](https://arxiv.org/abs/1306.0121) [hep-ph].
- [116] Xin-Nian Wang and Miklos Gyulassy. “hijing.” In: *Phys. Rev. D* 44 (11 1991), pp. 3501–3516. DOI: [10.1103/PhysRevD.44.3501](https://doi.org/10.1103/PhysRevD.44.3501). URL: <http://link.aps.org/doi/10.1103/PhysRevD.44.3501>.
- [117] Ostapchenko, S. “QGSJET-II: physics, recent improvements, and results for air showers.” In: *EPJ Web of Conferences* 52 (2013), p. 02001. DOI: [10.1051/epjconf/20125202001](https://doi.org/10.1051/epjconf/20125202001). URL: <http://dx.doi.org/10.1051/epjconf/20125202001>.
- [118] Torbjörn Sjöstrand et al. “An introduction to PYTHIA 8.2.” In: *Computer Physics Communications* 191 (2015), pp. 159–177. ISSN: 0010-4655. DOI: [http://dx.doi.org/10.1016/j.cpc.2015.01.024](https://doi.org/10.1016/j.cpc.2015.01.024). URL: [//www.sciencedirect.com/science/article/pii/S0010465515000442](http://www.sciencedirect.com/science/article/pii/S0010465515000442).
- [119] Tanguy Pierog and Klaus Werner. “Parton Saturation and Hydrodynamics in EPOS 3.” In: *Acta Phys. Polon. Supp.* 8 (2015), p. 1031. DOI: [10.5506/APhysPolBSupp.8.1031](https://doi.org/10.5506/APhysPolBSupp.8.1031).

- [120] Sergey Ostapchenko. “Monte Carlo treatment of hadronic interactions in enhanced Pomeron scheme: I. QGSJET-II model.” In: *Phys. Rev. D* 83 (2011), p. 014018. DOI: [10.1103/PhysRevD.83.014018](https://doi.org/10.1103/PhysRevD.83.014018). arXiv: [1010.1869](https://arxiv.org/abs/1010.1869) [hep-ph].
- [121] B. Andersson, G. Gustafson, and B. Nilsson-Almqvist. “A model for low-pT hadronic reactions with generalizations to hadron-nucleus and nucleus-nucleus collisions.” In: *Nuclear Physics B* 281.1 (1987), pp. 289–309. ISSN: 0550-3213. DOI: [http://dx.doi.org/10.1016/0550-3213\(87\)90257-4](http://dx.doi.org/10.1016/0550-3213(87)90257-4). URL: <http://www.sciencedirect.com/science/article/pii/0550321387902574>.
- [122] A. Capella, U. Sukhatme, and Z. J. Tran Thanh Van. In: *Phys. C* 3, 329 (1980) 329.3 (1980).
- [123] A.H. Mueller and Jianwei Qiu. “Gluon recombination and shadowing at small values of x.” In: *Nuclear Physics B* 268.2 (1986), pp. 427–452. ISSN: 0550-3213. DOI: [http://dx.doi.org/10.1016/0550-3213\(86\)90164-1](http://dx.doi.org/10.1016/0550-3213(86)90164-1). URL: <http://www.sciencedirect.com/science/article/pii/0550321386901641>.
- [124] Frank E. Close, Jianwei Qiu, and R. G. Roberts. “QCD parton recombination and applications to nuclear structure functions.” In: *Phys. Rev. D* 40 (9 1989), pp. 2820–2831. DOI: [10.1103/PhysRevD.40.2820](https://doi.org/10.1103/PhysRevD.40.2820). URL: <https://link.aps.org/doi/10.1103/PhysRevD.40.2820>.
- [125] Leonid Frankfurt and Mark Strikman. “Hard nuclear processes and microscopic nuclear structure.” In: *Physics Reports* 160.5 (1988), pp. 235–427. ISSN: 0370-1573. DOI: [https://doi.org/10.1016/0370-1573\(88\)90179-2](https://doi.org/10.1016/0370-1573(88)90179-2). URL: <http://www.sciencedirect.com/science/article/pii/0370157388901792>.
- [126] J. Ashman et al. “Measurement of the ratios of deep inelastic muon-nucleus cross sections on various nuclei compared to deuterium.” In: *Physics Letters B* 202.4 (1988), pp. 603–610. ISSN: 0370-2693. DOI: [https://doi.org/10.1016/0370-2693\(88\)91872-2](https://doi.org/10.1016/0370-2693(88)91872-2). URL: <http://www.sciencedirect.com/science/article/pii/0370269388918722>.
- [127] P. et al. Amaudruz. “Precision measurement of structure function ratios for ^6Li , ^{12}C and ^{40}Ca .” In: *Zeitschrift für Physik C Particles and Fields* 53.1 (1992), pp. 73–77. ISSN: 1431-5858. DOI: [10.1007/BF01483873](https://doi.org/10.1007/BF01483873). URL: <https://doi.org/10.1007/BF01483873>.
- [128] S. Catani, M. Ciafaloni, and F. Hautmann. “High energy factorization and small-x heavy flavour production.” In: *Nuclear Physics B* 366.1 (1991), pp. 135–188. ISSN: 0550-3213. DOI: [http://dx.doi.org/10.1016/0550-3213\(91\)90055-3](http://dx.doi.org/10.1016/0550-3213(91)90055-3). URL: <http://www.sciencedirect.com/science/article/pii/0550321391900553>.
- [129] M. Deak, F. Hautmann, H. Jung, and K. Kutak. “Forward Jet Production at the Large Hadron Collider.” In: *JHEP* 09 (2009), p. 121. DOI: [10.1088/1126-6708/2009/09/121](https://doi.org/10.1088/1126-6708/2009/09/121). arXiv: [0908.0538](https://arxiv.org/abs/0908.0538) [hep-ph].
- [130] Krzysztof Kutak, Hans Van Haevermaet, and Pierre Van Mechelen. “Single inclusive jet transverse momentum and energy spectra at very forward rapidity in proton-proton collisions with $\sqrt{s} = 7$ and 13 TeV.” In: *Phys. Lett. B* 770 (2017), pp. 412–417. DOI: [10.1016/j.physletb.2017.05.009](https://doi.org/10.1016/j.physletb.2017.05.009). arXiv: [1701.07370](https://arxiv.org/abs/1701.07370) [hep-ph].

- [131] E. A. Kuraev, L. N. Lipatov, and Victor S. Fadin. "Multi - Reggeon Processes in the Yang-Mills Theory." In: *Sov. Phys. JETP* 44 (1976). [*Zh. Eksp. Teor. Fiz.* 71,840(1976)], pp. 443–450.
- [132] I. Balitsky. "Operator expansion for high-energy scattering." In: *Nucl. Phys.* B463 (1996), pp. 99–160. DOI: [10.1016/0550-3213\(95\)00638-9](https://doi.org/10.1016/0550-3213(95)00638-9). arXiv: [hep-ph/9509348](https://arxiv.org/abs/hep-ph/9509348) [[hep-ph](#)].
- [133] Yuri V. Kovchegov. "Small- x F_2 structure function of a nucleus including multiple Pomeron exchanges." In: *Phys. Rev. D* 60 (3 1999), p. 034008. DOI: [10.1103/PhysRevD.60.034008](https://doi.org/10.1103/PhysRevD.60.034008). URL: <https://link.aps.org/doi/10.1103/PhysRevD.60.034008>.
- [134] Hung-Liang Lai, Marco Guzzi, Joey Huston, Zhao Li, Pavel M. Nadolsky, Jon Pumplin, and C. P. Yuan. "New parton distributions for collider physics." In: *Phys. Rev.* D82 (2010), p. 074024. DOI: [10.1103/PhysRevD.82.074024](https://doi.org/10.1103/PhysRevD.82.074024). arXiv: [1007.2241](https://arxiv.org/abs/1007.2241) [[hep-ph](#)].
- [135] A. van Hameren. "KaTie : For parton-level event generation with k_T -dependent initial states." In: *Comput. Phys. Commun.* 224 (2018), pp. 371–380. DOI: [10.1016/j.cpc.2017.11.005](https://doi.org/10.1016/j.cpc.2017.11.005). arXiv: [1611.00680](https://arxiv.org/abs/1611.00680) [[hep-ph](#)].
- [136] H. Jung et al. "The CCFM Monte Carlo generator CASCADE version 2.2.03." In: *Eur. Phys. J.* C70 (2010), pp. 1237–1249. DOI: [10.1140/epjc/s10052-010-1507-z](https://doi.org/10.1140/epjc/s10052-010-1507-z). arXiv: [1008.0152](https://arxiv.org/abs/1008.0152) [[hep-ph](#)].
- [137] J. Pumplin, D. R. Stump, J. Huston, H. L. Lai, Pavel M. Nadolsky, and W. K. Tung. "New generation of parton distributions with uncertainties from global QCD analysis." In: *JHEP* 07 (2002), p. 012. DOI: [10.1088/1126-6708/2002/07/012](https://doi.org/10.1088/1126-6708/2002/07/012). arXiv: [hep-ph/0201195](https://arxiv.org/abs/hep-ph/0201195) [[hep-ph](#)].
- [138] T. Pierog, C. Baus, and R. Ulrich. *The CRMC program can be found at:* <https://web.ikp.kit.edu/rulrich/crmc.html>.
- [139] Spencer R. Klein and Joakim Nystrand. "Exclusive vector meson production in relativistic heavy ion collisions." In: *Phys. Rev. C* 60 (1 1999), p. 014903. DOI: [10.1103/PhysRevC.60.014903](https://doi.org/10.1103/PhysRevC.60.014903). URL: <http://link.aps.org/doi/10.1103/PhysRevC.60.014903>.
- [140] W Kienzle et al. *TOTEM, Total Cross Section, Elastic Scattering and Diffraction Dissociation at the LHC: Technical Proposal*. Tech. rep. CERN-LHCC-99-007. LHCC-P-5. Geneva: CERN, 1999. URL: <https://cds.cern.ch/record/385483>.
- [141] "Alignment of CASTOR with 2013 pA TOTEM-Data." In: *CMS-DP-2014-014* (2014). URL: <https://cds.cern.ch/record/1697694>.
- [142] Torbjorn Sjostrand, Stephen Mrenna, and Peter Z. Skands. "A Brief Introduction to PYTHIA 8.1." In: *Comput. Phys. Commun.* 178 (2008), pp. 852–867. DOI: [10.1016/j.cpc.2008.01.036](https://doi.org/10.1016/j.cpc.2008.01.036). arXiv: [0710.3820](https://arxiv.org/abs/0710.3820) [[hep-ph](#)].
- [143] Richard Corke and Torbjorn Sjostrand. "Interleaved Parton Showers and Tuning Prospects." In: *JHEP* 03 (2011), p. 032. DOI: [10.1007/JHEP03\(2011\)032](https://doi.org/10.1007/JHEP03(2011)032). arXiv: [1011.1759](https://arxiv.org/abs/1011.1759) [[hep-ph](#)].
- [144] Matteo Cacciari, Gavin P. Salam, and Gregory Soyez. "The Anti- $k(t)$ jet clustering algorithm." In: *JHEP* 04 (2008), p. 063. DOI: [10.1088/1126-6708/2008/04/063](https://doi.org/10.1088/1126-6708/2008/04/063). arXiv: [0802.1189](https://arxiv.org/abs/0802.1189) [[hep-ph](#)].

- [145] Alex van Spilbeeck and Benoit Roland. *The identification criteria were derived originally by Benoit Roland for pions and electrons, and later revised for jets by Alex van Spilbeeck. Regrettably, the cuts are CMS-restricted.*
- [146] Alex van Spilbeeck. *Study of the very forward jet energy spectrum in proton-proton collisions at $\sqrt{s} = 7$ TeV with the CASTOR calorimeter at the CMS experiment.* URL: <https://repository.uantwerpen.be/desktop/irua/core/index.phtml?language=&user=&session=&service=opacirua&robot=&deskservice=desktop&desktop=irua&workstation=&extra=loi=c:irua:144023>.
- [147] Alex Van Spilbeeck, Hans Van Haeveermaet, Pierre Van Mechelen, and Merijn van de Klundert. "Determination of the CASTOR jet energy scale from MC simulation at 7 TeV." In: CMS AN-2016/060 (2016). This note is restricted to CMS users.
- [148] G. Cowan. "A survey of unfolding methods for particle physics." In: *Conf. Proc. C0203181* (2002). [248(2002)], pp. 248–257.
- [149] CMS statistics committee. *The (restricted) website of the CMS statistics committee on unfolding*: <https://twiki.cern.ch/twiki/bin/view/CMS/ScrecUnfolding>.
- [150] G. D'Agostini. "A multidimensional unfolding method based on Bayes' theorem." In: *Nuclear Instruments and Methods in Physics Research Section A: Accelerators, Spectrometers, Detectors and Associated Equipment* 362.2 (1995), pp. 487–498. ISSN: 0168-9002. DOI: [https://doi.org/10.1016/0168-9002\(95\)00274-X](https://doi.org/10.1016/0168-9002(95)00274-X). URL: <http://www.sciencedirect.com/science/article/pii/016890029500274X>.
- [151] Tim Adye. "Unfolding algorithms and tests using RooUnfold." In: arXiv:1105.1160 (2011). Comments: 6 pages, 5 figures, presented at PHYSTAT 2011, CERN, Geneva, Switzerland, January 2011, to be published in a CERN Yellow Report, 6 p. URL: <https://cds.cern.ch/record/1349242>.
- [152] "Luminosity Calibration for the 2013 Proton-Lead and Proton-Proton Data Taking." In: CMS-PAS-LUM-13-002 (2014). URL: <https://cds.cern.ch/record/1643269>.
- [153] Edmond Iancu. "Resumming large collinear logarithms in the non-linear QCD evolution at high energy." In: *PoS QCDEV2016* (2017), p. 009.
- [154] *The Twiki page of CASTOR (restricted) can be found at: <https://twiki.cern.ch/twiki/bin/view/CMS/CASTOR>.*

COLOPHON

This document was typeset using the typographical look-and-feel classicthesis developed by André Miede. The style was inspired by Robert Bringhurst's seminal book on typography *"The Elements of Typographic Style"*.